Sensitivities to neutrino non-standard interactions from the disappearance of muon (anti)neutrinos at the NOvA experiment

LUIZ RICARDO PRAIS

Physics Graduate Program

Institute of Physics

Federal University of Goias

Thesis presented as a partial fulfillment of the requirements for the degree of

Master of Physics

GOIÂNIA

2020

UNIVERSIDADE FEDERAL DE GOIÁS
INSTITUTO DE FÍSICA

TERMO DE CIÊNCIA E DE AUTORIZAÇÃO (TECA) PARA DISPONIBILIZAR VERSÕES ELETRÔNICAS DE TESES

E DISSERTAÇÕES NA BIBLIOTECA DIGITAL DA UFG

Na qualidade de titular dos direitos de autor, autorizo a Universidade Federal de Goiás (UFG) a disponibilizar, gratuitamente, por meio da Biblioteca Digital de Teses e Dissertações (BDTD/UFG), regulamentada pela Resolução CEPEC nº 832/2007, sem ressarcimento dos direitos autorais, de acordo com a Lei 9.610/98, o documento conforme permissões assinaladas abaixo, para fins de leitura, impressão e/ou download, a título de divulgação da produção científica brasileira, a partir desta data.

O conteúdo das Teses e Dissertações disponibilizado na BDTD/UFG é de responsabilidade exclusiva do autor. Ao encaminhar o produto final, o autor(a) e o(a) orientador(a) firmam o compromisso de que o trabalho não contém nenhuma violação de quaisquer direitos autorais ou outro direito de terceiros.

1. Identificação do material bibliográfico

[X] Dissertação [ ] Tese

2. Nome completo do autor

Luiz Ricardo Prais

3. Título do trabalho

Sensitivities to neutrino non-standard interactions from the disappearance of muon (anti)neutrinos at the NOvA experiment

4. Informações de acesso ao documento (este campo deve ser preenchido pelo orientador)

Concorda com a liberação total do documento [X] SIM [ ] NÃO[1]

[1] Neste caso o documento será embargado por até um ano a partir da data de defesa. Após esse período, a possível disponibilização ocorrerá apenas mediante:
a) consulta ao(à) autor(a) e ao(à) orientador(a);
b) novo Termo de Ciência e de Autorização (TECA) assinado e inserido no arquivo da tese ou dissertação.
O documento não será disponibilizado durante o período de embargo.
Casos de embargo:
- Solicitação de registro de patente;
- Submissão de artigo em revista científica;
- Publicação como capítulo de livro;
- Publicação da dissertação/tese em livro.

Obs. Este termo deverá ser assinado no SEI pelo orientador e pelo autor.

Documento assinado eletronicamente por **Ricardo Avelino Gomes**, **Professor do Magistério Superior**, em 10/11/2020, às 17:39, conforme horário oficial de Brasília, com fundamento no art. 6º, § 1º, do Decreto nº 8.539, de 8 de outubro de 2015.

Documento assinado eletronicamente por **LUIZ RICARDO PRAIS**, **Discente**, em 10/11/2020, às 19:12, conforme horário oficial de Brasília, com fundamento no art. 6º, § 1º, do Decreto nº 8.539, de 8 de outubro de 2015.

A autenticidade deste documento pode ser conferida no site https://sei.ufg.br/sei/controlador_externo.php?acao=documento_conferir&id_orgao_acesso_externo=0, informando o código verificador **1670002** e o código CRC **73509526**.

Referência: Processo nº 23070.044500/2020-87 SEI nº 1670002

UNIVERSIDADE FEDERAL DE GOIÁS

Instituto de Física

Programa de Pós-Graduação em Física

LUIZ RICARDO PRAIS

Sensitivities to neutrino non-standard interactions from the disappearance of muon (anti)neutrinos at the NOvA experiment

Thesis submitted to the Physics Graduate Program of the Institute of Physics at the Federal University of Goias, in partial fulfillment for the degree of Master of Physics, under the adivising of Prof. Dr. Ricardo Avelino Gomes.

Goiânia - GO

2020

Ficha de identificação da obra elaborada pelo autor, através do
Programa de Geração Automática do Sistema de Bibliotecas da UFG.

Prais, Luiz Ricardo
Sensitivities to neutrino non-standard interactions from the disappearance of muon (anti)neutrinos at the NOvA experiment [manuscrito] / Luiz Ricardo Prais. - 2020.
134 f.: il.

Orientador: Prof. Dr. Ricardo Avelino Gomes.
Dissertação (Mestrado) - Universidade Federal de Goiás, Instituto de Física (IF), Programa de Pós-Graduação em Física, Goiânia, 2020.
Bibliografia. Apêndice.
Inclui siglas, fotografias, abreviaturas, símbolos, gráfico, tabelas, lista de figuras, lista de tabelas.

1. Oscilações de neutrinos. 2. Interações não-padrão. 3. Neutrinos de aceleradores. I. Gomes, Ricardo Avelino, orient. II. Título.

CDU 539.12

UNIVERSIDADE FEDERAL DE GOIÁS

INSTITUTO DE FÍSICA

ATA DE DEFESA DE DISSERTAÇÃO

Ata nº 187 da sessão de Defesa de Dissertação de Luiz Ricardo Prais, que confere o título de Mestre em Física, na área de concentração em Física.

Aos 13 dias do mês de outubro de 2020, a partir das 14h30min, por meio de videoconferência, realizou-se a sessão pública de Defesa de Dissertação intitulada “Sensitivities to neutrino non-standard interactions from the disappearance of muon (anti)neutrinos at the NOvA experiment”. Os trabalhos foram instalados pelo Orientador, Professor Doutor Ricardo Avelino Gomes (IF/UFG), com a participação dos demais membros da Banca Examinadora: Professor Doutor Hélio da Motta Filho (CBPF), membro titular externo; e Professor Doutor Celio Adrega de Moura Junior (CCNH/UFABC), membro titular externo. Durante a arguição, os membros da banca não fizeram sugestão de alteração do título do trabalho. A Banca Examinadora reuniu-se em sessão secreta a fim de concluir o julgamento da Dissertação, tendo sido o candidato aprovado pelos seus membros. Proclamados os resultados pelo Professor Doutor Ricardo Avelino Gomes, Presidente da Banca Examinadora, foram encerrados os trabalhos e, para constar, lavrou-se a presente ata que é assinada pelos Membros da Banca Examinadora.

TÍTULO SUGERIDO PELA BANCA

Documento assinado eletronicamente por **Celio Adrega de Moura Junior**, **Usuário Externo**, em 10/11/2020, às 15:06, conforme horário oficial de Brasília, com fundamento no art. 6º, § 1º, do Decreto nº 8.539, de 8 de outubro de 2015.

Documento assinado eletronicamente por **Ricardo Avelino Gomes**, **Professor do Magistério Superior**, em 10/11/2020, às 15:38, conforme horário oficial de Brasília, com fundamento no art. 6º, § 1º, do Decreto nº 8.539, de 8 de outubro de 2015.

Documento assinado eletronicamente por **Hélio da Motta Filho**, **Usuário Externo**, em 10/11/2020, às 15:55, conforme horário oficial de Brasília, com fundamento no art. 6º, § 1º, do Decreto nº 8.539, de 8 de outubro de 2015.

A autenticidade deste documento pode ser conferida no site https://sei.ufg.br/sei/controlador_externo.php?acao=documento_conferir&id_orgao_acesso_externo=0, informando o código verificador **1669119** e o código CRC **5F400284**.

Referência: Processo nº 23070.044500/2020-87 SEI nº 1669119

To my grandmother, Toninha (in memoriam), who always warmed my heart and believed that I would see the Universe.

Acknowledgements

I would like to thank my parents, Luiz Fernando and Adriana, and my brothers, Adriano and Gabriel, for all the support, encouraging, and moments of distraction in family, evidencing the importance of the loved ones during challenging times.

To my beloved partner, Aryanny, I sincerely leave my deep gratitude for her unconditional love and comprehension. Our happy moments and uncountable cooking nights provided me a place where I could find peace and rest when in need.

I am thankful to my supervisor, Ricardo, not only for the precise and rich mentoring in Physics or how to become a good researcher, but also for being a source of inspiration on how to fight for our goals.

I would like to thank my housemates and colleagues from the HEP group at Goias, Abner and Sheldon, for the enlightening conversations on neutrino physics that we had, and also for the friendship and joyful moments. I am also deeply grateful to Stefano Tognini, also member of our HEP group, for his surprising patience and altruism that helped me on uncountable moments, be it on physics or life advice.

My colleagues from the physics graduate program at UFG made my course path more clear and colorful through our regular coffees and philosophical discussions about the universe, life, and personal dreams, which I am thankful to have known each of them. I leave also my gratitude to the staff of the Institute of Physics, always working hard and with effectiveness to attend the numerous daily needs from the students.

I have a profound feeling of gratitude to the whole Fermilab team and the NOvA collaboration. I would like to specially thank Mario Acero and Rijeesh Keloth for the enormous amount of help and discussions during our analysis. Working with them made me realise the real meaning of *collaboration*. I am also pleased to have worked with Gavin Davies, Adam Aurisano, and Brian Rebel, committed scientists who provided me plenty of knowledge and suggestions through our group meetings. To all members of the NOvA collaboration, my sincerely thank you for the support and friendship raised during the months.

I am beyond grateful to the Brazilian *National Council for Scientific and Technological Development* (CNPq, *Conselho Nacional de Desenvolvimento Científico e Tecnológico*) for the scholarship and funding (process 131612/2018-2), without which I have no doubts that this work would be possible to be performed.

Finally, my genuine thank you to everyone who, one way or another, was by my side and believed in this accomplishment.

The best that most of us can hope to achieve in physics is simply to misunderstand at a deeper level
(Wolfgang Pauli)

Abstract

The experimental confirmation of the phenomenon of neutrino oscillations provided evidence for a non-zero value for the mass of neutrinos, a property not initially predicted by the Standard Model of Physics. Investigations of the existence of the so called Physics Beyond the Standard Model is a subject of growing interest and effort in the field of particle physics. Interactions of neutrinos with matter are well described by the Standard Model, however in the presence of new Physics, additional phenomena regarding neutrino properties would be possible, including non-standard interactions of neutrinos with matter. The NOvA experiment, at Fermilab, has been investigating neutrino oscillations through studies of ν_μ produced at the Fermilab accelerator facilities, and also comprise a suitable environment for investigation of additional phenomena taking part in the neutrino oscillation framework. We show in this thesis the results of the sensitivity studies to neutrino non-standard interactions in the NOvA experiment through investigation of the disappearance of muon (anti)neutrinos during their evolution in the NOvA 810 km baseline. We investigate the effect of the NSI parameters, $|\varepsilon_{\mu\tau}|$ and $\delta_{\mu\tau}$, on the determination of the standard oscillation parameters $\sin^2(\theta_{23})$ and Δm^2_{32}, as well as the relation between each parameter, for both neutrino mass hierarchies. This study makes use of an exposure of 9.48×10^{20} POT for neutrino beam (FHC), and 12.33×10^{20} POT for antineutrino beam (RHC). No deviations from the standard oscillation scenario is found at the 90% CL limit. The joint neutrino and antineutrino fit yields a limit of $|\varepsilon_{\mu\tau}| \leq 0.086$ (0.085) for a fixed value of $\delta_{\mu\tau} = 0$, and $|\varepsilon_{\mu\tau}| \leq 1.054$ (1.053) for the case where both NSI parameters are fitted, for the normal (inverted) neutrino mass hierarchy, at the 90% CL. In the current sensitivity, all values of $\delta_{\mu\tau}$ are found to be allowed. The 90% CL interval for the standard oscillation parameters are $\Delta m^2_{32} \in [2.379, 2.580]$ and $\sin^2(\theta_{23}) \in [0.420, 0.602]$ for the normal hierarchy scenario, and $\Delta m^2_{32} \in [-2.639, -2.438]$ and $\sin^2(\theta_{23}) \in [0.418, 0.602]$ for the inverted hierarchy scenario.

Keywords: Neutrino oscillations. Non-standard interactions. Accelerator neutrinos.

Resumo

A confirmação experimental do fenômeno de oscilações de neutrinos fornece evidência para um valor não nulo para a massa dos neutrinos, uma propriedade inicialmente não incluída no Modelo Padrão da Física de Partículas. Investigações acerca da existência da chamada Física Além do Modelo Padrão é tópico de crescente interesse e esforço no campo da física de partículas. Interações de neutrinos com a matéria são bem descritas pelo Modelo Padrão, porém, em presença de uma nova física, fenômenos adicionais são passíveis de serem observados, tais como interações não-padrão de neutrinos com a matéria (NSI). O experimento NOvA, sediado no Fermilab, tem investigado as oscilações de neutrinos através de estudos de ν_μ produzidos pelo complexo de aceleradores do Fermilab, e fornece também um ambiente adequado para investigações de fenômenos adicionais que podem coexistir dentro do contexto das oscilações de neutrinos. Nesta dissertação mostramos os resultados dos estudos de sensibilidade a interações não-padrão de neutrinos com a matéria no experimento NOvA, através de investigações do desaparecimento de (anti)neutrinos do muon a medida que estes evoluem pela linha de feixe de 810km do experimento. Nós investigamos os efeitos dos parâmetros não-padrão $|\varepsilon_{\mu\tau}|$ e $\delta_{\mu\tau}$ na determinação dos parâmetros de oscilação $\text{sen}^2(\theta_{23})$ e Δm^2_{32}, bem como as relações entre cada um dos parâmetros, para os dois cenários de hierarquia de massa dos neutrinos. Este estudo faz uso de uma exposição de 9.48×10^{20} POT no modo de feixe de neutrinos (FHC) e 12.33×10^{20} POT no modo de feixe de antineutrinos (RHC). Não são observados desvios do modelo de interação padrão no limite de 90% de nível de confiança. A análise conjunta de neutrinos e antineutrinos fornece um limite superior de $|\varepsilon_{\mu\tau}| \leq 0.086$ (0.085) para um valor fixo de $\delta_{\mu\tau} = 0$, e $|\varepsilon_{\mu\tau}| \leq 1.054$ (1.053) no cenário onde ambos os parâmetros NSI são ajustados ao fit, para a hierarquia normal (invertida) de massa dos neutrinos, no limite de 90% de nível de confiança. Na presente sensibilidade, todos os valores de $\delta_{\mu\tau}$ são permitidos. O intervalo de valores permitidos para os parâmetros de oscilação padrão, no limite de 90% de nível de confiança, são $\Delta m^2_{32} \in [2.379, 2.580]$ e $\text{sen}^2(\theta_{23}) \in [0.420, 0.602]$ para o cenário de hierarquia de massa normal, e $\Delta m^2_{32} \in [-2.639, -2.438]$ e $\text{sen}^2(\theta_{23}) \in [0.418, 0.602]$ para o cenário de hierarquia de massa invertida.

Palavras-chave: Oscilações de neutrinos. Interações não-padrão. Neutrinos de aceleradores.

List of Figures

List of Tables

List of Acronyms and Abbreviations

APD Avalanche Photodiode . . . 53

CP Charge-Parity . . . 26

CC Charged Current . . . 22

CC-NSI Charged Current-like NSI . . . 37

CL Confidence Level . . . 40

DONUT Direct Observation of the Nu Tau . . . 19

FD Far Detector . . . 46

FHC Forward Horn Current . . . 50

IH Inverted Hierarchy . . . 35

LFU Lepton Flavor Universality . . . 38

MINOS Main Injector Neutrino Oscillation Search . . . 42

ND Near Detector . . . 46

NC Neutral Current . . . 22

NC-NSI Neutral Current-like NSI . . . 37

NuMI Neutrinos at the Main Injector . . . 47

Contents

Introduction

Neutrinos are among the most abundant particles in the cosmos, and have starred a series of important discoveries, compiling a couple of Nobel Prizes in Physics and leading a worldwide effort towards large scale experiments. Neutrinos are known to possess energies ranging from a few MeV to up $\mathcal{O}\left(10^{15}\text{eV}\right)$, being produced in a variety of sources, such as nuclear reactors, stellar core, cosmic ray interactions with the atmosphere, and even bananas. Despite of its abundance and variety of sources, the physical properties and the elusive characteristic of neutrinos require an impressive instrumentation at the frontier of Science and Technology in order to study this particle.

Since its discovery, neutrinos have been widely studied through several experiments around the world, and yet many questions remain unanswered. The observation of the phenomenon of neutrino oscillations is a direct evidence for the existence of mass for neutrinos, a property not initially in accordance to predictions of the Standard Model (SM) of Particle Physics. Extensions of the Standard Model naturally give rise to additional properties subjected to be investigated, such as Non-Standard Interactions (NSI) not initially present in the model. In the presence of additional, non-standard interactions, neutrino oscillations are subject to be affected due to the existence of new parameters in the model, which may have impact on our knowledge of the standard oscillation parameters.

The NuMI Off-axis ν_e Appearance (NOvA) experiment was built aiming to perform investigations primarily on neutrino properties. The experiment is hosted at Fermilab, USA, and as of August 2020 is made of more than 240 collaborators from 51 institutions in 7 countries. The High Energy Physics group at the Federal University of Goiás, Brazil, together with Universidad del Atlántico (Colombia) and Cochin University of Science and Technology (India), is leading the analysis on neutrino non-standard interactions on neutrino oscillations at NOvA. Using a set of Monte Carlo simulated data, we perform studies to neutrino non-standard interactions on the NOvA experiment by investigating the effects on neutrino oscillations as they travel through the Earth's crust. We investigate the impact of the non-standard parameters $|\varepsilon_{\mu\tau}|$ and $\delta_{\mu\tau}$ on the determination of the standard oscillation parameters Δm^2_{32} and $\sin^2\left(\theta_{23}\right)$, as well as correlations between each of the parameters of our interest in this analysis.

In this thesis we report a summary of the current results. The structure of this work is organized as follows:

- Chapter 1 presents an overview on the history of neutrinos and the physics that rules their properties.
- Chapter 2 is dedicated to discussions on the mathematical evaluation of the phenomenon of neutrino oscillations.
- Chapter 3 introduces the concept of non-standard interactions and their inclusion on the formalism of neutrino oscillations.
- Chapter 4 describes the NOvA experiment.
- Chapter 5 presents the methodology and the analysis strategy used for this work.
- Chapter 6 shows the results obtained by the author and collaborators.
- Chapter 7 concludes.

1 Neutrino Physics

1.1 History of the neutrino

By the beginning of the 20th century it was thought that the process known as beta decay was the spontaneous emission of an electron by an atom, a two-body process. It was expected for the electrons emitted in the process to have the same energy, but experimental results showed the energy distribution to be continuous rather than discrete [1], indicating a possible contradiction to the law of conservation of energy.

In 1930, Wolfgang Pauli, in his famous letter [2] addressed to the participants of the Tübingen conference, proposes the existence of another particle participating in the process, with well specific properties, such as very small mass (or even massless), electrically neutral, and of spin $\frac{1}{2}$, named *neutron*[1]. Two years latter, in 1932, James Chadwick discovers a neutral particle with properties similar to the proton, such as mass, which then caused this particle to be named as neutron instead [3], where latter Enrico Fermi renamed Pauli's particle as *neutrino* (roughly translated as *little neutron*).

The physical properties of neutrinos resulted in an initial skepticism about the possibility of ever detecting it. It was estimated for the neutrino to have a mean free path of thousands of light-years in water, which means that a neutrino could travel through huge amounts of matter without interacting with the surrounding. Pauli itself quoted "*I have done a terrible thing, I have postulated a particle that cannot be detected*". It was only in 1956, almost 3 decades latter, that Clyde Cowan and Frederick Reines [4] discovered the neutrino by investigating a nuclear reactor at Savannah River, USA, leading to the 1995 Nobel Prize in Physics to Reines *et. al.* In fact, the investigation led by Cowan and Reines was the interaction of antineutrinos from the nuclear reactor with protons of the detector, described by[2]

$$\bar{\nu}_e + p \rightarrow n + e^+. \tag{1.1}$$

The characteristic signal was the detection of the two resulting photons from the annihilation of the generated positron with surrounding electrons in the detector, followed by the capture of the neutron by the surrounding nucleons, leading to a de-excitation of the nucleus as a whole through the emission of a photon with a delay of $5\,\mu$s with respect to the first signal from the two photons. Additionally, it was observed a significant decrease on the events when the reactor was turned off, providing further evidence for the observed flux in the detector.

In 1962, Leon Lederman *et. al.* found the existence of another neutrino [5], of different type from the one detected by Cowan and Reines, through observation of "heavy electrons" associated with neutrino interactions, which is what we know today as muons, characterizing the evidence for the existence of a second neutrino $\nu_\mu \neq \nu_e$. This yielded the 1988 Nobel Prize in Physics to Lederman *et. al.*

After the discovery of the third type of charged lepton, the tau (τ) , it was already expected that a third neutrino associated to this lepton, ν_τ, would also exist. The evidence was then supported by hints of missing energy on tau decay observations, and the experimental confirmation came in 2000 by the Direct Observation of the Nu Tau (DONUT) collaboration [6], at Fermilab, by observing characteristic ν_τ interactions.

The observation of the third neutrino marks the closing picture of the three known generations of leptons

[1] By the time the only known particles were the proton, the electron, and the photon.
[2] The notation used for neutrinos (antineutrinos) was simply $\nu\,(\bar{\nu})$, since it was thought that just one type existed.

in the Standard Model, grouped as

$$\begin{pmatrix}\nu_e\\ e\end{pmatrix}, \quad \begin{pmatrix}\nu_\mu\\ \mu\end{pmatrix}, \quad \begin{pmatrix}\nu_\tau\\ \tau\end{pmatrix}. \tag{1.2}$$

1.1.1 The Solar Neutrino Problem

As the field of neutrino physics grew, several experiments were built in order to better understand neutrino properties. Among them are the experiments investigating electron neutrinos produced in the Sun. According to the called Standard Solar Model (SSM) [7], the flux of ν_e in the Earth is expected to be around 6.5×10^{10} neutrinos per cm^2, mainly resulting from the proton-proton chain in the core of the Sun.

What was in fact observed, however, was always a number of events bellow the expected rate. Among the experiments observing a deficit in its counting rate was the Homestake experiment [8] (the first to measure neutrinos from the Sun), led by Ray Davis and John Bahcall, which used a detector based on chlorine through interactions of the type

$$\nu_e + {}^{37}\text{Cl} \rightarrow {}^{37}\text{Ar} + e^-. \tag{1.3}$$

Other experiments also investigating neutrinos from the Sun were the Kamiokande-II experiment [9] and the Sudburry Neutrino Observatory (SNO) [10], these having a detection method based on the Cherenkov radiation in water resulting from electrons ejected from the atoms through neutrino scattering. Both experiments also accounted a deficit in the observed events compared to prediction.

The whole picture of the "missing neutrinos" has became known as the solar neutrino problem, and naturally several models and theories arised as an attempt to explain the observed data, specially a concern with respect to the precision of the predictions from the SSM developed by Bahcall. Fig. 1 shows the predicted rate in comparison to experimental results for different experiments investigating solar neutrinos through various detection methods in terms of a Solar Neutrino Unit (SNU)[3].

[3] 1 SNU corresponds to a neutrino flux producing 10^{-36} captures per target atom per second.

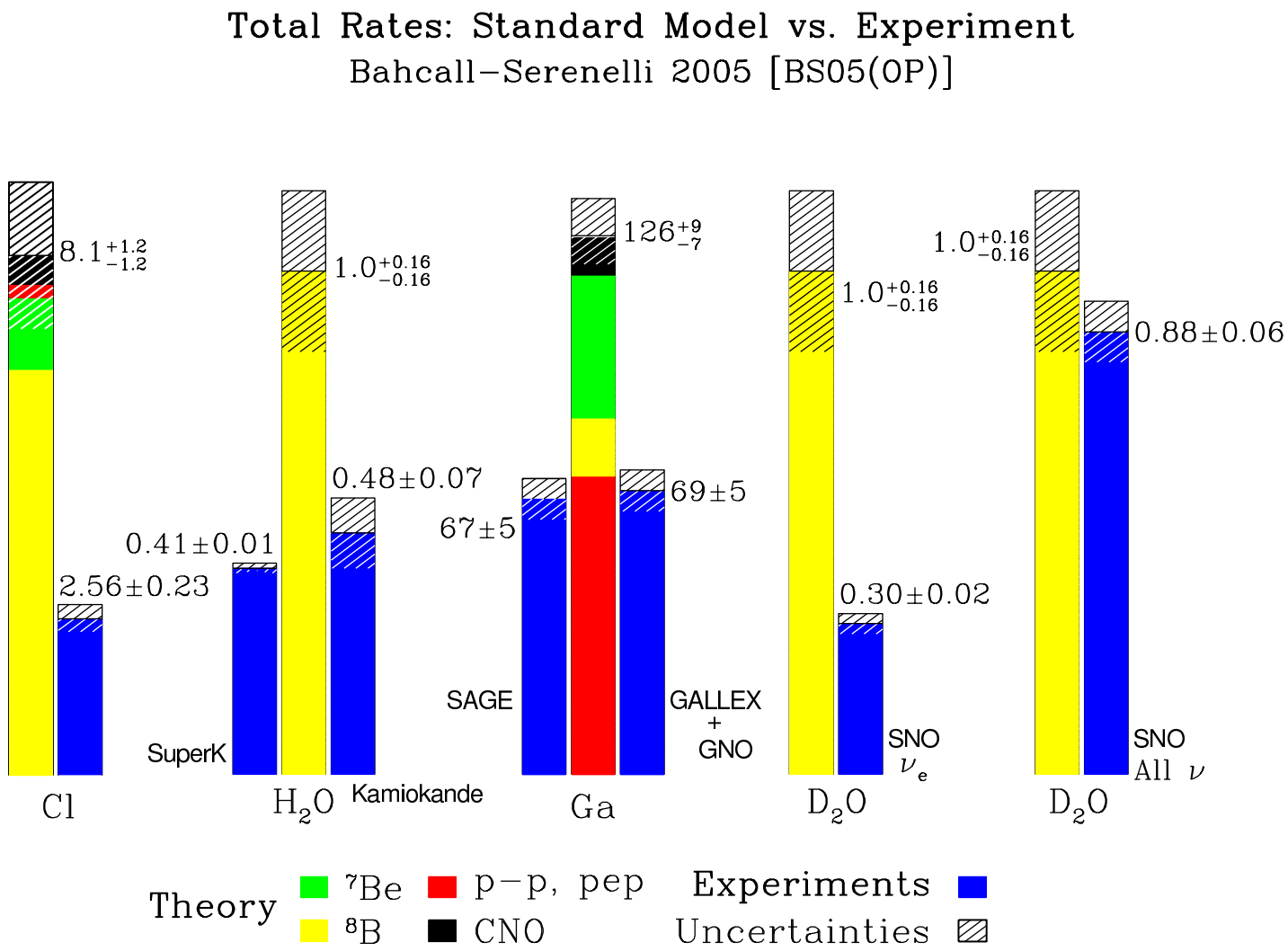

Figure 1 – Total rates for solar neutrinos at various experiments. In green, yellow, red, and black are the flux predictions from the Standard Solar Model for neutrinos produced by different solar process, and in blue are the experimental results obtained by the respective experiments, along with the corresponding uncertainties. From `http://www.sns.ias.edu/~jnb/SNviewgraphs/snviewgraphs.html`

Apart from ν_e produced in the Sun, the SNO experiment was also sensitive to ν_μ and ν_τ[4]. Since ν_μ and ν_τ are not produced in the Sun, the observation of a total predicted flux for solar neutrinos through measurement of all neutrinos provided evidence [11] for the electron neutrinos produced in the Sun to be "changing type" during their way to the Earth, a phenomenon that was explained by a model known as *neutrino oscillations*, which we will cover on Chapter 2. For the contributions on the studies regarding neutrino oscillations, Takaaki Kajita from the Super-Kamiokande experiment, and Arthur McDonald from SNO were awarded the 2015 Nobel Prize In Physics.

[4] The SNO experiment is able to detect all neutrino flavors through Neutral Current scattering.

1.2 Neutrinos in the Standard Model

Neutrinos are elementary particles of spin $\frac{1}{2}$, possessing no electric or color charge, thus classified as neutral leptons, and interact only through the Weak interaction within the Standard Model (SM)[5]. Thought to be massless, it was found that neutrinos do actually have mass, and current bounds indicate such particles to have a considerably small mass compared to other known particles, with an upper limit of $m_\nu < 1.1\,\text{eV}$ (90% confidence level) on the absolute mass scale of neutrinos [12], about 5.0×10^5 times lighter than an electron. Being leptons (antileptons), neutrinos (antineutrinos) hold lepton number $L = +1$ (-1).

Interactions of neutrinos with matter are known to be either due to the exchange of charged $W^\pm$ bosons, classified as Charged Current (CC) interaction, or by the exchange of a neutral Z^0 boson, known as Neutral Current (NC) interaction. In the SM, CC and NC interactions of neutrinos with matter mediated by the massive Weak interaction bosons are parameterized as [13, 14]

$$\mathcal{L}_{\text{CC}} = -\frac{g}{\sqrt{2}} \sum_{\alpha=e,\mu,\tau} \bar{\nu}_\alpha \gamma_\mu P_L \ell_\alpha W_\mu + hc, \tag{1.4}$$

$$\mathcal{L}_{\text{NC}} = -\frac{g}{2\cos(\theta_W)} \sum_{\alpha=e,\mu,\tau} \bar{\nu}_\alpha \gamma_\mu P_L \nu_\alpha Z^0_\mu, \tag{1.5}$$

where g is the electroweak interaction constant, $\alpha \in \{e, \mu, \tau\}$ are the lepton flavors, $\nu_\alpha\,(\bar{\nu}_\alpha)$ are the neutrino (antineutrino) fields, ℓ_α is a charged lepton, P_L is the left hand projection operator, θ_W is the weak (Weinberg) angle, γ_μ are the gamma matrices, and W_μ and Z^0_μ are fields of $W^\pm$ and Z^0 vector bosons, respectively.

In the SM, helicity is a quantity defined as the component of the spin along the direction of a particle's momentum. Particles that have its spin in the same direction of its momentum are said to be *right-handed*, while particles with spin in the opposite direction of its propagation are classified as *left-handed*, as represented in Fig. 2.

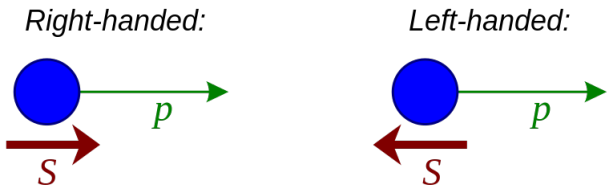

Figure 2 – Representation of the concept of helicity. From `https://www.wikiwand.com/en/Chirality_(physics)`

So far only left-handed neutrinos and right-handed antineutrinos were observed [15]. If right-handed neutrinos (left-handed antineutrinos) exist, they are said do be sterile, i.e., do not participate in the weak interaction, and are source of several extensions of the SM. Particles with a well defined and fixed helicity requires the mass of this particle to be exactly zero, because it is traveling at the speed of light, thus the *handedness* manifests as the same for all observers, while particles with a non-zero mass are possible to be found at either helicities depending on the frame of reference. In other words, the observed helicity of neutrinos is strictly attached to a massless particle, but the evidence for neutrino oscillations directly proves the existence of mass for neutrinos, and thus the SM must be extended in order to account the observed behavior.

Interactions are commonly referred as scattering, from which, depending on the nature of the process, are classified as elastic or inelastic scattering. For neutrino physics, a few scattering of interest are:

- Elastic Scattering

[5] Gravity effects are not included in the Standard Model framework.

Redistribution of the total energy and momentum between the participating particles. Under this process there is no production of additional particles as final states.

- Inelastic Scattering

  For neutrinos with energies above the lepton production threshold[6], the interaction can lead to the production of additional particles as final states, meaning that kinetic energy is not conserved. For situations where the energy transfer is small when compared to the incident scattered particles, this process is also known as quasielastic scattering.

- Deep Inelastic Scattering

  Neutrinos possessing higher energies[7] can result in the production of an additional hadronic component as part of final states in the neutrino interaction with nucleons.

1.2.1 Charged Current

Charged Current interactions involve the presence of charged leptons in the process mediated by the exchange of $W^{\pm}$ bosons. Neutrino CC interactions arise from the decay of the mentioned gauge bosons, which follow the relations [16]:

$$W^+ \to \ell^+ + \nu_\ell, \tag{1.6}$$

$$W^- \to \ell^- + \bar{\nu}_\ell, \tag{1.7}$$

with $\ell \in \{e, \mu, \tau\}$. When interacting with the baryons that make up ordinary matter, namely neutrons (n) and protons (p), and with electrons (e^-) in the medium, a few relevant CC interactions are [17]:

- Elastic scattering of ν_e or $\bar{\nu}_e$ with electrons:

$$\nu_e + e^- \to \nu_e + e^-, \tag{1.8}$$

$$\bar{\nu}_e + e^- \to \bar{\nu}_e + e^-. \tag{1.9}$$

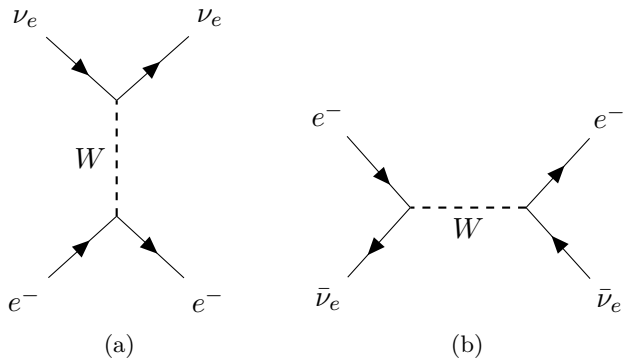

Figure 3 – Feynman diagrams for CC elastic scattering of ν_e with an electron (a), and CC elastic scattering of $\bar{\nu}_e$ with an electron (b).

[6] $E_{\nu_\ell} > m_\ell$, where ℓ is a correspondent charged lepton (electron, muon or tau).
[7] Usually $E_\nu >> m_N$, where N is a nucleon (proton or neutron).

- Inelastic scattering of neutrinos or antineutrinos with nucleons:

$$\nu_\ell + n \rightarrow \ell^- + p, \tag{1.10}$$

$$\bar{\nu}_\ell + p \rightarrow \ell^+ + n, \tag{1.11}$$

resulting in the production of a correspondent charged lepton of flavor ℓ associated with the incoming neutrino of flavor ν_ℓ.

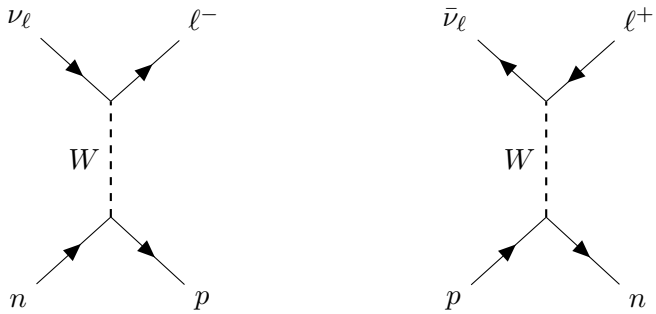

Figure 4 – Feynman diagram for CC inelastic scattering of a neutrino of flavor ν_ℓ with a neutron (a), resulting in the production of a correspondent charged lepton ℓ^- and a proton, and inelastic scattering of an antineutrino of flavor $\bar{\nu}_\ell$ with a proton (b), resulting in the production of a correspondent charged lepton ℓ^+ and a neutron.

- Deep Inelastic Scattering of neutrinos or antineutrinos with nucleons:

$$\nu_\ell + n \rightarrow \ell^- + p + \sum_i X_i, \tag{1.12}$$

$$\bar{\nu}_\ell + p \rightarrow \ell^+ + n + \sum_i X_i, \tag{1.13}$$

where in this case, besides from the correspondent charged lepton, a set of hadrons X_i are also produced as a result of the higher energetic interaction.

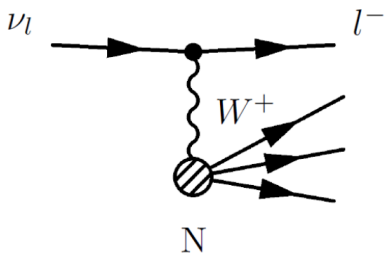

Figure 5 – Feynman diagram for CC deep inelastic scattering of a neutrino of flavor ν_ℓ with a nucleon N, resulting in the production of a correspondent charged lepton and a hadronic shower. From Ref. [18].

Hence, in neutrino experiments one is able to determine the neutrino flavor involved in the interaction by detecting the correspondent charged lepton produced through a CC scattering.

1.2.2 Neutral Current

Interactions characterized by the Neutral Current process have the Z^0 boson as mediator, which in contrast to the $W^\pm$ boson, possesses no electric charge. Neutrinos interacting with matter through NC do not have charged leptons associated in the process. Some neutrino NC interactions are [17]:

- Elastic scattering of neutrinos or antineutrinos with electrons and nucleons:

$$\nu_\ell + e^- \to \nu_\ell + e^-, \tag{1.14}$$
$$\nu_\ell + N \to \nu_\ell + N, \tag{1.15}$$
$$\bar{\nu}_\ell + e^- \to \bar{\nu}_\ell + e^-, \tag{1.16}$$
$$\bar{\nu}_\ell + N \to \bar{\nu}_\ell + N, \tag{1.17}$$

with $N \in \{n, p\}$, for all ℓ.

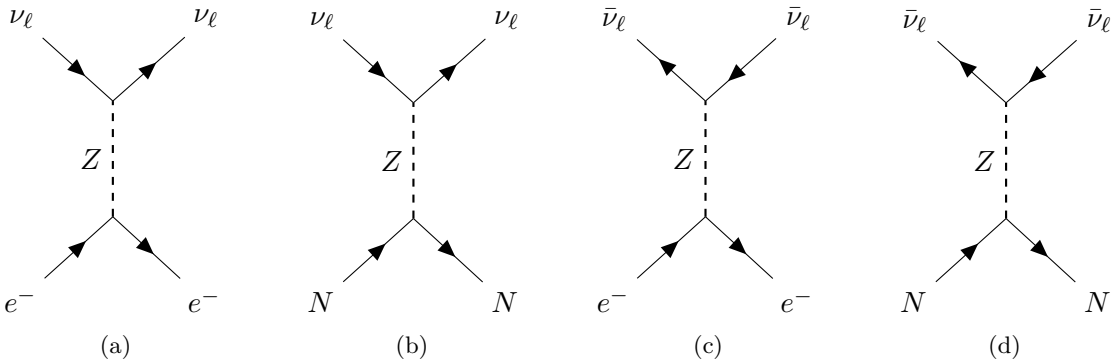

Figure 6 – Feynman diagram for NC elastic scattering of a neutrino with an electron (a), and with a nucleon (b), and NC elastic scattering of an antineutrino with an electron (c), and with a nucleon (d).

- Deep Inelastic Scattering of neutrinos or antineutrinos with nucleons:

$$\nu_\ell + N \to \nu_\ell + N + \sum_i X_i, \tag{1.18}$$

$$\bar{\nu}_\ell + N \to \bar{\nu}_\ell + N + \sum_i X_i, \tag{1.19}$$

where $\sum_i X_i$ accounts for the hadronic component, which by conservation of electric charge, has total electric charge equal to zero.

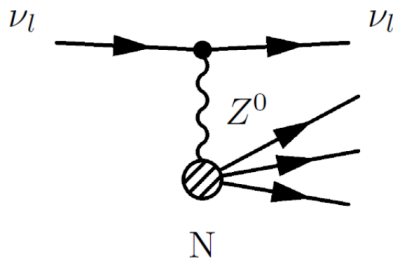

Figure 7 – Feynman diagram for NC deep inelastic scattering of a neutrino of flavor ν_ℓ with a nucleon N, resulting in the production of a hadronic shower. From Ref. [18].

The hadronic products can be π^0, $\pi^+\pi^-$ pairs, or even K^+K^- pairs, depending on the initial neutrino energy, and so on. By identifying the nucleon recoil or the hadronic components, usually more challenging than detecting charged leptons due to CC interactions, one can characterize a neutrino interaction due to NC process, although not able to determine its flavor.

2 Formalism of neutrino oscillations

From the perspective of Quantum Mechanics, the flavor basis is the one where neutrinos interact with the medium, i.e., production and detection, while the mass basis, however, describes their evolution in time. The assumption that the flavor and the mass basis are not coincident was first proposed by Bruno Pontecorvo [19], and the mathematical evaluation was developed by Ziro Maki, Masami Nakagawa and Soichi Sakata.

The flavor basis $\{\nu_\alpha\}$ and the mass basis $\{\nu_i\}$ are related by an unitary transformation which states that the flavor eigenstates $|\nu_\alpha\rangle$ are a quantum superposition of the mass eigenstates $|\nu_i\rangle$ of the form [20, 21]

$$|\nu_\alpha\rangle = \sum_i U^*_{\alpha i} |\nu_i\rangle , \tag{2.1}$$

where $\alpha = e, \mu, \tau$ is the neutrino flavor, and $i = 1, 2, 3$ is related to the mass states. This relation can also be written as

$$|\nu_i\rangle = \sum_\alpha U_{\alpha i} |\nu_\alpha\rangle , \tag{2.2}$$

and U is known as the Pontecorvo-Maki-Nakagawa-Sakata (PMNS) mixing matrix, represented by

$$U \doteq \begin{pmatrix} U_{e1} & U_{e2} & U_{e3} \\ U_{\mu 1} & U_{\mu 2} & U_{\mu 3} \\ U_{\tau 1} & U_{\tau 2} & U_{\tau 3} \end{pmatrix} . \tag{2.3}$$

For a 3 neutrino scenario, the mixing between the flavor and the mass states can be expressed as

$$\begin{pmatrix} |\nu_e\rangle \\ |\nu_\mu\rangle \\ |\nu_\tau\rangle \end{pmatrix} \doteq \begin{pmatrix} U_{e1} & U_{e2} & U_{e3} \\ U_{\mu 1} & U_{\mu 2} & U_{\mu 3} \\ U_{\tau 1} & U_{\tau 2} & U_{\tau 3} \end{pmatrix} \begin{pmatrix} |\nu_1\rangle \\ |\nu_2\rangle \\ |\nu_3\rangle \end{pmatrix} . \tag{2.4}$$

The mixing matrix U is parameterized [22] as $U = R_{23} S_{13} R_{12}$, where R_{ij} (S_{ij}) is a real (complex) rotation by an angle θ_{ij} in the ij plane

$$U = R_{23} S_{13} R_{12} \doteq \begin{pmatrix} 1 & 0 & 0 \\ 0 & c_{23} & s_{23} \\ 0 & -s_{23} & c_{23} \end{pmatrix} \begin{pmatrix} c_{13} & 0 & s_{13} e^{-\imath\delta} \\ 0 & 1 & 0 \\ -s_{13} e^{+\imath\delta} & 0 & c_{13} \end{pmatrix} \begin{pmatrix} c_{12} & s_{12} & 0 \\ -s_{12} & c_{12} & 0 \\ 0 & 0 & 1 \end{pmatrix} , \tag{2.5}$$

$$U \doteq \begin{pmatrix} c_{12} c_{13} & s_{12} c_{13} & s_{13} e^{-i\delta_{CP}} \\ -s_{12} c_{23} - c_{12} s_{23} s_{13} e^{i\delta_{CP}} & c_{12} c_{23} - s_{12} s_{23} s_{13} e^{i\delta_{CP}} & s_{23} c_{13} \\ s_{12} s_{23} - c_{12} c_{23} s_{13} e^{i\delta_{CP}} & -c_{12} s_{23} - s_{12} c_{23} s_{13} e^{i\delta_{CP}} & c_{23} c_{13} \end{pmatrix} , \tag{2.6}$$

where $c_{ij} = \cos(\theta_{ij}), s_{ij} = \sin(\theta_{ij})$, and $\delta = \delta_{CP}$ is the Dirac phase that allows Charge-Parity (CP) violation in the lepton sector. If found that δ_{CP} is non-integer (i.e. $\delta_{CP} \neq 0, \pi, 2\pi$)[1], it states that neutrinos and antineutrinos would oscillate differently [23]. This parameterization leads to $\frac{1}{2} N (N-1)$ mixing angles and $\frac{1}{2} (N-1)(N-2)$ phases, for a total of $(N-1)^2$ parameters.

Historically, each of the matrices associated in this parameterization is related to a regime that has been investigated. The sector for θ_{23} is known as the *atmospheric sector*, as this regime was mostly studied by atmospheric

[1] This investigation mainly depends on the term proportional to $\sin(\delta_{CP})$, which is non-zero only for non-integer values of δ_{CP}. See Section 2.2 for details.

and accelerator experiments, which are sensitive to ν_μ produced by cosmic ray interactions with the Earth's upper atmosphere or by collisions of protons with targets in particle accelerators. The sector associated with θ_{12} has became known as the *solar sector*, since most of the experiments sensitive to this mixing angle are the ones investigating ν_e produced in the Sun (and $\bar{\nu}_e$ produced in nuclear reactors). The matrix associated with θ_{13} couples to both the atmospheric and solar sectors, usually referred as the *reactor sector*, and allow investigations of 3 flavor oscillations, also offering the possibility to inspect the value of the phase δ_{CP} [24].

For the case of antineutrinos [25], the corresponding equivalence is obtained by taking the complex conjugates of Eq. (2.1),

$$|\bar{\nu}_\alpha\rangle = \sum_i U_{\alpha i} \, |\bar{\nu}_i\rangle \, , \tag{2.7}$$

and the mathematical evaluation follow the same assumptions as that for neutrinos.

2.1 Neutrino oscillations in vacuum

In general, there could be an n arbitrary number of orthogonal neutrino mass eigenstates which are solution to the Hamiltonian in the mass basis. In the mass basis the Hamiltonian of the system is diagonal,

$$\mathcal{H}_0 \doteq \begin{pmatrix} E_1 & \cdots & 0 \\ \vdots & \ddots & 0 \\ 0 & 0 & E_i \end{pmatrix} , \tag{2.8}$$

and we write

$$\mathcal{H}_0 \, |\nu_i\rangle = E_i \, |\nu_i\rangle \, , \tag{2.9}$$

where E_i is the eigenenergy of the neutrino ν_i.

Applying the time evolution and the translation operators on the initial state $|\nu_i(0,0)\rangle$ at $t_0 = 0$ and $x_0 = 0$, and working on the natural units convention[2], we obtain for the state $|\nu_i(x,t)\rangle$ at some point x and time t of the space to be

$$|\nu_i(x,t)\rangle = e^{-\imath E_i t} e^{\imath p_i x} \, |\nu_i\rangle \, , \tag{2.10}$$

where p_i is the momentum of the neutrino ν_i. Therefore, from Eq.(2.1) the evolution of a neutrino of flavor ν_α is written as

$$|\nu_\alpha(x,t)\rangle = \sum_i U^*_{\alpha i} e^{-\imath E_i t} e^{\imath p_i x} \, |\nu_i\rangle \, . \tag{2.11}$$

At $(x,t) = (0,0)$ a neutrino of flavor ν_α is produced, and the probability for one to detect a different neutrino of flavor ν_β after a distance x and time t is

$$P_{\nu_\alpha \to \nu_\beta} = |\langle \nu_\beta \, (x,t) \, |\nu_\alpha(0,0)\rangle \, |^2 \, , \tag{2.12}$$

where $\langle \nu_\beta \, (x,t)| = \sum_j U_{\beta j} e^{\imath E_j t} e^{-\imath p_j x} \, \langle \nu_j|$. The inner product is then

$$\langle \nu_\beta \, (x,t) \, |\nu_\alpha(0,0)\rangle \, = \sum_i U^*_{\alpha i} \sum_j U_{\beta j} e^{\imath E_j t} e^{-\imath p_j x} \, \langle \nu_j| \, \nu_i\rangle \, , \tag{2.13}$$

and due to the orthogonality $\langle \nu_j| \, \nu_i\rangle = \delta_{ij}$ of the mass eigenstates,

$$\langle \nu_\beta \, (x,t) \, |\nu_\alpha(0,0)\rangle \, = \sum_i U^*_{\alpha i} U_{\beta i} e^{\imath E_i t} e^{-\imath p_i x} , \tag{2.14}$$

[2] $c = \hbar = 1$.

which is known as the transition amplitude for $\nu_\alpha \to \nu_\beta$. The probability becomes

$$P_{\nu_\alpha \to \nu_\beta} = \left| \sum_i U^*_{\alpha i} U_{\beta i} e^{\imath E_i t} e^{-\imath p_i x} \right|^2 , \tag{2.15}$$

$$P_{\nu_\alpha \to \nu_\beta} = \sum_i |U^*_{\alpha i} U_{\beta i}|^2 + 2 \sum_{j>i} \Re \left(U^*_{\alpha i} U_{\beta i} U_{\alpha j} U^*_{\beta j} e^{-\imath (E_j - E_i) t} e^{\imath (p_j - p_i) x} \right), \tag{2.16}$$

where we have made use of $\left| \sum_i z_i \right|^2 = \sum_i |z_i|^2 + \sum_{j>i} 2\Re \left(z_i z_j^* \right)$ for complex numbers.

Due to their small masses, neutrinos are relativistic particles with energy

$$E_i = \sqrt{p_i^2 + m_i^2} = p_i \sqrt{1 + \frac{m_i^2}{p_i^2}} \simeq p_i + \frac{m_i^2}{2p_i}. \tag{2.17}$$

Also, as their rest masses are very small, most of the energy of a neutrino is kinetic energy, i.e., $E = p_i$, and we obtain

$$E_i \simeq E + \frac{m_i^2}{2E}, \tag{2.18}$$

where E is the total energy of the neutrino. In the natural units system we can write $x = L = \frac{t}{v} \approx \frac{t}{c} \approx t$, where L is the distance traveled by the neutrino between its production point (source) and the detector. The exponential terms on the probability reduces to

$$e^{-\imath (E_j - E_i) t} e^{\imath (p_j - p_i) x} = e^{-\imath \left(\frac{\Delta m^2_{ji} L}{2E} \right)}, \tag{2.19}$$

with

$$\Delta m^2_{ji} \equiv m_j^2 - m_i^2, \tag{2.20}$$

from where we write

$$P_{\nu_\alpha \to \nu_\beta} = \sum_i |U^*_{\alpha i} U_{\beta i}|^2 + 2 \sum_{j>i} \Re \left(U^*_{\alpha i} U_{\beta i} U_{\alpha j} U^*_{\beta j} e^{-\imath \left(\frac{\Delta m^2_{ji} L}{2E} \right)} \right). \tag{2.21}$$

Another relation with respect to complex numbers is

$$\Re(z_1 z_2) = \Re(z_1)\Re(z_2) - \Im(z_1)\Im(z_2), \tag{2.22}$$

where for our case in Eq. (2.21)

$$z_1 = U^*_{\alpha i} U_{\beta i} U_{\alpha j} U^*_{\beta j}, \tag{2.23}$$

$$z_2 = e^{-\imath \left(\frac{\Delta m^2_{ji} L}{2E} \right)} = \cos \left(\frac{\Delta m^2_{ji} L}{2E} \right) - \imath \sin \left(\frac{\Delta m^2_{ji} L}{2E} \right), \tag{2.24}$$

allowing to evaluate the second sum in Eq. (2.21), from where we obtain

$$\begin{aligned} P_{\nu_\alpha \to \nu_\beta} = \sum_i |U^*_{\alpha i} U_{\beta i}|^2 &+ 2 \sum_{j>i} \Re \left(U^*_{\alpha i} U_{\beta i} U_{\alpha j} U^*_{\beta j} \right) \cos \left(\frac{\Delta m^2_{ji} L}{2E} \right) \\ &+ 2 \sum_{j>i} \Im \left(U^*_{\alpha i} U_{\beta i} U_{\alpha j} U^*_{\beta j} \right) \sin \left(\frac{\Delta m^2_{ji} L}{2E} \right) \end{aligned} . \tag{2.25}$$

The first sum in the expression above can be written as

$$\sum_i |U^*_{\alpha i}U_{\beta i}|^2 = \left|\sum_i U^*_{\alpha i}U_{\beta i}\right|^2 - 2\sum_{j>i}\Re\left(U^*_{\alpha i}U_{\beta i}U_{\alpha j}U^*_{\beta j}\right), \tag{2.26}$$

and since $\sum_i U^*_{\alpha i}U_{\beta i} = \delta_{\alpha\beta}$,

$$\sum_i |U^*_{\alpha i}U_{\beta i}|^2 = \delta_{\alpha\beta} - 2\sum_{j>i}\Re\left(U^*_{\alpha i}U_{\beta i}U_{\alpha j}U^*_{\beta j}\right). \tag{2.27}$$

Inserting back into the probability,

$$\begin{aligned} P_{\nu_\alpha\to\nu_\beta} = \delta_{\alpha\beta} &- 2\sum_{j>i}\left\{\Re\left(U^*_{\alpha i}U_{\beta i}U_{\alpha j}U^*_{\beta j}\right)\left[1-\cos\left(\frac{\Delta m^2_{ji}L}{2E}\right)\right]\right\} \\ &+2\sum_{j>i}\Im\left(U^*_{\alpha i}U_{\beta i}U_{\alpha j}U^*_{\beta j}\right)\sin\left(\frac{\Delta m^2_{ji}L}{2E}\right), \end{aligned} \tag{2.28}$$

and identifying $1-\cos\left(\frac{\Delta m^2_{ji}L}{2E}\right) = 2\sin^2\left(\frac{\Delta m^2_{ji}L}{4E}\right)$, the transition probability is finally written as

$$\begin{aligned} P_{\nu_\alpha\to\nu_\beta} = \delta_{\alpha\beta} &- 4\sum_{j>i}\Re\left(U^*_{\alpha i}U_{\beta i}U_{\alpha j}U^*_{\beta j}\right)\sin^2\left(\frac{\Delta m^2_{ji}L}{4E}\right) \\ &+2\sum_{j>i}\Im\left(U^*_{\alpha i}U_{\beta i}U_{\alpha j}U^*_{\beta j}\right)\sin\left(\frac{\Delta m^2_{ji}L}{2E}\right). \end{aligned} \tag{2.29}$$

The case where $\alpha = \beta$ corresponds to the survival probability for the neutrino to be detected in the same flavor it was produced. In this scenario, the matrix elements arrangement become real and Eq. (2.29) reduces to

$$P_{\nu_\alpha\to\nu_\alpha} = 1 - 4\sum_{j>i}|U_{\alpha i}U_{\alpha j}|^2\sin^2\left(\frac{\Delta m^2_{ji}L}{4E}\right). \tag{2.30}$$

2.2 Antineutrino oscillations in vacuum

The eigenstates of antineutrinos of flavor $\bar\nu_\alpha$ are connected with the mass eigenstates through

$$|\bar\nu_\alpha\rangle = \sum_i U_{\alpha i}\,|\bar\nu_i\rangle, \tag{2.31}$$

from where we also obtain

$$|\bar\nu_i\rangle = \sum_\alpha U^*_{\alpha i}\,|\bar\nu_\alpha\rangle. \tag{2.32}$$

The evolution in space and time, as well as the assumptions made in the previous section are the same for antineutrinos, and we obtain for the probability for an initial antineutrino $\bar\nu_\alpha$ to oscillate into a different antineutrino $\bar\nu_\beta$ to be

$$\begin{aligned} P_{\bar\nu_\alpha\to\bar\nu_\beta} = \delta_{\alpha\beta} &- 4\sum_{j>i}\Re\left(U_{\alpha i}U^*_{\beta i}U^*_{\alpha j}U_{\beta j}\right)\sin^2\left(\frac{\Delta \bar m^2_{ji}L}{4E}\right) \\ &+2\sum_{j>i}\Im\left(U_{\alpha i}U^*_{\beta i}U^*_{\alpha j}U_{\beta j}\right)\sin\left(\frac{\Delta \bar m^2_{ji}L}{2E}\right). \end{aligned} \tag{2.33}$$

Notice that the difference for the neutrino case is the already expected interchange of the matrix element's complex conjugates. This allows us to inspect the differences between neutrino and antineutrino probabilities, and then look for hints into different behaviors on oscillations. For instance, we note that

$$\Delta P = P_{\nu_\alpha\to\nu_\beta} - P_{\bar\nu_\alpha\to\bar\nu_\beta} = 2\sum_{j>i}\Im\left(U^*_{\alpha i}U_{\beta i}U_{\alpha j}U^*_{\beta j}\right)\sin\left(\frac{\Delta m^2_{ji}L}{2E}\right) - 2\sum_{j>i}\Im\left(U_{\alpha i}U^*_{\beta i}U^*_{\alpha j}U_{\beta j}\right)\sin\left(\frac{\Delta \bar m^2_{ji}L}{2E}\right), \tag{2.34}$$

and since $-\Im\left(U_{\alpha i}U^*_{\beta i}U^*_{\alpha j}U_{\beta j}\right) = \Im\left(U^*_{\alpha i}U_{\beta i}U_{\alpha j}U^*_{\beta j}\right)$, and $\Delta m^2_{ji} = \Delta\bar{m}^2_{ji}$, we obtain[3]

$$\Delta P = P_{\nu_\alpha\to\nu_\beta} - P_{\bar{\nu}_\alpha\to\bar{\nu}_\beta} = 4\sum_{j>i}\Im\left(U^*_{\alpha i}U_{\beta i}U_{\alpha j}U^*_{\beta j}\right)\sin\left(\frac{\Delta m^2_{ji}L}{2E}\right), \tag{2.35}$$

from where the effects of a phase δ_{ij} can be probed. For the current 3 neutrino scenario, Eq. (2.35) will be [26]

$$\Delta P \propto s_{13}c^2_{13}s_{12}c_{12}s_{23}c_{23}\sin\left(\delta_{CP}\right), \tag{2.36}$$

and searches for the value of δ_{CP} are among the most important measurements to be performed by neutrino oscillation experiments.

2.3 2 flavor oscillations in vacuum

A 2 flavor approximation is in most cases enough to reasonably explain a set of experimental data [27]. In the same sense, a full probability expression concerning the 3 neutrino flavors is not suitable to observe the individual effects of each parameter, and an effective probability for oscillations between only two neutrinos is practical for didactic purposes.

Oscillations between 2 neutrino flavors ν_α and ν_β can be effectively reduced to a problem concerning only one mixing angle and two mass eigenstates, and the mixing relation (2.4) reduces to

$$\begin{pmatrix}|\nu_\alpha\rangle\\ |\nu_\beta\rangle\end{pmatrix} \doteq \begin{pmatrix}\cos(\theta_{ij}) & \sin(\theta_{ij})\\ -\sin(\theta_{ij}) & \cos(\theta_{ij})\end{pmatrix}\begin{pmatrix}|\nu_i\rangle\\ |\nu_j\rangle\end{pmatrix}, \tag{2.37}$$

writing for the respective flavor states

$$|\nu_\alpha\rangle = \cos(\theta_{ij})\,|\nu_i\rangle + \sin(\theta_{ij})\,|\nu_j\rangle\,, \tag{2.38}$$

$$|\nu_\beta\rangle = -\sin(\theta_{ij})\,|\nu_i\rangle + \cos(\theta_{ij})\,|\nu_j\rangle\,. \tag{2.39}$$

In the same way discussed in the general formalism, the evolution in time of an initial neutrino ν_α is ruled by

$$|\nu_\alpha(t)\rangle = \cos(\theta_{ij})e^{-\imath E_i t}\,|\nu_i\rangle + \sin(\theta_{ij})e^{-\imath E_j t}\,|\nu_j\rangle\,, \tag{2.40}$$

and the probability to detect a ν_β after the neutrino has traveled a distance L ($t \approx L$) is then

$$P_{\nu_\alpha\to\nu_\beta} = \left|\langle\nu_\beta\,|\nu_\alpha(t)\rangle\right|^2. \tag{2.41}$$

The above expression can be evaluated using the same assumptions discussed in the previous section, and one can find for the transition probability to be

$$P_{\nu_\alpha\to\nu_\beta} = \sin^2(2\theta_{ij})\sin^2\left(\frac{\Delta m^2_{ji}L}{4E}\right), \tag{2.42}$$

from where it is also possible to note[4] that the survival probability for the initial neutrino to be detected in the same flavor it was produced is

$$P_{\nu_\alpha\to\nu_\alpha} = 1 - \sin^2(2\theta_{ij})\sin^2\left(\frac{\Delta m^2_{ji}L}{4E}\right). \tag{2.43}$$

[3] The mass of a particle and its respective antiparticle is the same.

[4] Because of the fact that the evolution is unitary, $P_{\nu_\alpha\to\nu_\beta} + P_{\nu_\alpha\to\nu_\alpha} = 1$.

Notice that we can also make use of Eq. (2.30) in order to obtain the same expression for the survival probability,

$$\begin{aligned} P_{\nu_\alpha \to \nu_\alpha} &= 1 - 4\left|U_{\alpha i} U_{\alpha j}\right|^2 \sin^2\left(\frac{\Delta m^2_{ji} L}{4E}\right) \\ &= 1 - 4\cos^2(\theta_{ij})\sin^2(\theta_{ij})\sin^2\left(\frac{\Delta m^2_{ji} L}{4E}\right) \end{aligned} \tag{2.44}$$

$$P_{\nu_\alpha \to \nu_\alpha} = 1 - \sin^2(2\theta_{ij})\sin^2\left(\frac{\Delta m^2_{ji} L}{4E}\right), \tag{2.45}$$

which is identical to Eq. (2.43). As an exemplification, the 2 flavor survival probability for a ν_μ produced in accelerators or by cosmic ray interactions is

$$P_{\nu_\mu \to \nu_\mu} = 1 - \sin^2(2\theta_{23})\sin^2\left(\frac{\Delta m^2_{32} L}{4E}\right), \tag{2.46}$$

while for ν_e produced in the Sun, for example, would be

$$P_{\nu_e \to \nu_e} = 1 - \sin^2(2\theta_{12})\sin^2\left(\frac{\Delta m^2_{21} L}{4E}\right). \tag{2.47}$$

The parameter Δm^2_{ji} is expressed in eV^2, L in km and the energy E in GeV, and in order to correctly conduct the experiment it is necessary to reconsider c and $\hbar$, allowing us to obtain

$$\frac{\Delta m^2_{ji} L}{4E} \to \frac{1}{4}\frac{1}{\hbar\,[\mathrm{eV}\cdot s]\,c\left[\frac{km}{s}\right]}\frac{\Delta m^2_{ji}\left[\mathrm{eV}^2\right] L\,[km]}{E\,[\mathrm{GeV}]} = 1.27\frac{\Delta m^2_{ji} L}{E}. \tag{2.48}$$

Therefore, in an experimental analysis the probability to be used should be given by

$$P_{\nu_\alpha \to \nu_\alpha} = 1 - \sin^2(2\theta_{ij})\sin^2\left(1.27\frac{\Delta m^2_{ji} L}{E}\right). \tag{2.49}$$

Observe that 2 flavor oscillations in vacuum has a degeneracy on both the mixing angle θ_{ij} and the mass squared difference Δm^2_{ji}. For the mixing angle it is not possible to get information if $\theta_{ij} > 45°$ or $\theta_{ij} < 45°$, and likewise for the mass eigenstates it is also not possible to investigate if $m^2_j > m^2_i$ or $m^2_j < m^2_i$. The degeneracies on θ_{ij} and Δm^2_{ji} are commonly known as the octant problem and the mass hierarchy problem, respectively. Additional information, such as 3 flavor oscillations and matter effects are needed in order to evaluate the mentioned degeneracies, which we will cover in sequence.

2.4 3 flavor oscillations in vacuum

It was thought that the mixing angle θ_{13} was zero, but important measurements performed in 2012 by the Daya Bay [28], Double Chooz [29] and Reactor Experiment for Neutrino Oscillation (RENO) [30] collaborations found that, even small, $\theta_{13} \neq 0$, and this implies two major possibilities:

- Investigate the value of δ_{CP},
- Transitions between the three neutrinos allow investigations of the mixing angle octant, e.g. of θ_{23}, not sensitive on the 2 flavor approximation.

Under this more realistic scenario, according to Eq. (2.30) the survival probability for an initially produced ν_μ is

$$P_{\nu_\mu \to \nu_\mu} = 1 - 4\left[|U_{\mu 1}U_{\mu 2}|^2 \sin^2\left(\frac{\Delta m^2_{21}L}{4E}\right) + |U_{\mu 1}U_{\mu 3}|^2 \sin^2\left(\frac{\Delta m^2_{31}L}{4E}\right) + |U_{\mu 2}U_{\mu 3}|^2 \sin^2\left(\frac{\Delta m^2_{32}L}{4E}\right)\right], \quad (2.50)$$

where

$$|U_{\mu 1}U_{\mu 2}|^2 = \left|\left(-s_{12}c_{23} - c_{12}s_{23}s_{13}e^{i\delta_{CP}}\right)\left(c_{12}c_{23} - s_{12}s_{23}s_{13}e^{i\delta_{CP}}\right)\right|^2, \quad (2.51)$$

$$|U_{\mu 1}U_{\mu 3}|^2 = \left|\left(-s_{12}c_{23} - c_{12}s_{23}s_{13}e^{i\delta_{CP}}\right)(s_{23}c_{13})\right|^2, \quad (2.52)$$

$$|U_{\mu 2}U_{\mu 3}|^2 = \left|\left(c_{12}c_{23} - s_{12}s_{23}s_{13}e^{i\delta_{CP}}\right)(s_{23}c_{13})\right|^2. \quad (2.53)$$

Approximate 3 flavor oscillation probabilities[5] in vacuum [24] are obtained by

$$P_{\nu_\mu \to \nu_\mu} \approx 1 - 4\cos^2(\theta_{13})\sin^2(\theta_{23})\left[1 - \sin^2(\theta_{23})\cos^2(\theta_{13})\right]\sin^2\left(\frac{\Delta m^2_{32}L}{4E}\right), \quad (2.54)$$

and

$$P_{\nu_\mu \to \nu_e} \approx 4\cos^2(\theta_{13})\sin^2(\theta_{13})\sin^2(\theta_{23})\sin^2\left(\frac{\Delta m^2_{32}L}{4E}\right). \quad (2.55)$$

Observe that the presence of θ_{13} breaks the degeneracy on θ_{23}, allowing investigations on determining the unknown octant. Also, as $\theta_{13} \to 0$, Eq. (2.46) is recovered and the transition $\nu_\mu \to \nu_e$ is zero. Transitions of the type $\nu_\mu \to \nu_e$ have been investigated in a variety of experiments, including NOvA [31]. However, by examining the expressions (2.54) and (2.55), mass hierarchy is still not possible to be investigated under the approximation for oscillations in vacuum. A consistent treatment of oscillations in matter is needed in order to evaluate the sign of Δm^2_{32}, and therefore the hierarchy regarding the masses of the neutrino eigenstates.

2.5 Neutrino oscillations in matter

When propagating through a medium instead of in the vacuum, neutrinos are subject to interact with the constituent matter of this medium. In a general approximation, ordinary matter is made up of neutrons, protons, and electrons. Neutrinos, as we saw in section 1.2, interact via the Weak interaction through the exchange of $W^\pm$ and Z^0 bosons, defined as Charged Current and Neutral Current, respectively.

The flavor states are the ones to interact with matter, so it is necessary to express the Hamiltonian from Eq. (2.8) in the flavor basis,

$$\mathcal{H} = U^\dagger \mathcal{H}_0 U, \quad (2.56)$$

and the evolution equation will be written as

$$\imath \frac{d}{dt}|\nu_\alpha\rangle = U^\dagger \mathcal{H}_0 U |\nu_\alpha\rangle. \quad (2.57)$$

The presence of matter gives rise to an interaction term $\mathcal{H}_{matter}$ in the Hamiltonian in the flavor basis,

$$\mathcal{H} = U^\dagger \mathcal{H}_0 U + \mathcal{H}_{matter}, \quad (2.58)$$

where $\mathcal{H}_{matter}$ accounts for all contributions from various possible interactions with the matter constituents.

[5] Neglecting Δm^2_{21}, because $\frac{\Delta m^2_{21}}{\Delta m^2_{32}} = \mathcal{O}\left(10^{-2}\right)$, and also ignoring the phase δ_{CP}.

Because of the fact that there are virtually no free muons and taus in ordinary matter, and since standard interactions through NC are flavor-conserving[6], the only participating component to affect neutrino oscillations are those due to coherent forward scattering (zero momentum transfer) of ν_e through CC interactions with electrons in the medium [32, 33]. This means that the standard matter effect is due to a potential represented by

$$\mathcal{H}_{matter} \doteq \pm V \begin{pmatrix} 1 & 0 & 0 \\ 0 & 0 & 0 \\ 0 & 0 & 0 \end{pmatrix}, \tag{2.59}$$

with

$$V = \sqrt{2} G_F N_e, \tag{2.60}$$

where G_F is the Fermi coupling constant and N_e is the density of electrons, considered here as constant, with the sign $\pm$ in Eq. (2.59) being positive for neutrinos and negative for antineutrinos, respectively. Therefore, matter effects are only suitable to be investigated when considering oscillations including ν_e.

In order to numerically implement matter effects within an experimental framework, the potential defined at Eq. (2.60) can be written in terms of more suitable quantities, such as the matter density ρ of the medium [34], expressed as

$$V \simeq 3.8 \times 10^{-14} \left(\frac{\rho}{\mathrm{g/cm^3}} \right) \mathrm{eV}. \tag{2.61}$$

2.5.1 2 flavor neutrino oscillations in matter

We proceed to an evaluation of the term $U^\dagger \mathcal{H}_0 U$ in Eq. (2.58). In a 2 flavor approximation we have

$$U^\dagger \mathcal{H}_0 U \doteq \begin{pmatrix} \cos(\theta_{ij}) & -\sin(\theta_{ij}) \\ \sin(\theta_{ij}) & \cos(\theta_{ij}) \end{pmatrix} \begin{pmatrix} E_i & 0 \\ 0 & E_j \end{pmatrix} \begin{pmatrix} \cos(\theta_{ij}) & \sin(\theta_{ij}) \\ -\sin(\theta_{ij}) & \cos(\theta_{ij}) \end{pmatrix} \tag{2.62}$$

$$= \begin{pmatrix} \cos^2(\theta_{ij}) E_i + \sin^2(\theta_{ij}) E_j & \sin(\theta_{ij})\cos(\theta_{ij}) E_i - \sin(\theta_{ij})\cos(\theta_{ij}) E_j \\ \sin(\theta_{ij})\cos(\theta_{ij}) E_i - \sin(\theta_{ij})\cos(\theta_{ij}) E_j & \sin^2(\theta_{ij}) E_i + \cos^2(\theta_{ij}) E_j \end{pmatrix} \tag{2.63}$$

$$= \frac{\Delta m^2_{ji}}{2E} \begin{pmatrix} \sin^2(\theta_{ij}) & -\sin(\theta_{ij})\cos(\theta_{ij}) \\ -\sin(\theta_{ij})\cos(\theta_{ij}) & \cos^2(\theta_{ij}) \end{pmatrix} + \propto \mathbf{1}, \tag{2.64}$$

where the same assumptions made in the last section were applied. Terms proportional to identity are denoted by $\propto \mathbf{1}$, which can be neglected [7]. After a couple of trigonometric rearrangement, it is possible to write

$$U \mathcal{H}_0 U^\dagger \doteq \frac{\Delta m^2_{ji}}{4E} \begin{pmatrix} -\cos(2\theta_{ij}) & -\sin(2\theta_{ij}) \\ -\sin(2\theta_{ij}) & \cos(2\theta_{ij}) \end{pmatrix}. \tag{2.65}$$

A close inspection on Eq. (2.59) makes it clear that the standard matter potential is felt when ν_e is present in the framework, i.e., when there is the presence of either θ_{12} or θ_{13}, allowing couplings of V within the mixing. Oscillations of 2 flavors between only ν_μ and ν_τ would have no contribution from this term. In order to maintain our general formalism applied to any 2 flavors, we define

$$\kappa_i = \begin{cases} 1, \text{if } i = 1 \\ 0, \text{otherwise} \end{cases}, \tag{2.66}$$

[6] NC interactions affects all neutrino flavors, hence no effects on neutrino oscillations.

[7] These terms contribute to an overall phase, which have no physical implications on oscillations.

from where the total Hamiltonian including matter effects will be

$$\mathcal{H} \doteq \begin{pmatrix} -\frac{\Delta m^2_{ji}}{4E}\cos(2\theta_{ij}) + \kappa_i V & -\frac{\Delta m^2_{ji}}{4E}\sin(2\theta_{ij}) \\ -\frac{\Delta m^2_{ji}}{4E}\sin(2\theta_{ij}) & \frac{\Delta m^2_{ji}}{4E}\cos(2\theta_{ij}) \end{pmatrix}. \tag{2.67}$$

Then, the evolution equation in the flavor basis in the presence of standard matter effects is

$$\imath\frac{d}{dt}\begin{pmatrix} |\nu_\alpha\rangle \\ |\nu_\beta\rangle \end{pmatrix} \doteq \begin{pmatrix} -\frac{\Delta m^2_{ji}}{4E}\cos(2\theta_{ij}) + \kappa_i V & -\frac{\Delta m^2_{ji}}{4E}\sin(2\theta_{ij}) \\ -\frac{\Delta m^2_{ji}}{4E}\sin(2\theta_{ij}) & \frac{\Delta m^2_{ji}}{4E}\cos(2\theta_{ij}) \end{pmatrix}\begin{pmatrix} |\nu_\alpha\rangle \\ |\nu_\beta\rangle \end{pmatrix}. \tag{2.68}$$

The solution to the equation above can be accomplished by a process of rediagonalization of $\mathcal{H}$ by considering an unitary transformation to a new basis, as a result of a rotation by an effective angle θ_M in matter. This allows us to write the effective oscillation probability in matter [35] in a similar way as given by Eq. (2.42),

$$P_{\nu_\alpha\to\nu_\beta} = \sin^2(2\theta_M)\sin^2\left(\frac{\Delta m^2_M L}{4E}\right), \tag{2.69}$$

where

$$\sin^2(2\theta_M) = \frac{\sin^2(2\theta_{ij})}{\sin^2(2\theta_{ij}) + \left[\cos(2\theta_{ij}) - 2E\frac{\kappa_i V}{\Delta m^2_{ji}}\right]^2} \tag{2.70}$$

and

$$\Delta m^2_M = \Delta m^2_{ji}\sqrt{\sin^2(2\theta_{ij}) + \left[\cos(2\theta_{ij}) - 2E\frac{\kappa_i V}{\Delta m^2_{ji}}\right]^2}. \tag{2.71}$$

Notice that in the vacuum $V = 0$, and Eq. (2.43) is recovered. From Eq. (2.70) and (2.71) it is now clear how the presence of matter effects can break the degeneracy on Δm^2_{ji} and θ_{ij}, and then we are able to investigate the mass hierarchy and the octant problem, respectively. For completeness, the survival probability for the neutrino to be detected in the same flavor it was produced is then

$$P_{\nu_\alpha\to\nu_\alpha} = 1 - P_{\nu_\alpha\to\nu_\beta} = 1 - \sin^2(2\theta_M)\sin^2\left(\frac{\Delta m^2_M L}{4E}\right). \tag{2.72}$$

According to the definition of V in Eq. (2.60) and the convention adopted for the sign for neutrinos and antineutrinos in Eq. (2.59), the antineutrino transition and survival probabilities $P_{\bar\nu_\alpha\to\bar\nu_\beta}$ and $P_{\bar\nu_\alpha\to\bar\nu_\alpha}$, respectively, can be obtained by replacing $V \to -V$ in Eq. (2.70) and Eq. (2.71).

2.5.2 3 flavor neutrino oscillations in matter

As for the case of oscillations between 2 neutrino flavors in matter, in the 3 flavor framework the matter effect is felt by electron neutrinos (antineutrinos), since the matter Hamiltonian represented in Eq. (2.59) has only the 1-1 element as non-zero. In this sense, 3 flavor neutrino (antineutrino) oscillations in matter are relevant in the solar and reactor channels $\nu_e \to \nu_e, \nu_\mu, \nu_\tau$ ($\bar\nu_e \to \bar\nu_e, \bar\nu_\mu, \bar\nu_\tau$), as well as on the atmospheric and accelerator channel $\nu_\mu \to \nu_e$ ($\bar\nu_\mu \to \bar\nu_e$). The approximate oscillation probability for the $\nu_\mu \to \nu_e$ ($\bar\nu_\mu \to \bar\nu_e$) transition at long-baseline experiments, assuming a constant matter density, can be derived as a second order expansion in the small parameters $\sin(\theta_{13})$ and $\frac{\Delta m^2_{21}}{\Delta m^2_{31}}$ as demonstrated by the authors in Ref. [36–38], and is written as

$$\begin{aligned} P_{\nu_\mu\to\nu_e} \approx\ & 4\sin^2(\theta_{13})\sin^2(\theta_{23})\frac{\sin^2(\Delta)}{(1-A)^2} + \alpha^2\sin^2(2\theta_{12})\cos^2(\theta_{23})\frac{\sin^2(A\Delta)}{A^2} \\ & + 8\alpha J_{\rm CP}\cos(\Delta + \delta_{\rm CP})\frac{\sin(A\Delta)\sin[\Delta(1-A)]}{A(1-A)}, \end{aligned} \tag{2.73}$$

where

$$J_{\mathrm{CP}} = \cos(\theta_{12})\sin(\theta_{12})\cos(\theta_{23})\sin(\theta_{23})\cos^2(\theta_{13})\sin(\theta_{13}), \tag{2.74}$$

and

$$\Delta \equiv \frac{\Delta m^2_{31} L}{4E}, \qquad A \equiv \frac{2EV}{\Delta m^2_{31}}, \qquad \alpha \equiv \frac{\Delta m^2_{21}}{\Delta m^2_{31}}. \tag{2.75}$$

The corresponding antineutrino channel $P_{\bar{\nu}_\mu \to \bar{\nu}_e}$ is obtained by taking $\delta_{\mathrm{CP}} \to -\delta_{\mathrm{CP}}$ and $V \to -V$ in Eq. (2.73) and Eq. (2.75), respectively.

2.6 Open questions and current status of neutrino oscillations

We can see that besides from the three mixing angles and the δ_{CP} phase arising from the parameterization of the mixing matrix, the oscillation probability also depends on the parameter Δm^2_{ji} defined in Eq. (2.20). Oscillation experiments cannot directly measure the mass of each neutrino, but only its mass squared difference. In the current scenario for 3 neutrinos, there are two different independent mass squared splittings, Δm^2_{21} and Δm^2_{32}, since $\Delta m^2_{31} = \Delta m^2_{32} + \Delta m^2_{21}$.

The parameter θ_{13} has been well measured by reactor experiments, while θ_{12} and Δm^2_{21} were widely studied by solar experiments, and it was found that $m^2_2 > m^2_1$. In the other hand, current knowledge of neutrino oscillations has only allowed us to measure the absolute value of Δm^2_{32}, as well as a present degeneracy on θ_{23}, which cannot yet be stated if $\theta_{23} > 45°$ (upper octant) or $\theta_{23} < 45°$ (lower octant), known as the problem of the θ_{23} octant. This is due to the fact that the majority of information that we have about Δm^2_{32} and θ_{23} so far was mostly obtained through studies of the $\nu_\mu \to \nu_\mu$ survival rate, sometimes in a 2 flavor approximation. However, recently studies considering $\nu_\mu \to \nu_e$ transitions in matter will make it suitable to investigate the sign of Δm^2_{32} and the octant of θ_{23}, since in this approach the degeneracies in these parameters are broken, as seen on Eq. (2.73) and Eq. (2.75). Regarding the parameter Δm^2_{32}, two possible hierarchies, Normal Hierarchy (NH) or Inverted Hierarchy (IH), for the masses of neutrinos are in place:

$$\begin{aligned} \Delta m^2_{32} > 0 \to m^2_3 > m^2_2 > m^2_1 \quad &- \quad \text{NH}, \\ \Delta m^2_{32} < 0 \to m^2_2 > m^2_1 > m^2_3 \quad &- \quad \text{IH}. \end{aligned} \tag{2.76}$$

Fig. 8 shows an illustration of the possible neutrino mass hierarchies.

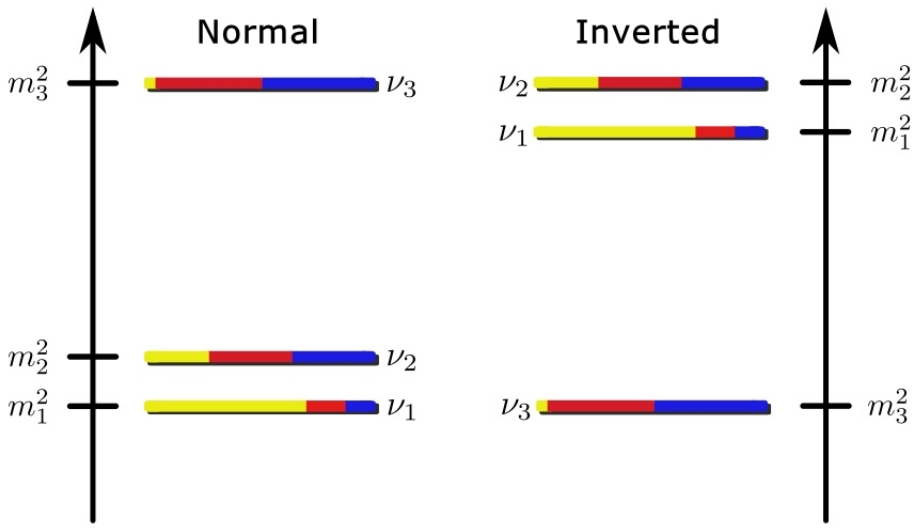

Figure 8 – Normal and Inverted mass hierarchy for neutrinos.
The colors yellow, red, and blue accounts for the proportional mixture of ν_e, ν_μ, and ν_τ, respectively, present in each mass state ν_i.
(Adapted from `https://scienceblogs.com/startswithabang/2012/01/16/neutrinos-to-ring-in-the-new-y`).

Determination of the neutrino mass hierarchy has a direct impact on our measurements of the oscillation parameters, and is also of importance for cosmological studies. Neutrino mass hierarchy, the octant of θ_{23} and the value of δ_{CP} are currently on the forefront of measurements being performed on neutrino oscillation experiments.

Table 1 summarizes the current best fit for the neutrino oscillation parameters obtained through a global analysis of available data [24, 39].

Parameter	best fit	3σ range
$\sin^2(\theta_{12})$	0.307 ± 0.013	$0.275 \to 0.350$
$\sin^2(\theta_{23})$(NH)	$0.542^{+0.019}_{-0.022}$	$0.433 \to 0.609$
$\sin^2(\theta_{23})$(IH)	$0.536^{+0.023}_{-0.028}$	$0.436 \to 0.610$
$\sin^2(\theta_{13})$	0.0218 ± 0.0007	$0.02044 \to 0.02435$
$\delta_{CP}(\pi\,\mathrm{rad})$	$1.37^{+0.18}_{-0.16}$	$0.8 \to 1.98$
Δm^2_{21} $(10^{-5}\mathrm{eV}^2)$	7.53 ± 0.18	$6.79 \to 8.01$
Δm^2_{32} $(10^{-3}\mathrm{eV}^2)$(NH)	2.444 ± 0.034	$2.436 \to 2.618$
Δm^2_{32} $(10^{-3}\mathrm{eV}^2)$(IH)	-2.55 ± 0.04	$-2.601 \to -2.419$

Table 1 – Best fits for the three flavor neutrino oscillation parameters [24] and the $3\,\sigma$ range allowed interval [39].

3 Neutrino Non-Standard Interactions

Although neutrino oscillations are well established as the explanation of the non-conservation of lepton flavor during neutrino propagation, additional phenomena could take part within the whole neutrino physics picture. Such hypothetical properties include the possibility for neutrino decay [40], neutrino quantum decoherence [41], sterile neutrinos [42], and a wide range of other topics currently under investigation, such as neutrino Non-Standard Interactions with matter [43–45].

3.1 Non-Standard Interactions and Physics Beyond the Standard Model

The Standard Model can be assumed to be a low energy effective model of a more general high energy theory [46]. In the same manner, neutrino Non-Standard Interactions (NSI) provide a general effective field theory to quantify other interactions not previously included in the neutrino sector within the SM framework. With respect to neutrino interactions and propagation, NSIs can arise as Charged Current-like NSI (CC-NSI) or Neutral Current-like NSI (NC-NSI) with matter fermions.

The presence of additional neutrino NC-NSI and CC-NSI, respectively, are usually parameterized at Lagrangian level [45] in the form

$$\mathcal{L}_{\text{NC-NSI}} = -2\sqrt{2}G_F \sum_{f,P,\alpha,\beta} \varepsilon_{\alpha\beta}^{f,P} \left(\bar{\nu}_\alpha \gamma^\mu P_L \nu_\beta\right) \left(\bar{f}\gamma_\mu P f\right), \tag{3.1}$$

$$\mathcal{L}_{\text{CC-NSI}} = -2\sqrt{2}G_F \sum_{f,P,\alpha,\beta} \varepsilon_{\alpha\beta}^{f,P} \left(\bar{\nu}_\alpha \gamma^\mu P_L \ell_\beta\right) \left(\bar{f}\gamma_\mu P f'\right), \tag{3.2}$$

where G_F is the Fermi coupling constant, $\alpha,\beta \in \{e,\mu,\tau\}$ are the lepton flavors, $f,f' \in \{e,u,d\}$ are SM matter fermions, $P \in \{P_L, P_R\}$ are the chirality projection operators, and $\varepsilon_{\alpha\beta}^{f,P}$ parameterizes the strength of the new interaction. Under this parameterization, $\varepsilon_{\alpha\beta}^{f,P}$ can be thought as the strength of the new interaction relative to the Fermi constant, i.e., $\varepsilon_{\alpha\beta}^{f,P} \propto \mathcal{O}\left(\frac{G_X}{G_F}\right)$, where G_X is the coupling constant related to a new mediator X of mass m_X responsible for the new interaction. From the relation $G_F \simeq \frac{\sqrt{2}}{8}\frac{g^2}{m_W^2}$ it is found for the NSI parameters to be

$$\varepsilon_{\alpha\beta}^{f,P} \propto \frac{m_W^2}{m_X^2}, \tag{3.3}$$

where $m_W = 80.379 \pm 0.012\,\text{GeV} \sim 0.1\text{TeV}$ is the $W^\pm$ boson mass [24, 47]. Therefore, if such hypothetical particle X has mass of the order of 1 (10) TeV, then it is expected for the NSI parameters to be approximately of the order of $\varepsilon_{\alpha\beta}^{f,P} \propto 10^{-2}\,(10^{-4})$.

3.2 NSI effects on neutrino oscillations

While CC-NSI is responsible to affect neutrino production and detection [47], NC-NSI comes into place to alter neutrino propagation. This is due to additional Hamiltonian terms that impact the neutrino survival and transition probabilities, similar to the case of neutrinos propagating through matter. In fact, NSI can be thought as a generalized version of the matter potential introduced in Eq. (2.59), and were even introduced by L. Wolfenstein in 1978 in the same landmark paper [32] that identified the standard matter effects discussed in section 2.5. However, standard interactions with matter as described by Eq. (2.59) only lead to propagation effects due to CC interactions

of neutrinos with electrons in the medium, with no flavor conversion induced by NC, while the presence of NSIs can imply flavor conversion even via NC interactions. Throughout this work, only NC-NSI effects will be considered.

In the presence of NSI, the Hamiltonian of the system is again subjected to an additional interaction part, $\mathcal{H}_{NSI}$, which is responsible for such effects. The effective Hamiltonian becomes

$$\mathcal{H} = U^{\dagger}\mathcal{H}_0 U + \mathcal{H}_{matter} + \mathcal{H}_{NSI}. \tag{3.4}$$

In the 3 flavor neutrino scenario, and accounting all the possible additional parameters [48], the corresponding Hamiltonian for NSI can be expressed as

$$\mathcal{H}_{NSI} \doteq \pm\sqrt{2}G_F N_e \begin{pmatrix} \varepsilon_{ee} & \varepsilon_{e\mu} & \varepsilon_{e\tau} \\ \varepsilon_{\mu e} & \varepsilon_{\mu\mu} & \varepsilon_{\mu\tau} \\ \varepsilon_{\tau e} & \varepsilon_{\tau\mu} & \varepsilon_{\tau\tau} \end{pmatrix}, \tag{3.5}$$

with the property of $\varepsilon_{\alpha\beta} = \varepsilon^{*}_{\beta\alpha}$ due to hermiticity, and being positive for neutrinos and negative for antineutrinos.

The SM predicts that, apart from the difference in the masses, electrons, muons and taus all have the same properties, e.g., electric charge and spin, among other quantities. This means that the couplings of the leptons to the gauge bosons are the same for all leptons. This implies, for example, that one can expect quantities, such as decay ratios, to be the same for all leptons [49],

$$\Gamma_{Z^0\to e^- e^+} = \Gamma_{Z^0\to \mu^- \mu^+} = \Gamma_{Z^0\to \tau^- \tau^+}, \tag{3.6}$$

which is known as Lepton Flavor Universality (LFU). In this sense, the NSI diagonal terms are responsible to provide a mechanism for breaking LFU, as these parameters provide a test by measuring the couplings with the different $\varepsilon_{\alpha\alpha}$, and are thus referred as non-universal. The off-diagonal terms are known as flavor-changing, since they couple with more than one neutrino state, being the responsible for neutrino flavor conversion through NC under NSI.

The diagonal NSI terms are real, and the off-diagonal are in general complex, and can be parameterized[1] as

$$\varepsilon_{\alpha\beta} = |\varepsilon_{\alpha\beta}|\, e^{i\delta_{\alpha\beta}}. \tag{3.7}$$

As the δ_{CP} phase introduced in the parameterization of the mixing matrix in Eq. (2.6), the current NSI parameterization also introduce new and additional possible CP-violating phases $\delta_{\alpha\beta}$ related to each parameter $\varepsilon_{\alpha\beta}$. It is important to note the distinction between $\varepsilon^{f,P}_{\alpha\beta}$, presented in Eq. (3.1) and (3.2), and the $\varepsilon_{\alpha\beta}$ defined in Eq. (3.5). The first are referred as Lagrangian level NSI, while the latter are known as Hamiltonian level NSI, and the difference is that at the Hamiltonian level the strength of the new interaction has been parameterized to be relative to the electron number density N_e, responsible for the standard matter effects, and the relation between both representations is given by

$$\varepsilon_{\alpha\beta} = \sum_{f,P} \varepsilon^{f,P}_{\alpha\beta} \frac{N_f}{N_e}, \tag{3.8}$$

where N_f accounts for the density of the matter fermion $f \in \{e, u, d\}$.

3.2.1 2 flavor neutrino oscillations including NSI

In the same way we have been doing, we now consider here the approximation for a 2 neutrino flavor scenario ongoing oscillations in the presence of non-standard interactions. For a 2 flavor approximation, and identifying the

[1] For antineutrinos, the NSI parameters are taken to be the corresponding complex conjugate, given by $\varepsilon_{\alpha\beta} = |\varepsilon_{\alpha\beta}|\, e^{-i\delta_{\alpha\beta}}$.

multiplicative factor on Eq. (3.5) as being the standard matter potential V defined in Eq. (2.60), the Hamiltonian term for NSI reduces to

$$\mathcal{H}_{NSI} \doteq V \begin{pmatrix} \varepsilon_{\alpha\alpha} & \varepsilon_{\alpha\beta} \\ \varepsilon_{\beta\alpha} & \varepsilon_{\beta\beta} \end{pmatrix}. \tag{3.9}$$

The effective Hamiltonian from Eq. (3.4) is the one presented in Eq. (2.67) summed with the contribution from Eq. (3.9),

$$\mathcal{H} \doteq \begin{pmatrix} -\frac{\Delta m^2_{ji}}{4E}\cos(2\theta_{ij}) + \kappa_i V & -\frac{\Delta m^2_{ji}}{4E}\sin(2\theta_{ij}) \\ -\frac{\Delta m^2_{ji}}{4E}\sin(2\theta_{ij}) & \frac{\Delta m^2_{ji}}{4E}\cos(2\theta_{ij}) \end{pmatrix} + V \begin{pmatrix} \varepsilon_{\alpha\alpha} & \varepsilon_{\alpha\beta} \\ \varepsilon_{\beta\alpha} & \varepsilon_{\beta\beta} \end{pmatrix}, \tag{3.10}$$

$$\mathcal{H} \doteq \begin{pmatrix} -\frac{\Delta m^2_{ji}}{4E}\cos(2\theta_{ij}) + V(\kappa_i + \varepsilon_{\alpha\alpha}) & -\frac{\Delta m^2_{ji}}{4E}\sin(2\theta_{ij}) + V\varepsilon_{\alpha\beta} \\ -\frac{\Delta m^2_{ji}}{4E}\sin(2\theta_{ij}) + V\varepsilon_{\beta\alpha} & \frac{\Delta m^2_{ji}}{4E}\cos(2\theta_{ij}) + V\varepsilon_{\beta\beta} \end{pmatrix}, \tag{3.11}$$

from where the evolution equation for the neutrino flavor states is

$$\imath\frac{d}{dt}\begin{pmatrix} |\nu_\alpha\rangle \\ |\nu_\beta\rangle \end{pmatrix} = \begin{pmatrix} -\frac{\Delta m^2_{ji}}{4E}\cos(2\theta_{ij}) + V(\kappa_i + \varepsilon_{\alpha\alpha}) & -\frac{\Delta m^2_{ji}}{4E}\sin(2\theta_{ij}) + V\varepsilon_{\alpha\beta} \\ -\frac{\Delta m^2_{ji}}{4E}\sin(2\theta_{ij}) + V\varepsilon_{\beta\alpha} & \frac{\Delta m^2_{ji}}{4E}\cos(2\theta_{ij}) + V\varepsilon_{\beta\beta} \end{pmatrix}\begin{pmatrix} |\nu_\alpha\rangle \\ |\nu_\beta\rangle \end{pmatrix}. \tag{3.12}$$

As done in the case for oscillations in matter, the same process of finding the solution through diagonalization of the Hamiltonian from Eq. (3.11) is applied. However, in presence of NSI, results are expressed in terms of the effective parameters $\tilde{\theta}_M$ and $\Delta\tilde{m}^2_M$, which will naturally depend on the standard oscillation and NSI parameters. If we take the parameters to be real, and make all $\delta_{\alpha\beta} = 0$, the transition probability [50] should be

$$P_{\nu_\alpha\to\nu_\beta} = \sin^2(2\tilde{\theta}_M)\sin^2\left(\frac{\Delta\tilde{m}^2_M L}{4E}\right), \tag{3.13}$$

where now

$$\sin^2(2\tilde{\theta}_M) = \frac{\left[\Delta m^2_{ji}\sin(2\theta_{ij}) + 4EV\varepsilon_{\alpha\beta}\right]^2}{\left(\Delta m^2_{ji}\right)^2\left\{\left[\sin(2\theta_{ij}) + 4E\frac{V}{\Delta m^2_{ji}}\varepsilon_{\alpha\beta}\right]^2 + \left[\cos(2\theta_{ij}) - 2E\frac{V}{\Delta m^2_{ji}}(\kappa_i + \varepsilon_{\alpha\alpha} - \varepsilon_{\beta\beta})\right]^2\right\}} \tag{3.14}$$

and

$$\Delta\tilde{m}^2_M = \Delta m^2_{ji}\sqrt{\left[\sin(2\theta_{ij}) + 4E\frac{V}{\Delta m^2_{ji}}\varepsilon_{\alpha\beta}\right]^2 + \left[\cos(2\theta_{ij}) - 2E\frac{V}{\Delta m^2_{ji}}(\kappa_i + \varepsilon_{\alpha\alpha} - \varepsilon_{\beta\beta})\right]^2}. \tag{3.15}$$

In the same sense, the survival probability will be then

$$P_{\nu_\alpha\to\nu_\alpha} = 1 - P_{\nu_\alpha\to\nu_\beta} = 1 - \sin^2(2\tilde{\theta}_M)\sin^2\left(\frac{\Delta\tilde{m}^2_M L}{4E}\right). \tag{3.16}$$

We highlight here two limiting cases:

- If $V = 0$, oscillations in vacuum are recovered,
- If $V \neq 0$, but the NSI terms are zero, standard oscillations in matter is recovered.

The antineutrino transition and survival probabilities $P_{\bar{\nu}_\alpha\to\bar{\nu}_\beta}$ and $P_{\bar{\nu}_\alpha\to\bar{\nu}_\alpha}$, respectively, can be obtained by replacing $V \to -V$ in Eq. (3.14) and Eq. (3.15).

As an example, under this scenario a transition of the type $\nu_\mu \to \nu_\mu$, of interest for atmospheric and accelerator based experiments, would be given by

$$P_{\nu_\mu\to\nu_\mu} = 1 - \sin^2(2\tilde{\theta}_M)\sin^2\left(\frac{\Delta\tilde{m}^2_M L}{4E}\right), \tag{3.17}$$

with[2]

$$\sin^2(2\tilde{\theta}_M) = \frac{\left[\Delta m^2_{32}\sin(2\theta_{23}) + 4EV\varepsilon_{\mu\tau}\right]^2}{(\Delta m^2_{32})^2\left\{\left[\sin(2\theta_{23}) + 4E\frac{V}{\Delta m^2_{32}}\varepsilon_{\mu\tau}\right]^2 + \left[\cos(2\theta_{23}) - 2E\frac{V}{\Delta m^2_{32}}(\varepsilon_{\mu\mu} - \varepsilon_{\tau\tau})\right]^2\right\}}, \tag{3.18}$$

and

$$\Delta\tilde{m}^2_M = \Delta m^2_{32}\sqrt{\left[\sin(2\theta_{23}) + 4E\frac{V}{\Delta m^2_{32}}\varepsilon_{\mu\tau}\right]^2 + \left[\cos(2\theta_{23}) - 2E\frac{V}{\Delta m^2_{32}}(\varepsilon_{\mu\mu} - \varepsilon_{\tau\tau})\right]^2}. \tag{3.19}$$

As mentioned on subsection 2.5.1, the $\nu_\mu \leftrightarrow \nu_\tau$ sector as a 2 flavor approximation is not affected by the standard matter potential that affects electron neutrinos, represented in Eq. (2.59). However, note now that if NSI effects are present, transitions of the type $\nu_\mu \to \nu_\mu$ are affected, even if this sector has no effect from the standard matter potential, as seen on Eq. (3.18) and Eq. (3.19).

Another important observation is that oscillation experiments are not sensitive to the individual NSI diagonal elements shown in Eq. (3.5), in the same way that oscillation experiments cannot directly measure the absolute neutrino mass scale, but only its mass squared difference as defined in Eq. (2.20). On the other hand, the off-diagonal NSI parameters can be directly probed at neutrino oscillation experiments.

3.3 Current status of NSI

3.3.1 Experimental bounds from neutrino oscillation experiments

In 2011, the Super-Kamiokande collaboration performed an analysis for the NSI parameter $\varepsilon_{\mu\tau} = \varepsilon^d_{\mu\tau}$ using their atmospheric neutrino data from the SK-I and SK-II run periods [51]. The model used was a 2 flavor approximation (θ_{12}, θ_{13}, and $\Delta m^2_{21} = 0$) in the $\nu_\mu \leftrightarrow \nu_\tau$ sector, with all $\varepsilon_{e\beta} = 0$, and considering only NSI with down-quarks, with $\varepsilon^d_{\mu\tau} \equiv \varepsilon$ and $\varepsilon^d_{\tau\tau} - \varepsilon^d_{\mu\mu} \equiv \varepsilon'$. The experiment obtained a bound of $|\varepsilon| < 1.1 \times 10^{-2}$ at 90% Confidence Level (CL), with a best fit of $\varepsilon = 1.0 \times 10^{-3}$.

More recently, in 2018 the IceCube collaboration performed an analysis [52] for the NSI parameter $\varepsilon^d_{\mu\tau}$ under the same model used by the Super-Kamiokande collaboration for the $\nu_\mu \leftrightarrow \nu_\tau$ sector (all ν_e related terms set to zero and only NSI interactions with down-quarks). The experiment performed the analysis using 4625 DeepCore[3] neutrino events. The limits from the IceCube analysis yields a 90% CL range of $-0.0067 < \varepsilon^d_{\mu\tau} < 0.0081$, with a best fit of $\varepsilon^d_{\mu\tau} = -0.0005$. Fig. 9 shows the allowed regions for the NSI parameter $\varepsilon^d_{\mu\tau}$ obtained by the Super-Kamiokande and IceCube collaborations.

[2] As defined in Eq. (2.66), for this case $\kappa_i = 0$.

[3] DeepCore is a part of the IceCube detector with a higher density of detection devices, making it suitable for investigations of neutrinos with energies in the few GeV range.

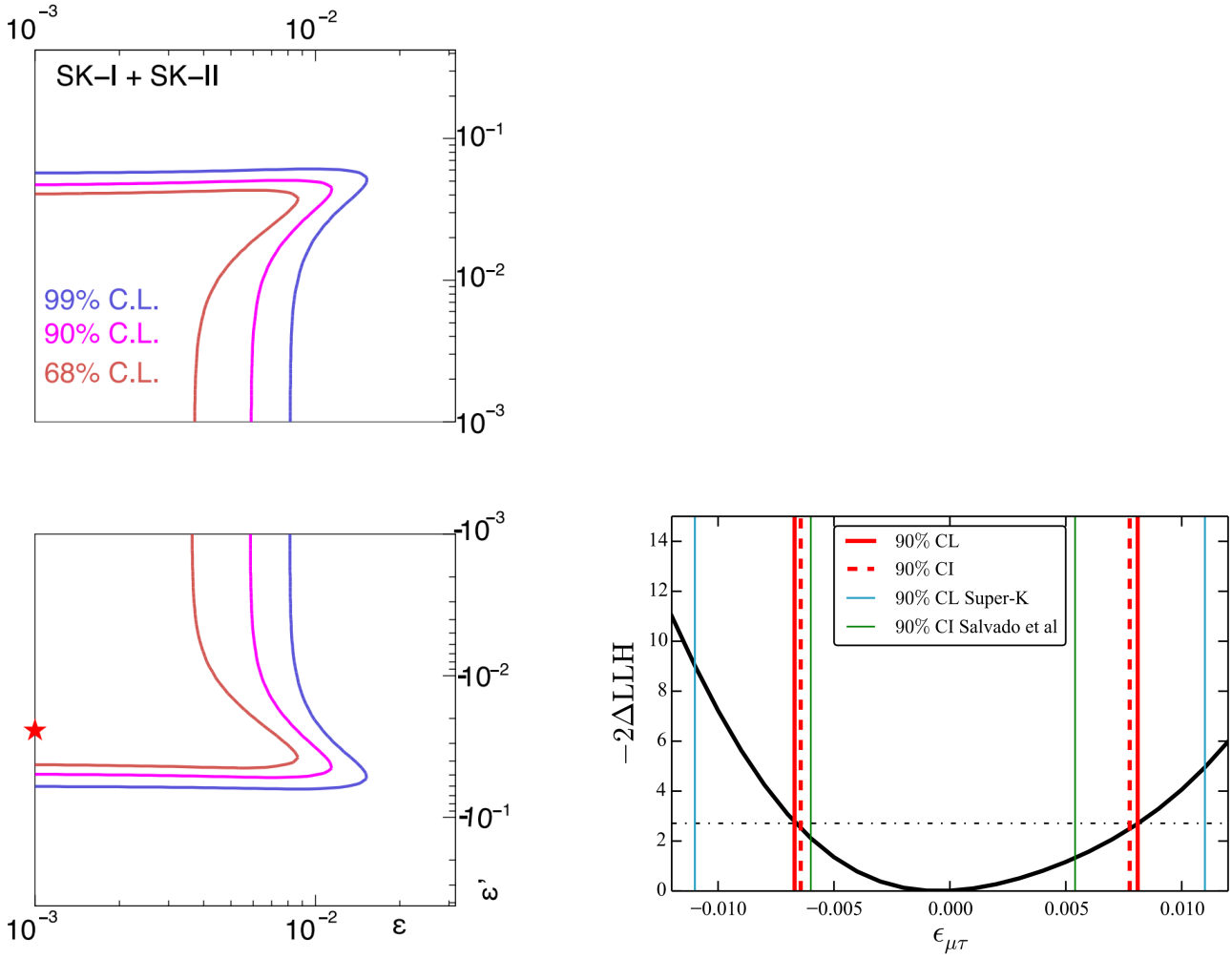

(a) (b)

Figure 9 – Allowed regions for the NSI flavor-changing parameter $\varepsilon^d_{\mu\tau}$ from atmospheric experiments. (a) Results from the Super-Kamiokande collaboration [51] at 68%, 90%, and 99% CL, with $\varepsilon^d \equiv \varepsilon_{\mu\tau}$ and $\varepsilon' \equiv \varepsilon^d_{\tau\tau} - \varepsilon^d_{\mu\mu}$. (b) Results from the IceCube collaboration [52] at 90% CL (solid vertical red line). The dashed vertical red line shows the 90% CL interval when profiling over the nuisance parameters. Shown is a comparison with the previous results from Super-Kamiokande (light-blue vertical line) and the allowed region from Ref. [53] (light-green vertical line).

Accelerator experiments have also been involved in previous NSI searches. In 2013, the Main Injector Neutrino Oscillation Search (MINOS) collaboration performed an analysis for the NSI parameter $\varepsilon_{\mu\tau}$ by measuring the disappearance of ν_μ and $\bar{\nu}_\mu$ in a predominantly dominated neutrino and antineutrino beam, respectively [54]. A 2 flavor neutrino scenario in the $\nu_\mu \leftrightarrow \nu_\tau$ sector was used, under the assumption of real valued NSI parameters. The experiment makes use of an exposure of 7.09×10^{20} Protons on Target (POT) in neutrino beam, combined with a 2.95×10^{20} POT exposure in antineutrino beam. The analysis yelds a 90% CL limit of $-0.20 < \varepsilon_{\mu\tau} < 0.07$ with a best fit of $\varepsilon_{\mu\tau} = -0.07^{+0.08}_{-0.08}$. Fig. 10 shows the mentioned results obtained by the MINOS collaboration for the NSI parameter $\varepsilon_{\mu\tau}$.

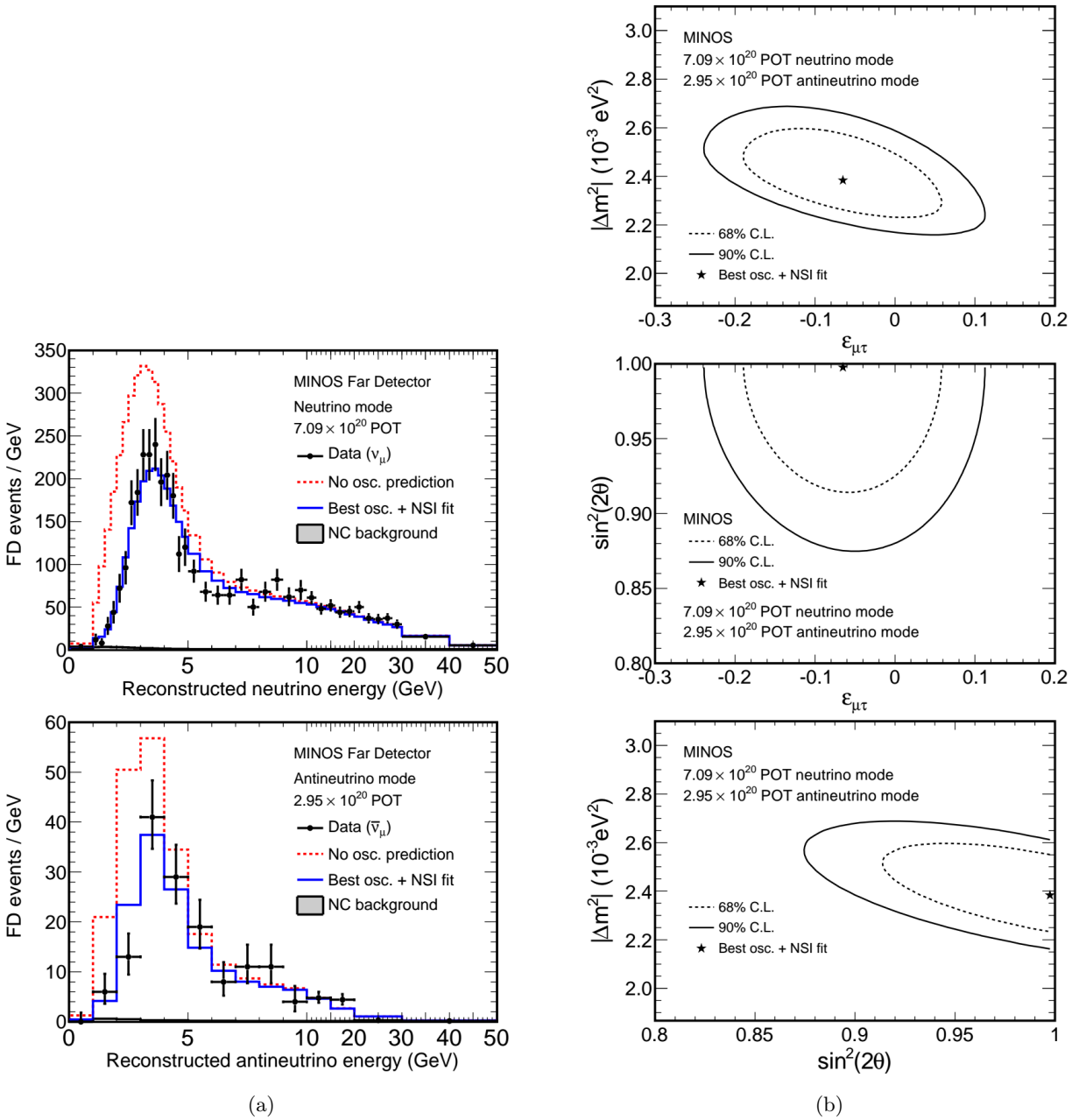

(a) (b)

Figure 10 – Results from the MINOS collaboration [54] for the NSI flavor-changing parameter $\varepsilon_{\mu\tau}$. (a) Far Detector CC events spectra for neutrino (top) and antineutrino (bottom) events, along with the histograms for the prediction in the absence of oscillations (red dashed) and for oscillations including NSI under the assumptions made (blue solid). (b) The 68% (dashed contour) and 90% CL (solid contour) allowed regions for the parameters $|\Delta m| \equiv |\Delta m^2_{32}|$, $\sin^2(2\theta) \equiv \sin^2(2\theta_{23})$, and $\varepsilon_{\mu\tau}$, along with the best fit and the exposures used in the analysis.

Later, in 2017, the MINOS collaboration reported constraints on the $\varepsilon_{e\tau}$ parameter and the effective phase $(\delta_{CP} + \delta_{e\tau})$ using ν_e and $\bar{\nu}_e$ appearance data in a predominantly initial ν_μ and $\bar{\nu}_\mu$ beam, respectively [55]. Mixing within the 3 neutrino flavors was considered, and all other NSI parameters are set to zero. The analysis makes use of an exposure of 10.6×10^{20} POT in neutrino beam, combined with a 3.3×10^{20} POT exposure in antineutrino beam. By performing an analysis in the $|\varepsilon_{e\tau}|$, $(\delta_{CP} + \delta_{e\tau})$ parameter space, the collaboration obtained at 90% CL for the NH scenario a best fit of $|\varepsilon_{e\tau}| = 0.74$ and $(\delta_{CP} + \delta_{e\tau}) = 1.35\pi$. Fig. 11 shows the mentioned results obtained by the MINOS collaboration for the NSI parameter $\varepsilon_{e\tau}$ and $(\delta_{CP} + \delta_{e\tau})$.

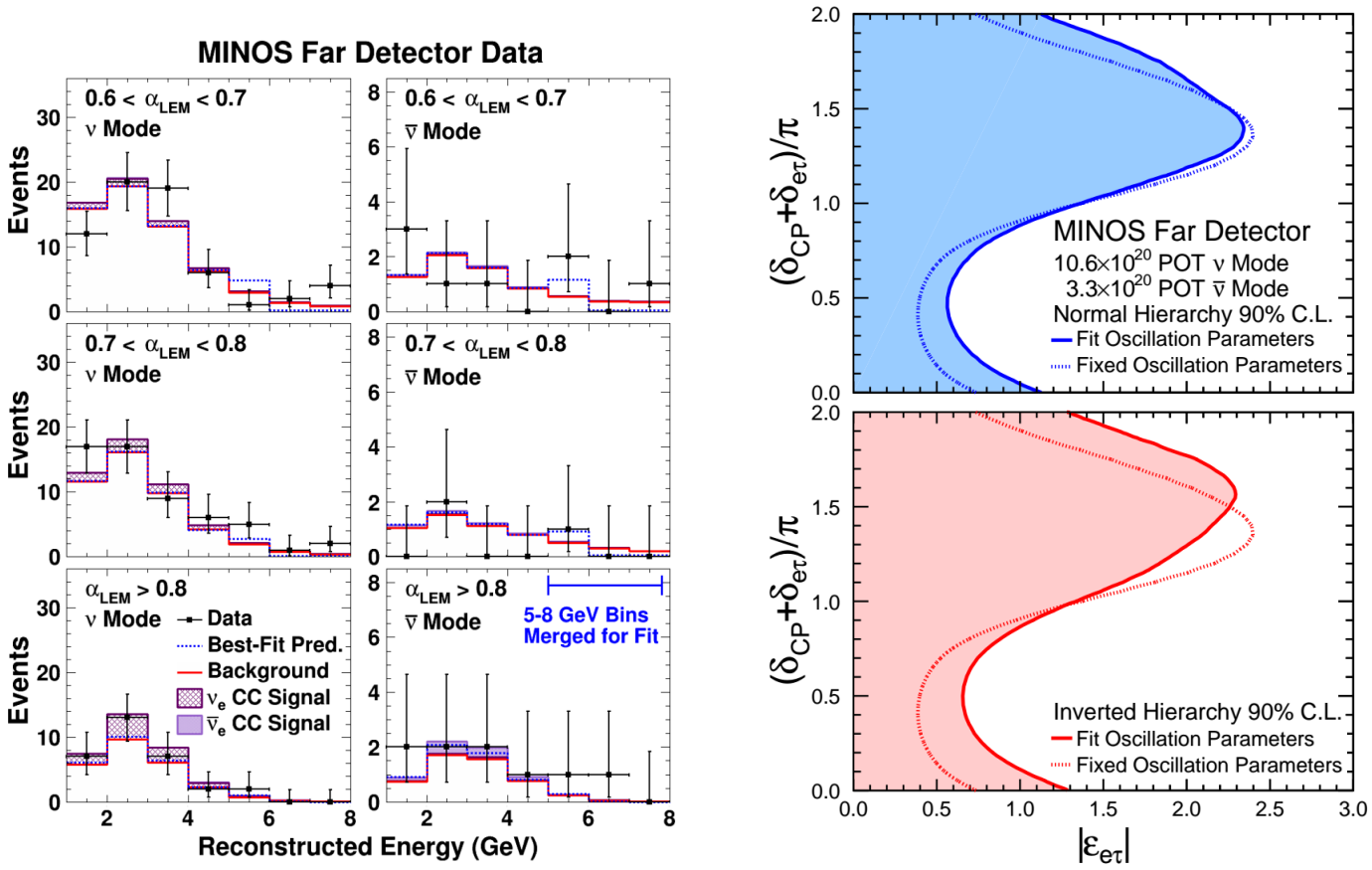

Figure 11 – Results from the MINOS collaboration [55] for the NSI flavor-changing parameter $\varepsilon_{e\tau}$ and the effective phase $(\delta_{CP} + \delta_{e\tau})$. (a) Far Detector CC events spectra for neutrino (left) and antineutrino (right) events for different ranges of α_{LEM} (Library Event Matching, part of a statistical selection algorithm used by the MINOS collaboration). (b) 90% CL allowed regions in the $|\varepsilon_{e\tau}|$, $(\delta_{CP} + \delta_{e\tau})$ parameter space for normal (top) and inverted (bottom) neutrino mass hierarchy, along with the exposures used in the analysis. The solid contour line show the limits where both the standard oscillation and NSI parameters are included on the fit, while the dotted contours correspond to a fit performed only over the NSI parameters.

Table 2 summarizes the mentioned results obtained by the respective experiments.

	Limits obtained	best fit	Data/Exposure
Super-Kamiokande [51]	$\left\|\varepsilon^d_{\mu\tau}\right\| < 1.1 \times 10^{-2}$	$\varepsilon^d_{\mu\tau} = 1.0 \times 10^{-3}$	SK-I+SK-II
IceCube DeepCore [52]	$-0.0067 < \varepsilon^d_{\mu\tau} < 0.0081$	$\varepsilon^d_{\mu\tau} = -0.0005$	4625 events
MINOS [54]	$-0.20 < \varepsilon_{\mu\tau} < 0.07$	$\varepsilon_{\mu\tau} = -0.07^{+0.08}_{-0.08}$	7.09×10^{20} POT ν-mode + 2.95×10^{20} POT $\bar{\nu}$-mode
MINOS [55]		$\lvert\varepsilon_{e\tau}\rvert = 0.74$ $(\delta_{CP} + \delta_{e\tau}) = 1.35\pi$	10.6×10^{20} POT ν-mode + 3.3×10^{20} POT $\bar{\nu}$-mode

Table 2 – Limits obtained, best fit value and experimental data/exposure used by the Super-Kamiokande, IceCube DeepCore and MINOS collaborations for the NSI flavor-changing parameters at 90% CL assuming normal neutrino mass hierarchy.

3.3.2 Constraints from Global Analysis of Oscillation Data

As in the case for determining the standard oscillation parameters, each experiment has different sensitivities for different NSI parameters. Similarly, when performing the analysis, a few approximations can be done, such as working on a 2 flavor scenario or setting subleading parameters to zero, which directly impacts how comparable two or more results are.

It should be noted that, as mentioned, the results presented in Refs. [51] and [52] were obtained through the consideration of interactions with only down-quarks. This means that the results obtained under this approach are not directly comparable to the way our model is parameterized. For example, if we neglect contributions from electrons and up-quarks in our model in Eq. (3.8), the mentioned parameters obtained by the respective collaborations should be multiplied by a factor 3, once the number of down-quarks is approximately 3 for each electron, $N_d = 3N_e$. It is then desirable to obtain a general panorama considering the global overview and contributions available.

Apart from direct experimental searches, several works have reported constraints over the NSI parameters through a global analysis of available oscillation data. Model-independent bounds for the NSI parameters $|\varepsilon_{\alpha\beta}|$ accounting neutrino propagation in Earth-like matter[4] is presented in Ref. [47], given by

$$\begin{pmatrix} |\varepsilon_{ee}| < 4.2 & |\varepsilon_{e\mu}| < 0.33 & |\varepsilon_{e\tau}| < 3.0 \\ & |\varepsilon_{\mu\mu}| < 0.068 & |\varepsilon_{\mu\tau}| < 0.33 \\ & & |\varepsilon_{\tau\tau}| < 21 \end{pmatrix}. \tag{3.20}$$

A more recent analysis of global available oscillation data as of 2019 is reported in Ref. [46], where the authors also present the allowed values for the effective NSI parameters $\varepsilon_{\alpha\beta}$ at different $\Delta\chi^2$, considering propagation of neutrinos in Earth-like matter, of interest for long-baseline experiments. Results were obtained through analysis of solar,

[4] Electrically neutral matter and equal number of protons and neutrons.

atmospheric, accelerator and reactor data, with the inclusion or not of data from the COHERENT experiment[5]. Shown are results in light of the called LMA[6] solution, and also for the LMA-D solution (known as *Dark Sector*). The LMA-D solution is characterized by allowed values of $\theta_{12} > 45°$, in contrast to the strongly favored value of $\theta_{12} < 45°$ from the standard LMA scenario. The solutions for both scenarios can be seen in Fig. 12, where we see a preference for rejection of solutions in light of LMA-D.

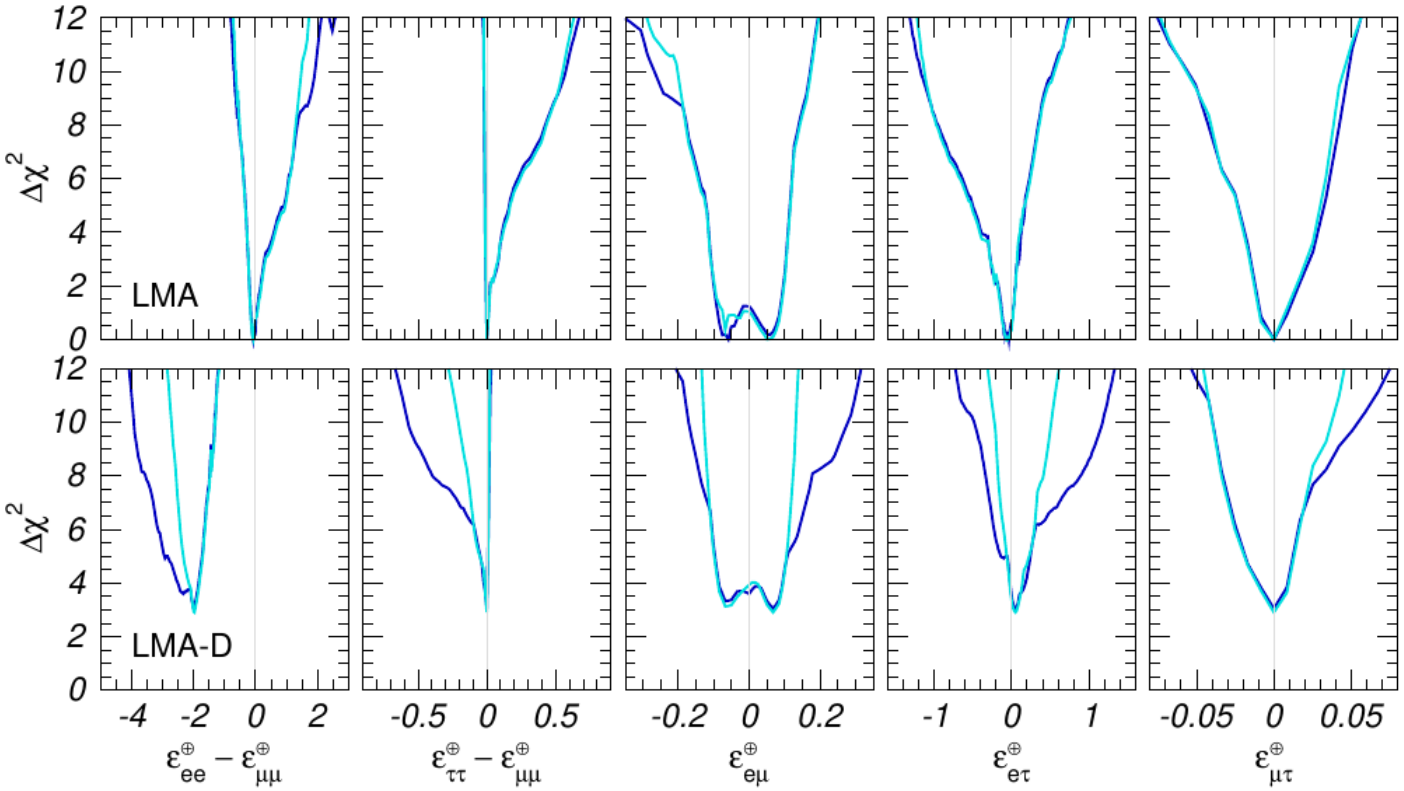

Figure 12 – Allowed values for the effective NSI parameters at different $\Delta\chi^2$ considering neutrino propagation in Earth-like matter, with and without inclusion of COHERENT data, shown in cyan and blue, respectively. The upper plots show solutions for the LMA case, while the lower plots present solutions for the LMA-D scenario [46].

[5] Inclusion of COHERENT data is valid for NSI models where the NSI mediator is necessarily heavier than about 10 MeV, an assumption not explicitly needed at other NSI models.

[6] LMA stands for Large Mixing Angle.

4 The NOvA experiment

The NOvA experiment [56] is a second-generation[1] long-baseline neutrino experiment hosted at Fermilab, USA. It consists of two functionally identical tracking calorimeters, the Near Detector (ND) and the Far Detector (FD), primarily designed to study oscillations from neutrinos and antineutrinos produced by the Fermilab accelerator facilities.

Its primary goals are:

- Precision measurement of the mixing angle θ_{23}, and thus the investigation of the octant problem.
- Search for the value of the δ_{CP} phase, allowing investigations of possible CP symmetry violation in the leptonic sector.
- Precision measurement of the parameter Δm^2_{32}, leading to investigations of the neutrino mass hierarchy.

Besides from the investigation of the parameters with respect to neutrino oscillations, NOvA has also sensitivity to a broad range of further topics, such as neutrino cross section measurements at the ND, cosmic ray physics, supernovae neutrinos, gravitational wave neutrino coincidence, sterile neutrinos, and other phenomena.

The NOvA experiment is 14 mrad (0.8°) off-axis with respect to the on-axis neutrino beam propagation direction, in contrast with the MINOS experiment [57], which was aligned and on-axis with the neutrino beam. The off-axis concept was already used by the Tokai to Kamioka (T2K) experiment [58] and marks an important advance design for long-baseline oscillation experiments because it significantly reduces the contamination in a $\nu_\mu \rightarrow \nu_e$ analysis[2].

Neutrinos and antineutrinos for the NOvA experiment are produced by the collision of a 120 GeV proton beam with a fixed target, producing a set of mesons which decay into charged leptons and neutrinos.

In order to perform oscillation studies, data is taken at the ND, which is located at Fermilab and 1 km away from the fixed target, being responsible for measuring the initial neutrino flux, and also at the FD located 810 km away from the target (809 km from the ND), at Ash River (Minnesota), which by comparison of the measured fluxes at each detector allows one to investigate the oscillation phenomenon. The effect of such a long-baseline implies that matter effects through the propagation of neutrinos from the target to the FD are relevant, and this makes NOvA a suitable experiment able to contribute to the already mentioned open questions on neutrino oscillations. Fig. 13 shows a schematic representation of the NOvA baseline in comparison to the MINOS setup.

[1] Prior to NOvA construction, the MINOS experiment was the first long-baseline neutrino experiment in operation at Fermilab.
[2] See section 4.2 for details.

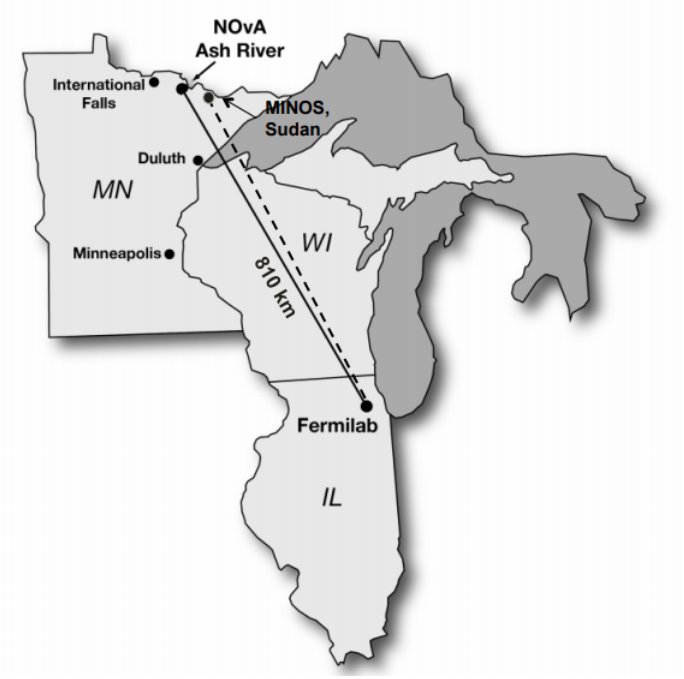

Figure 13 – Schematic representation of the NOvA baseline. The ND is located at Fermilab, while the FD is located at Ash River. The dashed line shows the on-axis path traveled by the neutrino beam, which was the case for the MINOS experimental setup. The contour line stands for the off-axis path used by NOvA [59].

4.1 NuMI neutrino beam

Neutrinos at the Main Injector (NuMI) is the facility at Fermilab responsible to create an intense and collimated neutrino beam. In order to produce the neutrino beam, the process start with a source providing H^- ions with energies of 35 keV to 750 keV to the linear accelerator (Linac), where the beam reach the energy of 400 MeV. At the end of the Linac a carbon foil is used to transform the H^- ions into a H^+ (proton) beam. The initial proton beam is transferred to the Booster, a synchrotron that accelerates the protons to the energy of 8 GeV, from where they follow to the Main Injector, a seven times larger synchrotron responsible for accelerating the beam to the energy of 120 GeV. The Main Injector delivers $\sim 5 \times 10^{13}$ protons to the NuMI target during a $10\,\mu$s spill, repeating the pulse with an average of 1.33 s [60]. The amount of data collected and used in the analyses is then presented in terms of our exposure of Protons on Target (POT). Fig. 14 shows a schematic representation of the Fermilab Accelerator Complex.

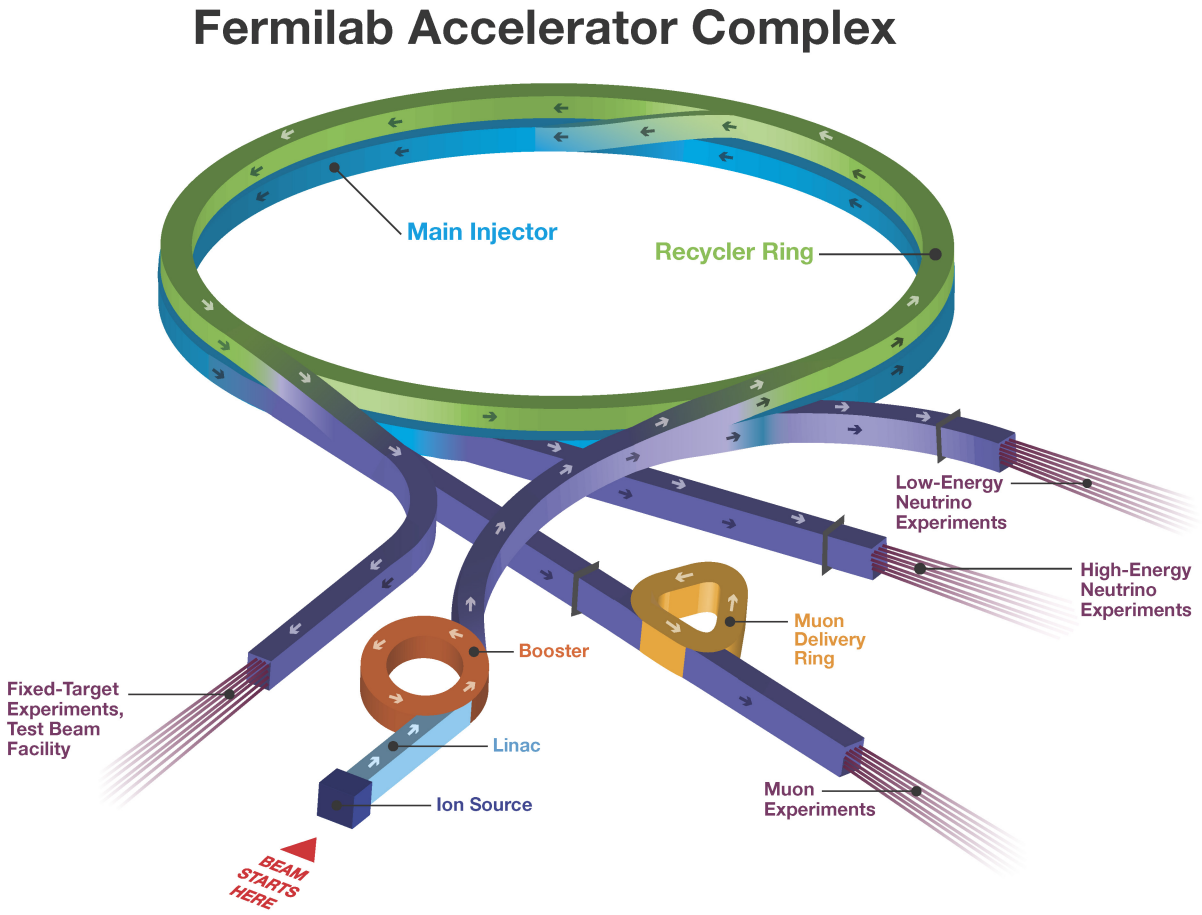

Figure 14 – Schematic representation of the Fermilab Accelerator Complex. Shown is the ion source, from where the beam follows to Linac, the Booster and the Main Injector, being ready to be delivered to the various experiments at Fermilab. From `https://vms.fnal.gov/`

The batches of 120 GeV protons from Fermilab's accelerator facilities are sent towards a thin graphite target composed of 47 vertical segments, each one being 20.0 mm long and 6.4 mm wide, separated by a 0.3 mm spacing, being 95.38 cm long in total [61], as seen in the schematic representation in Fig. 15.

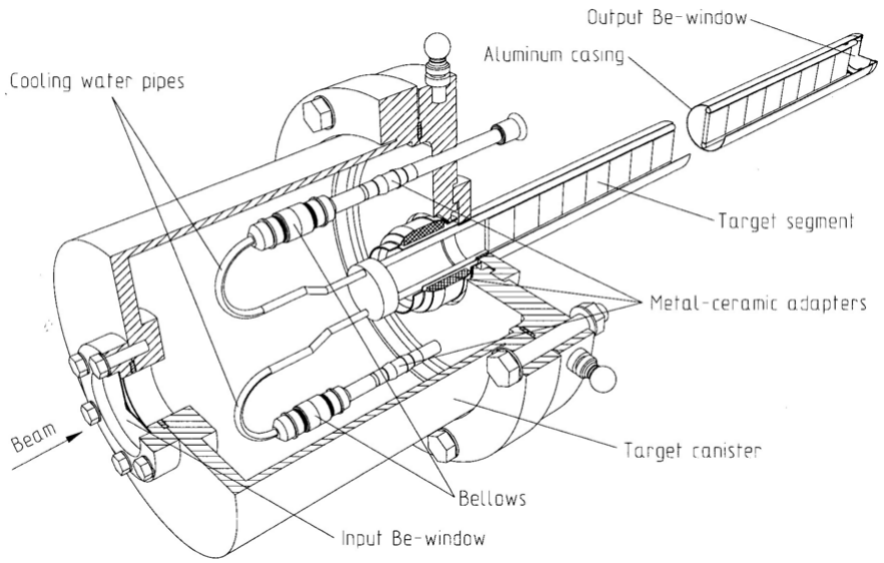

Figure 15 – Schematic representation of the NuMI target. Shown is the graphite target segment along the cooling water pipes. The beam incident direction is seen at the bottom left [61].

The interaction of protons with the target produces a set of mesons, mostly charged pions and kaons, which then are subjected to a pair of horn-shaped magnetic lenses and collimated into a 675 m decay pipe[3]. The magnetic lens is comprised of two parabolic magnetic horns operating in pulses of 2.3 ms at an electric current of 200 kA in order to create a magnetic field of up to 3 T, with a repetition rate of 1.87 s, and can have the direction of the electric current switched in order to switch the magnetic field as well, allowing to deflect positive or negative particles by choice. Fig. 16 shows a schematic representation of the magnetic lens used by NOvA.

[3] The decay pipe is the region used to maximize the decaying of the pions.

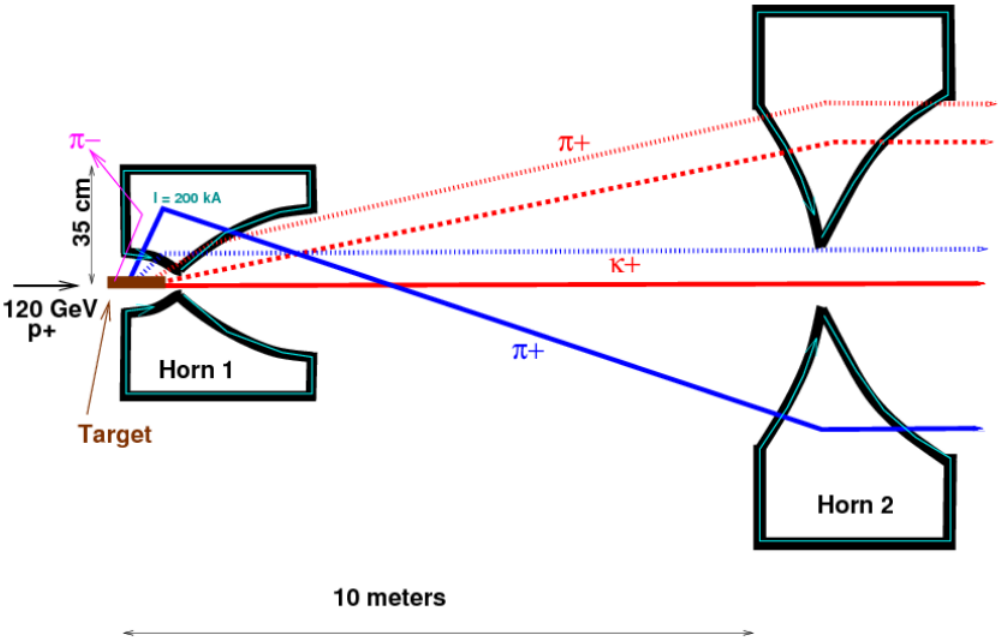

Figure 16 – Schematic representation of the magnetic focusing horns used by NOvA. Shown is the example of charged particles produced by the collision of 120 GeV protons with a fixed target. Negative charged particles are deflected from the beam line by horn 1, and positive charged particles are first focused by horn 1, with horn 2 being used for trajectory corrections. [62]

The particles under focused or over focused by the horn 1 are further corrected by the second horn. The distance between the target, horn 1 and horn 2 can be adjusted to tune the energy of the beam, with the medium-energy setup being chosen for NOvA by placing the horn 1 at 1.3 m from the target, and the horn 2 at 10 m with respect to the front face of horn 1.

The pions produced decay mainly according to

$$\pi^+ \to \mu^+ + \nu_\mu, \tag{4.1}$$

$$\pi^- \to \mu^- + \bar{\nu}_\mu. \tag{4.2}$$

The focusing of π^+ is known as Forward Horn Current (FHC), and the choice for π^- is known as Reverse Horn Current (RHC), which according to Eq. (4.1) and (4.2) will result in a neutrino-dominated beam or an antineutrino-dominated beam, respectively. The FHC (RHC) operation mode gives a 96% (83%) pure ν_μ ($\bar{\nu}_\mu$) beam, where most of the contamination is wrong-sign ($\bar{\nu}_\mu$ in the ν_μ beam, or vice versa), with less than 1% ($\nu_e + \bar{\nu}_e$) contamination [63]. Following the decay pipe is a hadron monitor, an absorber and a set of muon monitors intercalled with layers of rock. This arrangement is so that the neutrino flux can be quantitatively measured, and the presence of the absorber and rocks maximize the stopping power of any particle other than neutrinos from entering the Near Detector, lowering the contamination and background. A comprehensive schema is shown in Fig. 17.

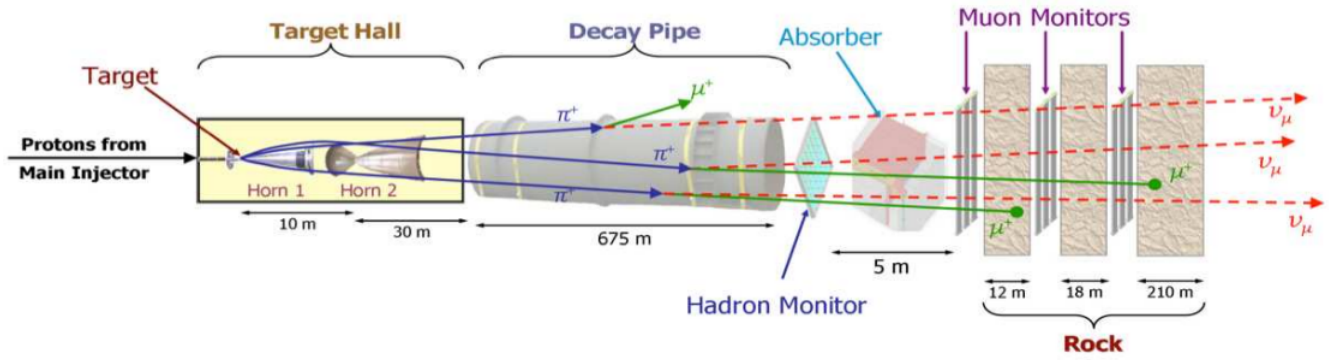

Figure 17 – Schematic representation of the NuMI beam containing all the important elements. Shown is the Target Hall (comprising the target itself and the two magnetic horns used to collimate the beam), the Decay Pipe, Hadron Monitor, Absorber and the Muon Monitors intercalled with solid rock, from where the resulting neutrinos follow the path into the Near Detector [62].

4.2 Off-axis configuration for NOvA

The flux ϕ_ν and energy E_ν of the neutrinos [56] resulting from pion decay are expressed by

$$\phi_\nu = \left(\frac{2\gamma}{1+\gamma^2\theta^2}\right)^2 \frac{A}{4\pi z^2}, \tag{4.3}$$

and

$$E_\nu = \left(1 - \frac{m_\mu^2}{m_\pi^2}\right) \frac{E_\pi}{1+\gamma^2\theta^2}, \tag{4.4}$$

where A is the area of the detector, z is the distance between the detector and decaying point, E_π and m_π are the energy and the mass of the parent pion, respectively, with $\gamma = \frac{E_\pi}{m_\pi}$, and θ is the angle between the pion direction and the neutrino direction. The area A of the detector is constant, and the energy E_π of the pions depends on the incident protons from the accelerator, and can be considered constant as well. This leaves the variables z and θ as the remaining factors to be considered when designing the experiment.

The $\nu_\mu \to \nu_e$ ($\bar{\nu}_\mu \to \bar{\nu}_e$) transition probability curve shows a maximum for a baseline of ~ 810 km with an energy of ~ 2 GeV [4], where the experiment is also sensitive to the sign of Δm^2_{32}, as seen in Fig. 18.

[4] The oscillation probability depends on the ratio L/E, which peaks a maximum at $\frac{L}{E} = \frac{\pi}{2} \cdot \frac{1}{1.27\left|\Delta m^2_{32}\right|}$ for $L \approx 810\,\text{km}$ and $E \approx 2$ GeV [59].

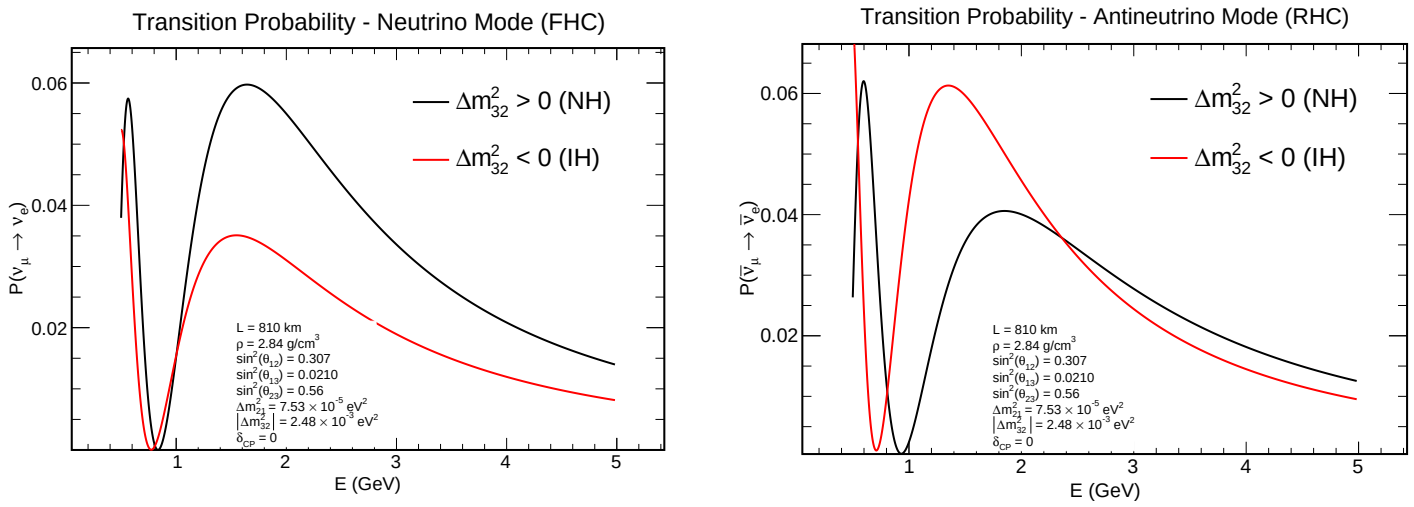

(a) neutrino beam

(b) antineutrino beam

Figure 18 – $\nu_\mu \to \nu_e$ ($\bar{\nu}_\mu \to \bar{\nu}_e$) transition probability for the NOvA configuration for neutrinos (a) and antineutrinos (b), for normal hierarchy (black) and inverted hierarchy (red) neutrino mass ordering.

This leaves the angle θ as the remaining choice to be made. Fig. 19 (a), (b) and (c) shows the estimated neutrino flux, neutrino energy and number of ν_μ CC events at the FD, respectively, for different values of θ, from where it can be seen that the choice for the 14 mrad off-axis configuration ensures a narrowly peaked band at the desired neutrino energy around 2 GeV that maximizes the $\nu_\mu \to \nu_e$ transition. Additionally, the absence of higher energetic neutrinos significantly reduces the contamination from ν_τ interactions at the FD[5], and such configuration also makes possible to neglect the contribution from kaon decay, since neutrinos resulting from this process have energies well above the signal band of 2 GeV [64].

[5] E_ν above 2 GeV is linked to τ production due to oscillated ν_τ interactions at the detector, which then can decay into other leptons as final state and thus is a source of background.

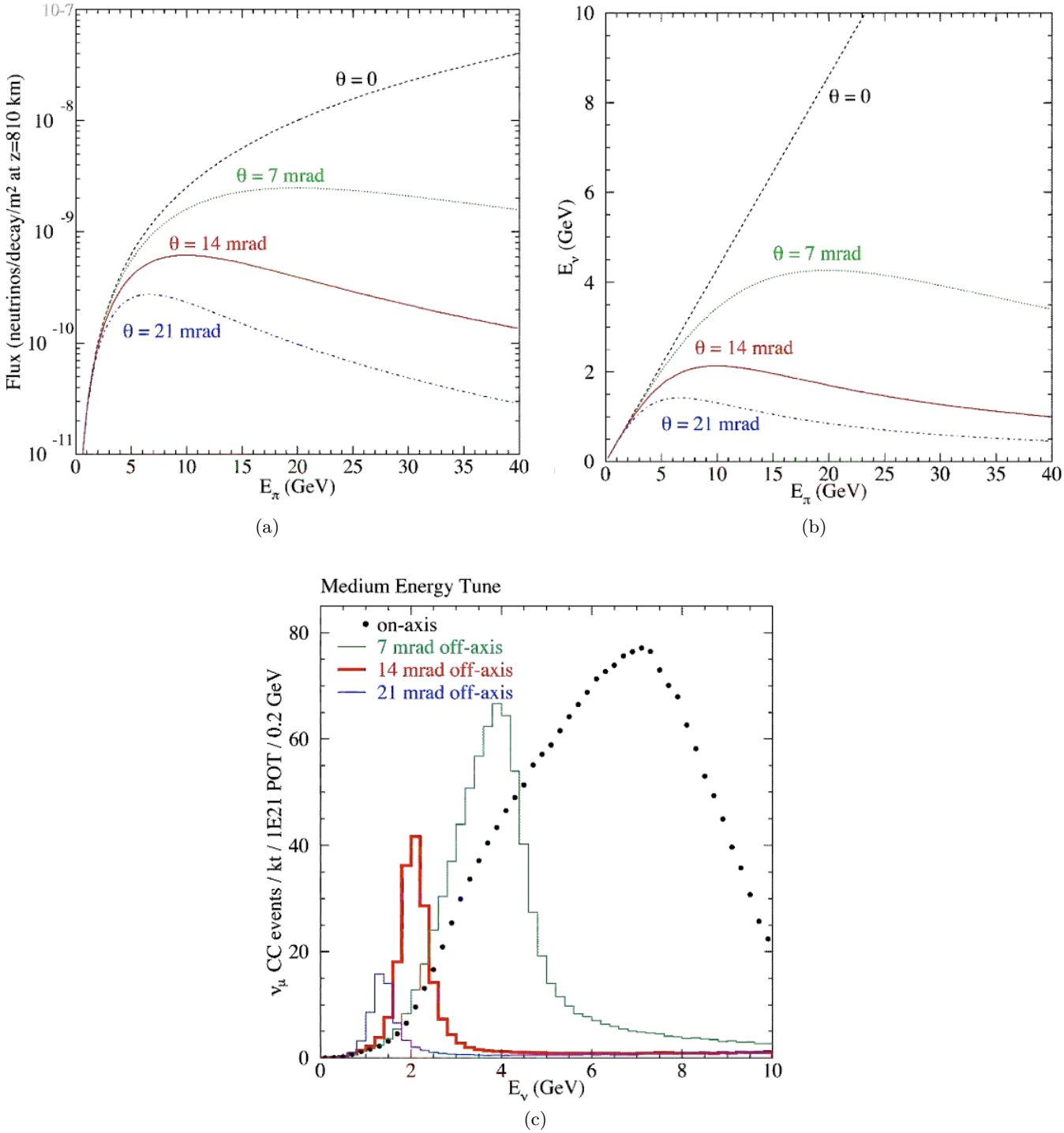

Figure 19 – Neutrino flux (a), energy (b) and ν_μ CC events (c) for various choice of θ considered the proton beam provided by the Main Injector and a Far Detector located at 810 km from the target. It is clear the suppression of the high energy tail for a 14 mrad off-axis choice [65].

4.3 Detector structure and assembly

The general and basic unit responsible for particle detection on NOvA is a rectangular Polyvinyl Chloride (PVC) cell filled with liquid scintillator and containing a Wavelength-shifting fiber (WLS) connected to an Avalanche Photodiode (APD) [65]. Each cell has an interior cross section of $3.8 \times 5.9\,\mathrm{cm}^2$, and an interior length of 15.5 m for those at the FD, while the length for a ND cell is 4 m. The interior surface of the cell is coated with highly

reflective titanium dioxide (TiO_2), and the liquid scintillator used inside the cells is mainly composed of mineral oil with 5.23% pseudocumene as the scintillant. Table 3 presents an overview of the liquid scintillator composition used in the NOvA experiment.

Component	Purpose	Mass fraction	Mass (kg)
Mineral oil	Solvent	94.63%	7,658,656
Pseudocumene	Scintillator	5.23%	423,278
PPO	Wavelength-shifter	0.14%	11,331
bis-MSB	Wavelength-shifter	0.0016%	129
Stadis-425	Anti-static	0.001%	81
Vitamin E	Anti-oxidant	0.001%	78
Total			8,093,264

Table 3 – Overview of the liquid scintillator composition used in the NOvA experiment [66].

The WLS fiber inside the cell is looped on the bottom of the cell, and both ends are connected to an APD pixel, as seen in Fig. 20 (a). The APD is responsible for converting the light conducted by the WLS into electrical signals to be read by the detector electronics. The cells are arranged together into a set of 16 units, as represented in Fig. 20 (b), which are then attached to other set in order to create a module consisting of a flat row of 32 cells, connected by a side seal and the electronics box, along with a manifold cover on the top, as seen in Fig. 20 (c).

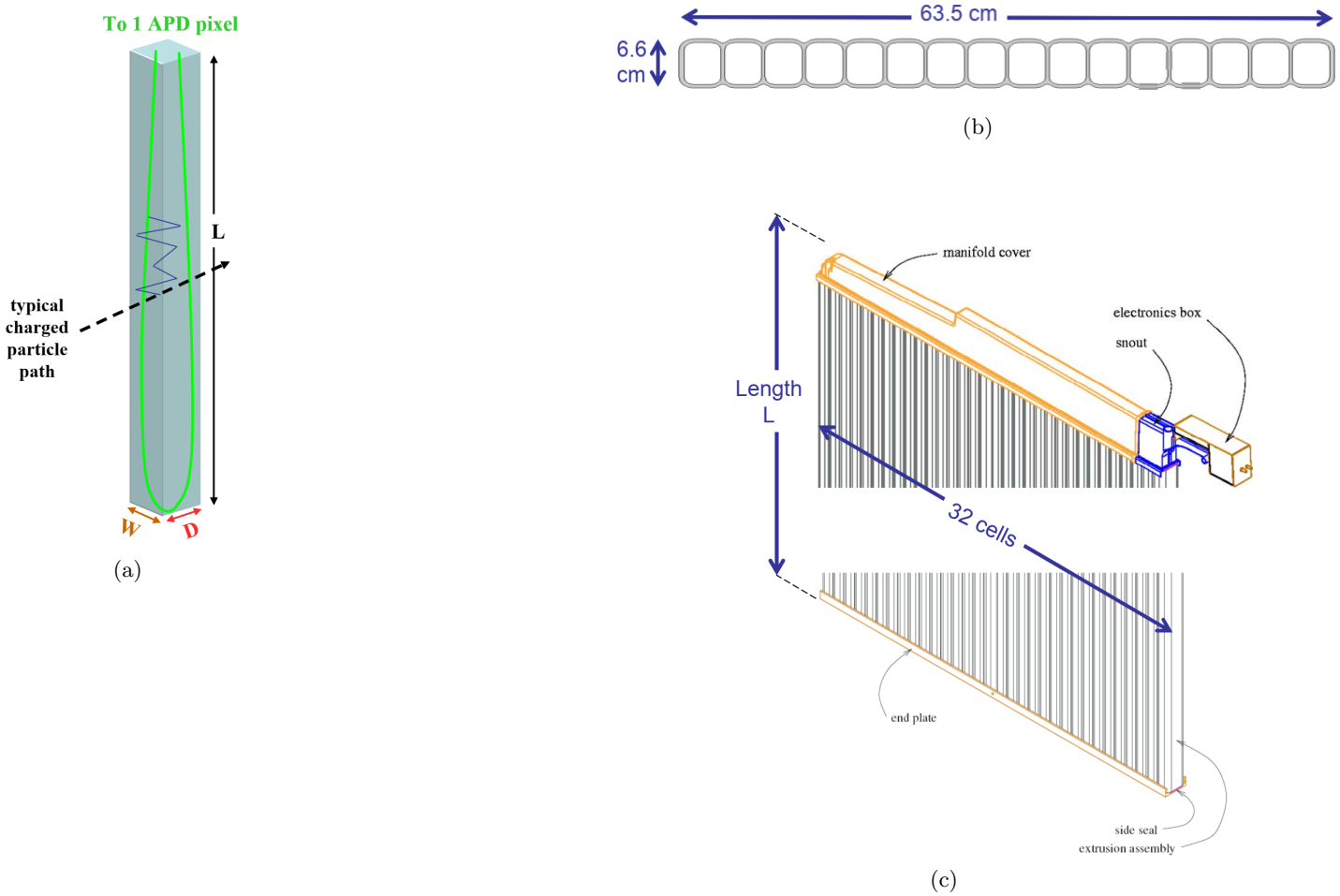

Figure 20 – Schematic representation of a unit PVC cell of dimensions (W, D, L) containing liquid scintillator and a Wavelength-shifting fiber (green) looped on the bottom with both ends towards an APD pixel (a). In dotted lines is represented a path of a charged particle producing light (blue). Drawing of a NOvA extrusion composed of 16 parallel unit cells (b), and a module composed of two side by side extrusions of 16 cells each, for a total of 32 cells per module (c). Together is shown the manifold cover, which routes the 64 fiber ends into the avalanche photodiode array and the electronics box [65].

The modules, each with 32 cells, are disposed in parallel in order to create a layer of cells known as the detector planes, where each adjacent planes of the detector are mutually orthogonal arranged to allow 3D track reconstruction, as seen in Fig. 21, and are assembled together to finally reach the desired size for the full detector.

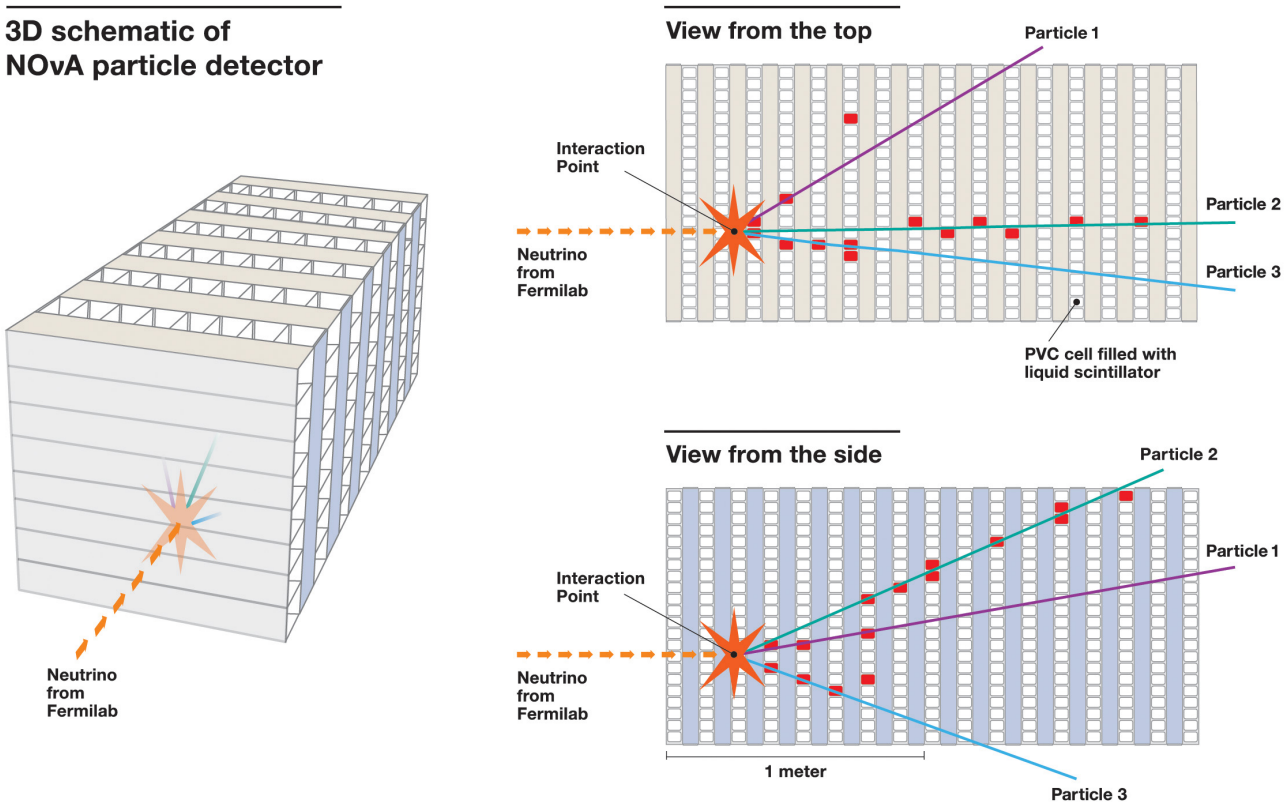

Figure 21 – 3D schematic of NOvA particle detector (left), along with its top and side views (right), showing the orthogonal alternating planes to allow for 3D particle track reconstruction. A representation of a general neutrino interaction leaving a signal in individual cells is shown, from where track reconstructions for the resulting particles is possible. From `https://vms.fnal.gov/`

4.4 Particle detection and signal processing

When a charged particle pass through the detector it excites the material causing photons to be emitted during the de-excitation. These photons remain being reflected inside the PVC until it is captured by the WLS fiber, from where it is transported to the APD.

The scintillant material produces light with a spectrum peaked at 360 - 390 nm, and the presence of other chemical additives[6] shift such initial light to the range of 400 - 450 nm, making it possible to be captured by the WLS fiber, from where the wavelength is shifted to around 490 - 550 nm and conducted to the APD pixel readout. When it reaches the APD pixel, the light signal is ready to be converted into electrical signal in order to be processed by the experiment's electronics. The APDs are highly sensitive[7] and efficient semiconductor devices based on the photoelectric effect, functional under a process called impact-ionization. When photons hit the APD pixel it excites electrons of the material, which then are accelerated by a high electric field created by an applied voltage of 375 volts inside the APD. The electrons quickly interact with the surrounding electrons of the material, which are then moved to the conduction band of the semiconductor. Such free electrons repeat the aforementioned process, which creates an avalanche of charge carriers in the diode, resulting in a significantly amplified photocurrent.

[6] PPO [2.5-diphenyloxazole] and bis-MSB [1.4-di(methylstyryl)benzene] [65].

[7] The APD has an 85% efficiency, compared to only 20% provided by Photomultiplier Tubes (PMT). Given NOvA's long cell length, this is specially important [65, 67].

Depending on the type of interaction, ν_μ or ν_e events have well characteristic topologies, as exemplified in Fig. 22.

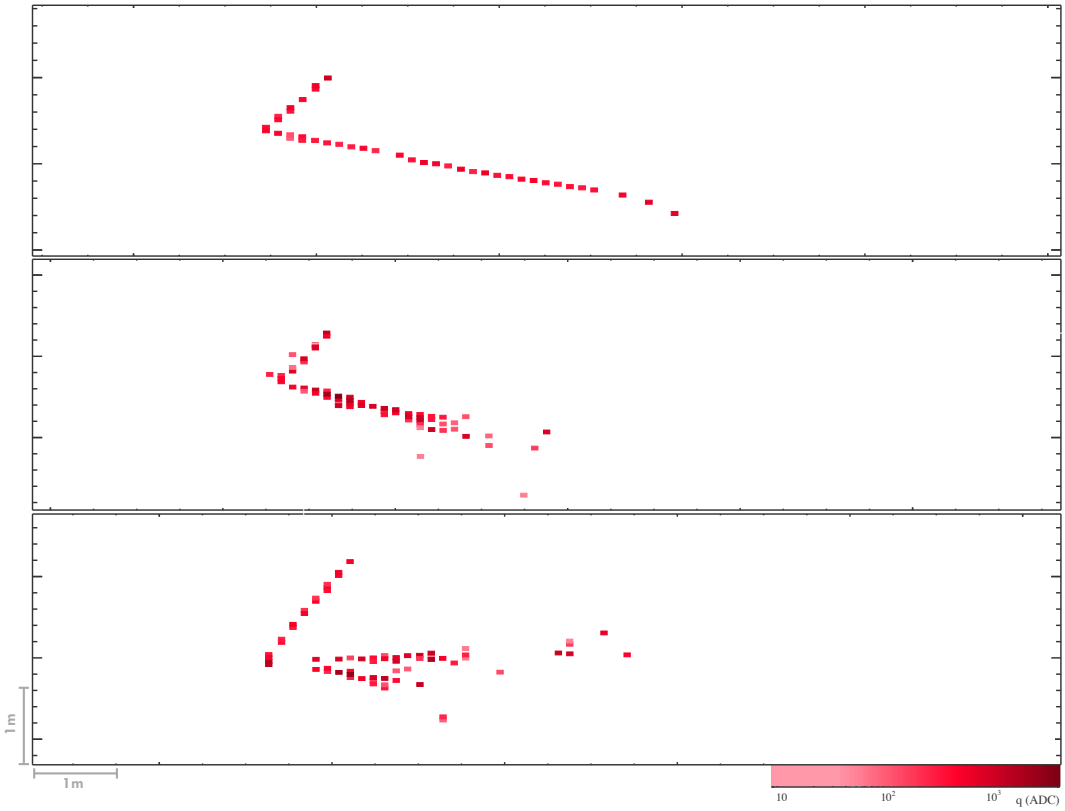

Figure 22 – Event topology for a simulated ν_μ CC event (top), ν_e CC event (middle) and a general neutrino NC event (bottom) [68].

Muons have a higher penetrating power, thus leaving a characteristic track of deposited energy while going through the detector. Electrons, in the other hand, have a shorter and diffuse track due to consecutive scatterings with the surrounding material. Events arising from NC interactions, for all neutrino flavors, do not result in charged leptons as final states. Instead, charged mesons, such as π^+ or π^-, can be produced and deposit energy as they propagate through the detector. Neutral mesons, mostly π^0, can also be produced, which then decay into two photons, leaving a signal as they propagate as well. In some cases, NC events can possess an event topology similar to the events from ν_e CC interactions, leading to possible mismatches on the identification of the interaction, which depending on the analysis of interest, could comprise a source of systematic uncertainty. The emerging particles are identified by using calorimetry, where muons, specifically, can be identified by its characteristic energy deposition patterns along the cells, $\frac{dE}{dX}$.

4.5 Near Detector and Far Detector

The Near Detector is located at Fermilab, being placed ∼100 m underground at a 1 km distance from the NuMI target, and became fully operational in August of 2014. The underground positioning provides a better shielding of the detector from cosmic rays, reducing the background from such source. It comprises two distinct parts, the Active Region and the Muon Catcher. Together, they make the ND as being 4 m wide, 4 m tall and 15.6 m long, as a result of 214 planes, giving a total of 20,192 cells used. The Active Region is the functional part of the detector responsible for measuring particles that leave a signal when passing through the detector. Each plane in

this region is composed of 3 modules, resulting in a row of 96 cells, for a total of 192 planes were used. Differently from the Active Region, the Muon Catcher has also a 10 cm thick steel plane between every pair of the detector planes, designed to enhance the stopping power and containment of the muons produced by neutrino interactions in the detector. Each plane in this region is made of 3 modules placed vertically and 2 horizontally, being then 96 cells at the vertical and 64 disposed horizontally. In total, 22 PVC planes were used on this component.

The Far Detector is a much larger and massive detector, and is located in Ash River (MN), distant 809 km from the ND at Fermilab (810 km from the target). Differently from the ND, the FD is at surface level at an altitude of 380 m, which significantly increase the counting of cosmic rays. As an attempt of lowering such background, a layer of 1.2 m of concrete and 0.15 m of rock was added to the top of the detector, considerably decreasing the cosmic ray counting. In addition, due to NOvA's high performance computational power, the remaining background is efficiently processed in order to not affect the experimental measurements on particles originating from the neutrino beam. Last, as mentioned, NOvA is able to use such cosmic ray data to perform additional studies other than the primary goals stipulated. Each plane is composed of 12 modules, and the FD is 15.5 m wide, 15.5 m tall and 60 m long, as a result of 896 planes, giving a total of 344,064 cells. Fig. 23 presents a picture of the NOvA Near and Far detectors.

(a) NOvA Near Detector

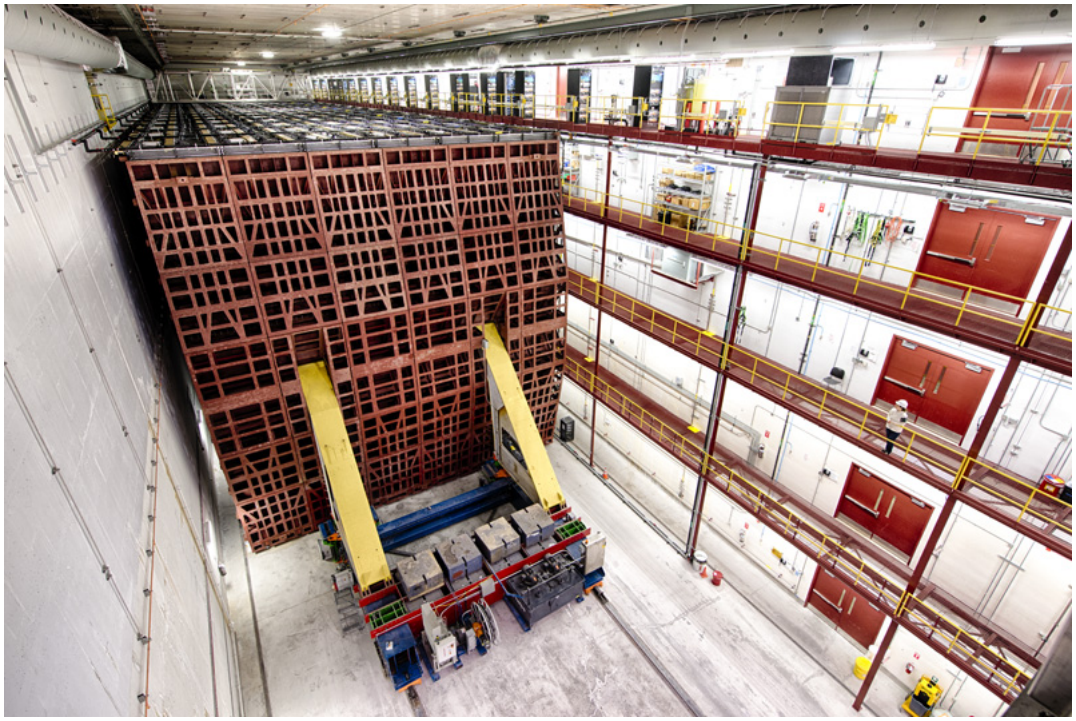

(b) NOvA Far Detector

Figure 23 – The NOvA detectors. From `https://vms.fnal.gov/`

5 NSI Sensitivity Studies on NOvA

NOvA is able to perform neutrino oscillation analyses investigating both the disappearance of ν_μ and appearance of ν_e by comparing predictions with the Far Detector data. The disappearance analysis makes use of the survival probability to predict the probability for an initially ν_μ in the beam to be detected in the same flavor after it evolved in the 810 km NOvA baseline, which is the approach and channel adopted for this analysis.

5.1 NSI model

The model used in this analysis is the 3 flavor neutrino oscillations in matter in the presence of non-standard interactions, as described by the Hamiltonian defined in Eq. (3.4), represented by

$$\mathcal{H} \doteq U^\dagger \begin{pmatrix} 0 & 0 & 0 \\ 0 & \frac{\Delta m^2_{21}}{2E} & 0 \\ 0 & 0 & \frac{\Delta m^2_{31}}{2E} \end{pmatrix} U + \pm\sqrt{2} G_F N_e \begin{pmatrix} 1+\varepsilon_{ee} & \varepsilon_{e\mu} & \varepsilon_{e\tau} \\ \varepsilon_{\mu e} & \varepsilon_{\mu\mu} & \varepsilon_{\mu\tau} \\ \varepsilon_{\tau e} & \varepsilon_{\tau\mu} & \varepsilon_{\tau\tau} \end{pmatrix}. \tag{5.1}$$

The '1' in the 1-1 element in the effective matter potential is due to the standard interactions of $\nu_e\,(\bar{\nu}_e)$ with electrons in the medium, as already described by Eq. (2.59). In the disappearance channel, the survival probability for a ν_μ in the beam will be given by

$$P_{\nu_\mu \to \nu_\mu} = \left| \left\langle \nu_\mu\,(x,t) \left| e^{-\imath \mathcal{H} t} \right| \nu_\mu\,(0,0) \right\rangle \right|^2. \tag{5.2}$$

When performing the analysis, the diagonalization of Eq. (5.1) is done numerically, from where the evaluation of the probability is straightforward. The choice of parameterization for the NSI parameters in this analysis is the one defined in Eq. (3.7). This parameterization allow the investigation of both $|\varepsilon_{\alpha\beta}|$ and its associated phase $\delta_{\alpha\beta}$.

We compute the survival probability under the different NSI parameters in order to gain insight of which parameter plays the major effect during the neutrino evolution for the NOvA configuration. To do this, we take a given arbitrary value for a certain $|\varepsilon_{\alpha\beta}|$ and make all the other NSI parameters to be zero, including all phases.

Fig. 24 shows the survival probability for each $|\varepsilon_{\alpha\beta}|$, for both neutrinos and antineutrinos. The largest effect in the disappearance channel comes from $|\varepsilon_{\mu\tau}|$, being this parameter the one chosen to be investigated in this analysis. For the FHC mode, inclusion of $|\varepsilon_{\mu\tau}|$ is expected to decrease the survival probability, while for RHC we observe an increase for the survival probability. In other words, $|\varepsilon_{\mu\tau}|$ tends to decrease the survival rate for ν_μ and increase the survival rate for $\bar{\nu}_\mu$. As discussed before, neutrinos and antineutrinos are affected differently by the matter potential V, as defined in Eq. (2.59). The NSI parameters are also attached to the matter effects, which justifies the behavior observed in Fig. 24.

In order to understand the effects on neutrino and antineutrino evolution arising from the phase $\delta_{\mu\tau}$ associated in the parameterization, we compute the survival probability at a fixed arbitrary value of $|\varepsilon_{\mu\tau}| = 0.25$ for different values of $\delta_{\mu\tau}$. The effect of $\delta_{\mu\tau}$, for neutrinos and antineutrinos, can be seen in Fig. 25.

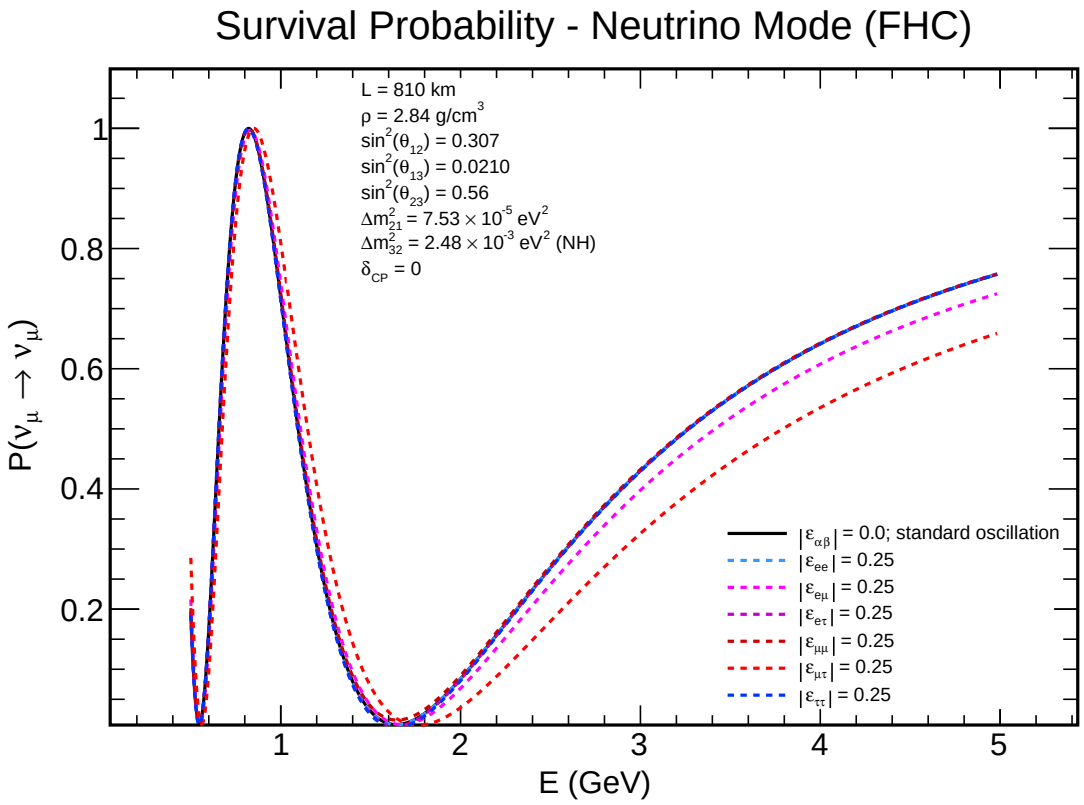

(a) neutrino beam (FHC)

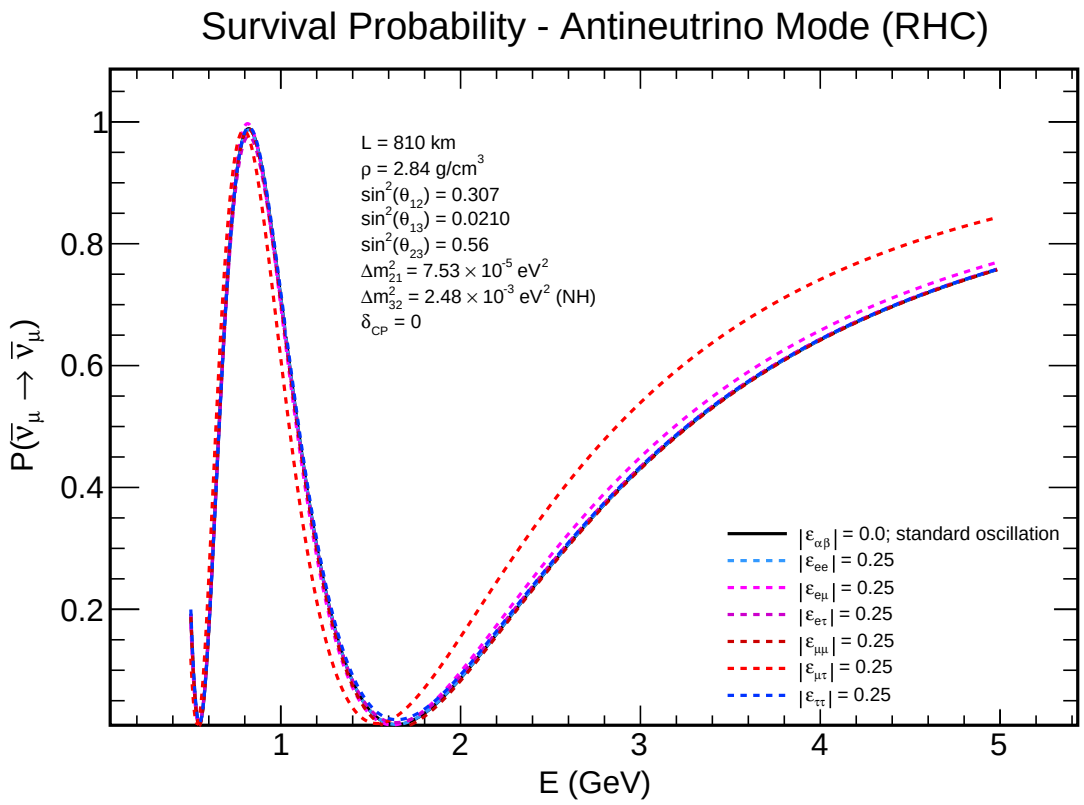

(b) antineutrino beam (RHC)

Figure 24 – Survival probability for muon neutrinos (a) and muon antineutrinos (b) under different NSI parameters $|\varepsilon_{\alpha\beta}|$. The case where all $|\varepsilon_{\alpha\beta}| = 0$ (solid black line) corresponds to the standard oscillation scenario.

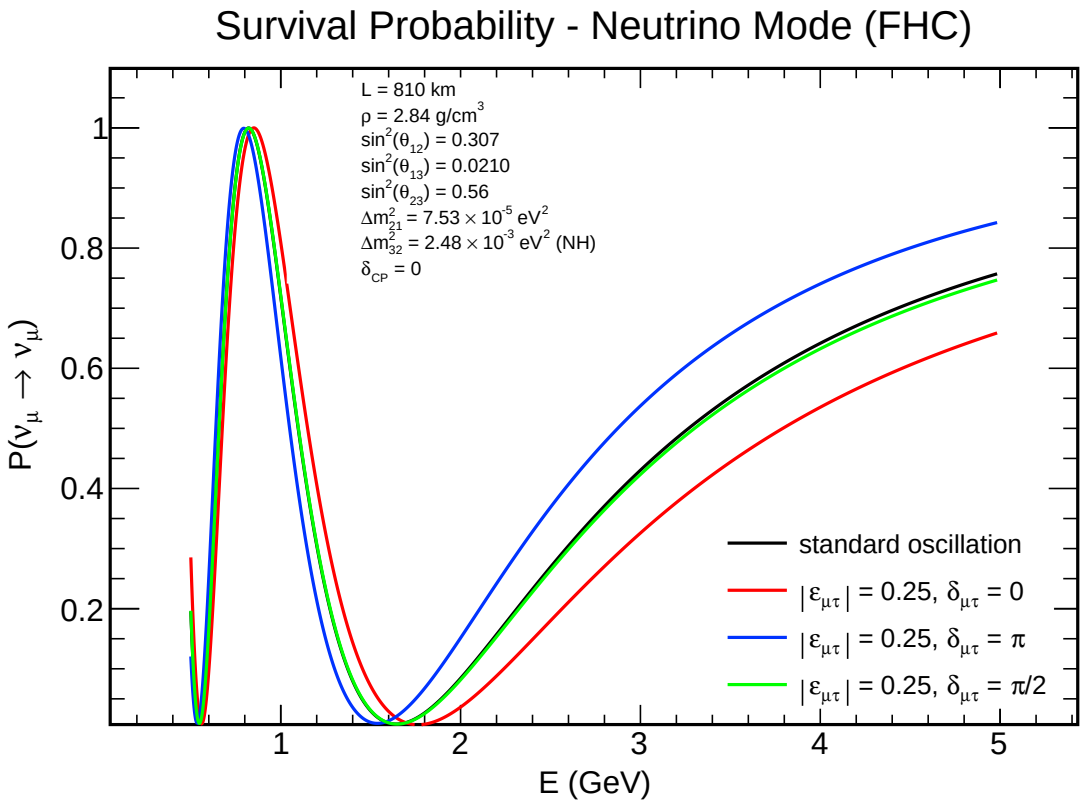

(a) neutrino beam (FHC)

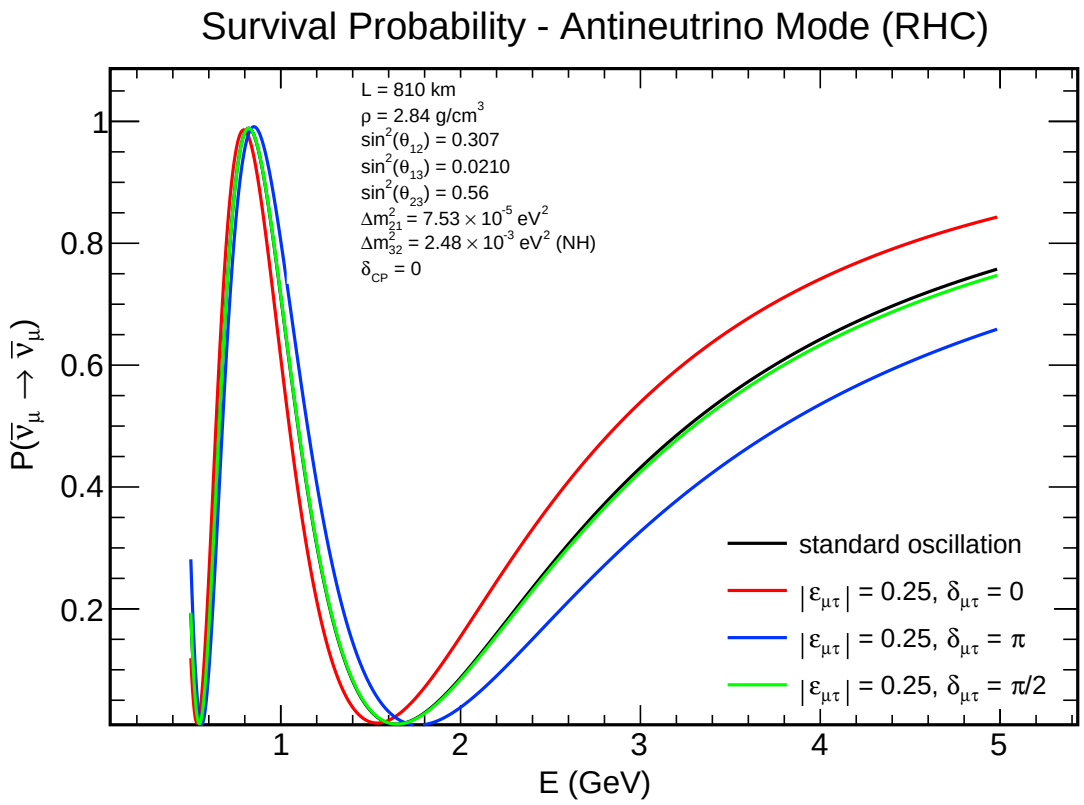

(b) antineutrino beam (RHC)

Figure 25 – Survival probability for muon neutrinos (a) and muon antineutrinos (b) under different values of $\delta_{\mu\tau}$ for a fixed $|\varepsilon_{\mu\tau}| = 0.25$. The case where all $|\varepsilon_{\alpha\beta}| = 0$ and $\delta_{\alpha\beta} = 0$ (solid black line) corresponds to the standard oscillation scenario.

It is clear that $\delta_{\mu\tau}$, due to its complex dependence, affects neutrinos and antineutrinos in a different manner. Additionally, the combination of $\delta_{\mu\tau}$ with the sign of the matter potential V may lead to further degeneracies. Note also that for the specific value of $\delta_{\mu\tau} = \frac{\pi}{2}$ the NSI scenario tends to mimic standard oscillations (green line in Fig. 25).

Considering the behaviors exhibited in Fig. 24 and Fig. 25, we focus our efforts on searching for the effects of $\varepsilon_{\mu\tau}$, i.e., $|\varepsilon_{\mu\tau}|$ and $\delta_{\mu\tau}$. Then, in this analysis we investigate both the effects of $|\varepsilon_{\mu\tau}|$ alone (i.e. fitting $|\varepsilon_{\mu\tau}|$ and setting $\delta_{\mu\tau} = 0$) and also the effects of $|\varepsilon_{\mu\tau}|\, e^{i\delta_{\mu\tau}}$ as a complex quantity (i.e. fitting both $|\varepsilon_{\mu\tau}|$ and $\delta_{\mu\tau}$). The adopted strategy is to individually compare the effects of the NSI parameters for neutrinos (FHC) and antineutrinos (RHC) separately, and then produce a joint neutrino-antineutrino fit (FHC+RHC), for both neutrino mass hierarchies. Fig. 26 illustrates schematically our strategy and the different scenarios of our investigation including the comparison of NSI effects on neutrino and antineutrino oscillations. The color-code inside the bottom boxes will be used to identify the different scenarios later, in most of the contour plots.

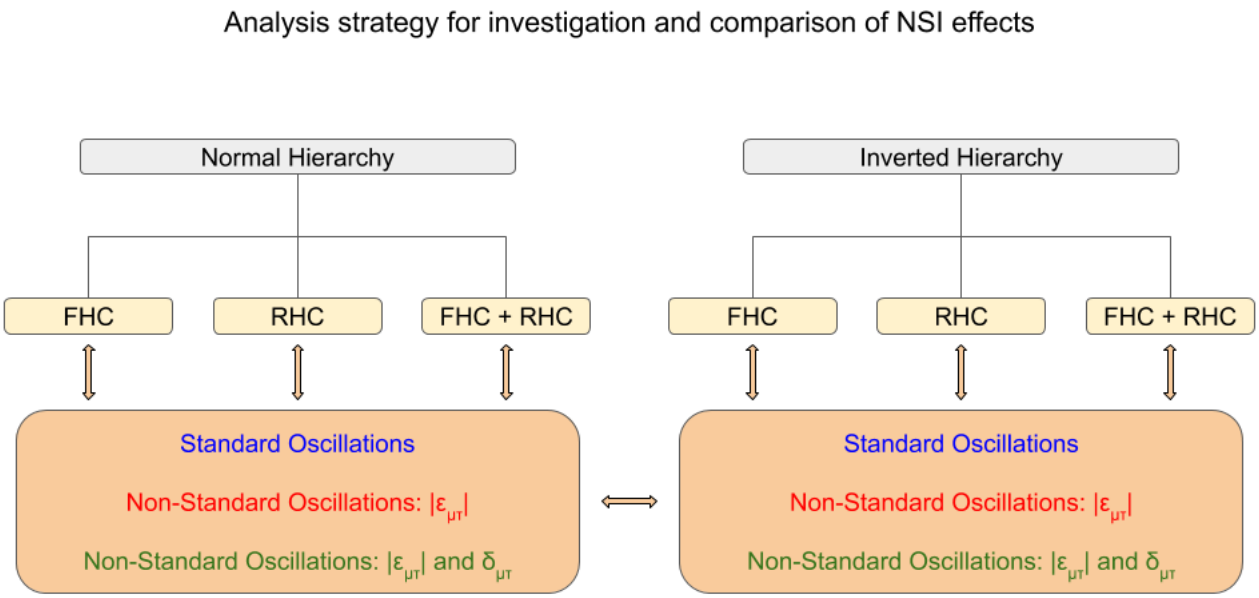

Figure 26 – Diagram of the strategy followed in this analysis, looking for understanding the sensitivity reached by NOvA on the NSI parameters involved in the disappearance channel, both in the neutrino and the antineutrino modes.

We emphasize that for the present sensitivity, no attempts are made to distinguish between the preference for each mass hierarchy scenario. Instead, we proceed to investigations on the effects that NSI would play on determination of our parameters of interest for Normal Hierarchy or Inverted Hierarchy scenario. A preference for one particular mass ordering might be tested by looking at the experimental data and comparing it to the predictions we produce for NH or IH. Additional information on addressing the degeneracies arising from the sign of Δm^2_{32} and the effects from $\delta_{\mu\tau}$, for both neutrinos and antineutrinos, is presented in Appendix B.7.

5.2 Data simulation

Before usage of data collected by the experiment, NOvA makes use of a series of simulations in order to create Monte Carlo simulated data for sensitivity studies prior to the final analysis, usually known as *fake data*. Once the sensitivity studies are done and discussed by the members in the collaboration, along with a series of additional studies, such as data quality, systematic uncertainties, background estimation, among others, the experiment proceed to the experimental analysis with the usage of real data collected by the detectors.

The simulation accounts all the components and aspects present in the experiment, and range from beam production to detector response and data processing. The neutrino beam is simulated using a Monte Carlo method with the software `GEANT4` [69], which accounts a detailed modeling of the target, magnetic horns, decay pipe and all other components. This ensures that the simulated beam will be as trustworthy as possible from the real one we get from NuMI. The simulated flux serves as input for the software `GENIE` [70], which is responsible to simulate neutrino interactions in the NOvA detectors. `GENIE` takes into account neutrino cross sections, type of interaction and all the kinematics in order to generate the resulting particles from the interaction. Following the simulation chain, the simulated particles emerging from a given neutrino interaction are then used again by `GEANT4` in order to simulate its propagation through the detector using a detailed model of the detectors geometry. The energy deposition, detector response and signal processing are modeled using internally developed software.

Once simulated data at the Near Detector is generated, this set of simulated data is compared to real experimental data in the same detector. This comparison is used in order to check if both simulation and data taking are in agreement, ensuring the integrity of the simulation chain. Fig. 27 shows a comparison of ND data with MC simulated events used for the NOvA analysis presented in Ref. [63].

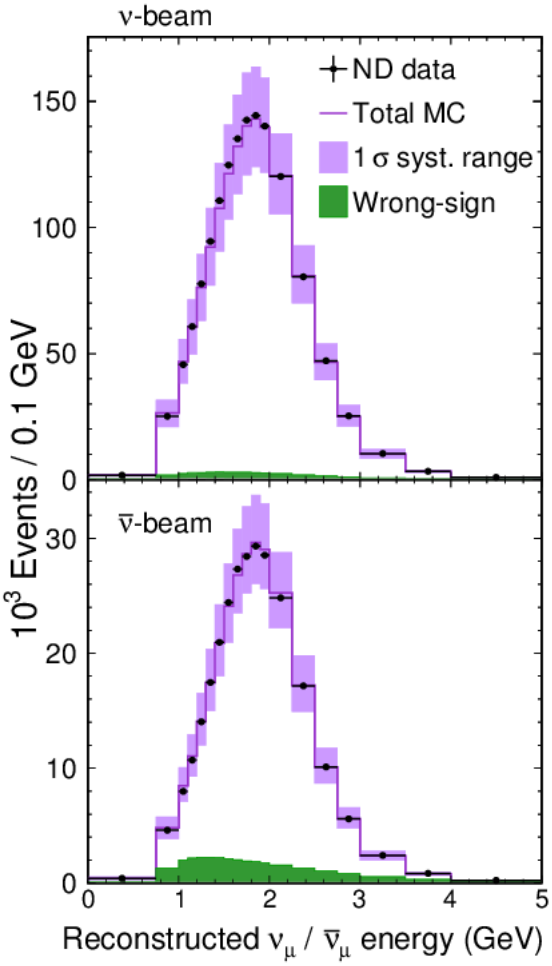

Figure 27 – Reconstructed neutrino energy spectra for the ND ν_μ ($\bar{\nu}_\mu$) CC for neutrino beam (antineutrino beam), along with the expected MC prediction, as presented in Ref. [63]. Backgrounds arise mostly from wrong-sign contamination.

For sensitivity studies, simulated data at the ND is taken and then extrapolated to inspect what we would observe at the FD, with or without oscillations, and is dependable on the oscillation parameters we chose to mock oscillate it. In order to produce the FD oscillated simulated data used in this analysis, we take a given set of oscillation parameters to use as input in our probability. The matter potential is taken as constant and with matter density $\rho = 2.84\,\mathrm{g/cm^3}$, as computed with the `CRUST2.0` model [71] for the average depth of the NuMI beam in the Earth's crust for the NOvA baseline of L = 810 km. The solar and reactor parameters are taken from the 2017 edition of the Particle Data Group (PDG) summary tables. Our standard parameters of interest for this analysis, $\sin^2(\theta_{23})$ and Δm^2_{32},[1] are taken to be the best fit values from the 2019 NOvA analysis, presented in Ref. [63]. The value for δ_{CP} is conservatively set to zero[2]. For the results presented in the next chapter, we investigate both neutrino mass hierarchy scenarios, thus we compute our predictions with the corresponding Δm^2_{32} for Normal or Inverted hierarchy. Table 4 summarizes our choice of parameters for mock oscillating the ND simulated data.

[1] The input value for $\sin^2(\theta_{23})$ is taken to be the same for both mass hierarchies, whereas for Δm^2_{32} we make the distinction between NH or IH.

[2] δ_{CP} may lead to degeneracies beyond the ones already produced by the NSI parameters, and as an initial approach is treated as constant and equal to zero.

Parameter	Value	Ref
L(km)	810	[63]
Δm^2_{32} (10^{-3}eV^2)	2.48(NH)	
Δm^2_{32} (10^{-3}eV^2)	-2.54(IH)	
$\sin^2(\theta_{23})$	0.56	
ρ (g/cm^3)	2.84	[71]
$\sin^2(\theta_{12})$	0.307	[72]
$\sin^2(\theta_{13})$	0.0210	
Δm^2_{21} (10^{-5}eV^2)	7.53	
δ_{CP} $(^\circ)$	0	
$\varepsilon_{\alpha\beta}$	0	

Table 4 – Summary of the values of the oscillation parameters used to generate the simulated data for this analysis.

Given the FD simulated data generated by our choice of parameters, we are then able to compare it to a prediction of what such data would be, given another different set of parameters.

5.3 Methodology

When performing the analysis, we are interested to know how well our model describe the observed data, along with an estimation of the corresponding parameters. Given a set of parameters $\vec{\theta}$ in our model, we compare it to data through a function called maximum likelihood,

$$\mathcal{L} = \mathcal{L}\left(\text{data},\vec{\theta}\right), \tag{5.3}$$

which tells how well the observed data matches a given model assuming the parameters $\vec{\theta}$ are true. For a likelihood function based on bins, with independent Poisson distributed data, we minimize[3] the quantity $-2\ln\mathcal{L}\left(\vec{\theta}\right)$, expressed as [73]

$$-2\ln\mathcal{L}\left(\vec{\theta}\right) = 2\sum_{i=1}^{\text{bins}}\left[\nu_i\left(\vec{\theta}\right) - n_i + n_i\ln\frac{n_i}{\nu_i\left(\vec{\theta}\right)}\right] = \chi^2, \tag{5.4}$$

where $\nu_i\left(\vec{\theta}\right)$ is the number of events expected at the defined parameters in the model, and n_i is the number of observed events, and this expression is also related to a χ^2 distribution. For additional information on the statistical methods, refer to Appendix A.

The parameters $\vec{\theta}_{\text{best}}$ that minimizes the χ^2 are known as best fits, which are the values of the parameters that best adjust the model to the observed data. In other words, a lower χ^2 value indicates a better good fit for a certain combination of parameters. We define a test statistic function $\Delta\chi^2$ as

$$\Delta\chi^2 = \chi^2\left(\vec{\theta}\right) - \chi^2\left(\vec{\theta}_{\text{best}}\right), \tag{5.5}$$

[3] Given that logarithmic properties demand less computing expenses, we chose to minimize $-2\ln\mathcal{L}\left(\vec{\theta}\right)$ instead of maximizing $\mathcal{L}\left(\vec{\theta}\right)$, which is equivalent.

which tells the deviation of a given set of parameters $\vec{\theta}$ compared to $\vec{\theta}_{\text{best}}$. This is a common approach in high energy physics, allowing the experiment to obtain not only the best fit for a given parameter, but also the interval in which its true value can range to within a given CL. For example, information about a given parameter can be obtained by looking into a 1D projection of the hypersurface produced by $\Delta\chi^2$ onto the axis of interest, from where constraints can be obtained. Similarly, 2D projections (usually known as *contours* or *surfaces*) can be constructed for 2 given parameters in order to create confidence intervals within that parameter space.

At NOvA, in order to get information about a certain parameter and a corresponding $\Delta\chi^2$, we profile over all the other parameters. This is done by taking the best fit in all the parameters that we do not show at each point of the parameter that we actually show. This process is better discussed in subsection 6.2.1.

The parameters θ_{12} and Δm^2_{21} are well constrained by solar experiments, and while this analysis has no sensitivity to them, we set their values as constant and they are not included in the fit. Although NOvA has sensitivity to the mixing angle θ_{13}, this parameter is also treated as constant and not included in the fit[4]. All the parameters treated as constant and not included in the fit have their values set and fixed according to the ones presented in Table 4, including $\delta_{CP} = 0$. The remaining parameters $(\theta_{23}, \Delta m^2_{32}, |\varepsilon_{\mu\tau}|, \delta_{\mu\tau})$ are not constrained[5], and therefore are free in the fitting process. For a discussion on the effects arising from the inclusion or not in the fit of the solar and reactor parameters, refer to Appendix B.2.

5.3.1 Energy Resolution Binning and event quantiles

NOvA separates ν_μ and $\bar{\nu}_\mu$ CC events into four quantiles (also known as quartiles) according to the fraction of hadronic energy deposited for each event. The analysis in this work follows the approach used at NOvA's 2018 and 2019 analyses, and uses 4 resolution quantiles for FHC and 4 resolution quantiles for RHC, 1 being the best resolution and 4 being the worst. The hadronic energy fraction is a technique that allows a better measurement of the energy resolution, and improves the energy reconstruction. As the fraction of hadronic energy of an event increases, the characteristic spacial dispersion tends to worse the resolution, where the choice for the binning and separation of lower and higher resolution events reduces the uncertainty for events with low hadronic energy fraction. Fig. 28 shows the distribution of ν_μ and $\bar{\nu}_\mu$ CC events (Z-axis) according to the amount of the fraction of hadronic energy, $\text{E}_{\text{had}}/\text{E}_\nu$, as function of the reconstructed energy, as used in the analysis presented in Ref. [74].

[4] The ν_e appearance channel is better suitable for investigations on the mixing angle θ_{13}.

[5] These parameters are kept within a physically accepted range in the fit.

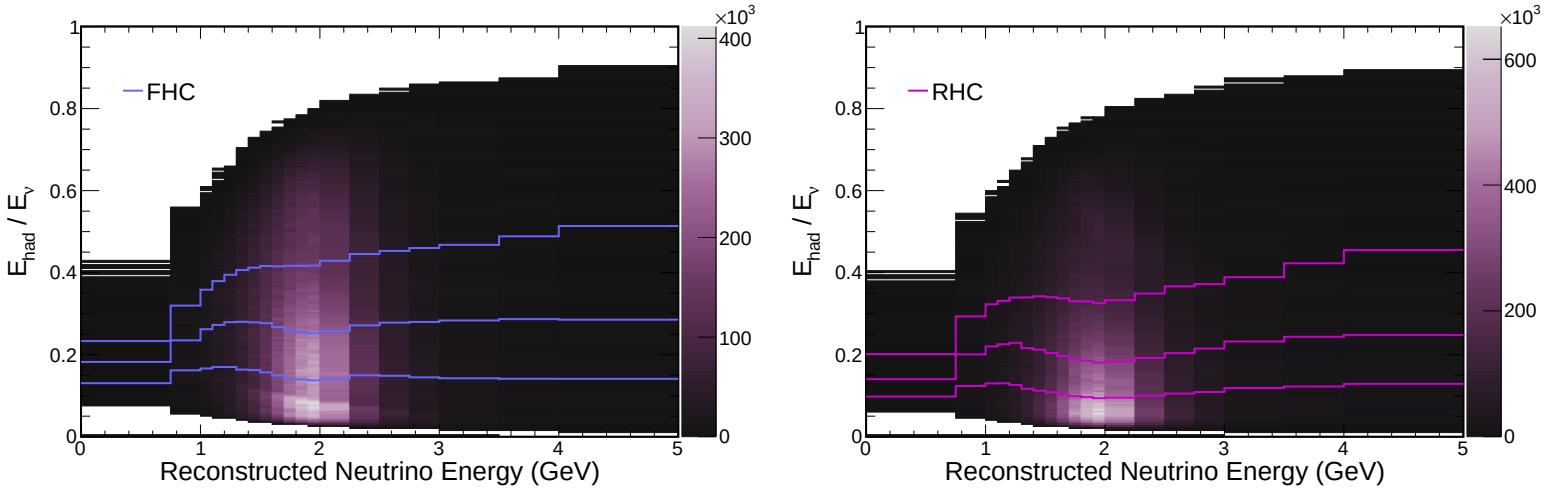

(a) neutrino beam (FHC)

(b) antineutrino beam (RHC)

Figure 28 – Distribution of ν_μ (a) and $\bar{\nu}_\mu$ (b) CC events according to the amount of E_{had}/E_ν as function of the reconstructed energy. The solid blue and pink lines mark the boundaries between each quantile for FHC and RHC modes, respectively, and the color scheme (z-axis) indicates number of events.

The quantiles are computed separately, each of them divided into 19 resolution bins. Accounting both FHC and RHC operation modes, each with 4 quantiles divided into 19 energy resolution bins, a total of $2 \times 4 \times 19 = 152$ bins are used in the fit for the FHC + RHC results presented in the next chapter. For the current sensitivity studies, results for prediction histograms are presented for all quantiles together.

5.4 Systematic uncertainties

NOvA assess systematic uncertainties in order to account effects inherent to an experimental analysis. Examples of potential systematic uncertainties are calibration, beam transport, cross section uncertainties, among others. We briefly discuss in this section the major sources of systematic uncertainties adopted at previous results reported from NOvA, for which we implement to the current NSI analysis.

In order to include the systematic uncertainties and their effects on our analysis, the following methodology is adopted: each source of systematic uncertainty is included in our fit to data and treated as an extra parameter allowed to float in the fit. This term is added as a nuisance parameter and additional degree of freedom to the loglikelihood to be minimized, shown in Eq. (5.4), from where we end with [75]

$$-2\ln\mathcal{L}\left(\vec{\theta},\vec{\delta}\right) = 2\sum_{i=1}^{\text{bins}}\left[\nu_i\left(\vec{\theta},\vec{\delta}\right) - n_i + n_i\ln\frac{n_i}{\nu_i\left(\vec{\theta},\vec{\delta}\right)}\right] + \sum_{j=1}^{\text{bins}}\frac{\delta_j^2}{\sigma_j^2}, \tag{5.6}$$

where the index j runs over the systematic parameters and σ_j are the corresponding error. All the systematic uncertainties are treated as orthogonal and uncorrelated.

A few sources of systematic uncertainties for a ν_μ and $\bar{\nu}_\mu$ disappearance analysis include, but is not limited to:

- Calibration

  - uncertainties arising from fluctuations on calibration.

- Cherenkov and light levels

  - variations on the Cherenkov light production and corresponding response from the scintillator and the optic fiber, as well as uncertainties related to light levels and thresholds.

- Flux uncertainties

  - variations on the NuMI neutrino flux, mainly the beam transport and hadron production. The beam transport is affected by possible differences between the simulated neutrino flux and the actual beam from NuMI, such as minor differences on the positioning of the magnetic horns and distance to the target. Uncertainties on cross sections and hadron production of the proton beam with the NuMI carbon target are also a factor of systematic error, for example uncertainties and discrepancies in the simulation of production of pions and kaons with real physical process.

- Cross Section

  - uncertainties related to neutrino energy, final state interactions, energy transfer, among others, based on the different theoretical models available.

The list of systematic uncertainties used for the current NSI sensitivity is the same adopted in the analyses presented in Ref. [63] and Ref. [74]. The evaluation and study of systematic uncertainties is the result from the work of many collaborators along the years, which we implement now for the current NSI analysis. It should be noted that this list is based mostly on properties of interest for a standard neutrino disappearance analysis. For this current sensitivity, a process of investigation regarding possible additional sources of systematic uncertainties, of particular interest to an NSI analysis, is likely to happen in the future. If additional sources of systematic uncertainties of interest to the current NSI sensitivity be found, the results presented in this thesis are likely to further include this effect in the future as well. The list of systematics, along with an investigation and comparison of the effects from the inclusion or not of systematic uncertainties are discussed in Appendix C.1.

6 Results

We present in this chapter the results obtained on the sensitivity analysis to non-standard interactions on neutrino oscillations by the author and collaborators for the NOvA collaboration. This report makes use of an exposure of 9.48×10^{20} POT for neutrino beam (FHC), and 12.33×10^{20} POT for antineutrino beam (RHC). We show the results for both Normal Hierarchy and Inverted Hierarchy neutrino mass ordering scenarios, for FHC and RHC separately, and also results for the combined FHC + RHC fit.

6.1 CC event rate predictions

Using the values presented in Table 4, we first investigate the standard oscillation scenario compared to the no oscillations assumption. Fig. 29 shows the prediction of CC ν_μ ($\bar{\nu}_\mu$) events at the FD under the assumption of standard oscillations, and without oscillations, for neutrino (antineutrino) beam.

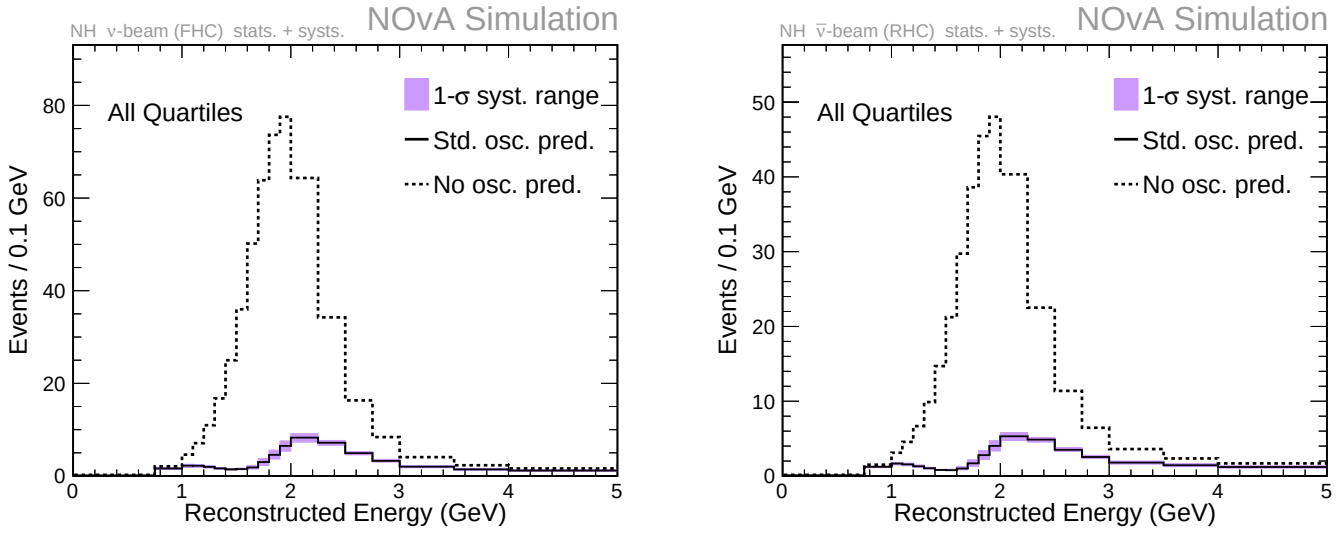

(a) Neutrino (FHC) beam

(b) Antineutrino (RHC) beam

Figure 29 – CC event rate predictions for beam operating in neutrino beam (a) and antineutrino beam (b). Shown is a comparison of no oscillations assumption (dashed line) against the 3 flavor neutrino oscillation model (solid line), along with the 1-σ systematic range.

As widely evidenced in the literature, we also see that at NOvA neutrino oscillations are responsible to greatly affect the CC event rate counting when compared to the assumption of no oscillations.

Given the neutrino oscillation phenomenon, we investigate now what we would expect to observe under different values of the NSI parameter $|\varepsilon_{\mu\tau}|$. As for the oscillation probability, we compute the predictions at the FD for both FHC and RHC beams for different arbitrary $|\varepsilon_{\mu\tau}|$ values, with $\delta_{\mu\tau} = 0$, in order to gain knowledge on how our spectra changes according to the magnitude of $|\varepsilon_{\mu\tau}|$. Comparisons with the standard case, for both beam operation modes, can be seen in Fig. 30.

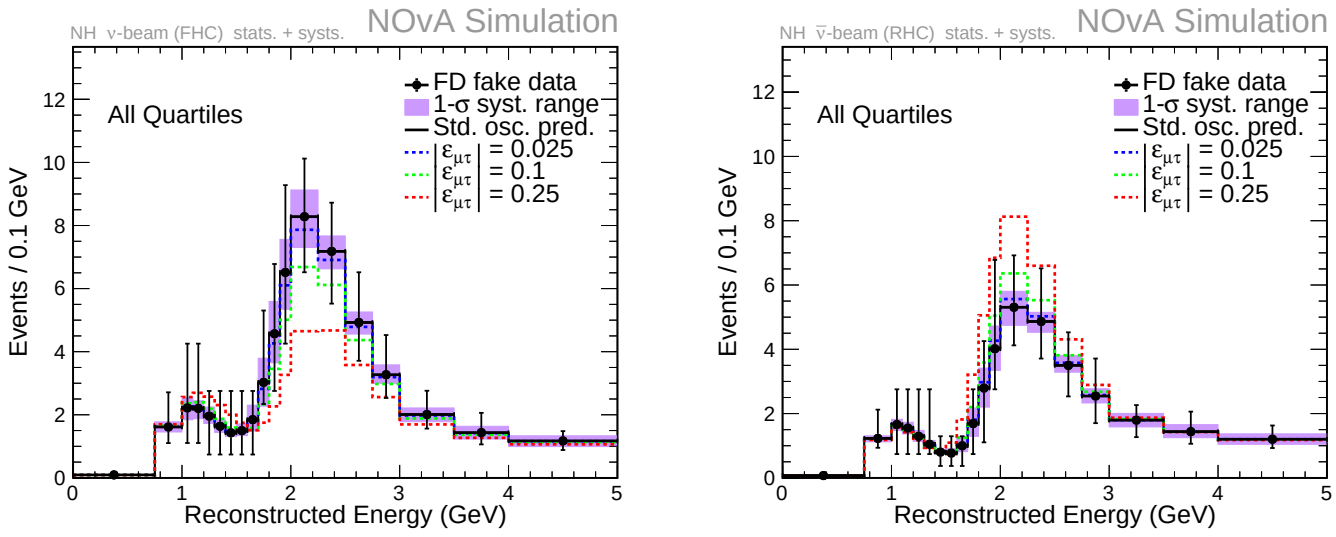

(a) Neutrino (FHC) beam

(b) Antineutrino (RHC) beam

Figure 30 – CC event rate predictions for beam operating in neutrino beam (a) and antineutrino beam (b) for different values of the NSI parameter $|\varepsilon_{\mu\tau}|$ (dashed lines) in comparison with the standard oscillation scenario (solid black line), along with the FD simulated data used for sensitivities.

As $|\varepsilon_{\mu\tau}|$ increases in magnitude, the effects on the predictions scale as well. For the FHC mode, as $|\varepsilon_{\mu\tau}|$ increases we expect a decrease in our events rate, while for RHC the opposite effect is observed, where an increase in the events rate is seen. This effect is supported by what we observe on the survival probabilities shown in Fig. 24, where we see that in the energy range around 2 GeV we expect the survival probability for neutrinos and antineutrinos to decrease or increase, respectively, which has a direct impact on the expected event rate. Notice how the FD simulated data exactly follows the standard oscillation prediction. This is due to the fact that we computed both the standard oscillation predictions and the ND oscillated data to the FD using the same set of parameters, and serves as a verification step. We therefore will let the FD simulated data shown along with the other plots for comparison purposes without loss of generality.

We now compute the event predictions at the FD at a fixed value of $|\varepsilon_{\mu\tau}| = 0.25$, for different values of interest for $\delta_{\mu\tau}$, as seen in Fig. 31. This allow us to investigate how the NSI phase $\delta_{\mu\tau}$ can impact our predictions given a fixed value of $|\varepsilon_{\mu\tau}|$, and thus understand its role on the analysis.

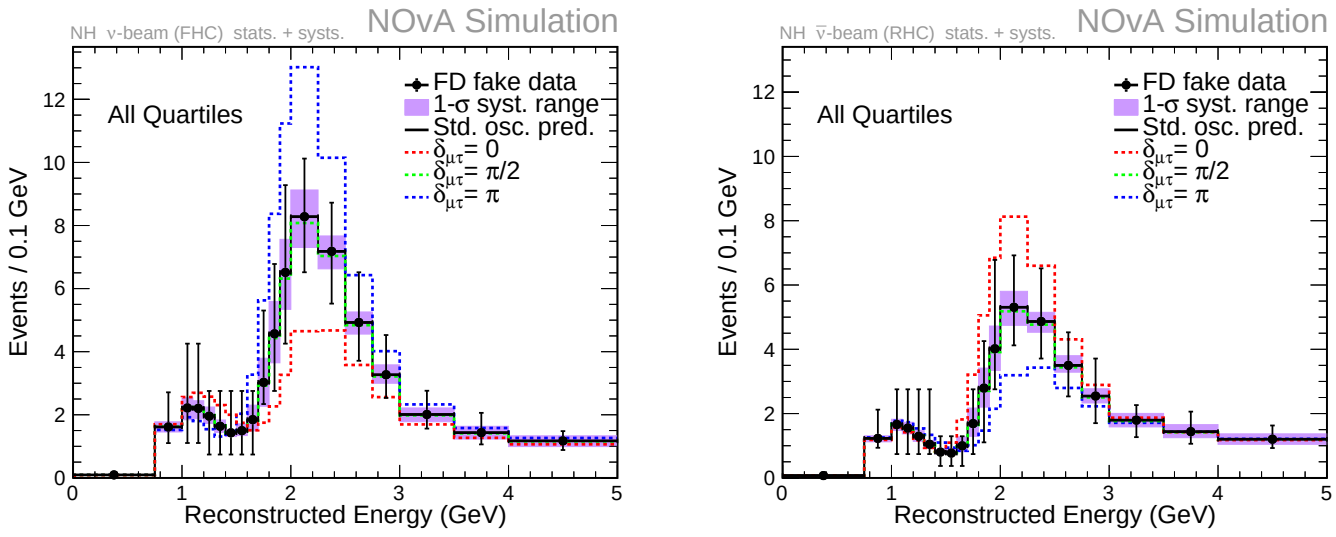

(a) Neutrino (FHC) beam

(b) Antineutrino (RHC) beam

Figure 31 – CC event rate predictions for neutrino beam (a) and antineutrino beam (b) for a fixed value of $|\varepsilon_{\mu\tau}| = 0.25$ and different values of the NSI phase $\delta_{\mu\tau}$ (dashed lines) in comparison with the standard oscillation scenario (solid black line), along with the FD simulated data used for sensitivities.

Observe that the case for $\delta_{\mu\tau} = 0$ (dashed red lines) is the one corresponding to the results shown in Fig. 31 when $|\varepsilon_{\mu\tau}| = 0.25$ (dashed red lines too), allowing a direct comparison. However, as $\delta_{\mu\tau}$ vary from 0 to π our predictions for FHC (RHC) increase (decrease). At the value of $\delta_{\mu\tau} = \frac{\pi}{2}$, both NSI predictions (dashed green lines) mimics the standard oscillation case, a behavior predicted by the observed on the probabilities shown in Fig. 24. The effects on predictions continue until we reach the maximum effect at the value of $\delta_{\mu\tau} = \pi$. In the range of $\pi \to 2\pi$ the effects will reverse until we end with the initial scenario for $\delta_{\mu\tau} = 0$. The explanation is that the NSI phase $\delta_{\mu\tau}$ is allowed to have values $\in [0, 2\pi]$, and according to Eq. (2.30) the survival probability is mostly dominated by the real part of our parameters. Then, $\Re\left(e^{i\delta_{\mu\tau}}\right) = \cos\left(\delta_{\mu\tau}\right) \in [-1, 1]$, which is the multiplicative factor on $|\varepsilon_{\mu\tau}|$, responsible for a cyclical effect on the predictions shown in Fig. 31 for different values of $\delta_{\mu\tau}$.

6.2 Sensitivities to Δm^2_{32}, $\sin^2(\theta_{23})$, $|\varepsilon_{\mu\tau}|$, and $\delta_{\mu\tau}$

We discuss in this section the NSI effects on the determination of the standard oscillation parameters Δm^2_{32} and $\sin^2(\theta_{23})$, for both scenarios with the inclusion of only $|\varepsilon_{\mu\tau}|$, and with $|\varepsilon_{\mu\tau}|$ and $\delta_{\mu\tau}$, along with NOvA's sensitivity for each NSI parameter. In order to get information about the NSI effects, we compare the standard oscillation case against the scenario when we fit for the NSI parameter $|\varepsilon_{\mu\tau}|$ ($\delta_{\mu\tau} = 0$), where we allow it to have values $\in [0, 0.25]$, motivated by the observed in Fig. 30, and also with the scenario when we include both $|\varepsilon_{\mu\tau}|$ and its associated phase $\delta_{\mu\tau}$, which in principle may allow higher values of $|\varepsilon_{\mu\tau}|$ beyond those initially assumed, as will become evidenced in the next sections. The standard oscillation parameters Δm^2_{32} and $\sin^2(\theta_{23})$ are always included in the fit, regardless of the scenario.

We follow the procedure illustrated in Fig. 26, briefly summarized as:

- Standard oscillations: no NSI parameters are included in the fit.
- NSI, with $|\varepsilon_{\mu\tau}|$ only ($\delta_{\mu\tau}$ is kept fixed at zero).
- NSI, with $|\varepsilon_{\mu\tau}|$, and $\delta_{\mu\tau} \in [0, 2\pi]$.

6.2.1 1D Profiles

The 1D profiles are projections of the $\Delta\chi^2$ hypersurface onto the parameter axis of our interest. For the parameter being shown, we profile over all the other parameters not shown. As mentioned earlier, at each step we pick the best fit for the profiled parameters and return a value for the projected parameter of interest, along with the corresponding $\Delta\chi^2$ at that step. For 1D projections, a 90% CL limit for the allowed values for a certain parameter are obtained at $\Delta\chi^2 = 2.71$.

6.2.1.1 Δm^2_{32}

Fig. 32 allows us to inspect the comparison between the standard and the NSI cases on determination of Δm^2_{32}. For neutrino beam, the inclusion of the NSI parameter $|\varepsilon_{\mu\tau}|$ pushes solutions to lower values of Δm^2_{32}, while for the antineutrino beam higher values are allowed, as seen from a comparison between the standard (solid blue line) and NSI (red dashed line) cases. If the associated NSI phase $\delta_{\mu\tau}$ is included in the fit it expands the allowed interval values for Δm^2_{32} on both neutrino and antineutrino modes. The joint analysis, combining neutrino and antineutrino data, shows no significant deviation from the standard and NSI models at the 90% CL limit, for both neutrino mass hierarchies.

Table 5 presents the 90% CL interval for Δm^2_{32} under the different investigated scenarios, for neutrino beam, antineutrino beam, and the joint neutrino-antineutrino fit, for both mass hierarchies.

90%CL interval for Δm^2_{32} (10^{-3}eV^2)				
Mass hierarchy	Beam mode	Standard Oscillations	NSI: fit $\|\varepsilon_{\mu\tau}\|$	NSI: fit $\|\varepsilon_{\mu\tau}\|$ and $\delta_{\mu\tau}$
Normal	ν-beam	$2.356 \to 2.605$	$2.181 \to 2.605$	$2.181 \to 2.783$
	$\bar{\nu}$-beam	$2.337 \to 2.631$	$2.337 \to 2.774$	$2.188 \to 2.774$
	Joint fit	$2.381 \to 2.578$	$2.379 \to 2.578$	$2.379 \to 2.580$
Inverted	ν-beam	$-2.667 \to -2.413$	$-2.847 \to -2.413$	$-2.846 \to -2.236$
	$\bar{\nu}$-beam	$-2.691 \to -2.396$	$-2.691 \to -2.248$	$-2.833 \to -2.248$
	Joint fit	$-2.638 \to -2.440$	$-2.639 \to -2.440$	$-2.639 \to -2.438$

Table 5 – 90%CL interval for the allowed values of the standard oscillation parameter Δm^2_{32}, for neutrino beam, antineutrino beam, and the joint neutrino-antineutrino fit, for both neutrino mass hierarchies, under the different analysis scenarios.

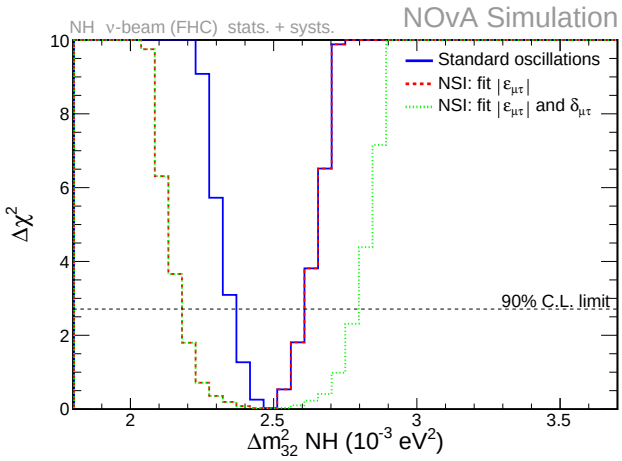

(a) Neutrino (FHC) beam - NH

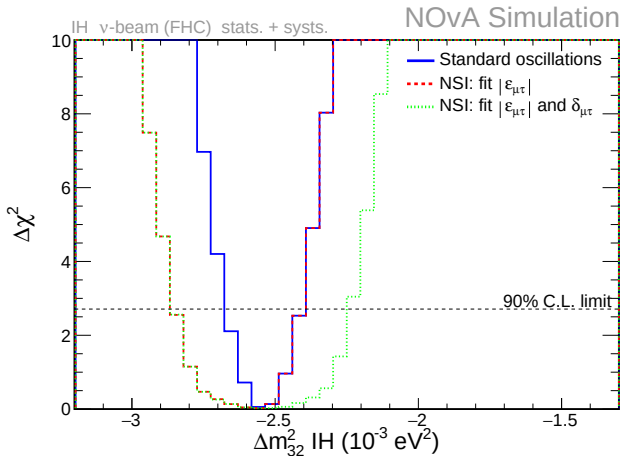

(b) Neutrino (FHC) beam - IH

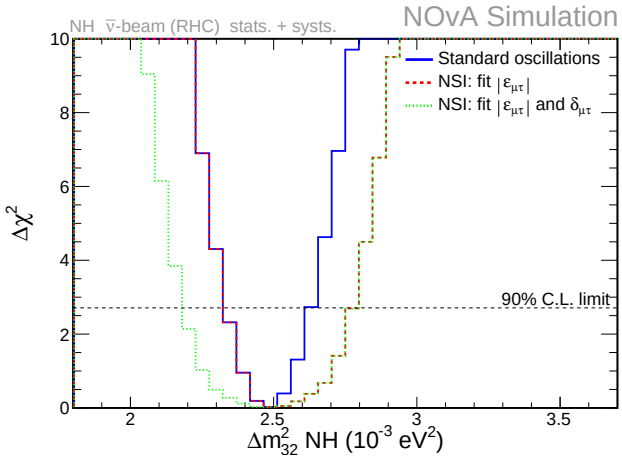

(c) Antineutrino (RHC) beam - NH

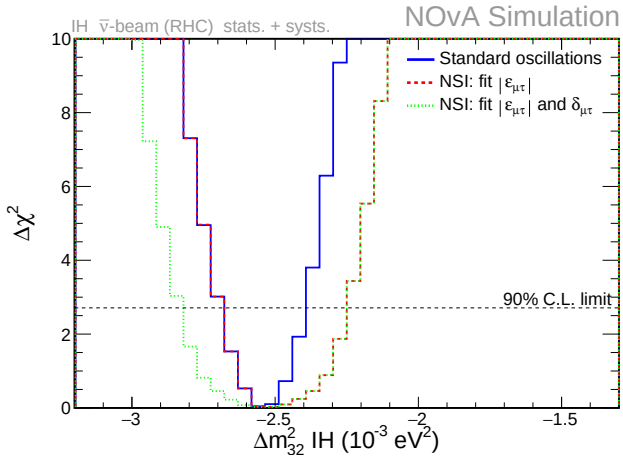

(d) Antineutrino (RHC) beam - IH

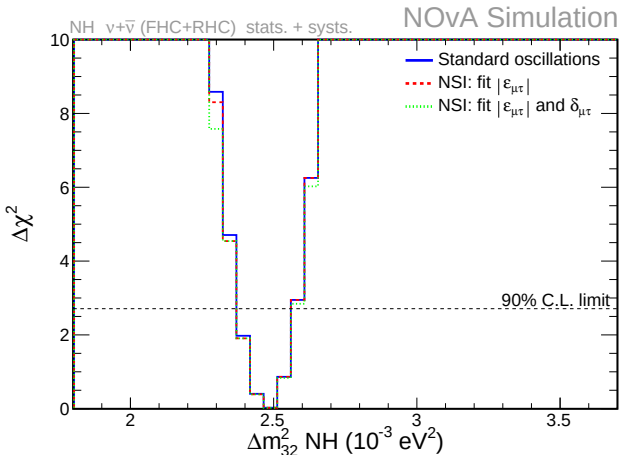

(e) FHC + RHC - NH

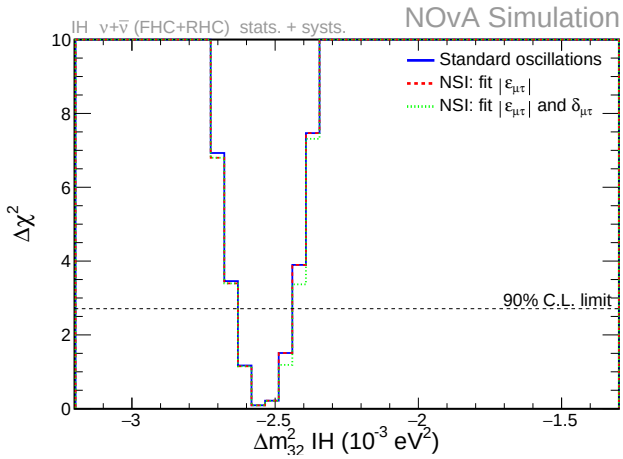

(f) FHC + RHC - IH

Figure 32 – $\Delta\chi^2$ values as function of Δm^2_{32} for Normal Hierarchy (left) and Inverted Hierarchy (right) neutrino mass ordering scenarios, for neutrino beam (top), antineutrino beam (middle), and the joint analysis (bottom). In solid blue line is shown the standard case, while the dashed red and dotted green lines are with the inclusion of $|\varepsilon_{\mu\tau}|$ only, and $|\varepsilon_{\mu\tau}|$ and $\delta_{\mu\tau}$, respectively. The horizontal dashed line marks the 90% CL interval for the investigated parameter.

6.2.1.2 $\sin^2(\theta_{23})$

The impact on measurements of $\sin^2(\theta_{23})$ arising from the inclusion of the NSI parameters are shown in Fig. 33. The parameter $\sin^2(\theta_{23})$ is less affected by the NSI effects. For the Normal Hierarchy scenario, on FHC mode, although the presence of the NSI parameters have a minor expansion on the allowed values of $\sin^2(\theta_{23})$, no difference is seen between the inclusion of only $|\varepsilon_{\mu\tau}|$ or $|\varepsilon_{\mu\tau}|$ and $\delta_{\mu\tau}$ (red dashed and green dotted lines, respectively). For the RHC mode, on the other hand, no difference is observed from the standard case (solid blue line) compared to the scenario including only $|\varepsilon_{\mu\tau}|$ (red dashed line), and a minor effect is seen when $|\varepsilon_{\mu\tau}|$ and $\delta_{\mu\tau}$ is included (green dashed line). The opposite is seen for the Inverted Hierarchy scenario for the FHC and RHC modes. Within the 90% CL limit, both octants for the mixing angle θ_{23} are allowed, and the joint analysis combining neutrino and antineutrino data shows no significant deviation from the standard and NSI models.

Table 6 presents the 90% CL interval for $\sin^2(\theta_{23})$ under the different investigated scenarios, for neutrino beam, antineutrino beam, and the joint neutrino-antineutrino fit, for both mass hierarchies.

90%CL interval for $\sin^2(\theta_{23})$				
Mass hierarchy	Beam mode	Standard Oscillations	NSI: fit $\|\varepsilon_{\mu\tau}\|$	NSI: fit $\|\varepsilon_{\mu\tau}\|$ and $\delta_{\mu\tau}$
Normal	ν-beam	$0.414 \rightarrow 0.613$	$0.403 \rightarrow 0.625$	$0.403 \rightarrow 0.625$
	$\bar{\nu}$-beam	$0.398 \rightarrow 0.618$	$0.398 \rightarrow 0.618$	$0.383 \rightarrow 0.633$
	Joint fit	$0.421 \rightarrow 0.602$	$0.420 \rightarrow 0.602$	$0.420 \rightarrow 0.602$
Inverted	ν-beam	$0.405 \rightarrow 0.611$	$0.405 \rightarrow 0.611$	$0.393 \rightarrow 0.623$
	$\bar{\nu}$-beam	$0.404 \rightarrow 0.621$	$0.388 \rightarrow 0.636$	$0.388 \rightarrow 0.636$
	Joint fit	$0.418 \rightarrow 0.602$	$0.418 \rightarrow 0.602$	$0.418 \rightarrow 0.602$

Table 6 – 90%CL interval for the allowed values of the standard oscillation parameter $\sin^2(\theta_{23})$, for neutrino beam, antineutrino beam, and the joint neutrino-antineutrino fit, for both neutrino mass hierarchies, under the different analysis scenarios.

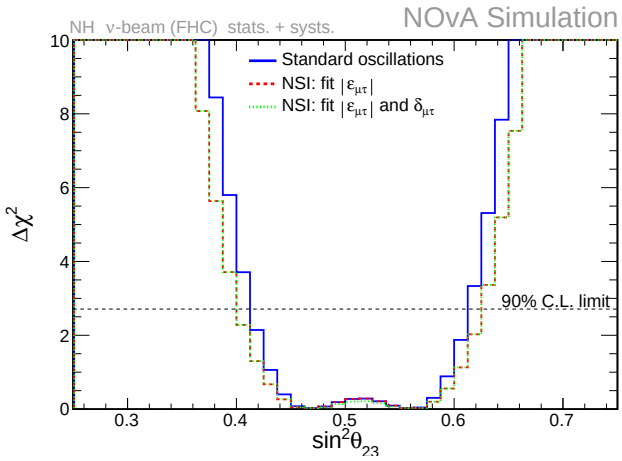

(a) Neutrino (FHC) beam - NH

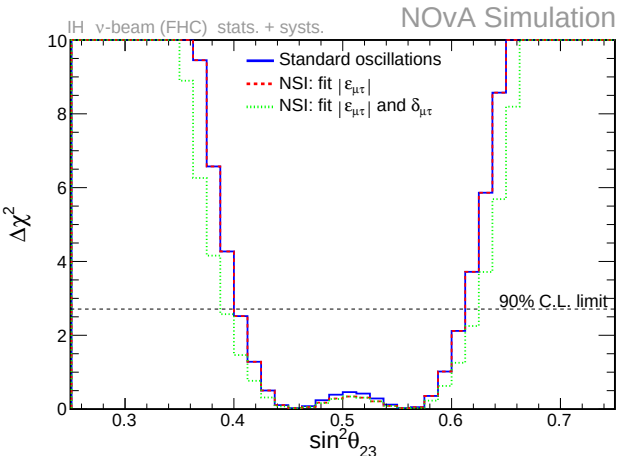

(b) Neutrino (FHC) beam - IH

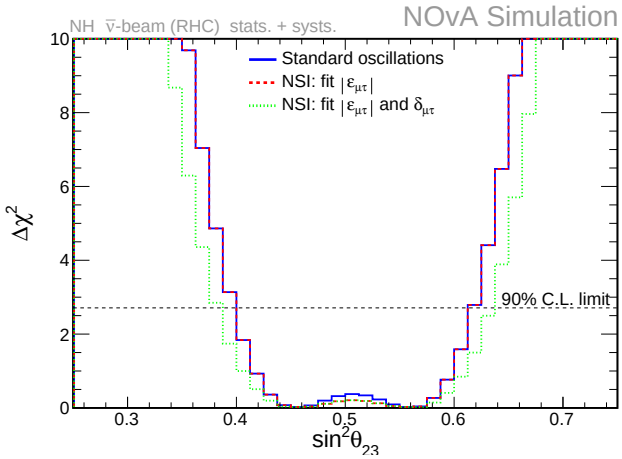

(c) Antineutrino (RHC) beam - NH

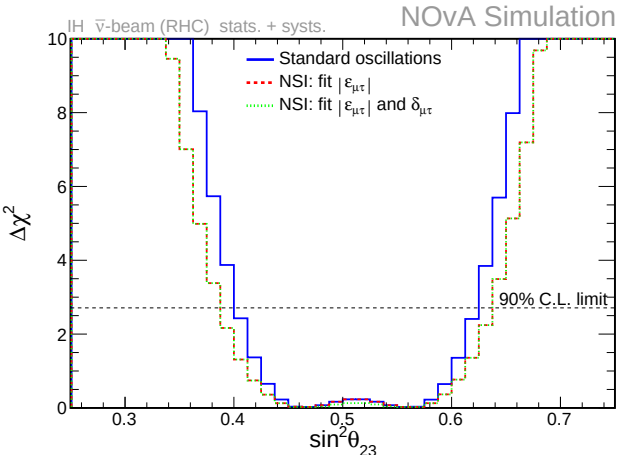

(d) Antineutrino (RHC) beam - IH

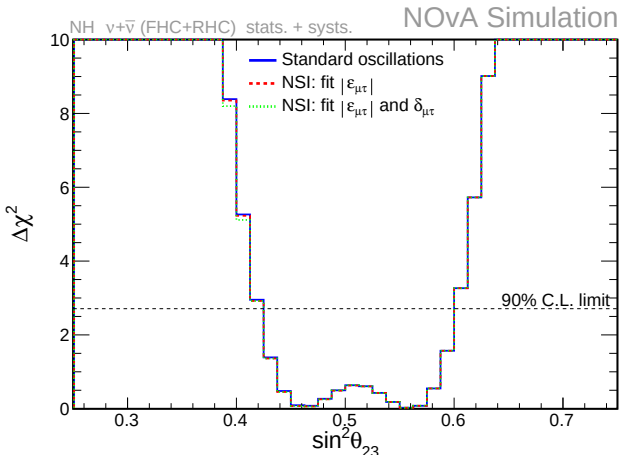

(e) FHC + RHC - NH

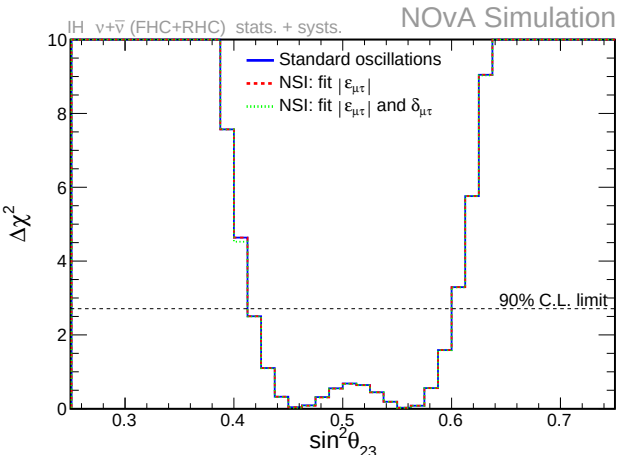

(f) FHC + RHC - IH

Figure 33 – $\Delta\chi^2$ values as function of $\sin^2(\theta_{23})$ for Normal Hierarchy (left) and Inverted Hierarchy (right) neutrino mass ordering scenarios, for neutrino beam (top), antineutrino beam (middle), and the joint analysis (bottom). In solid blue is shown the standard case, while the dashed red and dotted green lines are with the inclusion of $|\varepsilon_{\mu\tau}|$ only, and $|\varepsilon_{\mu\tau}|$ and $\delta_{\mu\tau}$, respectively. The horizontal dashed line marks the 90% CL interval for the investigated parameter.

6.2.1.3 $|\varepsilon_{\mu\tau}|$

Given our choice of parameterization as defined on Eq (3.7), the inclusion or not of the associated phase, $\delta_{\mu\tau}$, on the fit has a direct impact on our knowledge of $|\varepsilon_{\mu\tau}|$. When $\delta_{\mu\tau}$ is not included in the fit, thus not profiled over, results are computed for the particular case of $\delta_{\mu\tau} = 0$. If $\delta_{\mu\tau}$ is included in the fit, we let it float between 0 and 2π. Although so far we have constrained $|\varepsilon_{\mu\tau}| \leq 0.25$ in the fit , larger values for this parameter could in principle be allowed. In order to understand our knowledge of $|\varepsilon_{\mu\tau}|$, in Fig. 34 we show the 1D projection of this parameter for both FHC, RHC, and FHC + RHC. In the solid red line ($\delta_{\mu\tau}$ not included in the fit) we see that for FHC, $|\varepsilon_{\mu\tau}| \leq 0.647$ (≤ 0.666) for normal (inverted) mass hierarchy. For the RHC mode, we observe $|\varepsilon_{\mu\tau}| \leq 0.493$ (≤ 0.656) for normal (inverted) mass hierarchy. The joint FHC + RHC fit adds a more restrictive scenario, with $|\varepsilon_{\mu\tau}| \leq 0.086$ (≤ 0.085) for normal (inverted) mass hierarchy. On the other hand, for both FHC or RHC modes, as well as in the joint analysis, the inclusion of $\delta_{\mu\tau}$ in the fit (dashed green line) pushes solutions on $|\varepsilon_{\mu\tau}|$ to higher values. This scenario yields a limit of $|\varepsilon_{\mu\tau}| \leq 1.861$ ($|\varepsilon_{\mu\tau}| \leq 1.268$) for the FHC (RHC) mode for normal mass hierarchy, and a limit of $|\varepsilon_{\mu\tau}| \leq 1.911$ ($|\varepsilon_{\mu\tau}| \leq 1.265$) for the FHC (RHC) mode for inverted mass hierarchy. The joint fit brings a constraint of $|\varepsilon_{\mu\tau}| \leq 1.054$ ($|\varepsilon_{\mu\tau}| \leq 1.053$) for the normal (inverted) mass hierarchy scenario.

By inspecting our parameterization, this is justified by the balance between $|\varepsilon_{\mu\tau}|$ and $e^{i\delta_{\mu\tau}}$ in its multiplicative relation, where for certain values of the phase $\delta_{\mu\tau}$, the result of $e^{i\delta_{\mu\tau}}$ would be a small number, which causes the allowed value for $|\varepsilon_{\mu\tau}|$ to increase in order to keep the multiplicative balance in $\varepsilon_{\mu\tau} = |\varepsilon_{\mu\tau}|\, e^{i\delta_{\mu\tau}}$. This effect and dependence will also be discussed on subsection6.2.2.6.

The major difference observed between both mass hierarchies is seen on the FHC mode for when we keep $\delta_{\mu\tau}$ fixed (solid red line), where the Inverted Hierarchy scenario presents a larger upper limit when compared to the observed for the Normal Hierarchy case.

Table 7 presents the 90% CL interval for $|\varepsilon_{\mu\tau}|$ under the different investigated scenarios, for neutrino beam, antineutrino beam, and the joint neutrino-antineutrino fit, for both mass hierarchies.

90%CL interval for $\lvert\varepsilon_{\mu\tau}\rvert$			
Mass hierarchy	Beam mode	Fixed $\delta_{\mu\tau}$	Fit $\delta_{\mu\tau}$
Normal	ν-beam	≤ 0.647	≤ 1.861
	$\bar{\nu}$-beam	≤ 0.493	≤ 1.268
	Joint fit	≤ 0.086	≤ 1.054
Inverted	ν-beam	≤ 0.666	≤ 1.911
	$\bar{\nu}$-beam	≤ 0.656	≤ 1.265
	Joint fit	≤ 0.085	≤ 1.053

Table 7 – 90%CL interval for the allowed values of the NSI parameter $|\varepsilon_{\mu\tau}|$, for neutrino beam, antineutrino beam, and the joint neutrino-antineutrino fit, for both neutrino mass hierarchies, under the different analysis scenarios.

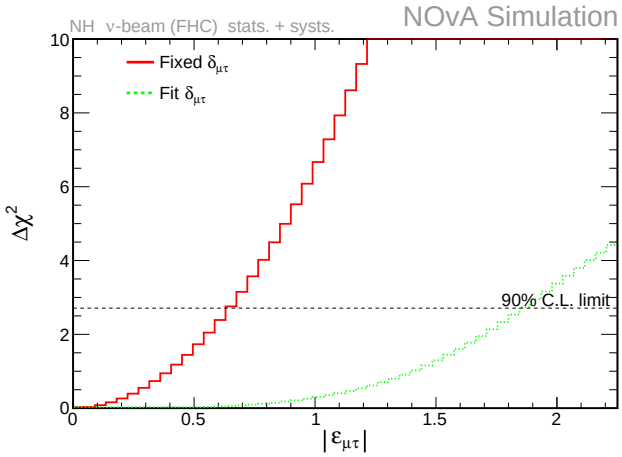

(a) Neutrino (FHC) beam - NH

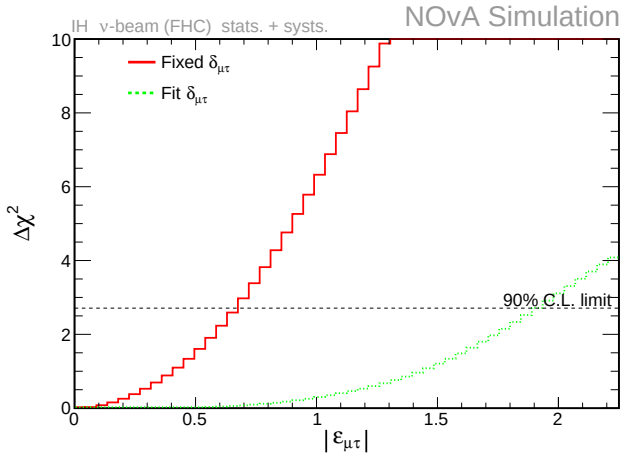

(b) Neutrino (FHC) beam - IH

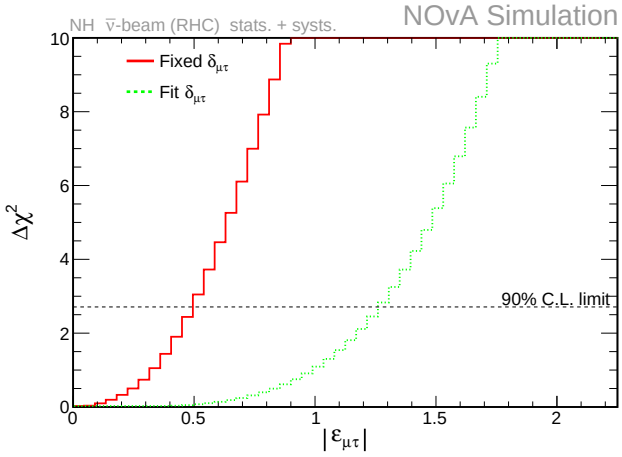

(c) Antineutrino (RHC) beam - NH

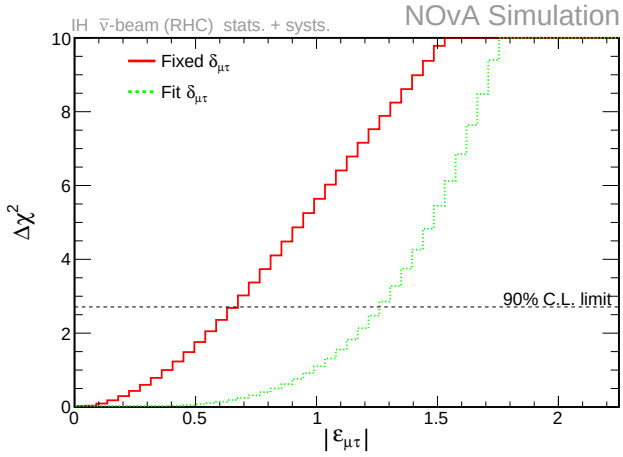

(d) Antineutrino (RHC) beam - IH

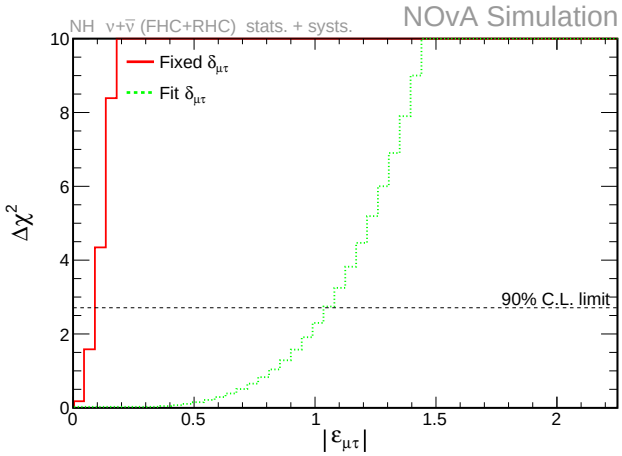

(e) FHC + RHC - NH

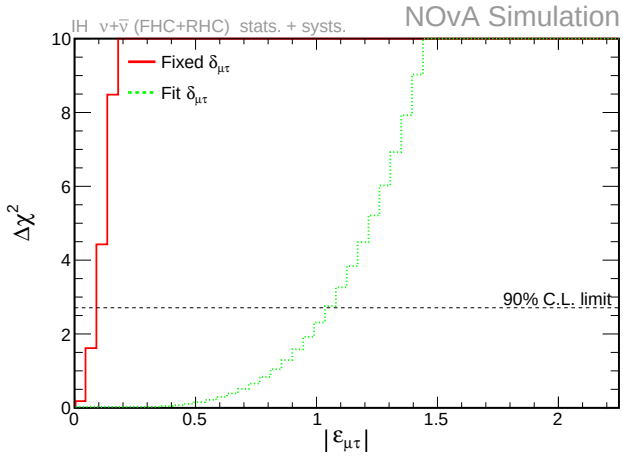

(f) FHC + RHC - IH

Figure 34 – $\Delta\chi^2$ values as function of $|\varepsilon_{\mu\tau}|$ for Normal Hierarchy (left) and Inverted Hierarchy (right) neutrino mass ordering scenarios, for neutrino beam (top), antineutrino beam (middle), and the joint analysis (bottom). Shown is a comparison for the case where $\delta_{\mu\tau}$ is included in the fit (dashed green line) or not (solid red line). The horizontal dashed line marks the 90% CL interval for the investigated parameter.

6.2.1.4 $\delta_{\mu\tau}$

Investigations of the NSI phase $\delta_{\mu\tau}$ are also attached to the knowledge that we have of $|\varepsilon_{\mu\tau}|$, justified again by the relationship between these two NSI parameters in the model. Fig. 35 we show the 1D projection of this parameter for both FHC, RHC, and FHC + RHC. For FHC mode, RHC mode, and the joint analysis, we have no sensitivity to the NSI phase $\delta_{\mu\tau}$ given our current choice of oscillation parameters for our simulated data. By initially assuming the oscillation parameters being used, shown in Table 4, the chosen value of $|\varepsilon_{\mu\tau}| = 0$ means that every possible value for $\delta_{\mu\tau}$ will match the data, once it is being multiplied by zero. However, note that if we fit $|\varepsilon_{\mu\tau}|$ as well (solid red line), still no sensitivity is observed for $\delta_{\mu\tau}$. A more detailed explanation of this behavior can be found in Appendix B.5.

Table 8 presents the 90% CL interval for $\delta_{\mu\tau}$ under the different investigated scenarios, for neutrino beam, antineutrino beam, and the joint neutrino-antineutrino fit, for both mass hierarchies.

90%CL interval for $\delta_{\mu\tau}$ (π rad)			
Mass hierarchy	Beam mode	Fixed $\|\varepsilon_{\mu\tau}\|$	Fit $\|\varepsilon_{\mu\tau}\|$
Normal	ν-beam	$0.0 \rightarrow 2.0$	$0.0 \rightarrow 2.0$
	$\bar{\nu}$-beam	$0.0 \rightarrow 2.0$	$0.0 \rightarrow 2.0$
	Joint fit	$0.0 \rightarrow 2.0$	$0.0 \rightarrow 2.0$
Inverted	ν-beam	$0.0 \rightarrow 2.0$	$0.0 \rightarrow 2.0$
	$\bar{\nu}$-beam	$0.0 \rightarrow 2.0$	$0.0 \rightarrow 2.0$
	Joint fit	$0.0 \rightarrow 2.0$	$0.0 \rightarrow 2.0$

Table 8 – 90%CL interval for the allowed values of the NSI parameter $\delta_{\mu\tau}$, for neutrino beam, antineutrino beam, and the joint neutrino-antineutrino fit, for both neutrino mass hierarchies, under the different analysis scenarios.

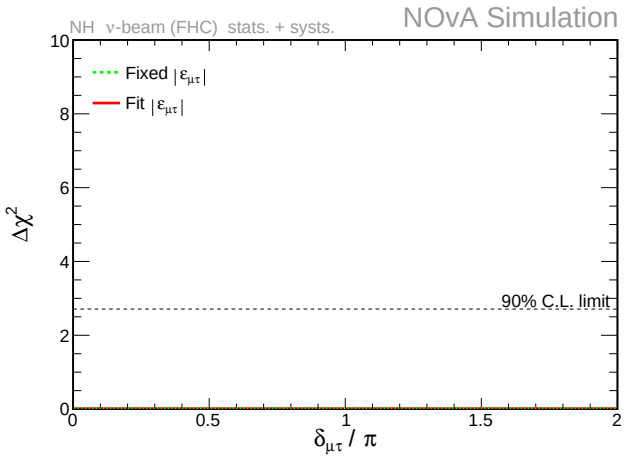

(a) Neutrino (FHC) beam - NH

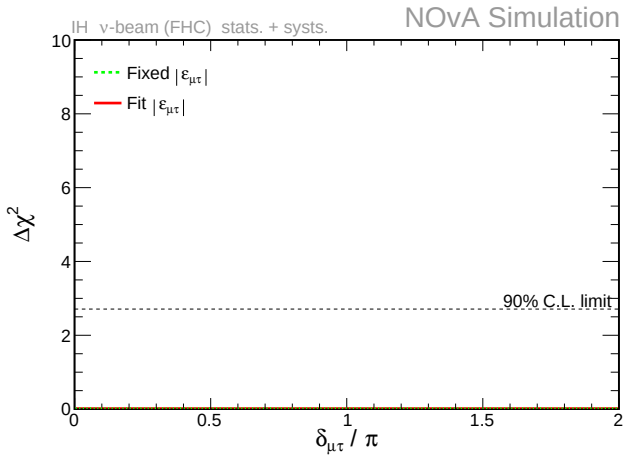

(b) Neutrino (FHC) beam - IH

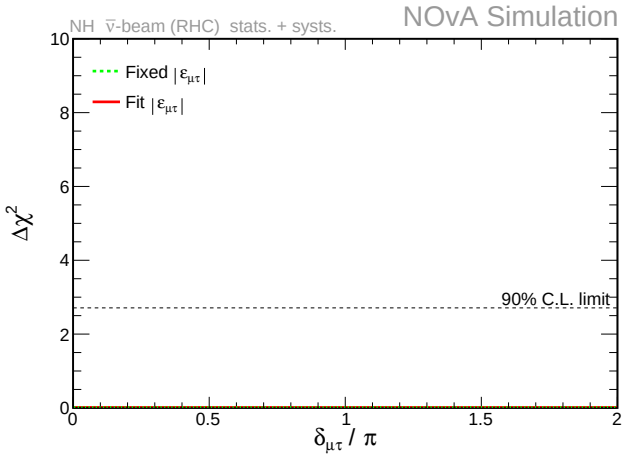

(c) Antineutrino (RHC) beam - NH

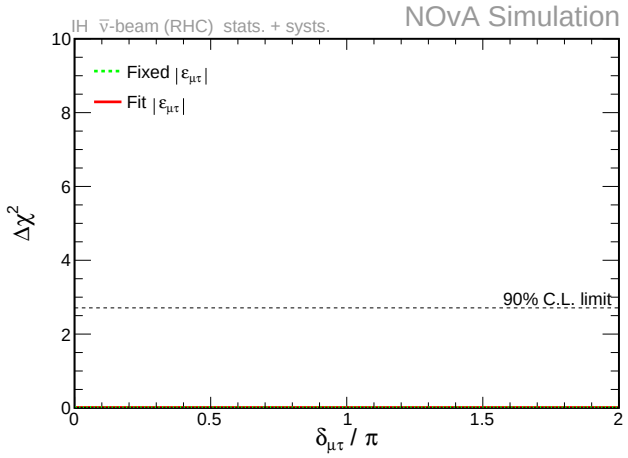

(d) Antineutrino (RHC) beam - IH

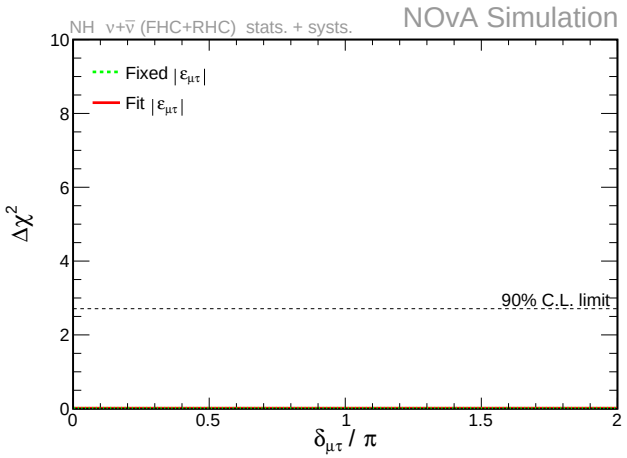

(e) FHC + RHC - NH

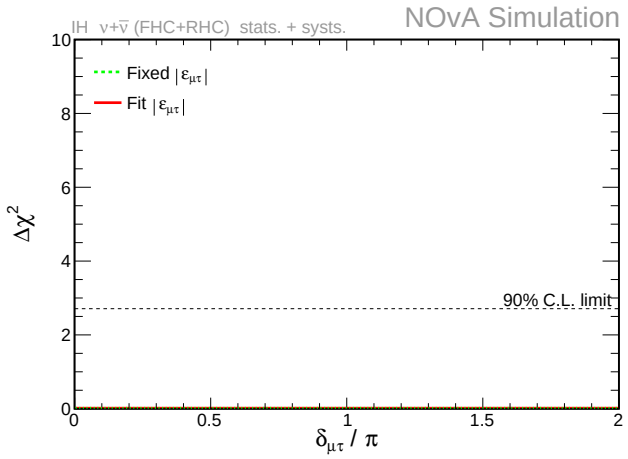

(f) FHC + RHC - IH

Figure 35 – $\Delta\chi^2$ values as function of $\delta_{\mu\tau}$ for Normal Hierarchy (left) and Inverted Hierarchy (right) neutrino mass ordering scenarios, for neutrino beam (top), antineutrino beam (middle), and the joint analysis (bottom). Shown is a comparison for the case where $|\varepsilon_{\mu\tau}|$ is included in the fit (solid red line) or not (dashed green line). The horizontal dashed line marks the 90% CL interval for the investigated parameter.

6.2.2 2D Surfaces

Surfaces are a 2-dimensional projection of the hypersurface generated by $\Delta\chi^2$ onto the axes of two parameters of interest. In this projection the depth (or z-axis, not shown) is the $\Delta\chi^2$ axis. Contours are obtained by choosing a "slice" at a given $\Delta\chi^2$ value. In our studies, we show results for $\Delta\chi^2 = 4.61$, which corresponds to the 90% CL limit for 2 parameters, producing contours with information regarding the allowed values for our parameters being projected.

6.2.2.1 $\sin^2(\theta_{23}) \times \Delta m^2_{32}$

As done for the 1D projections, in order to understand the effects of the NSI parameters on our knowledge of $\sin^2(\theta_{23})$ and Δm^2_{32} we compare the contours for this parameter space, specifically, at three different scenarios:

- Standard oscillations: no NSI parameters are included in the fit.
- NSI, with $|\varepsilon_{\mu\tau}|$ only: allow $|\varepsilon_{\mu\tau}|$ to float in the fit in the range $[0, 0.25]$; $\delta_{\mu\tau}$ is kept fixed at zero.
- NSI, with $|\varepsilon_{\mu\tau}|$ and $\delta_{\mu\tau}$: allow $|\varepsilon_{\mu\tau}|$ to float in the fit in the range $[0, 0.25]$, and $\delta_{\mu\tau} \in [0, 2\pi]$.

The choice for the range of $|\varepsilon_{\mu\tau}|$ is again based on the event rate predictions seen in Fig. 30. Fig. 36 shows the comparison between the different approaches and their effects. For the FHC mode the inclusion of $|\varepsilon_{\mu\tau}|$ pushes solutions to lower Δm^2_{32}, while the opposite is seen for RHC, where $|\varepsilon_{\mu\tau}|$ is responsible for allowing solutions to higher (*more negative*) Δm^2_{32}. On both cases, the inclusion of $\delta_{\mu\tau}$ is seen to equally expand the contours, allowing the neutrino or antineutrino modes to have solutions in the region not covered for only $|\varepsilon_{\mu\tau}|$. In other words, while the inclusion of only $|\varepsilon_{\mu\tau}|$ affects neutrinos and antineutrinos differently, in the scenario containing both $|\varepsilon_{\mu\tau}|$ and $\delta_{\mu\tau}$ the effects are the same. This behavior is in accordance to the observed in the 1D profiles shown in Fig. 32. The joint analysis, combining neutrino and antineutrino data, shows no significant deviation from the standard and NSI models at the 90% CL limit, for both neutrino mass hierarchies.

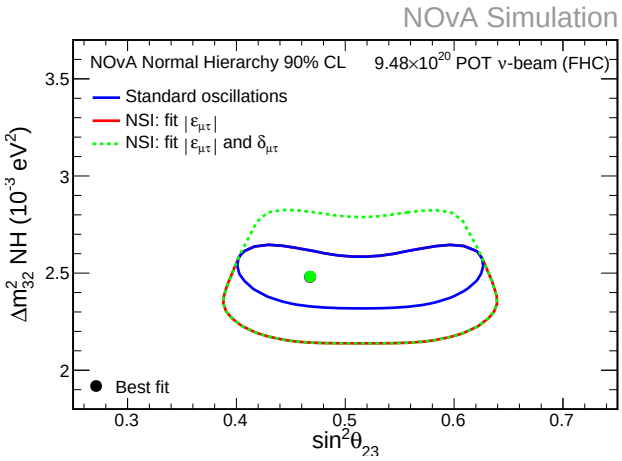

(a) Neutrino (FHC) beam - NH

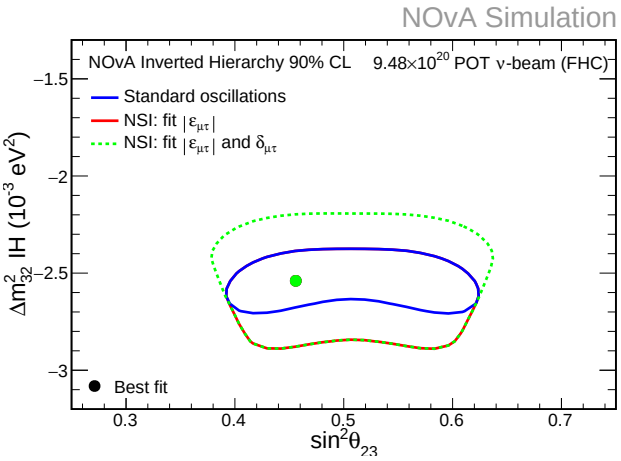

(b) Neutrino (FHC) beam - IH

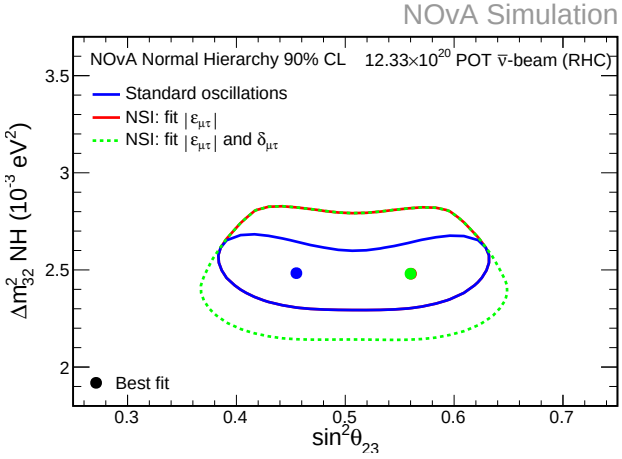

(c) Antineutrino (RHC) beam - NH

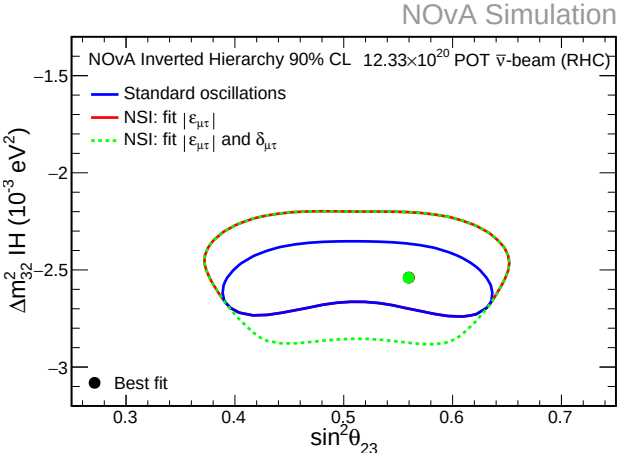

(d) Antineutrino (RHC) beam - IH

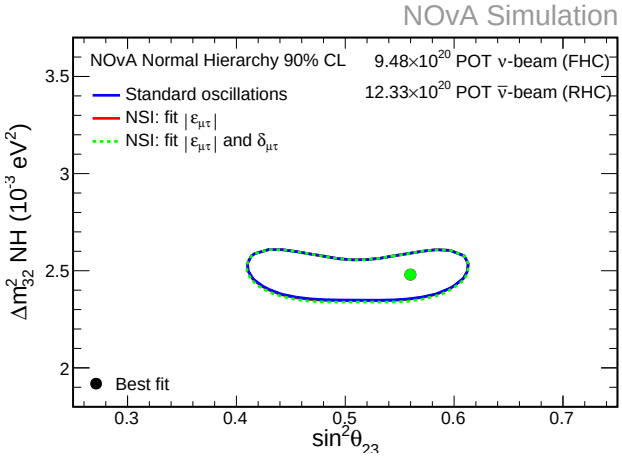

(e) FHC + RHC - NH

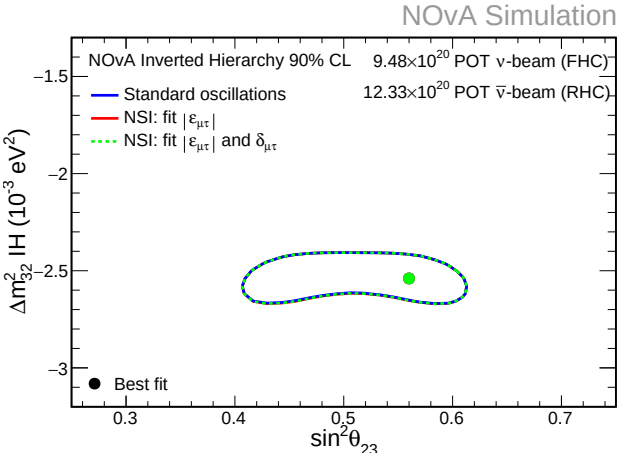

(f) FHC + RHC - IH

Figure 36 – NOvA 90% CL allowed region for the standard parameters Δm^2_{32} and $\sin^2(\theta_{23})$ for Normal Hierarchy (left) and Inverted Hierarchy (right) neutrino mass ordering scenarios, for neutrino beam (top), antineutrino beam (middle), and the joint analysis (bottom). In solid blue is shown the standard case, while the dashed red and dotted green lines are with the inclusion of $|\varepsilon_{\mu\tau}|$ only, and $|\varepsilon_{\mu\tau}|$ and $\delta_{\mu\tau}$, respectively.

6.2.2.2 $|\varepsilon_{\mu\tau}| \times \Delta m^2_{32}$

Given the relation between Δm^2_{32} and the NSI parameter $|\varepsilon_{\mu\tau}|$, we aim to understand how they are dependent on each other. We know from the results shown in Fig. 32 and Fig. 36 that inclusion of $|\varepsilon_{\mu\tau}|$ is responsible for direct effects on Δm^2_{32}, and from Fig. 34 we know that in principle $|\varepsilon_{\mu\tau}|$ could have larger values. Fig. 37 shows the 90% CL contours for this parameter space, where we compare their relationship for both cases with inclusion or not of the phase $\delta_{\mu\tau}$. We observe that for the FHC mode, as $|\varepsilon_{\mu\tau}|$ increases lower values of Δm^2_{32} are allowed, while for the RHC analysis the opposite is seen, with higher values of Δm^2_{32} being allowed as $|\varepsilon_{\mu\tau}|$ increases. This behavior is in accordance to the observed in the parameter space shown in Fig. 36. The joint neutrino-antineutrino analysis is better restrictive on both parameters. However, the inclusion of the phase $\delta_{\mu\tau}$ in the fit is responsible for expanding the contours, and thus the allowed values for both $|\varepsilon_{\mu\tau}|$ and Δm^2_{32}. This is observed due to the already discussed relationship between $|\varepsilon_{\mu\tau}|$ and the NSI phase $\delta_{\mu\tau}$ on our parameterization, where lack of knowledge of one has a direct impact on knowledge of the other. As $\delta_{\mu\tau}$ is allowed to float in the fit, larger values of $|\varepsilon_{\mu\tau}|$ may be allowed in order to keep the right balance between these 2 parameters and the data being fitted, with a direct impact on Δm^2_{32} as well.

The major difference between both mass hierarchy scenarios is for when $\delta_{\mu\tau}$ is included in the fit (dashed green lines), where we see different behaviors for NH or IH scenarios.

6.2.2.3 $|\varepsilon_{\mu\tau}| \times \sin^2(\theta_{23})$

Similarly to the previous discussion, we investigate the relation between $\sin^2(\theta_{23})$ and the NSI parameter $|\varepsilon_{\mu\tau}|$ by looking at the 90% CL contours for this parameter space shown in Fig. 38, also comparing to the effects of the NSI phase $\delta_{\mu\tau}$. We observe that for both FHC and RHC modes, the presence of $|\varepsilon_{\mu\tau}|$ only has a slight effect on the allowed values of $\sin^2(\theta_{23})$, and this effect is seen to greatly diminish at the joint analysis. However, as in the other parameter spaces, the presence of $\delta_{\mu\tau}$ is seen again to expand the allowed values of $|\varepsilon_{\mu\tau}|$, with the particular behavior of a preference close to maximal mixing for $\sin^2(\theta_{23})$ on FHC mode for large values of $|\varepsilon_{\mu\tau}|$. Still, no information regarding the octant of θ_{23} can be obtained at the 90% CL. For this parameter space, the difference between both mass hierarchy scenarios is observed when we include $|\varepsilon_{\mu\tau}|$ in the fit (solid red line), but not its phase $\delta_{\mu\tau}$. The FHC mode for NH tends to follow the same pattern that the RHC mode for IH, and the RHC mode for NH to that of the FHC mode for IH. In other words, this is a potential source of degeneracy, and we see that for the FHC + RHC fit no differences are observed between the NH and IH cases.

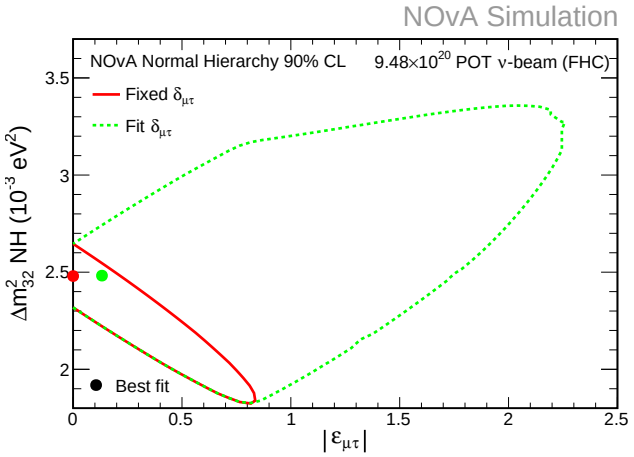

(a) Neutrino (FHC) beam - NH

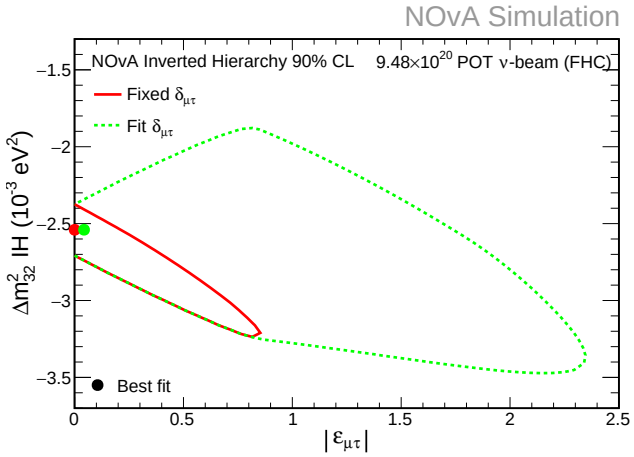

(b) Neutrino (FHC) beam - IH

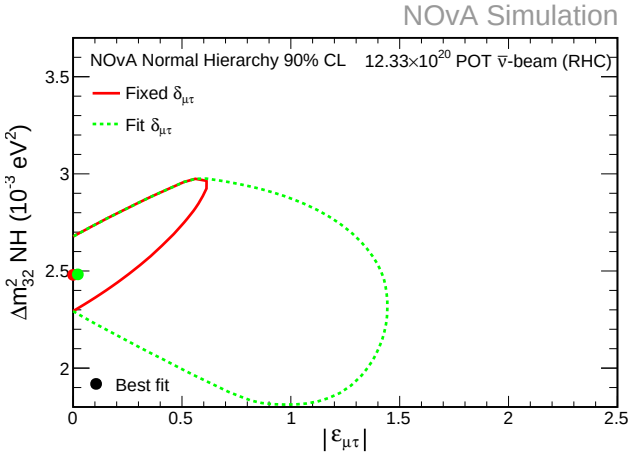

(c) Antineutrino (RHC) beam - NH

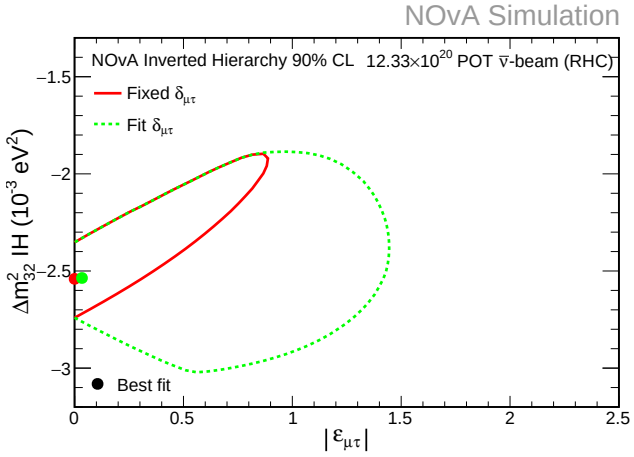

(d) Antineutrino (RHC) beam - IH

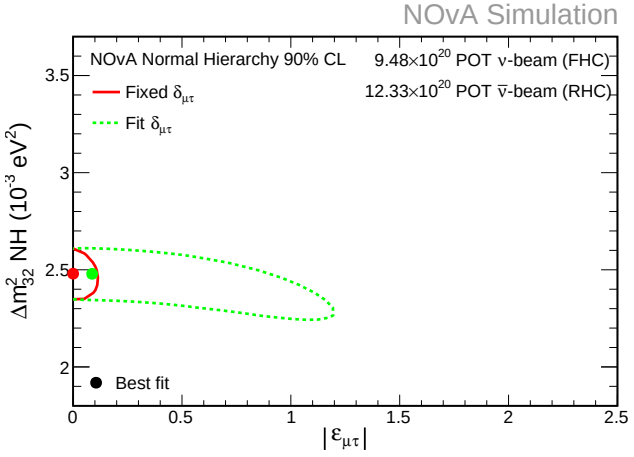

(e) FHC + RHC - NH

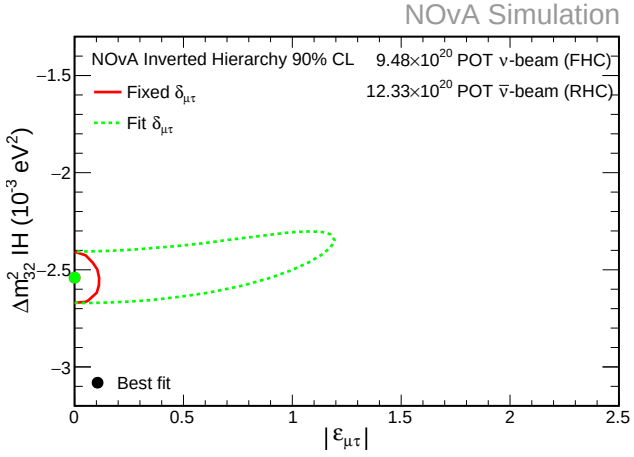

(f) FHC + RHC - IH

Figure 37 – NOvA 90% CL allowed region for the standard parameter Δm^2_{32} for Normal Hierarchy (left) and Inverted Hierarchy (right) neutrino mass ordering scenarios, for neutrino beam (top), antineutrino beam (middle), and the joint analysis (bottom). In solid red results are shown for a fixed value of $\delta_{\mu\tau} = 0$, while in dashed green we fit for $\delta_{\mu\tau}$ as well.

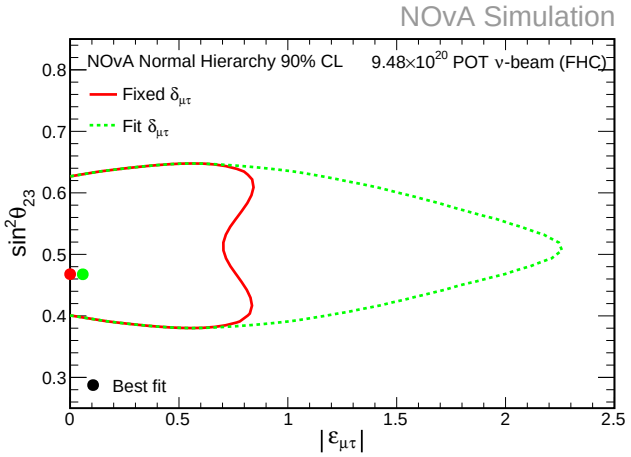

(a) Neutrino (FHC) beam - NH

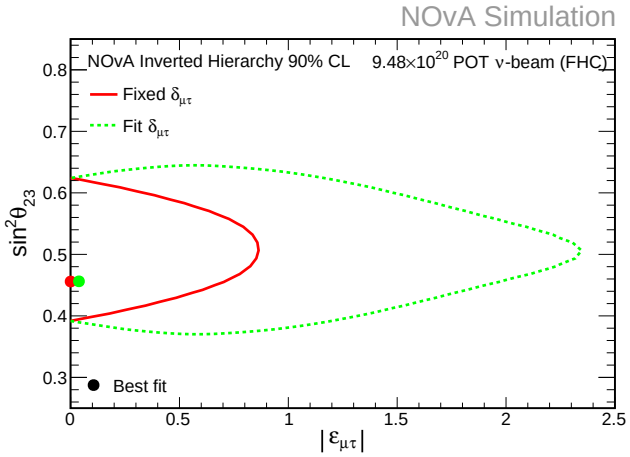

(b) Neutrino (FHC) beam - IH

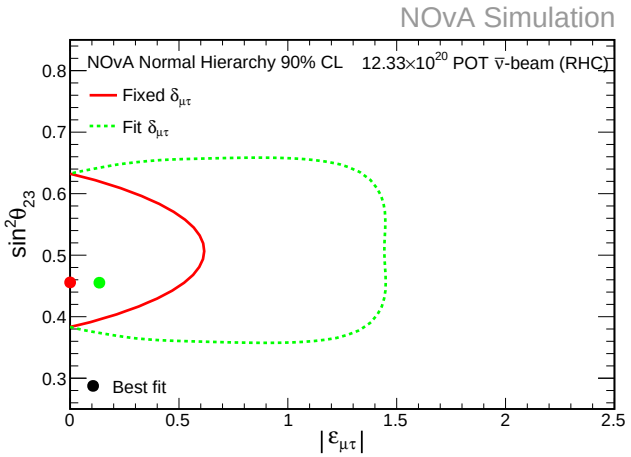

(c) Antineutrino (RHC) beam - NH

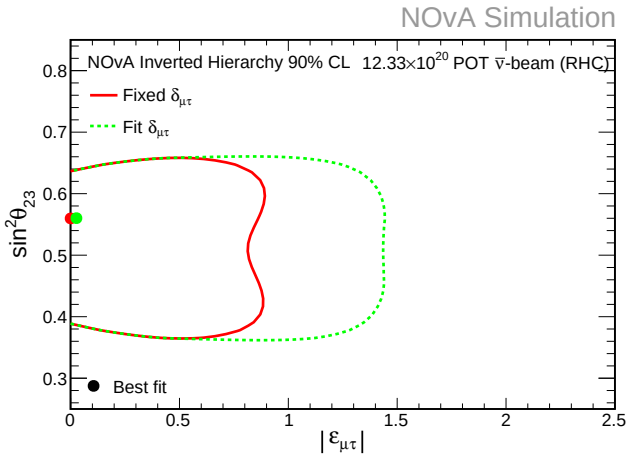

(d) Antineutrino (RHC) beam - IH

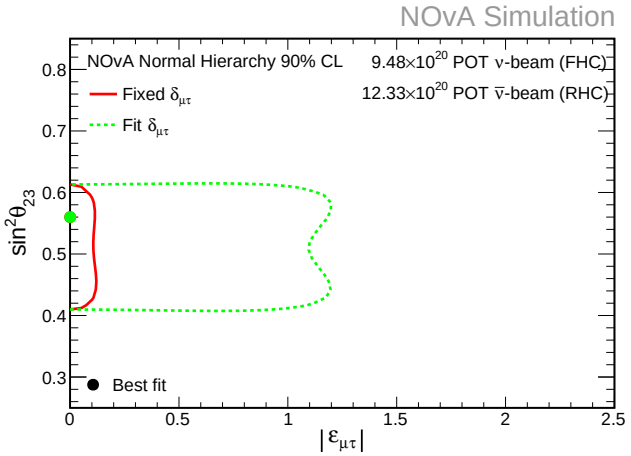

(e) FHC + RHC - NH

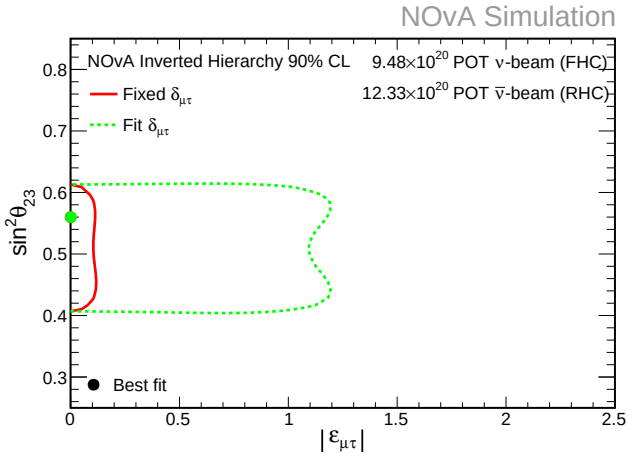

(f) FHC + RHC - IH

Figure 38 – NOvA 90% CL allowed region for the standard parameter $\sin^2(\theta_{23})$ and the NSI parameter $|\varepsilon_{\mu\tau}|$ for Normal Hierarchy (left) and Inverted Hierarchy (right) neutrino mass ordering scenarios, for neutrino beam (top), antineutrino beam (middle), and the joint analysis (bottom). In solid red results are shown for a fixed value of $\delta_{\mu\tau} = 0$, while in dashed green we fit for $\delta_{\mu\tau}$ as well.

6.2.2.4 $\delta_{\mu\tau} \times \Delta m^2_{32}$

We now investigate the relation between Δm^2_{32} and the NSI phase $\delta_{\mu\tau}$. Fig. 39 show the 90% CL contours for this parameter space for FHC, RHC, and FHC + RHC, along with a comparison of the effects of including $|\varepsilon_{\mu\tau}|$ in the fit or not. For all modes, when we fit only for the NSI phase $\delta_{\mu\tau}$ (dashed green line) no effects are observed in Δm^2_{32}. This is due to the fact that in this approach the value for $|\varepsilon_{\mu\tau}|$ is kept fixed at its initial input for our predictions, i.e., $|\varepsilon_{\mu\tau}| = 0$. This means that any value for $\delta_{\mu\tau}$ are allowed, since $e^{i\delta_{\mu\tau}}$ is multiplied by $|\varepsilon_{\mu\tau}| = 0$ at all times. If we allow $|\varepsilon_{\mu\tau}|$ to be fitted as well (solid red line), we see effects on Δm^2_{32} on both FHC and RHC modes. Note that for the FHC mode, in the range of $\delta_{\mu\tau} \in \left[0, \frac{\pi}{2}\right] \cup \left[\frac{3\pi}{2}, 2\pi\right]$ the effects of fitting for $|\varepsilon_{\mu\tau}|$ are responsible for pushing solutions to lower values of Δm^2_{32}, while for values of $\delta_{\mu\tau} \in \left[\frac{\pi}{2}, \frac{3\pi}{2}\right]$ we find higher allowed solutions for Δm^2_{32}. The exact opposite is seen for the RHC mode, where in the range of $\delta_{\mu\tau} \in \left[0, \frac{\pi}{2}\right] \cup \left[\frac{3\pi}{2}, 2\pi\right]$ we find higher values for solutions on Δm^2_{32}, while for $\delta_{\mu\tau} \in \left[\frac{\pi}{2}, \frac{3\pi}{2}\right]$ we obtain lower allowed values for Δm^2_{32}. This behavior support what we observed before on other parameter spaces. On FHC mode the lowest allowed values for Δm^2_{32} are those at $\delta_{\mu\tau} = 0, 2\pi$, which corresponds to the maximum positive factor[1] of $e^{i\delta_{\mu\tau}}$, i.e. 1. Note now that in these same values of $\delta_{\mu\tau}$, but for the RHC mode, we have the largest allowed values of Δm^2_{32}. The opposite effect is justified by the exchange of signs between neutrinos and antineutrinos on the NSI model. The joint FHC + RHC fit breaks this dependence, and no significant effects are seen on Δm^2_{32}, with all values for $\delta_{\mu\tau}$ being allowed within the current sensitivity. No major differences are observed between both mass hierarchy scenarios.

6.2.2.5 $\delta_{\mu\tau} \times \sin^2(\theta_{23})$

We now investigate the relation between $\sin^2(\theta_{23})$ and the NSI phase $\delta_{\mu\tau}$. The 90% CL contours for this parameter space is presented in Fig. 40. As observed for the contours of $\delta_{\mu\tau} \times \Delta m^2_{32}$, when $|\varepsilon_{\mu\tau}|$ is not present in the fit, no effects are seen, and the explanation follows as before. If $|\varepsilon_{\mu\tau}|$ is included in the fit, a slight expansion is seen for the allowed values for $\sin^2(\theta_{23})$ in the range of $\delta_{\mu\tau} \in \left[0, \frac{\pi}{2}\right] \cup \left[\frac{3\pi}{2}, 2\pi\right]$ for the FHC mode. In the RHC mode, we observe a minor expansion on the allowed values of $\sin^2(\theta_{23})$ for the range of $\delta_{\mu\tau} \in \left[\frac{\pi}{2}, \frac{3\pi}{2}\right]$. The joint FHC + RHC fit shows no major deviations on $\sin^2(\theta_{23})$, and within the current sensitivity all values of $\delta_{\mu\tau}$ are allowed, as well as both octants for the mixing angle θ_{23}. For this parameter space, the difference between both mass hierarchies is observed when we include $|\varepsilon_{\mu\tau}|$ in the fit (solid red line). The FHC mode for NH tends to follow the same pattern that the RHC mode for IH, and the RHC mode for NH to that of the FHC mode for IH. In the FHC + RHC fit no differences are observed between the NH and IH cases.

[1] Remember that the ν_μ,$\bar{\nu}_\mu$ disappearance analysis is sensitive to the real part of the parameters.

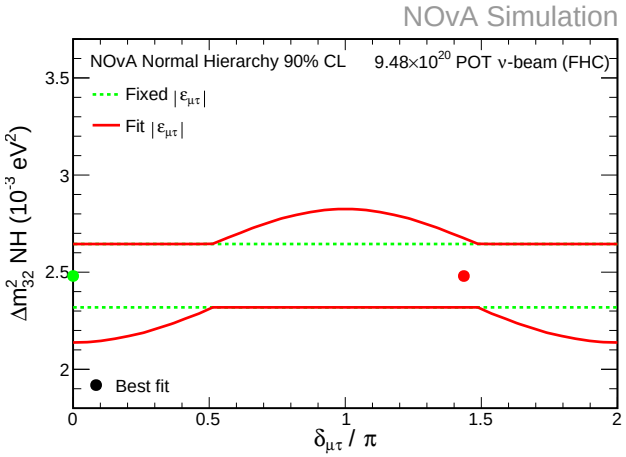

(a) Neutrino (FHC) beam - NH

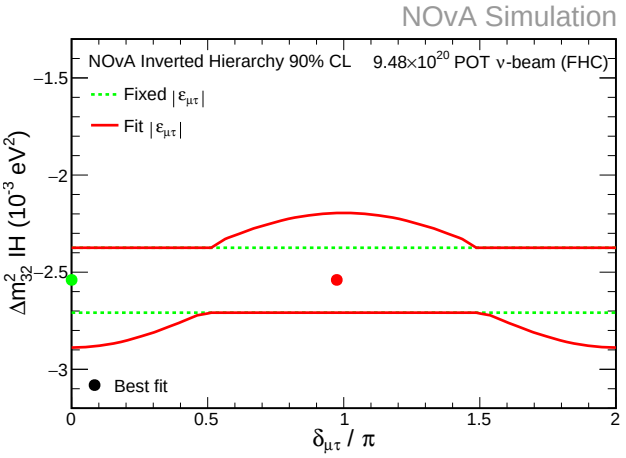

(b) Neutrino (FHC) beam - IH

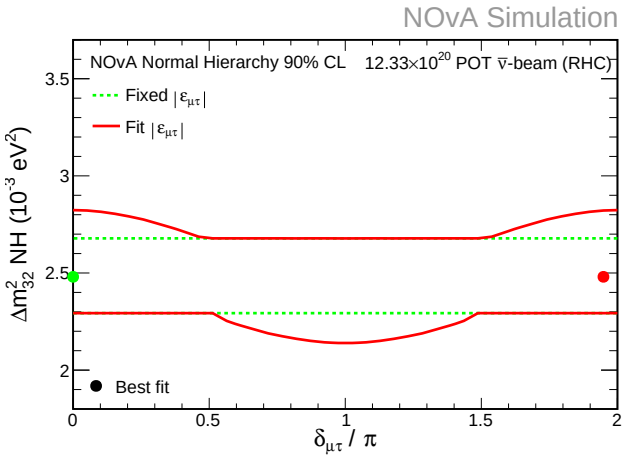

(c) Antineutrino (RHC) beam - NH

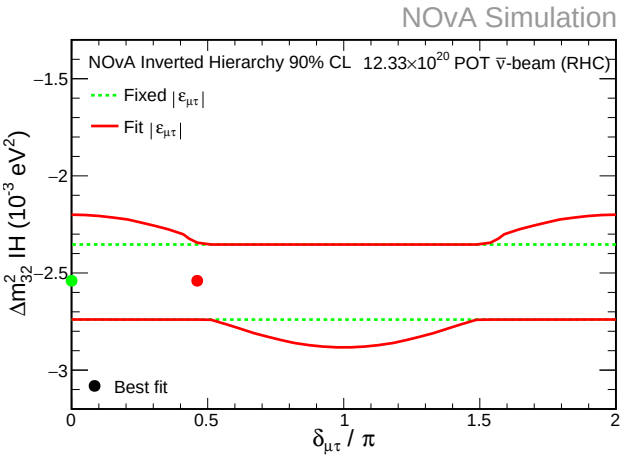

(d) Antineutrino (RHC) beam - IH

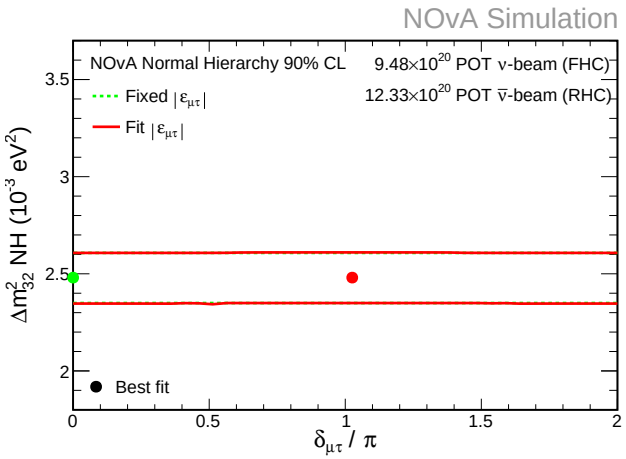

(e) FHC + RHC - NH

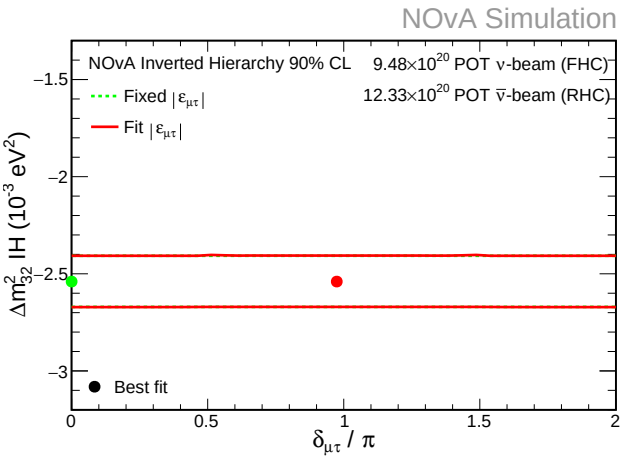

(f) FHC + RHC - IH

Figure 39 – NOvA 90% CL allowed region for the standard parameter Δm^2_{32} and the NSI phase $\delta_{\mu\tau}$ for Normal Hierarchy (left) and Inverted Hierarchy (right) neutrino mass ordering scenarios, for neutrino beam (top), antineutrino beam (middle), and the joint analysis (bottom). In dashed green results are shown for a fixed value of $|\varepsilon_{\mu\tau}| = 0$, while in solid red we fit for $|\varepsilon_{\mu\tau}|$ as well.

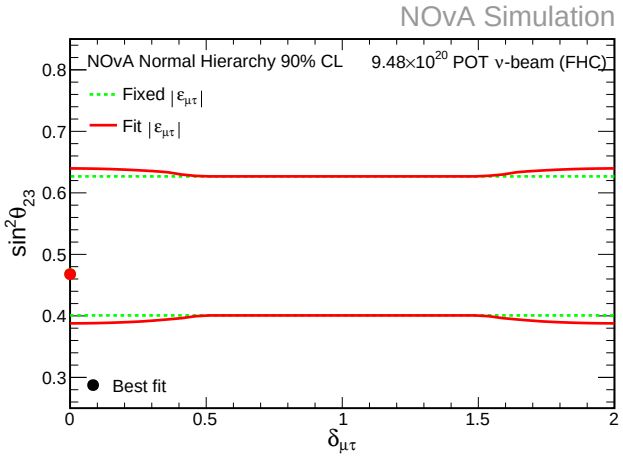

(a) Neutrino (FHC) beam - NH

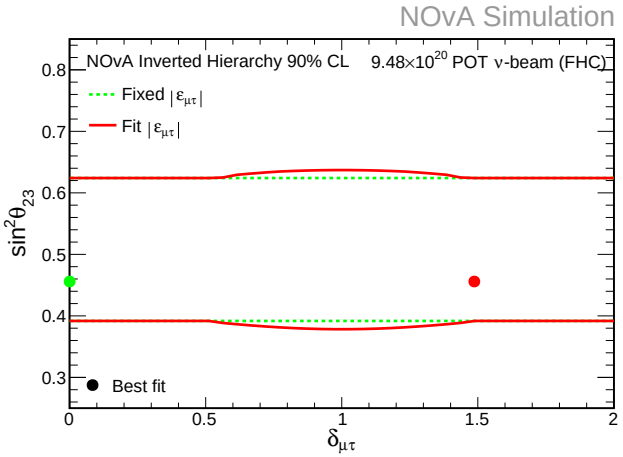

(b) Neutrino (FHC) beam - IH

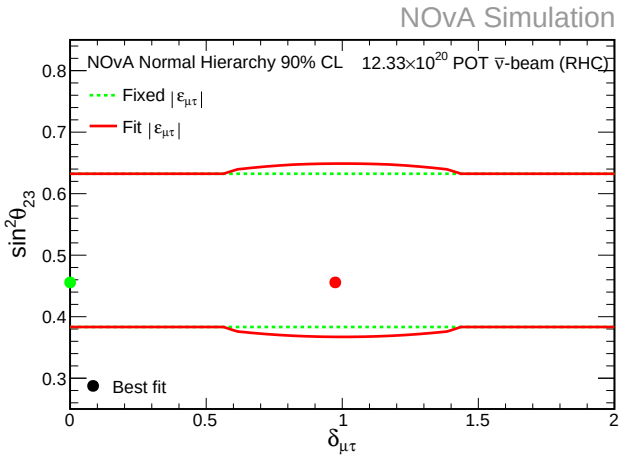

(c) Antineutrino (RHC) beam - NH

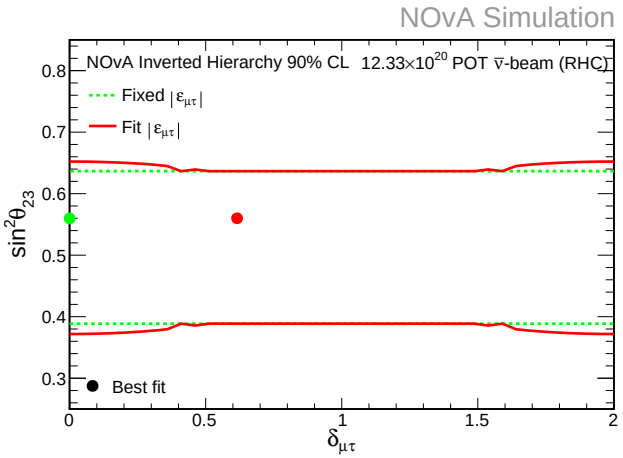

(d) Antineutrino (RHC) beam - IH

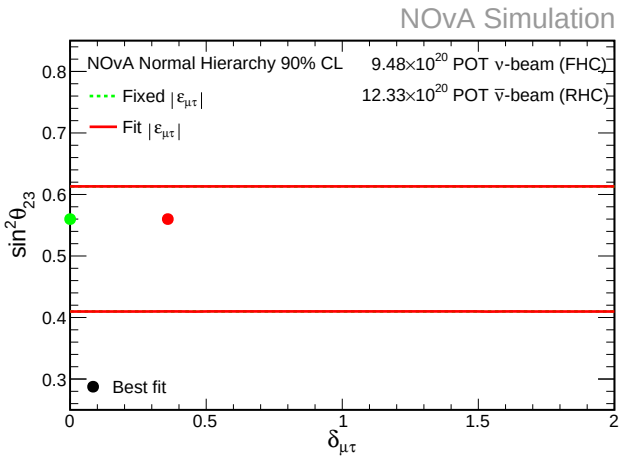

(e) FHC + RHC - NH

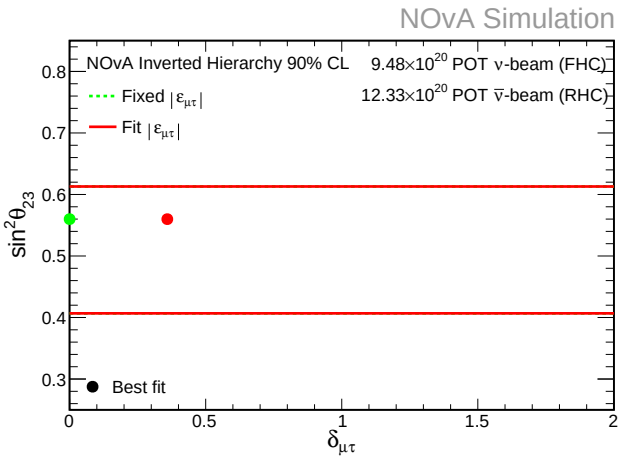

(f) FHC + RHC - IH

Figure 40 – NOvA 90% CL allowed region for the standard parameter $\sin^2(\theta_{23})$ and the NSI phase $\delta_{\mu\tau}$ for Normal Hierarchy (left) and Inverted Hierarchy (right) neutrino mass ordering scenarios, for neutrino beam (top), antineutrino beam (middle), and the joint analysis (bottom). In dashed green results are shown for a fixed value of $|\varepsilon_{\mu\tau}| = 0$, while in solid red we fit for $|\varepsilon_{\mu\tau}|$ as well.

6.2.2.6 $\delta_{\mu\tau} \times |\varepsilon_{\mu\tau}|$

So far we investigated the effects of the NSI parameters on the measurements of the standard oscillation parameters Δm^2_{32} and $\sin^2(\theta_{23})$, as well as their relations with the NSI parameters itself. We now aim to understand how the NSI parameters adopted in our current parameterization are related to each other. We perform a fit in the $\delta_{\mu\tau} \times |\varepsilon_{\mu\tau}|$ parameter space in order to investigate how the knowledge of each NSI parameter is related to a given value of the other. Fig. 41 show the 90% CL contours for this parameter space of interest. We observe that for both FHC, RHC, and FHC + RHC, the allowed values for $|\varepsilon_{\mu\tau}|$ are considerably affected by $\delta_{\mu\tau}$. When we are investigating the relation between these two parameters and their role in the fit, we are in fact measuring the best balance in $|\varepsilon_{\mu\tau}| e^{i\delta_{\mu\tau}}$. As discussed earlier, the survival probability is mostly affected by the real part of our parameters. Then, $\Re\left(e^{i\delta_{\mu\tau}}\right) = \cos(\delta_{\mu\tau})$, and as $\delta_{\mu\tau} \to \frac{\pi}{2}$ or $\frac{3\pi}{2}$, $\cos(\delta_{\mu\tau}) \to 0$, which causes the values for $|\varepsilon_{\mu\tau}|$ to greatly increase in order to keep the balance.

For this parameter space, the difference between both mass hierarchy scenarios is observed to be on the allowed values for $|\varepsilon_{\mu\tau}|$ given a certain value of $\delta_{\mu\tau}$, seen on both the FHC and RHC modes. In the FHC + RHC fit no differences are observed between the NH and IH cases.

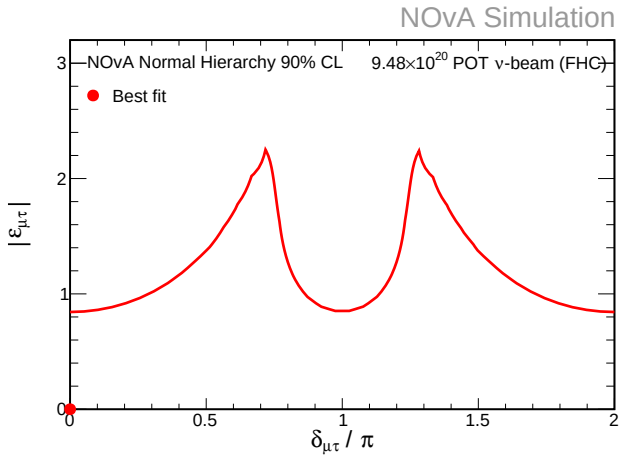

(a) Neutrino (FHC) beam - NH

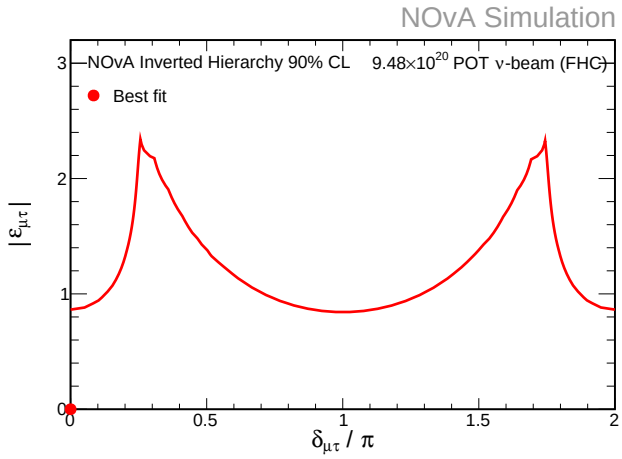

(b) Neutrino (FHC) beam - IH

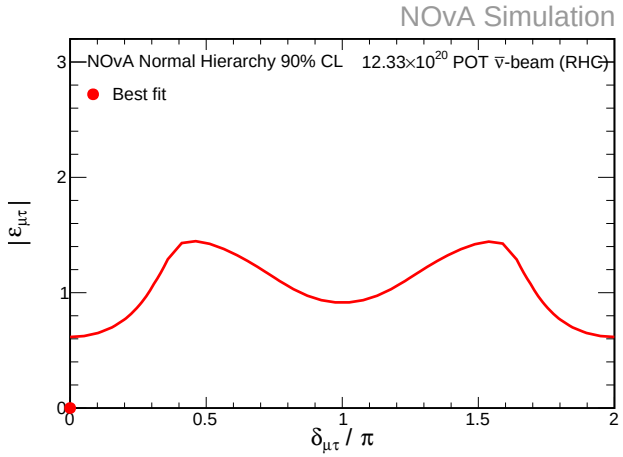

(c) Antineutrino (RHC) beam - NH

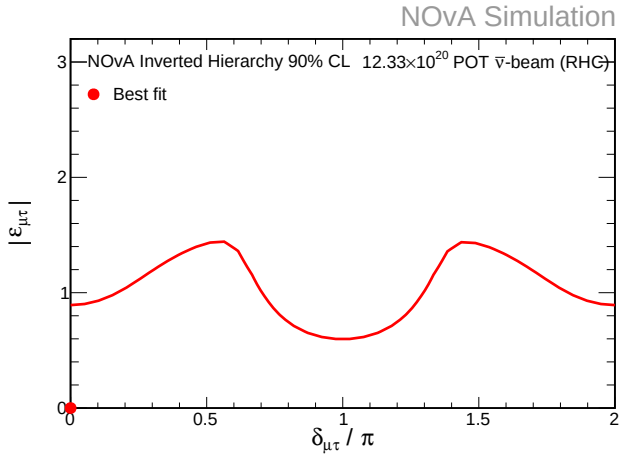

(d) Antineutrino (RHC) beam - IH

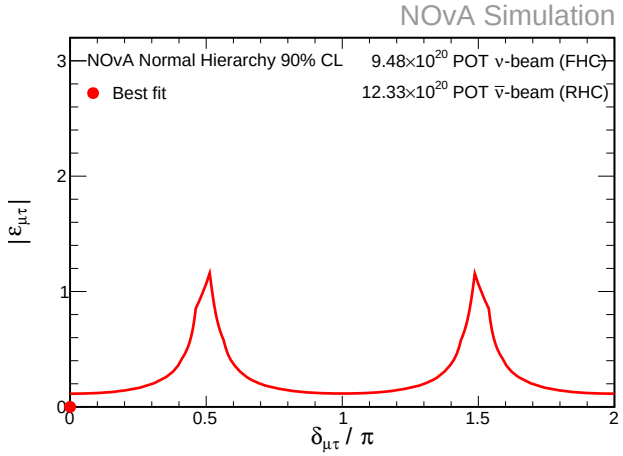

(e) FHC + RHC - NH

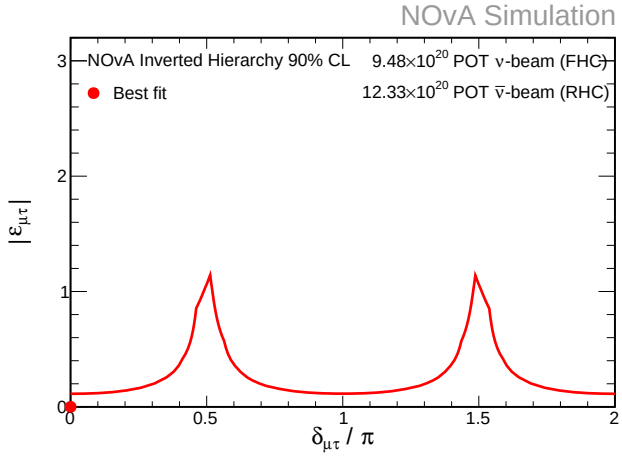

(f) FHC + RHC - IH

Figure 41 – NOvA 90% CL allowed region for the NSI parameters $|\varepsilon_{\mu\tau}|$ and $\delta_{\mu\tau}$ for Normal Hierarchy (left) and Inverted Hierarchy (right) neutrino mass ordering scenarios, for neutrino beam (top), antineutrino beam (middle), and the joint analysis (bottom).

6.3 Summary and future perspectives

It is seen that the inclusion of new, non-standard, parameters produce observable effects on neutrinos and antineutrinos, for both neutrino mass hierarchies. A joint fit on neutrino and antineutrino data reveals that the effects on the standard oscillation parameters arising from $|\varepsilon_{\mu\tau}|$ and $\delta_{\mu\tau}$ virtually vanishes. No major deviations from the standard oscillation scenario and the NSI case is observed at the 90% CL, and we set limits on the NSI parameters based on the current sensitivity. A summary of the corresponding 90% CL allowed interval for the investigated parameters in the context where we proceed to a joint neutrino-antineutrino fit to the standard oscillation parameters, Δm^2_{32} and $\sin^2(\theta_{23})$, as well as for the NSI parameters, $|\varepsilon_{\mu\tau}|$ and $\delta_{\mu\tau}$, is presented in Table 9.

Mass Hierarchy	Parameter	90% CL range
Normal	$\lvert\varepsilon_{\mu\tau}\rvert$	≤ 1.054
	$\delta_{\mu\tau}(\pi\,\mathrm{rad})$	$0 \rightarrow 2.0$
	$\sin^2(\theta_{23})$	$0.420 \rightarrow 0.602$
	$\Delta m^2_{32}\ (10^{-3}\mathrm{eV}^2)$	$2.379 \rightarrow 2.580$
Inverted	$\lvert\varepsilon_{\mu\tau}\rvert$	≤ 1.053
	$\delta_{\mu\tau}(\pi\,\mathrm{rad})$	$0 \rightarrow 2.0$
	$\sin^2(\theta_{23})$	$0.418 \rightarrow 0.602$
	$\Delta m^2_{32}\ (10^{-3}\mathrm{eV}^2)$	$-2.639 \rightarrow -2.438$

Table 9 – 90% CL range for the investigated parameters obtained through a joint neutrino and antineutrino fit, for both mass hierarchies. Shown are the results for the scenario where both the NSI parameters $|\varepsilon_{\mu\tau}|$ and $\delta_{\mu\tau}$ are included in the fit.

The NOvA experiment is scheduled to continue its data taking of neutrinos and antineutrinos from the NuMI beam until the year of 2025, where the experiment expect to reach an exposure of 31.5×10^{20} POT for neutrino beam (FHC), and 31.5×10^{20} POT for antineutrino beam (RHC), for a total of 63.0×10^{20} POT. Under this assumption, we investigate what information we expect to obtain for the NSI parameters $|\varepsilon_{\mu\tau}|$ and $\delta_{\mu\tau}$ by looking at our future sensitivities at this exposure. Fig. 42 shows the information presented in subsection 6.2.2.6, along with a comparison using our expected future exposure.

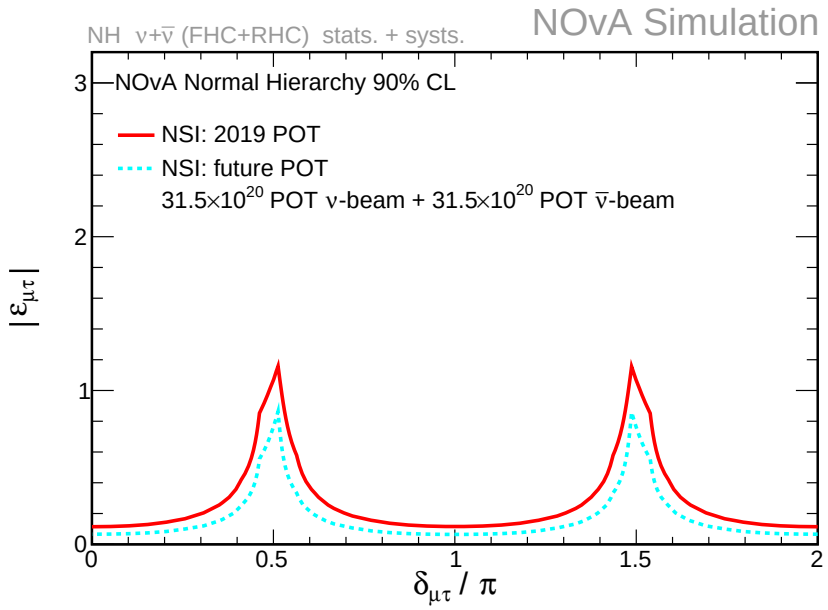

Figure 42 – NOvA 90% CL allowed region for the NSI parameters $|\varepsilon_{\mu\tau}|$ and $\delta_{\mu\tau}$ for Normal Hierarchy using a joint fit of antineutrinos and antineutrinos, showing a comparison of our results for the current exposure used in this work (solid red) with the expected result (solid cyan) using the predicted future exposure of 31.5×10^{20} POT for neutrino beam (FHC), and 31.5×10^{20} POT for antineutrino beam (RHC).

It is expected that the current sensitivities will be moderately improved with the addition of future data collected by the experiment, setting lower upper limits for the NSI parameter $|\varepsilon_{\mu\tau}|$. Still, all values of the NSI phase $\delta_{\mu\tau}$ remain allowed at the 90% CL limit, with hints for a preference to reject values close to 0, π, and 2π.

7 Conclusions

This thesis presents the results obtained by the author and collaborators on sensitivities to neutrino non-standard interactions on neutrino oscillations at the NOvA experiment. Following the model and strategy developed in this work, the NOvA experiment will perform its first experimental search for non-standard interactions on neutrino oscillations using data from ν_μ and $\bar{\nu}_\mu$ disappearance at the Far Detector.

The $\nu_\mu \to \nu_\mu$ ($\bar{\nu}_\mu \to \bar{\nu}_\mu$) channel is sensitive to the effective NSI flavor-changing parameter $\varepsilon_{\mu\tau}$, parameterized as $\varepsilon_{\mu\tau} = |\varepsilon_{\mu\tau}|\, e^{i\delta_{\mu\tau}}$. Through analysis of CC ν_μ and $\bar{\nu}_\mu$ events at the Far Detector, the experiment is able to perform a joint neutrino and antineutrino fit for the NSI parameters $|\varepsilon_{\mu\tau}|$ and $\delta_{\mu\tau}$, as well as for the standard oscillation parameters Δm^2_{32} and $\sin^2(\theta_{23})$, and look for effects and correlations between the parameters being investigated. With the inclusion of new, non-standard, parameters in the neutrino oscillation framework it is expected for the CC event rates for neutrinos and antineutrinos at the Far Detector to be considerably affected, depending on the magnitude of the additional parameters.

The NSI parameters are responsible for visible effects on the determination of Δm^2_{32} and $\sin^2(\theta_{23})$ when considering data from neutrinos (FHC mode) or antineutrinos (RHC mode). The parameter Δm^2_{32} is seen to be the most directly affected, for both cases when we fit for $\delta_{\mu\tau}$ or not. On the other hand, the parameter $\sin^2(\theta_{23})$ is less affected by this parameterization. Given our current knowledge, we see that the NSI phase $\delta_{\mu\tau}$ is responsible to allow considerably larger values of $|\varepsilon_{\mu\tau}|$, specially around the values of $\delta_{\mu\tau} = \frac{\pi}{2}$ and $\delta_{\mu\tau} = \frac{3\pi}{2}$, a behavior justified by the multiplicative relationship between $|\varepsilon_{\mu\tau}|$ and the resulting value of $e^{i\delta_{\mu\tau}}$, in order to keep the effective parameter $\varepsilon_{\mu\tau}$ within its small values range.

The joint neutrino and antineutrino fit shows no significant deviation at the 90% CL limit from the standard oscillation scenario with the one accounting non-standard interactions, and put constraints on the NSI parameters $|\varepsilon_{\mu\tau}|$ and $\delta_{\mu\tau}$. The present work, accounting a neutrino and antineutrino joint fit, yields a limit of $|\varepsilon_{\mu\tau}| \leq 0.086$ (0.085) for a fixed value of $\delta_{\mu\tau} = 0$, and $|\varepsilon_{\mu\tau}| \leq 1.054$ (1.053) for the case where both NSI parameters are fitted, for the normal (inverted) neutrino mass hierarchy, at the 90% CL. In the current sensitivity, all values of $\delta_{\mu\tau}$ are found to be allowed. The 90% CL interval for the standard oscillation parameters are $\Delta m^2_{32} \in [2.379, 2.580]$ and $\sin^2(\theta_{23}) \in [0.420, 0.602]$ for the normal hierarchy scenario, and $\Delta m^2_{32} \in [-2.639, -2.438]$ and $\sin^2(\theta_{23}) \in [0.418, 0.602]$ for the inverted hierarchy scenario. It is expected that the addition of data from the next years will moderately improve the measurements of the NSI parameters of interest. Improvements on sensitivities are possible to occur, specially a comprehensive study on the possible existence of potential sources of systematic uncertainties of special interest for an NSI analysis.

The upcoming experimental search using data from the NOvA Far Detector is a remarkable opportunity to test the open puzzles on neutrino oscillations, specially the mass ordering for neutrinos, as well as look for hints of Physics Beyond the Standard Model and a search for new sources of CP violation on the neutrino sector.

The NOvA collaboration is actively engaged on improvements of event selection criteria, mitigation of systematic uncertainties, MC simulation, analysis software, and many more crucial components for the success and effectiveness of the many analyses, from which the author is grateful for being part of this large team.

Bibliography

[1] Chadwick, J. The intensity distribution in the magnetic spectrum of beta particles from radium (B + C). *Verh. Phys. Gesell.* **16**, 383–391 (1914).

[2] Pauli, W. Dear radioactive ladies and gentlemen. *Phys. Today* **31N9**, 27 (1978).

[3] Chadwick, J. Possible Existence of a Neutron. *Nature* **129**, 312 (1932).

[4] Reines, F. & Cowan, C. L. The neutrino. *Nature* **178**, 446–449 (1956).

[5] Danby, G. *et al.* Observation of High-Energy Neutrino Reactions and the Existence of Two Kinds of Neutrinos. *Phys. Rev. Lett.* **9**, 36–44 (1962).

[6] Kodama, K. *et al.* Final tau-neutrino results from the DONuT experiment. *Phys. Rev. D* **78**, 052002 (2008). 0711.0728.

[7] Bahcall, J. N., Pinsonneault, M. & Basu, S. Solar models: Current epoch and time dependences, neutrinos, and helioseismological properties. *Astrophys. J.* **555**, 990–1012 (2001). astro-ph/0010346.

[8] Davis, R. A review of the Homestake solar neutrino experiment. *Prog. Part. Nucl. Phys.* **32**, 13–32 (1994).

[9] Oyama, Y. Results from Kamiokande-II experiment. *Nucl. Phys. B Proc. Suppl.* **13**, 362–367 (1990).

[10] Boger, J. *et al.* The Sudbury neutrino observatory. *Nucl. Instrum. Meth. A* **449**, 172–207 (2000). nucl-ex/9910016.

[11] Ahmad, Q. *et al.* Direct evidence for neutrino flavor transformation from neutral current interactions in the Sudbury Neutrino Observatory. *Phys. Rev. Lett.* **89**, 011301 (2002). nucl-ex/0204008.

[12] Aker, M. *et al.* Improved Upper Limit on the Neutrino Mass from a Direct Kinematic Method by KATRIN. *Phys. Rev. Lett.* **123**, 221802 (2019). 1909.06048.

[13] Bilenky, S. Neutrino in Standard Model and beyond. *Phys. Part. Nucl.* **46**, 475–496 (2015). 1501.00232.

[14] Mulders, M. & Zanderighi, G. (eds.). *Proceedings, 8th CERN–Latin-American School of High-Energy Physics (CLASHEP2015): Ibarra, Ecuador, March 05-17, 2015*, CERN Yellow Reports: School Proceedings (CERN, Geneva, 2016). 1708.02150.

[15] Goldhaber, M., Grodzins, L. & Sunyar, A. Helicity of Neutrinos. *Phys. Rev.* **109**, 1015–1017 (1958).

[16] Abbiendi, G. *et al.* W+ W- production cross-section and W branching fractions in e+ e- collisions at 189-GeV. *Phys. Lett.* **B493**, 249–265 (2000). hep-ex/0009019.

[17] Giunti, C. & Kim, C. W. *Fundamentals of Neutrino Physics and Astrophysics* (2007).

[18] Coleman, S. J. *A measurement of neutrino oscillations with muon neutrinos in the MINOS experiment.* Ph.D. thesis, College of William and Mary - Arts and Sciences (2011). Available at https://scholarworks.wm.edu/etd/1539623581/.

[19] Pontecorvo, B. Inverse beta processes and nonconservation of lepton charge. *Sov. Phys. JETP* **7**, 172–173 (1958). [Zh. Eksp. Teor. Fiz.34,247(1957)].

[20] Maki, Z., Nakagawa, M. & Sakata, S. Remarks on the unified model of elementary particles. *Prog. Theor. Phys.* **28**, 870–880 (1962). [,34(1962)].

[21] Pontecorvo, B. Neutrino Experiments and the Problem of Conservation of Leptonic Charge. *Sov. Phys. JETP* **26**, 984–988 (1968). [Zh. Eksp. Teor. Fiz.53,1717(1967)].

[22] Harari, H. & Leurer, M. Recommending a Standard Choice of Cabibbo Angles and KM Phases for Any Number of Generations. *Phys. Lett.* **B181**, 123–128 (1986).

[23] Cabibbo, N. Time Reversal Violation in Neutrino Oscillation. *Phys. Lett.* **72B**, 333–335 (1978).

[24] Tanabashi, M. *et al.* Review of particle physics. *Phys. Rev. D* **98**, 030001 (2018 and 2019 update). URL `https://link.aps.org/doi/10.1103/PhysRevD.98.030001`.

[25] Fantini, G., Gallo Rosso, A., Vissani, F. & Zema, V. Introduction to the Formalism of Neutrino Oscillations. *Adv. Ser. Direct. High Energy Phys.* **28**, 37–119 (2018). `1802.05781`.

[26] Denton, P. B. & Parke, S. J. Simple and Precise Factorization of the Jarlskog Invariant for Neutrino Oscillations in Matter. *Phys. Rev.* **D100**, 053004 (2019). `1902.07185`.

[27] Kayser, B. Neutrino Physics as Explored by Flavor Change (New) (2002).

[28] An, F. P. *et al.* Observation of electron-antineutrino disappearance at Daya Bay. *Phys. Rev. Lett.* **108**, 171803 (2012). `1203.1669`.

[29] Abe, Y. *et al.* Indication of Reactor $\bar{\nu}_e$ Disappearance in the Double Chooz Experiment. *Phys. Rev. Lett.* **108**, 131801 (2012). `1112.6353`.

[30] Ahn, J. K. *et al.* Observation of Reactor Electron Antineutrino Disappearance in the RENO Experiment. *Phys. Rev. Lett.* **108**, 191802 (2012). `1204.0626`.

[31] Adamson, P. *et al.* First measurement of electron neutrino appearance in NOvA. *Phys. Rev. Lett.* **116**, 151806 (2016). `1601.05022`.

[32] Wolfenstein, L. Neutrino Oscillations in Matter. *Phys. Rev.* **D17**, 2369–2374 (1978). [,294(1977)].

[33] Linder, J. Derivation of neutrino matter potentials induced by earth. *Submitted to: Am. J. Phys.* (2005). `hep-ph/0504264`.

[34] Bilenky, S. M., Giunti, C. & Grimus, W. Phenomenology of neutrino oscillations. *Prog. Part. Nucl. Phys.* **43**, 1–86 (1999). `hep-ph/9812360`.

[35] Sci., R. S. A. Scientific Background on the Nobel Prize in Physics 2015: Neutrino oscillations. *The Universe* **3**, 38–50 (2015).

[36] Cervera, A. *et al.* Golden measurements at a neutrino factory. *Nucl. Phys. B* **579**, 17–55 (2000). [Erratum: Nucl.Phys.B 593, 731–732 (2001)], `hep-ph/0002108`.

[37] Freund, M. Analytic approximations for three neutrino oscillation parameters and probabilities in matter. *Phys. Rev. D* **64**, 053003 (2001). `hep-ph/0103300`.

[38] Akhmedov, E. K., Johansson, R., Lindner, M., Ohlsson, T. & Schwetz, T. Series expansions for three flavor neutrino oscillation probabilities in matter. *JHEP* **04**, 078 (2004). hep-ph/0402175.

[39] Esteban, I., Gonzalez-Garcia, M. C., Hernandez-Cabezudo, A., Maltoni, M. & Schwetz, T. Global analysis of three-flavour neutrino oscillations: synergies and tensions in the determination of $\theta_2 3, \delta_C P$, and the mass ordering. *JHEP* **01**, 106 (2019). URL http://www.nu-fit.org/. 1811.05487.

[40] Choubey, S., Dutta, D. & Pramanik, D. Invisible neutrino decay in the light of NOvA and T2K data. *JHEP* **08**, 141 (2018). 1805.01848.

[41] Gomes, A. L. G. *Decoerência quântica em neutrinos de aceleradores*. Ph.D. thesis, Federal University of Goias (2019). Available at http://repositorio.bc.ufg.br/tede/handle/tede/9518.

[42] Adamson, P. *et al.* Search for active-sterile neutrino mixing using neutral-current interactions in NOvA. *Phys. Rev.* **D96**, 072006 (2017). 1706.04592.

[43] Roulet, E. MSW effect with flavor changing neutrino interactions. *Phys. Rev.* **D44**, R935–R938 (1991). [,365(1991)].

[44] Guzzo, M. M., Masiero, A. & Petcov, S. T. On the MSW effect with massless neutrinos and no mixing in the vacuum. *Phys. Lett.* **B260**, 154–160 (1991). [,369(1991)].

[45] Bhupal Dev, P. S. *et al.* Neutrino Non-Standard Interactions: A Status Report. In *NTN Workshop on Neutrino Non-Standard Interactions St Louis, MO, USA, May 29-31, 2019* (2019). URL http://lss.fnal.gov/archive/2019/conf/fermilab-conf-19-299-t.pdf. 1907.00991.

[46] Esteban, I., Gonzalez-Garcia, M. C., Maltoni, M., Martinez-Soler, I. & Salvado, J. Updated Constraints on Non-Standard Interactions from Global Analysis of Oscillation Data. *JHEP* **08**, 180 (2018). 1805.04530.

[47] Ohlsson, T. Status of non-standard neutrino interactions. *Rept. Prog. Phys.* **76**, 044201 (2013). 1209.2710.

[48] Blennow, M. & Ohlsson, T. Approximative two-flavor framework for neutrino oscillations with non-standard interactions. *Phys. Rev.* **D78**, 093002 (2008). 0805.2301.

[49] Bifani, S., Descotes-Genon, S., Romero Vidal, A. & Schune, M.-H. Review of Lepton Universality tests in B decays. *J. Phys.* **G46**, 023001 (2019). 1809.06229.

[50] Ohlsson, T. Phenomenology of non-standard neutrino interactions (2009). URL https://www.mpi-hd.mpg.de/lin/seminar_theory/talks/ohlsson.pdf. Particle and Astroparticle Theory Seminar. MPIK, Heidelberg, Germany.

[51] Mitsuka, G. *et al.* Study of Non-Standard Neutrino Interactions with Atmospheric Neutrino Data in Super-Kamiokande I and II. *Phys. Rev.* **D84**, 113008 (2011). 1109.1889.

[52] Aartsen, M. G. *et al.* Search for Nonstandard Neutrino Interactions with IceCube DeepCore. *Phys. Rev.* **D97**, 072009 (2018). 1709.07079.

[53] Salvado, J., Mena, O., Palomares-Ruiz, S. & Rius, N. Non-standard interactions with high-energy atmospheric neutrinos at IceCube. *JHEP* **01**, 141 (2017). 1609.03450.

[54] Adamson, P. *et al.* Search for flavor-changing non-standard neutrino interactions by MINOS. *Phys. Rev.* **D88**, 072011 (2013). 1303.5314.

[55] Adamson, P. *et al.* Search for flavor-changing nonstandard neutrino interactions using ν_e appearance in MINOS. *Phys. Rev.* **D95**, 012005 (2017). 1605.06169.

[56] Ayres, D. S. *et al.* NOvA: Proposal to Build a 30 Kiloton Off-Axis Detector to Study $\nu_\mu \to \nu_e$ Oscillations in the NuMI Beamline (2004). hep-ex/0503053.

[57] Ambats, I. *et al.* The MINOS Detectors Technical Design Report (1998).

[58] Abe, K. *et al.* The T2K Experiment. *Nucl. Instrum. Meth.* **A659**, 106–135 (2011). 1106.1238.

[59] Suter, L. Numi off-axis electron neutrino appearance (2015). URL http://nova-docdb.fnal.gov/cgi-bin/RetrieveFile?docid=13469&filename=nova_suter.pdf&version=8. Talk at the 48th Annual Fermilab Users Meeting.

[60] Department, A. D. O. *Concepts Rookie Book* (2013).

[61] Numi technical design handbook. Tech. Rep. (2002). URL https://www-numi.fnal.gov/numwork/tdh/tdh_index.html. Available at https://www-numi.fnal.gov/numwork/tdh/tdh_index.html.

[62] Adamson, P. *et al.* The NuMI Neutrino Beam. *Nucl. Instrum. Meth.* **A806**, 279–306 (2016). 1507.06690.

[63] Acero, M. A. *et al.* First measurement of neutrino oscillation parameters using neutrinos and antineutrinos by NOvA (2019). 1906.04907.

[64] Norman, A. J. Nova: The numi offaxis ve appearance experiment (2009). URL http://nova-docdb.fnal.gov/cgi-bin/ShowDocument?docid=4117. Talk for neutrinos parallel session at DPF 2009. Available at http://nova-docdb.fnal.gov/cgi-bin/ShowDocument?docid=4117.

[65] Ayres, D. S. *et al.* The NOvA Technical Design Report (2007).

[66] Mufson, S. *et al.* Liquid scintillator production for the NOvA experiment. *Nucl. Instrum. Meth. A* **799**, 1–9 (2015). 1504.04035.

[67] Tognini, S. C. *Observation of multiple-muon seasonal variations in the NOvA Near Detector.* Ph.D. thesis, Federal University Of Goias (2018). Available at https://lss.fnal.gov/archive/thesis/2000/fermilab-thesis-2018-13.pdf.

[68] Psihas, F. Event displays for nue selected events - blessing package (2016). NOvA Internal Document 15647.

[69] Agostinelli, S. *et al.* GEANT4: A Simulation toolkit. *Nucl. Instrum. Meth. A* **506**, 250–303 (2003).

[70] Andreopoulos, C. *et al.* The GENIE Neutrino Monte Carlo Generator. *Nucl. Instrum. Meth. A* **614**, 87–104 (2010). 0905.2517.

[71] Bassin, C., Laske, G. & Masters, G. The current limits of resolution for surface wave tomography in north america. eos trans agu 81:f897. *Eos* **81**, F897 (2000).

[72] Patrignani, C. *et al.* Review of Particle Physics. *Chin. Phys.* **C40**, 100001 (2016).

[73] Baker, S. & Cousins, R. D. Clarification of the Use of Chi Square and Likelihood Functions in Fits to Histograms. *Nucl. Instrum. Meth.* **221**, 437–442 (1984).

[74] Acero, M. A. *et al.* New constraints on oscillation parameters from ν_e appearance and ν_μ disappearance in the NOvA experiment. *Phys. Rev.* **D98**, 032012 (2018). 1806.00096.

[75] Baird, M., Suter, L. & Wolcott, J. Summary of the 2020 fhc+rhc 3-flavor oscillation analysis - technote (2020). NOvA Internal Document 44422.

[76] Taylor, J. R. *An Introduction to Error Analysis* (University Science Books, 1997), 2nd edn. The study of uncertainties in physical measurements.

APPENDIX A – The χ^2 distribution and confidence intervals

The χ^2 distribution is widely used in inferential analyses, which allows one to quantitatively test the compatibility of an observed phenomenon with an expected behavior given a model of interest within a given confidence interval.

Suppose a quantity x that follows a distribution $f(x)$. The probability [76] to measure a certain value of x in the interval $[a, b]$ is given by

$$P = \int_a^b f(x)\, dx. \tag{A.1}$$

As an illustration, if one assume a Gaussian $G_{x,\sigma}(x)$ distribution, for example, Eq. $(A.1)$ can be written as

$$P(\pm 1\sigma) = \frac{1}{\sigma\sqrt{2\pi}} \int_{X-\sigma}^{X+\sigma} e^{-\frac{(x-X)^2}{2\sigma^2}}\, dx, \tag{A.2}$$

which now tells us the probability that our measurement of the quantity x will fall within the 1 standard deviation $(\pm 1\sigma)$ from the true value X, as also illustrated in Fig. 43.

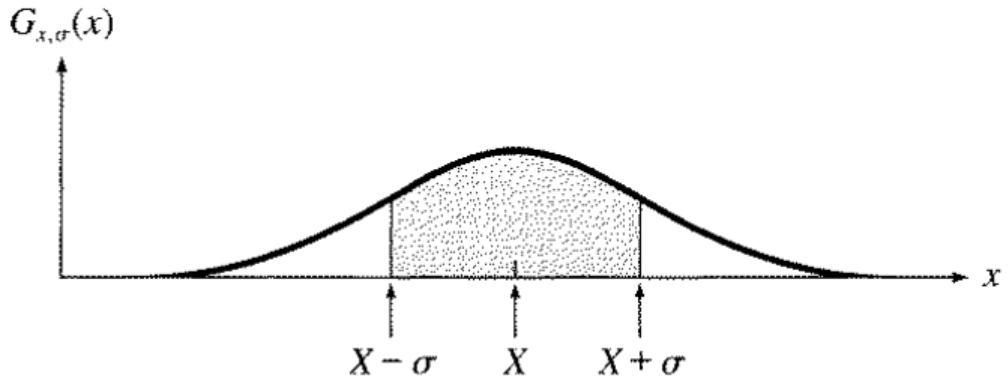

Figure 43 – Representation of the probability of a measurement to fall within the $\pm 1\sigma$ interval from the true value X [76].

We can take the substitution $\frac{(x-X)}{\sigma} = z$, hence $dx = \sigma dz$, and the limits of integration will be $z = \pm 1$, allowing to write Eq. $(A.2)$ now as

$$P(\pm 1\sigma) = \frac{1}{\sqrt{2\pi}} \int_{-1}^{+1} e^{-\frac{z^2}{2}} dz. \tag{A.3}$$

In general, one can obtain the probability for a measurement to fall within any arbitrary t standard deviations $(\pm t\sigma)$. Then, we simply write

$$P(\pm t\sigma) = \frac{1}{\sqrt{2\pi}} \int_{-t}^{+t} e^{-\frac{z^2}{2}} dz, \tag{A.4}$$

also illustrated in Fig. 44.

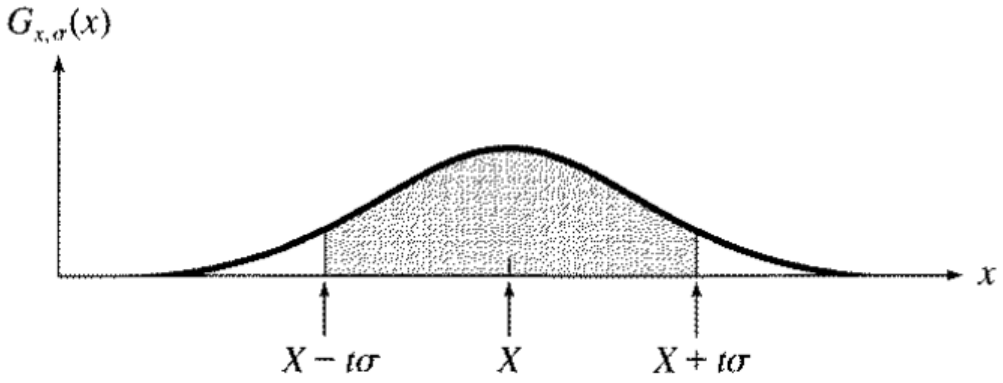

Figure 44 – Representation of the probability of a measurement to fall within the $\pm t\sigma$ interval from the true value X [76].

The shaded area can be quantitatively translated in terms of percentage for the measurement of the quantity x to fall within t standard deviations from the true value $x = X$. For example, a $\pm 1\sigma$ interval corresponds to a chance of 68%, and as the confidence interval t grows, the probability grows as well, as shown in Fig. 45.

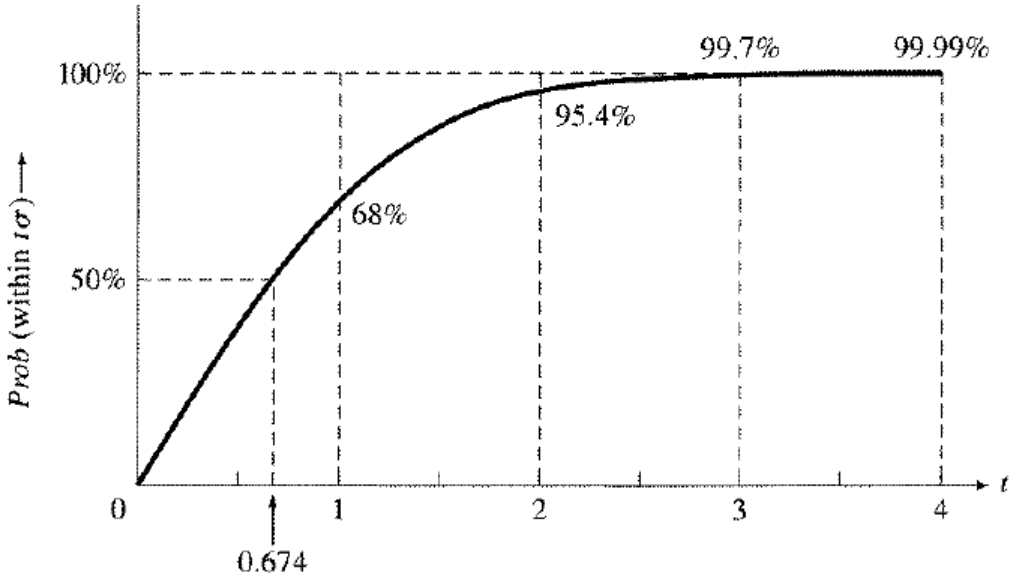

t	0	0.25	0.5	0.75	1.0	1.25	1.5	1.75	2.0	2.5	3.0	3.5	4.0
Prob (%)	0	20	38	55	68	79	87	92	95.4	98.8	99.7	99.95	99.99

Figure 45 – Probability that a measurement x will fall within the interval $\pm t\sigma$ from the true value $x = X$ [76].

For a χ^2 distribution approximately following a Gaussian distribution, we then obtain information about the confidence interval (Confidence Level) by computing the $\Delta\chi^2 = \chi^2\left(\vec{\theta}\right) - \chi^2\left(\vec{\theta}_{\text{best}}\right)$, defined in Eq. (5.5), where the range of $\Delta\chi^2$ can be interpreted as how a certain value of the parameter $\vec{\theta}$ deviates from the best fit $\vec{\theta}_{\text{best}}$. The value for which a $\Delta\chi^2$ will correspond to a certain CL is dependable on the number d of parameters being investigated. For example, for 1D profiles as shown in Subsection 6.2.1 we obtained a 90% CL for the allowed interval of our parameters at a $\Delta\chi^2 = 2.71$, whereas for a 90% CL interval for 2 parameters, as shown in Subsection 6.2.2, results were obtained at $\Delta\chi^2 = 4.61$. Additionally, for the case of 1 parameter, the corresponding interval in terms of

standard deviation can be obtained by $t\sigma = \sqrt{\Delta\chi^2}\,\sigma$. A few values of interest for $\Delta\chi^2$ and the corresponding confidence interval is shown in Table 10.

CL (%)	$\Delta\chi^2$ $(t\sigma)^*$		
	$d = 1$	$d = 2$	$d = 3$
68.27	1.00 (1.00σ)	2.30	3.53
90.00	2.71 (1.65σ)	4.61	6.25
95.00	3.84 (1.96σ)	5.99	7.82
95.45	4.00 (2.00σ)	6.18	8.03
99.00	6.63 (2.57σ)	9.21	11.34
99.73	9.00 (3.00σ)	11.83	14.16

Table 10 – Values of $\Delta\chi^2$ corresponding to a certain CL for d parameters [24]. *For 1D ($d = 1$) only.

APPENDIX B – Supporting Studies

As our studies advanced, many verifications and cross-checks were needed in order to establish a conclusion and a solid understanding of the observed effects. Among a few examples are how our 1D projections and surfaces are affected under certain assumptions, or even how our parameterization is compared to a different choice. In this appendix we expose a series of information that serves as verifications and support for the results presented in Chapter 6.

B.1 Equivalence of parameterizations

We have adopted the most general parameterization for the NSI model, where we take it to be complex, as defined on Eq. (3.7), where for our analysis $\varepsilon_{\mu\tau} = |\varepsilon_{\mu\tau}|\, e^{i\delta_{\mu\tau}}$. This introduce the possibility to look for both $|\varepsilon_{\mu\tau}|$ and $\delta_{\mu\tau}$. On the other hand, some experiments [54] have considered the NSI parameters to be real valued. We proceed to an investigation of the equivalence of a general, complex, parameterization against the assumption of real valued parameters. In order to do so, we compare in the $\sin^2(\theta_{23}) \times \Delta m^2_{32}$ parameter space the contours for the case where we fit for $|\varepsilon_{\mu\tau}|$ and $\delta_{\mu\tau}$, and when we account the effective NSI parameter to be real valued, denoted by $\varepsilon_{\mu\tau}$. In order to investigate the relation between both parameterizations, we take the following intervals:

- $|\varepsilon_{\mu\tau}| \leq 0.25$ and $\delta_{\mu\tau} \in [0, 2\pi]$, for the complex scenario,
- $-0.25 \leq \varepsilon_{\mu\tau} \leq 0.25$, for the real valued scenario.

The comparison between both choices and the standard case is presented in Fig 46. There is a clear equivalence between the two different parameterizations. Taking the NSI parameters to be complex and fit for both the norm and the phase is equivalent to account a real parameter allowed to have negative and positive values. As observed on Eq. (2.30), the ν_μ disappearance analysis is only sensitive to the real part of the oscillation parameters, since we make use of the survival probability in order to do so. On the complex parameterization, the phase $\delta_{\mu\tau}$ has values in the range of $[0\,,2\pi]$, such that $\Re\left(e^{i\delta_{\mu\tau}}\right) = \cos(\delta_{\mu\tau}) \in [-1, 1]$, which is a multiplicative factor on $|\varepsilon_{\mu\tau}|$. On a real valued parameterization, the NSI parameter $\varepsilon_{\mu\tau}$ behaves such that the multiplicative dependence from the phase $\delta_{\mu\tau}$ would be implicit. The complex parameterization was adopted in our analysis, motivated by the possibility of investigation of both $|\varepsilon_{\mu\tau}|$ and $\delta_{\mu\tau}$.

If for instance our choice was to look for the effective NSI parameter $\varepsilon_{\mu\tau}$, the 1D profiles for this parameter using a joint FHC + RHC fit is shown in Fig. 47. In this scenario, our present sensitivity yelds a constraint of $-0.089 \leq \varepsilon_{\mu\tau} \leq 0.088$ for the normal hierarchy scenario, and $-0.088 \leq \varepsilon_{\mu\tau} \leq 0.088$ for the inverted hierarchy scenario, at 90% CL.

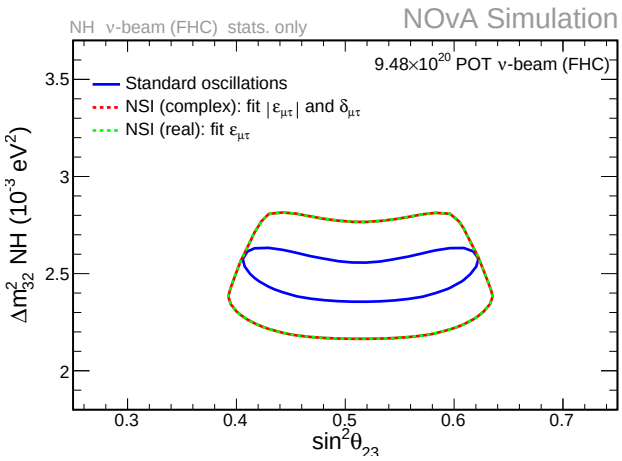

(a) Neutrino (FHC) beam

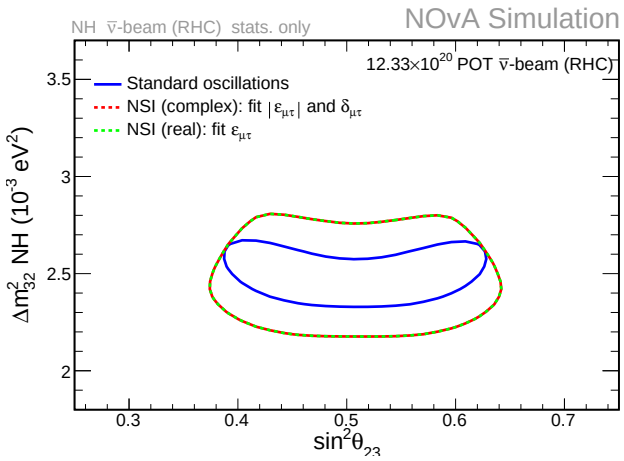

(b) Antineutrino (RHC) beam

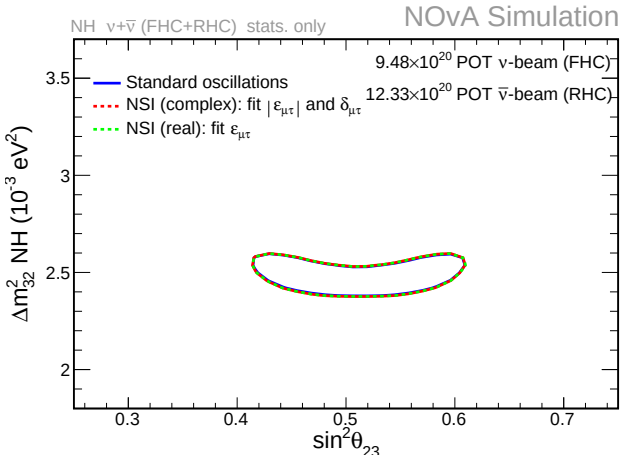

(c) FHC + RHC

Figure 46 – Comparison between different choices for the NSI parameterization for neutrino beam (a), antineutrino beam (b), and the joint analysis (c). In solid blue is shown the standard scenario, where no NSI effects are included. In dashed red we take the parameterization to be complex and fit for both $|\varepsilon_{\mu\tau}|$ and $\delta_{\mu\tau}$, while in dashed green we show the case where the NSI parameterization is taken to be real and expressed in terms of a real valued $\varepsilon_{\mu\tau}$.

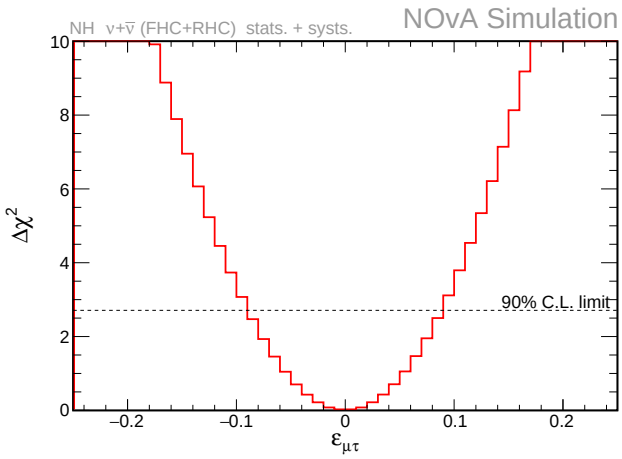

(a) FHC + RHC - NH

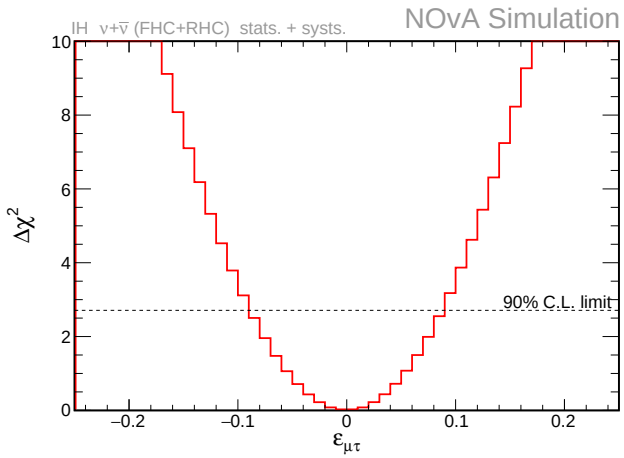

(b) FHC + RHC - NH

Figure 47 – $\Delta\chi^2$ values as function of the effective NSI parameter $\varepsilon_{\mu\tau}$ for Normal Hierarchy (a) and Inverted Hierarchy (b) neutrino mass ordering scenarios, the joint neutrino and antineutrino fit. The horizontal dashed line marks the 90% CL interval for the investigated parameter.

B.2 Inclusion of other standard oscillation parameters on the fit

On Section 5.3 we stated that only Δm^2_{32}, $\sin^2(\theta_{23})$, $|\varepsilon_{\mu\tau}|$, and $\delta_{\mu\tau}$, would be allowed for the fitter to pick. The remaining oscillation parameters were treated as constant and not included in the fit. We show in this section how the inclusion of the solar and reactor parameters Δm^2_{21}, $\sin^2(\theta_{12})$, $\sin^2(\theta_{13})$, and δ_{CP}, would affect our sensitivity studies. Fig. 48 shows a comparison of the contours for the standard case, and with $|\varepsilon_{\mu\tau}|$, presented in 6.2.2.1 against the case where the reactor and solar parameters are included in the fit as well.

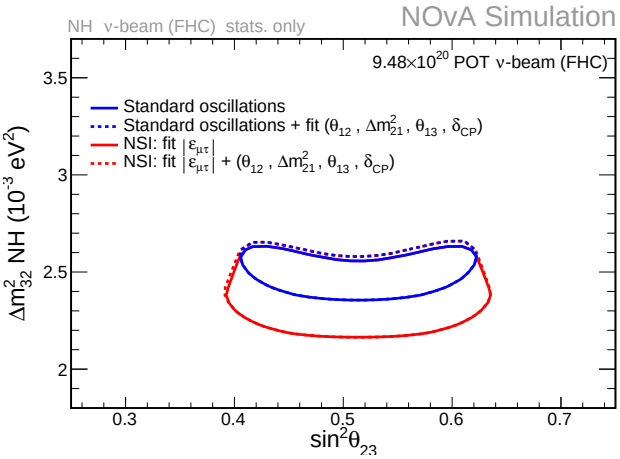

(a) Neutrino (FHC) beam

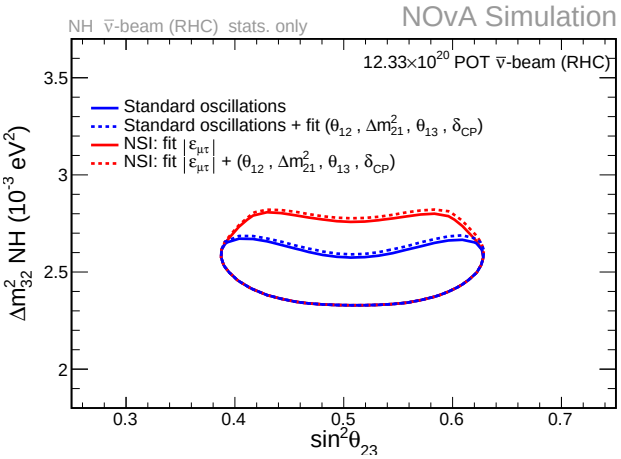

(b) Antineutrino (RHC) beam

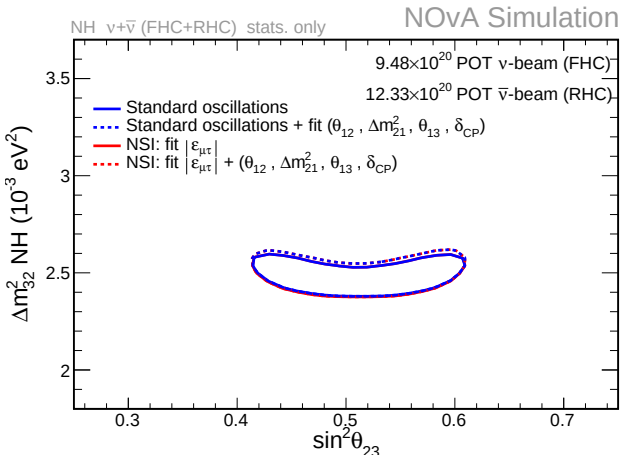

(c) FHC + RHC

Figure 48 – Effects of including the solar and reactor parameters in the fit for neutrino beam (a), antineutrino beam (b), and the joint analysis (c). In solid lines is shown the scenario where Δm^2_{21}, $\sin^2(\theta_{12})$, $\sin^2(\theta_{13})$, and δ_{CP}, are kept fixed to the values presented in Table 4, while in the dashed lines we show the case where we also fit for these parameters.

On both the contours for the standard case (solid blue line) and for when we also fit for $|\varepsilon_{\mu\tau}|$ (solid red line), the addition of the other standard oscillation parameters is seen to have an almost null effect (dashed lines) for this analysis, for both FHC, RHC, and FHC + RHC, which can then be neglected and treated as constant.

B.3 Effect of $|\varepsilon_{\mu\tau}|$

Motivated by the predictions shown in Fig. 30, we have constrained the NSI parameter $|\varepsilon_{\mu\tau}|$ to have a maximum value of 0.25 on most cases while being fitted. in Fig. 49 we show how the contours for the $\sin^2(\theta_{23}) \times \Delta m^2_{32}$ parameter space are affected according to the interval that we allow $|\varepsilon_{\mu\tau}|$ to range.

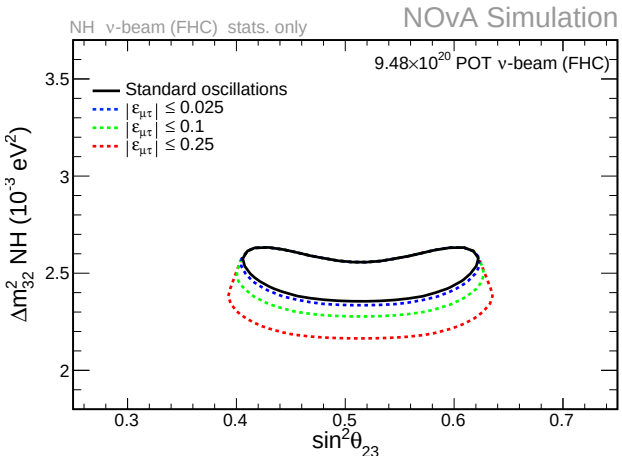

(a) Neutrino (FHC) beam

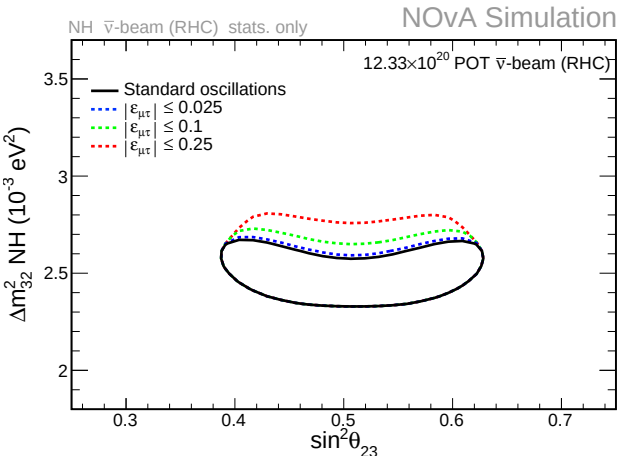

(b) Antineutrino (RHC) beam

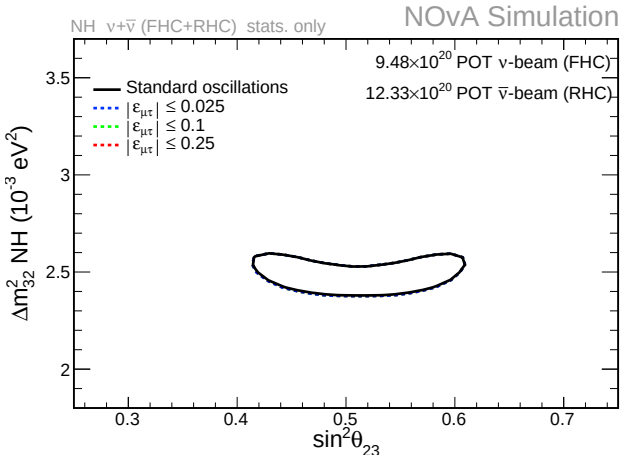

(c) FHC + RHC

Figure 49 – Comparison between different allowed ranges in the fit for the NSI parameter $|\varepsilon_{\mu\tau}|$ for neutrino beam (a), antineutrino beam (b), and the joint analysis (c). In solid black is shown the standard case, while in the dashed lines is shown the NSI scenario with $|\varepsilon_{\mu\tau}|$ allowed to have a maximum value of 0.025 (blue), 0.1 (green) and 0.25 (red).

It is visible that for both FHC and RHC modes, the expansion of the allowed parameter space is scalable to the maximum value we allow $|\varepsilon_{\mu\tau}|$ to have. The joint FHC + RHC fit shows no deviation from the standard case, regardless of the constraint chosen for $|\varepsilon_{\mu\tau}|$, therefore showing no loss of generality on the interval chosen for the results presented in Chapter 6.

B.4 Effect of $\delta_{\mu\tau}$

The phase $\delta_{\mu\tau}$ was treated unconstrained and with values allowed to float in the range of $[0\,,2\pi]$. When not included in the fit, it was treated as constant with the same value used for oscillating the simulated data, $\delta_{\mu\tau} = 0$, reflecting in the behavior observed in Fig. 36. In order to understand what our contours would be for a given value of $\delta_{\mu\tau}$ as it is being fitted, we investigate how different values of $\delta_{\mu\tau}$ affect the $\sin^2(\theta_{23}) \times \Delta m^2_{32}$ parameter space. We fix $\delta_{\mu\tau}$ to certain values of interest, and proceed to a fit in the other 3 free parameters, but not on $\delta_{\mu\tau}$. Fig 50 shows a comparison between each case.

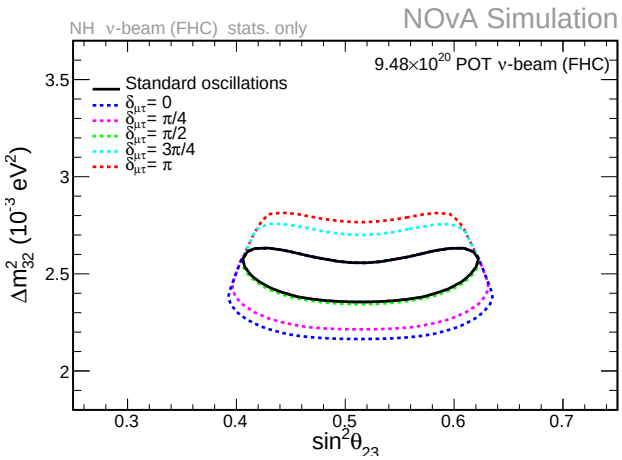

(a) Neutrino (FHC) beam

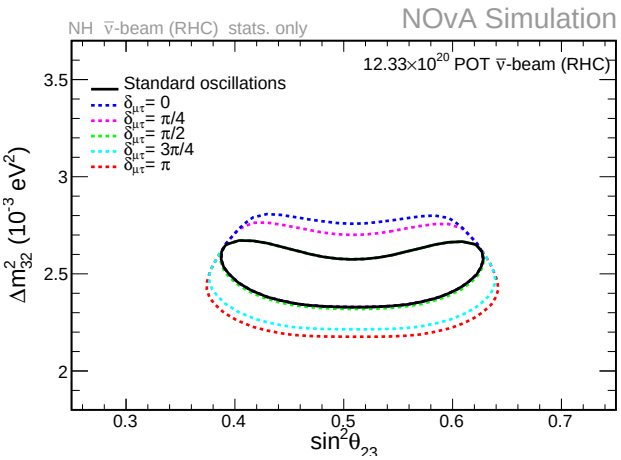

(b) Antineutrino (RHC) beam

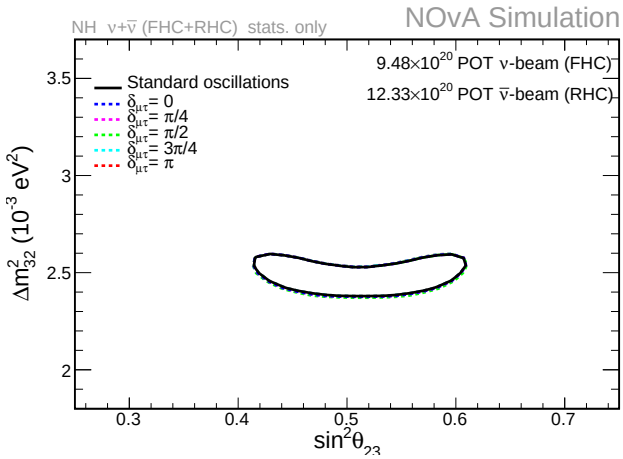

(c) FHC + RHC

Figure 50 – Comparison between different initial values of $\delta_{\mu\tau}$ for oscillating the simulated data for an allowed range of $|\varepsilon_{\mu\tau}| \leq 0.25$ for neutrino beam (a), antineutrino beam (b), and the joint analysis (c). In solid black is shown the standard case, while the dashed lines correspond to a fixed value of $\delta_{\mu\tau} = 0$ (blue), $\delta_{\mu\tau} = \frac{\pi}{4}$ (magenta), $\delta_{\mu\tau} = \frac{\pi}{2}$ (green), $\delta_{\mu\tau} = \frac{3\pi}{4}$ (cyan), and $\delta_{\mu\tau} = \pi$ (red).

For FHC mode, at $\delta_{\mu\tau} = 0$ we have the same scenario as observed in Fig. 36. As $\delta_{\mu\tau}$ increases, the contour change until it approaches the standard case for $\delta_{\mu\tau} = \frac{\pi}{2}$, a behavior seen on the probabilities shown in Fig. 25 and the predictions shown in Fig. 31, until it reaches its maximum opposite effect for $\delta_{\mu\tau} = \pi$. The same is observed for the RHC mode, but now having the opposite way. The joint FHC + RHC fit shows no major deviations from the standard case at 90% CL, regardless of the value of $\delta_{\mu\tau}$.

B.5 1D profile $\delta_{\mu\tau}$

While inspecting the 1D projections for the NSI phase $\delta_{\mu\tau}$, shown in 6.2.1.4, we observe no sensitivity in the way this study was conducted. As argumented, when we do not profile for $|\varepsilon_{\mu\tau}|$ the analysis proceed with the initial input of $|\varepsilon_{\mu\tau}| = 0$, hence every possible value of $\delta_{\mu\tau}$ will match the simulated data. This happens because, as we mentioned in 6.1, for sensitivity studies both the simulated data and the predictions are computed with the same set of parameters, as observed in Fig. 30 and 31. In order to understand how our sensitivity for $\delta_{\mu\tau}$ is dependable on the initial value of $|\varepsilon_{\mu\tau}|$ for predictions, we proceed with a test where we compute the simulated data at the same parameters used for this analysis, given in Table 4, however using a different general and arbitrary value of $|\varepsilon_{\mu\tau}| = 0.1$ for prediction. This allow us to inspect how a fixed value of $|\varepsilon_{\mu\tau}| \neq 0$ affect the knowledge of $\delta_{\mu\tau}$, as well as understand if this also has an impact when we fit for both parameters. Fig 51 show the $\Delta\chi^2$ values as function of $\delta_{\mu\tau}$ under this scenario.

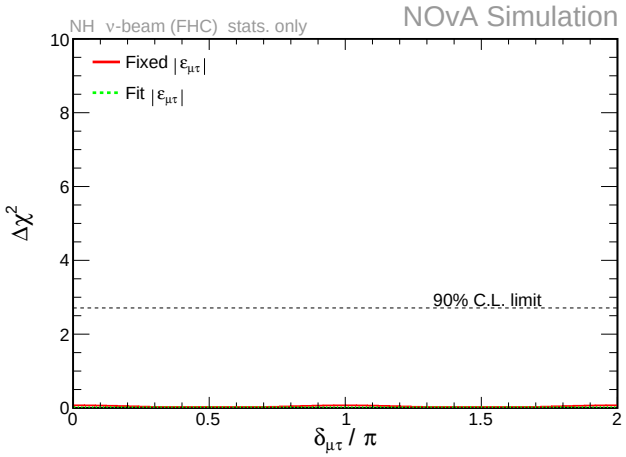

(a) Neutrino (FHC) beam

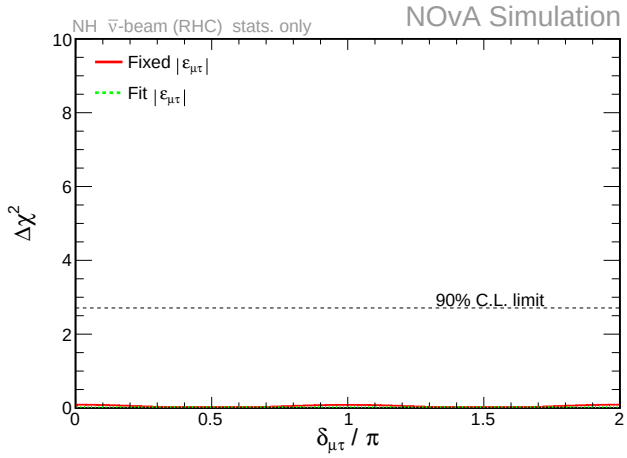

(b) Antineutrino (RHC) beam

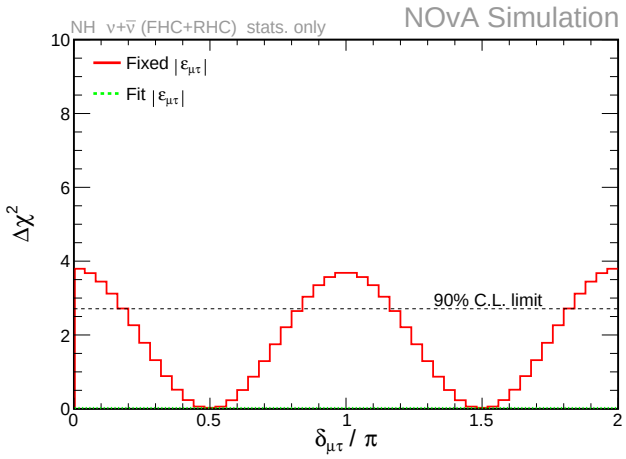

(c) FHC + RHC

Figure 51 – $\Delta\chi^2$ values as function of $\delta_{\mu\tau}$ for neutrino beam (a), antineutrino beam (b), and the joint analysis (c) for simulated data oscillated with a non-zero $|\varepsilon_{\mu\tau}| = 0.1$. In solid red is shown the case where $|\varepsilon_{\mu\tau}|$ is not included in the fit, thus fixed at the initial value, while in dashed green is shown for when we include $|\varepsilon_{\mu\tau}|$ in fit as well.

We see that the ν_μ ($\bar{\nu}_\mu$) disappearance channel is indeed sensitive to $\delta_{\mu\tau}$. By assuming a prediction with a fixed non-zero $|\varepsilon_{\mu\tau}|$ we happen to observe the allowed values for $\delta_{\mu\tau}$ (solid red line). However if we proceed with a

simultaneous fit for both $|\varepsilon_{\mu\tau}|$ and $\delta_{\mu\tau}$ we again see no sensitivity under this procedure (dashed green line), as in the case discussed in subsection 6.2.1.4. Under this test, for example, we observe a preference for values of $\delta_{\mu\tau}$ around $\frac{\pi}{2}$ and $\frac{3\pi}{2}$, while we reject values of 0, π, and 2π, at the 90% CL limit. While our first NSI analysis is likely to proceed with the current procedure of simultaneously fitting for $|\varepsilon_{\mu\tau}|$ and $\delta_{\mu\tau}$, the choice for predictions using the values presented in Table 4 remains valid without loss of generality. As the first upcoming NSI analysis from NOvA will result in a best fit for the NSI parameters, these experimental results could be applied as inputs for predictions for a second future NSI analysis, and the scenario discussed in Fig. 51 could be tested.

B.6 Comparison to MINOS results

We have shown in Table 2 the results obtained by a couple of experiments regarding investigations on NSI. As mentioned before, the NSI model adopted by the Super-Kamiokande and IceCube experiments accounts only interactions with down quarks, thus not directly comparable to the model used in our analysis. The model adopted by the MINOS experiment in its NSI analysis using ν_μ and $\bar{\nu}_\mu$ disappearance data makes use of a real valued NSI parameterization in a 2 flavor neutrino oscillations framework. Although our analysis accounts oscillations between the 3 neutrino flavors, it is possible for us to have a comparison of our sensitivities with the MINOS results presented in Ref. [54]. As demonstrated in Appendix B.1, there is an equivalence between the complex parameterization while fitting for $|\varepsilon_{\mu\tau}|$ and $\delta_{\mu\tau}$, which is the choice used in our analysis, and the real valued parameterization, used by MINOS. We proceed to a fit using a real valued parameterization for $\varepsilon_{\mu\tau}$ on the same parameter spaces investigated by MINOS, for the exposure used in our analysis, and compare against the official results presented in Ref. [54] by the MINOS collaboration. Fig. 52 shows our sensitivities compared to the experimental results from MINOS. It should be noted that, because the results obtained by MINOS were performed under a 2 neutrino flavor framework, the analysis was presented in terms of a mixing angle θ and the parameter $|\Delta m^2|$. However, as the analysis investigated muon neutrinos and antineutrinos, we know that a 2 flavor approximation for this sector is sensitive to the parameters θ_{23} and Δm^2_{32}, thus the comparison remains valid without loss of generality. Note also that we performed a fit for $\sin^2(2\theta_{23})$ in order for the results to be comparable. With respect to the standard oscillation parameters $\sin^2(2\theta_{23})$ and Δm^2_{32}, NOvA has an expressive higher precision, once this experiment was designed to make precision measurements of the mentioned parameters being investigated. Regarding the NSI parameter $\varepsilon_{\mu\tau}$, NOvA also shows a good potential for placement of constraints, although a minor tension is seen in Fig. 52 (a). Still, no major disagreements is seen between our sensitivities and previous experimental results from the MINOS collaboration.

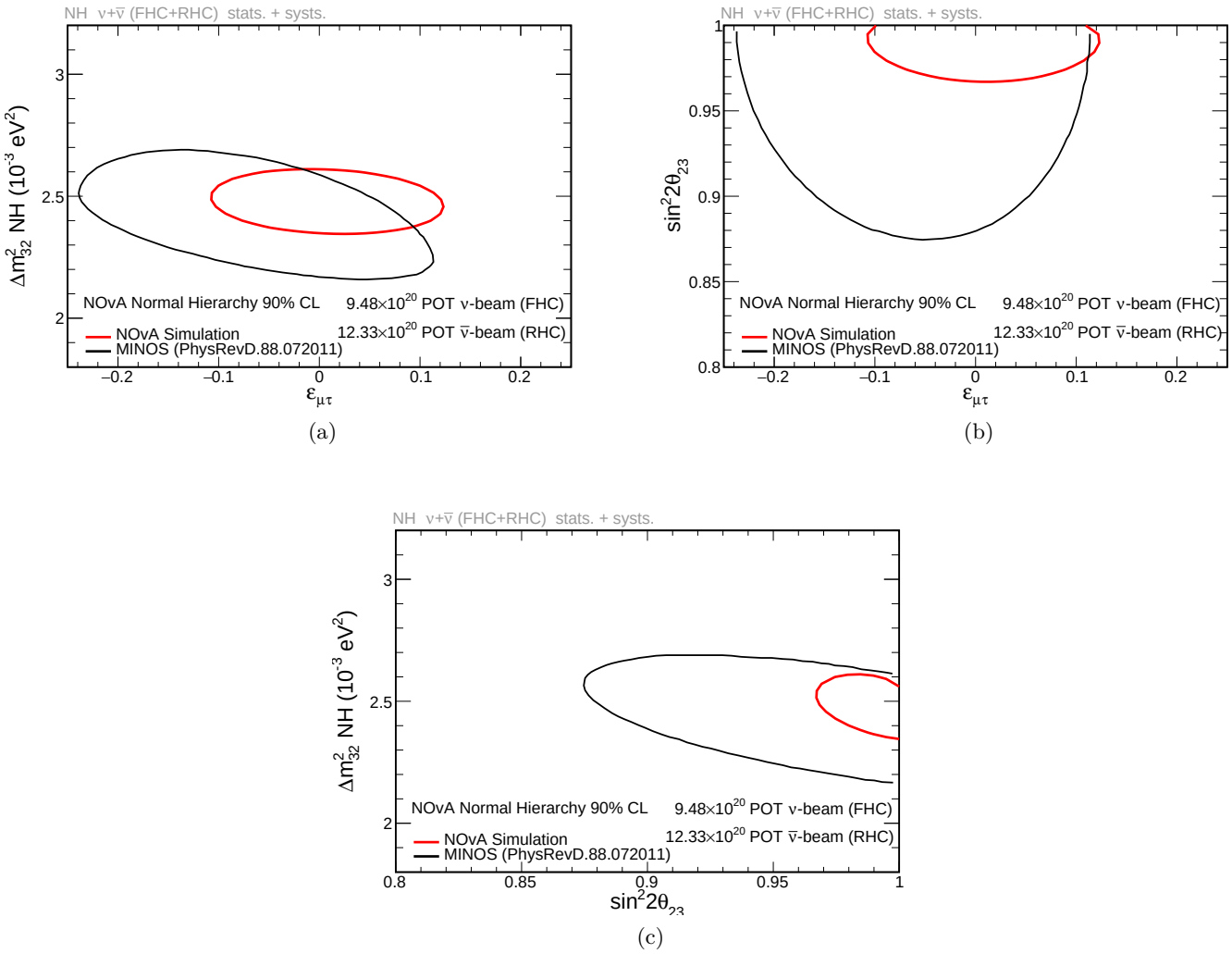

Figure 52 – NOvA's 90% CL NSI sensitivity in comparison to results from MINOS [54].

B.7 Addressing the mass hierarchy and CP-violation in the NSI model

By introducing new parameters arising from the NSI model, we may encounter degenerate scenarios, as well as opportunities to address some of the open puzzles on the neutrino oscillation phenomenon, such as the mass hierarchy for the mass of neutrinos, and also investigations on the new NSI CP-violating phases. Aiming to investigate the possible differences between each scenario, we proceed to a series of pedagogical plots showing information for a given combination of parameters. The overall strategy is as follows:

1. compute the survival (transition) probability for a given set of oscillation parameters, for both neutrinos and antineutrinos,
2. select a point of interest, at $E = 2\,\text{GeV}$, and collect the corresponding value for the probability,
3. for the specific value of interest, we insert in a plot called *biprobability*, which allows a comparison of differences between the behavior for neutrinos and antineutrinos, under different scenarios of choice.

In Fig. 53 we show the survival probabilities for neutrinos and antineutrinos under different values of interest for the NSI phase $\delta_{\mu\tau} = \left(0, \frac{\pi}{2}, \pi, \frac{3\pi}{2}\right)$, for both Normal Hierarchy and Inverted Hierarchy, for the set of oscillation parameters indicated in the plots.

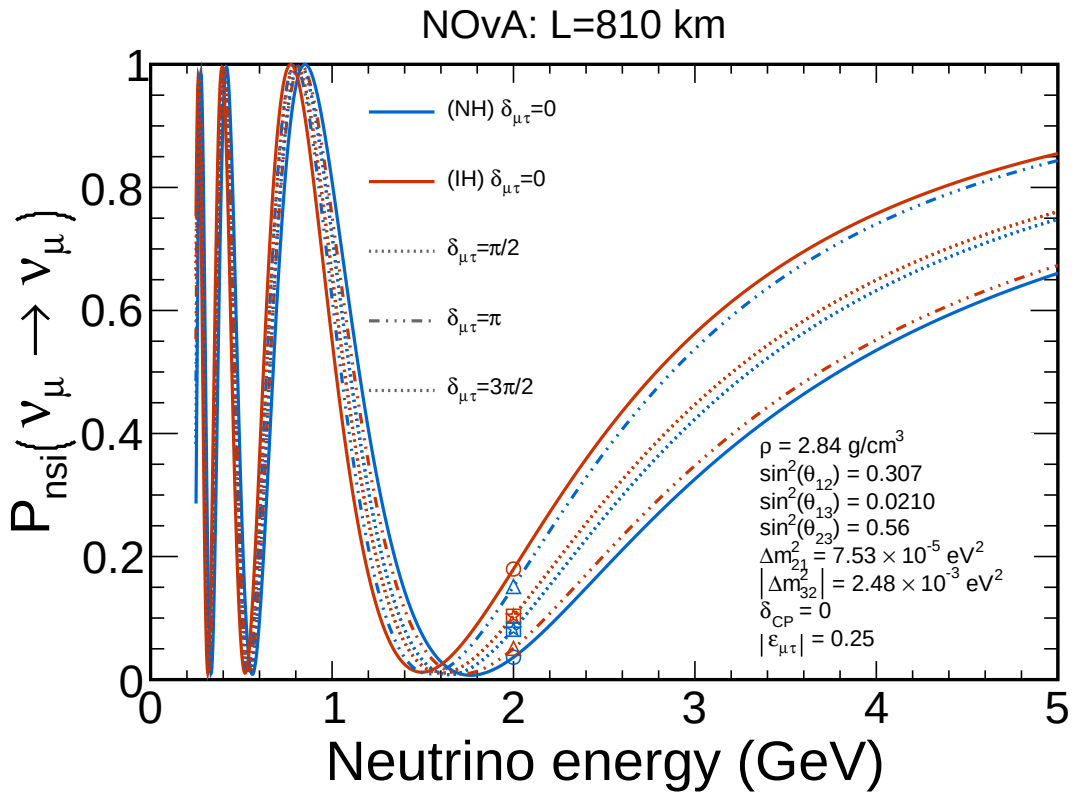

(a) $\nu_\mu \rightarrow \nu_\mu$ survival probability

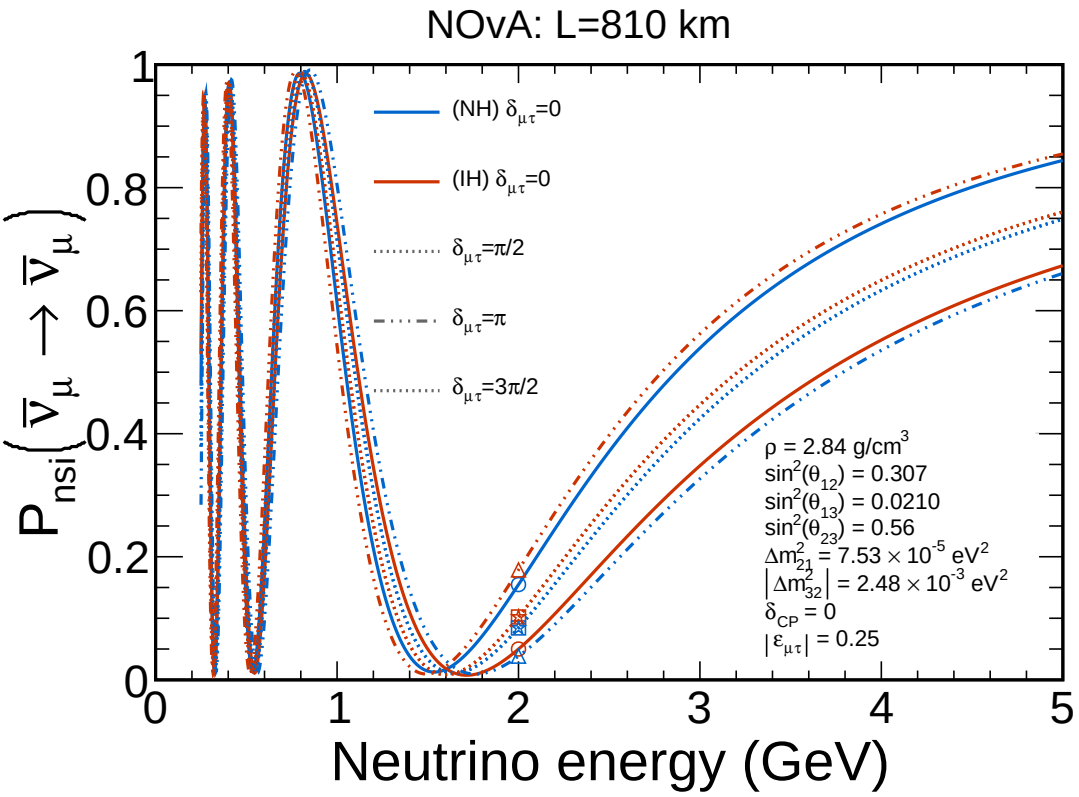

(b) $\bar{\nu}_\mu \rightarrow \bar{\nu}_\mu$ survival probability

Figure 53 – $\nu_\mu \rightarrow \nu_\mu$ ($\bar{\nu}_\mu \rightarrow \bar{\nu}_\mu$) survival probability for neutrinos (a) and antineutrinos (b), for normal hierarchy (blue) and inverted hierarchy (red) neutrino mass ordering. Shown is the probability for different values of interest for the NSI phase $\delta_{\mu\tau}$, indicated by the different line styles, along with the corresponding value of interest marked at $E = 2\,\text{GeV}$.

For each probability, we computed the Normal Hierarchy (blue) and Inverted Hierarchy (red) cases. Notice that for each scenario, a corresponding value is marked at the value of interest of $E = 2\,\text{GeV}$. The values of interest are now inserted in the biprobability plot, shown in Fig. 54.

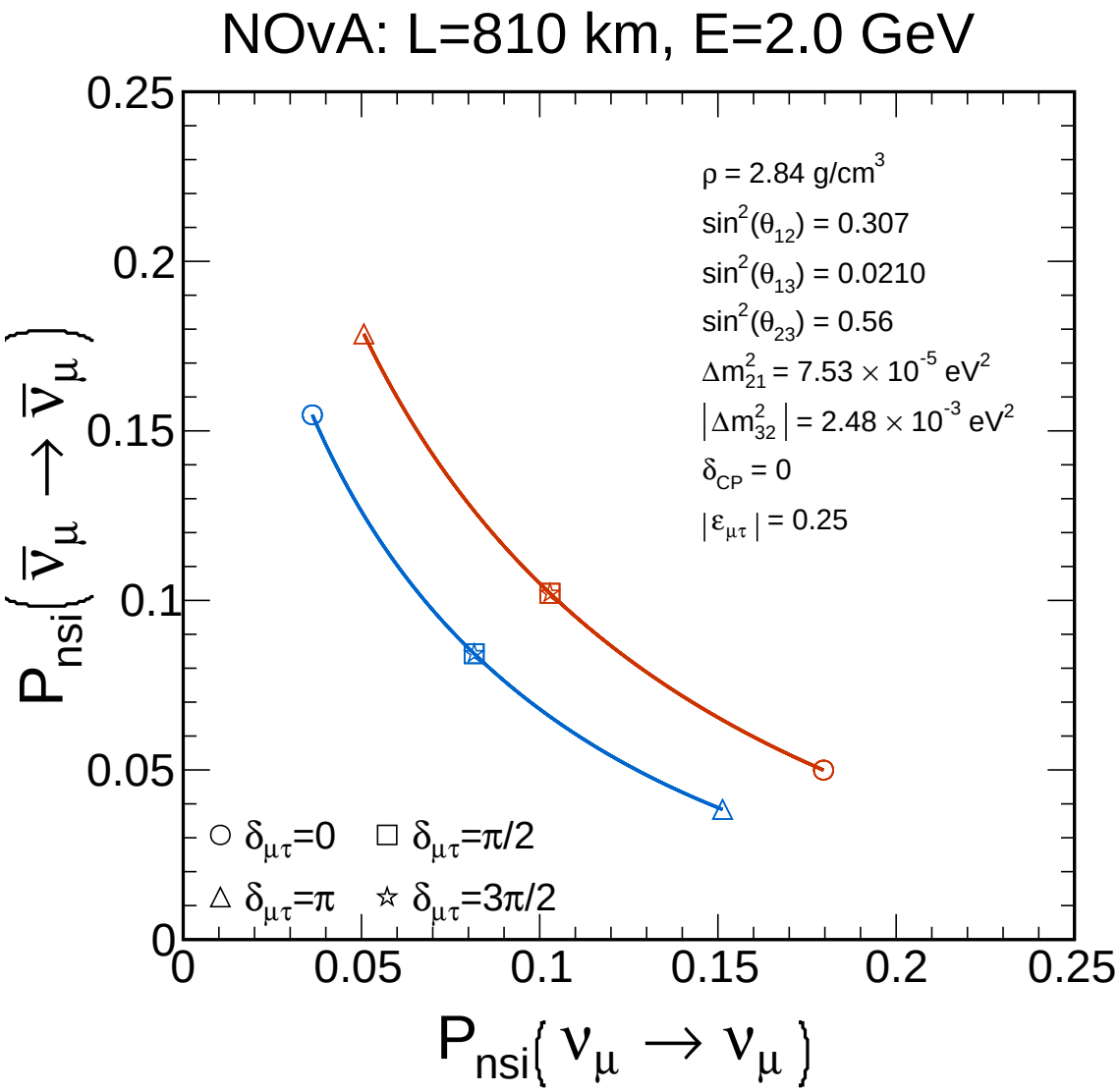

Figure 54 – Biprobability plot for the disappearance channel for normal hierarchy (blue) and inverted hierarchy (red) neutrino mass ordering. Shown is the corresponding value for each probability at $E = 2\,\text{GeV}$ under different values of the NSI phase $\delta_{\mu\tau}$.

It is observed that there is an apparent different behavior between neutrino and antineutrino oscillations for different values of the NSI CP-violating phase $\delta_{\mu\tau}$, as well as differences between the NH (blue) and IH (red) mass hierarchy scenarios, which directly allows investigations for the preference of one scenario or another. Notice that for the values of $\delta_{\mu\tau} = 0, \pi$ (open circle, open triangle), the differences between neutrino and antineutrino behaviors is seen to be most notable, for both mass hierarchies, while for the values of $\delta_{\mu\tau} = \frac{\pi}{2}, \frac{3\pi}{2}$ (open square, open star) the behavior is the same, with the difference lying only between the mass hierarchies. In other words, the neutrino mass ordering scenario can be probed under the current NSI model, regardless of the value for the NSI phase $\delta_{\mu\tau}$. Similarly, investigations on CP violation can be probed on both mass hierarchies, although for specific values of $\delta_{\mu\tau} = \frac{\pi}{2}, \frac{3\pi}{2}$ the CP symmetry is conserved.

As done for the disappearance channel, we now look at the effects present in the $\nu_\mu \to \nu_e\,(\bar{\nu}_\mu \to \bar{\nu}_e)$ transition, known as *appearance channel*. Fig. 55 shows the transition probabilities for neutrinos and antineutrinos under different values of interest for the NSI phase $\delta_{\mu\tau} = \left(0, \frac{\pi}{2}, \pi, \frac{3\pi}{2}\right)$, for both Normal Hierarchy and Inverted Hierarchy, for the set of oscillation parameters indicated in the plots. Notice that for each scenario, a corresponding value is marked at the value of interest of $E = 2\,\text{GeV}$. The values of interest are now inserted in the biprobability plot, shown in Fig. 56.

As in the disappearance channel, we also see for the appearance channel that neutrinos and antineutrinos may possess different oscillation behaviors arising from the NSI CP-violating phase $\delta_{\mu\tau}$, as well as differences between the NH (blue) and IH (red) mass hierarchy scenarios, which directly allows investigations for the preference of one scenario or another. Although the effects are less expressive in comparison to the disappearance channel, in the $\nu_\mu \to \nu_e\,(\bar{\nu}_\mu \to \bar{\nu}_e)$ transition one is able to observe differences between the values of $\delta_{\mu\tau} = \frac{\pi}{2}, \frac{3\pi}{2}$, which are degenerate in the $\nu_\mu \to \nu_\mu\,(\bar{\nu}_\mu \to \bar{\nu}_\mu)$ case. In the appearance channel, one is able to perform investigations on both the mass hierarchy and CP violation in light of the current NSI model.

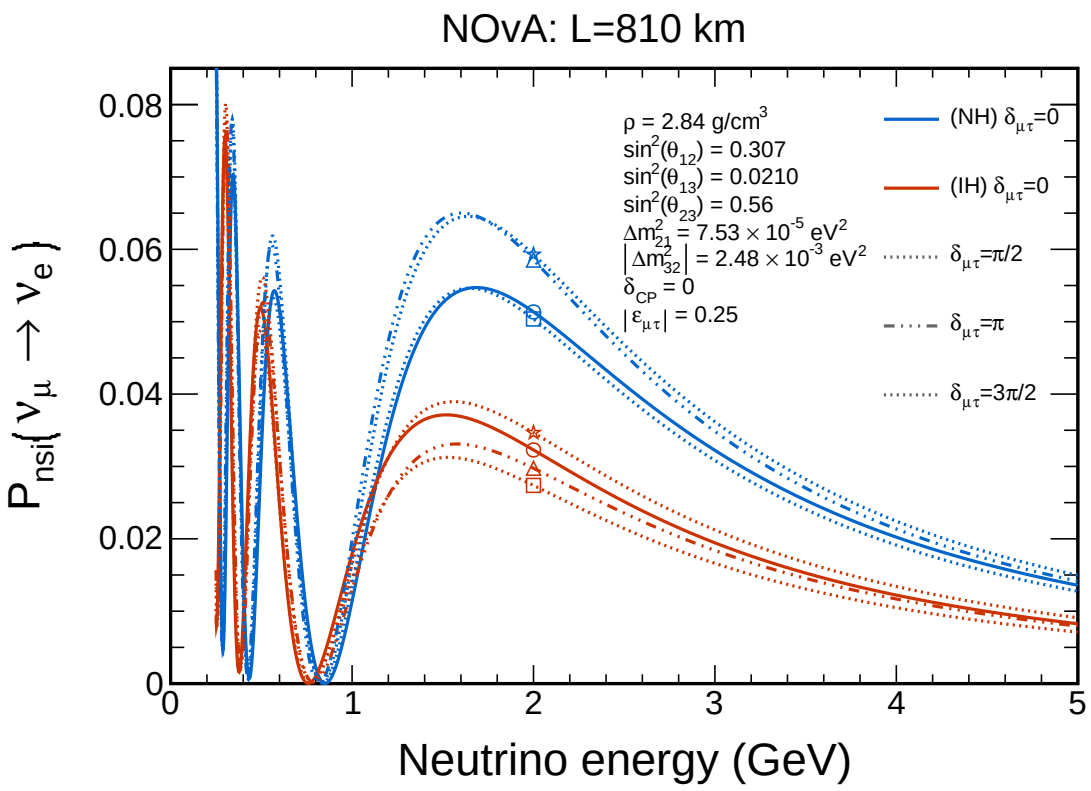

(a) $\nu_\mu \rightarrow \nu_e$ transition probability

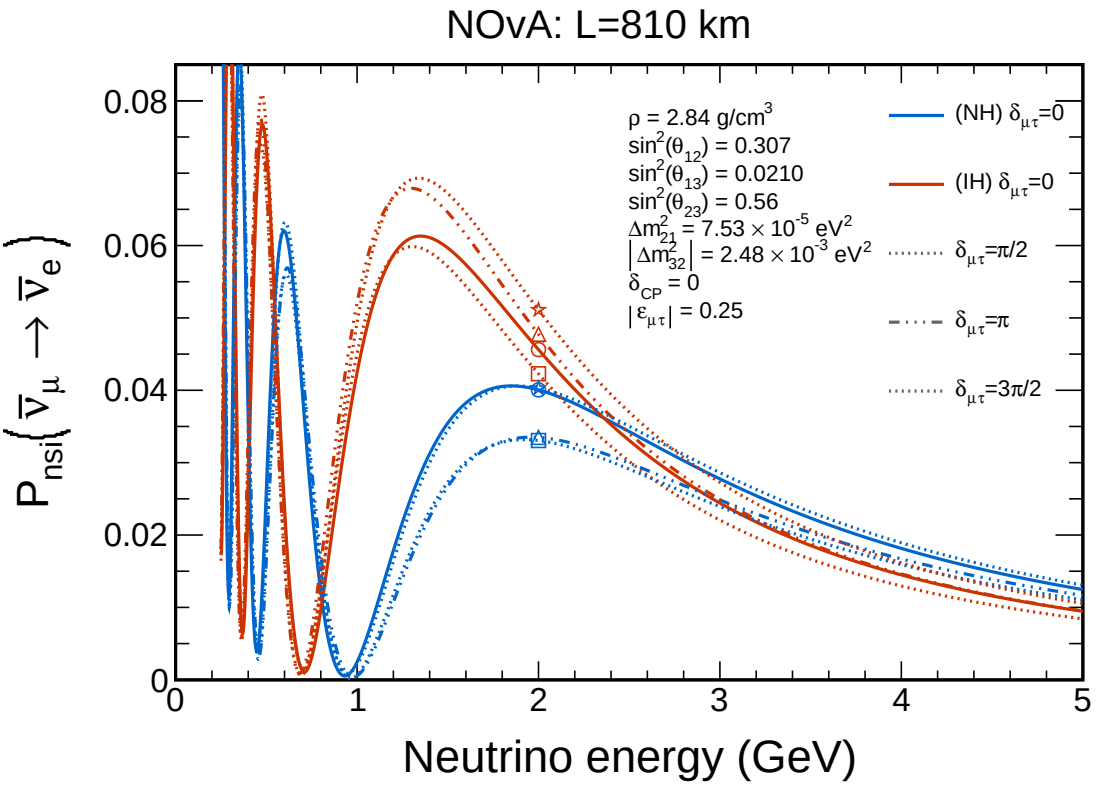

(b) $\bar{\nu}_\mu \rightarrow \bar{\nu}_e$ transition probability

Figure 55 – $\nu_\mu \rightarrow \nu_e$ ($\bar{\nu}_\mu \rightarrow \bar{\nu}_e$) transition probability for neutrinos (a) and antineutrinos (b), for normal hierarchy (blue) and inverted hierarchy (red) neutrino mass ordering. Shown is the probability for different values of interest for the NSI phase $\delta_{\mu\tau}$, indicated by the different line styles, along with the corresponding value of interest marked at $E = 2\,\text{GeV}$.

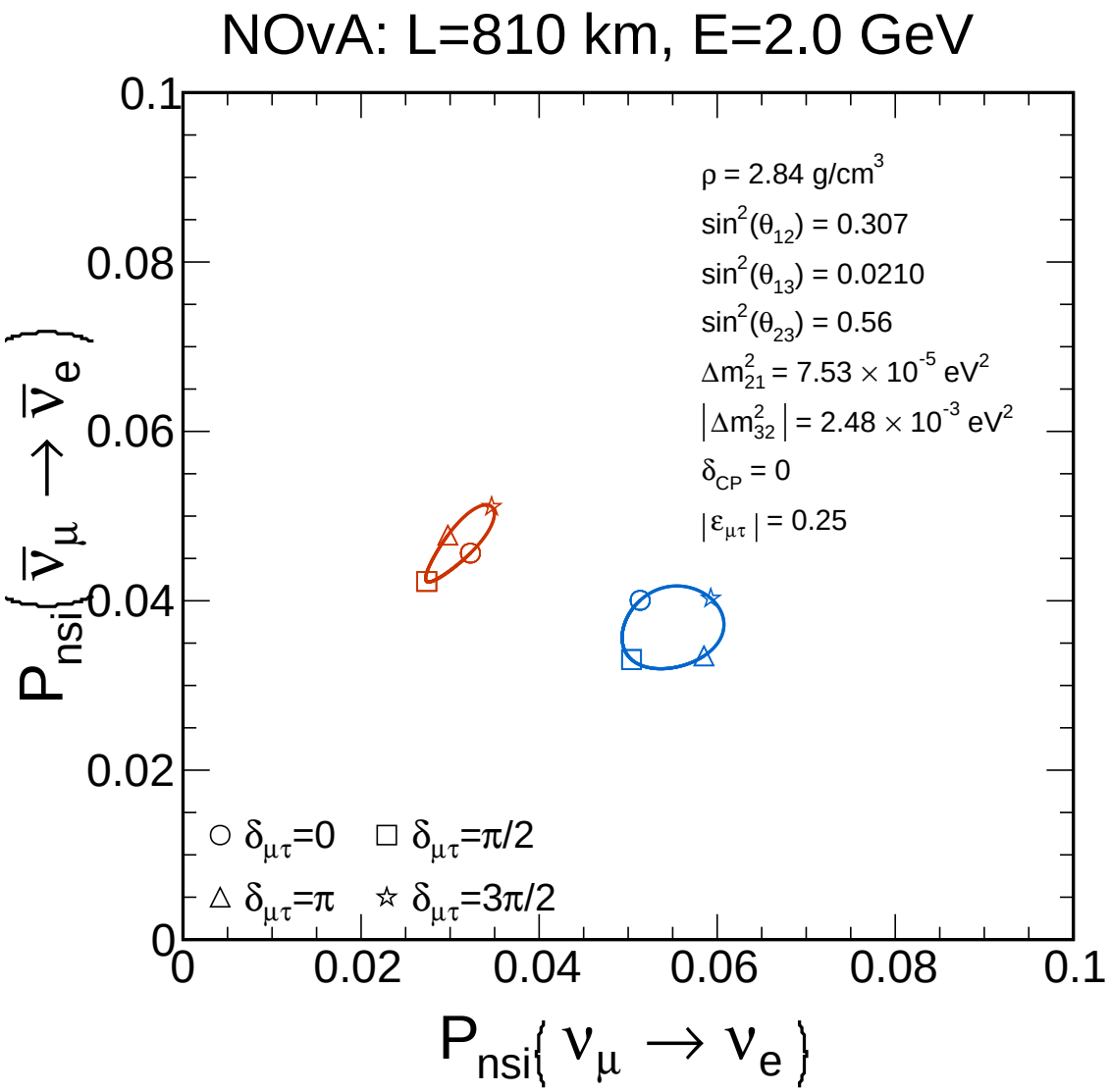

Figure 56 – Biprobability plot for the appearance channel for normal hierarchy (blue) and inverted hierarchy (red) neutrino mass ordering. Shown is the corresponding value for each probability at $E = 2\,\text{GeV}$ under different values of the NSI phase $\delta_{\mu\tau}$.

APPENDIX C – Systematic uncertainties evaluation

C.1 Impact of the systematic uncertainties

We presented in Chapter 6 our results accounting both statistical and systematic uncertainties. In order to understand how the inclusion or not of the systematic uncertainties impacts each of our parameters, we show an extensive collection of plots comparing the effects of the inclusion or not of systematic uncertainties.

C.1.1 1D Profiles

Δm^2_{32} - Normal Hierarchy

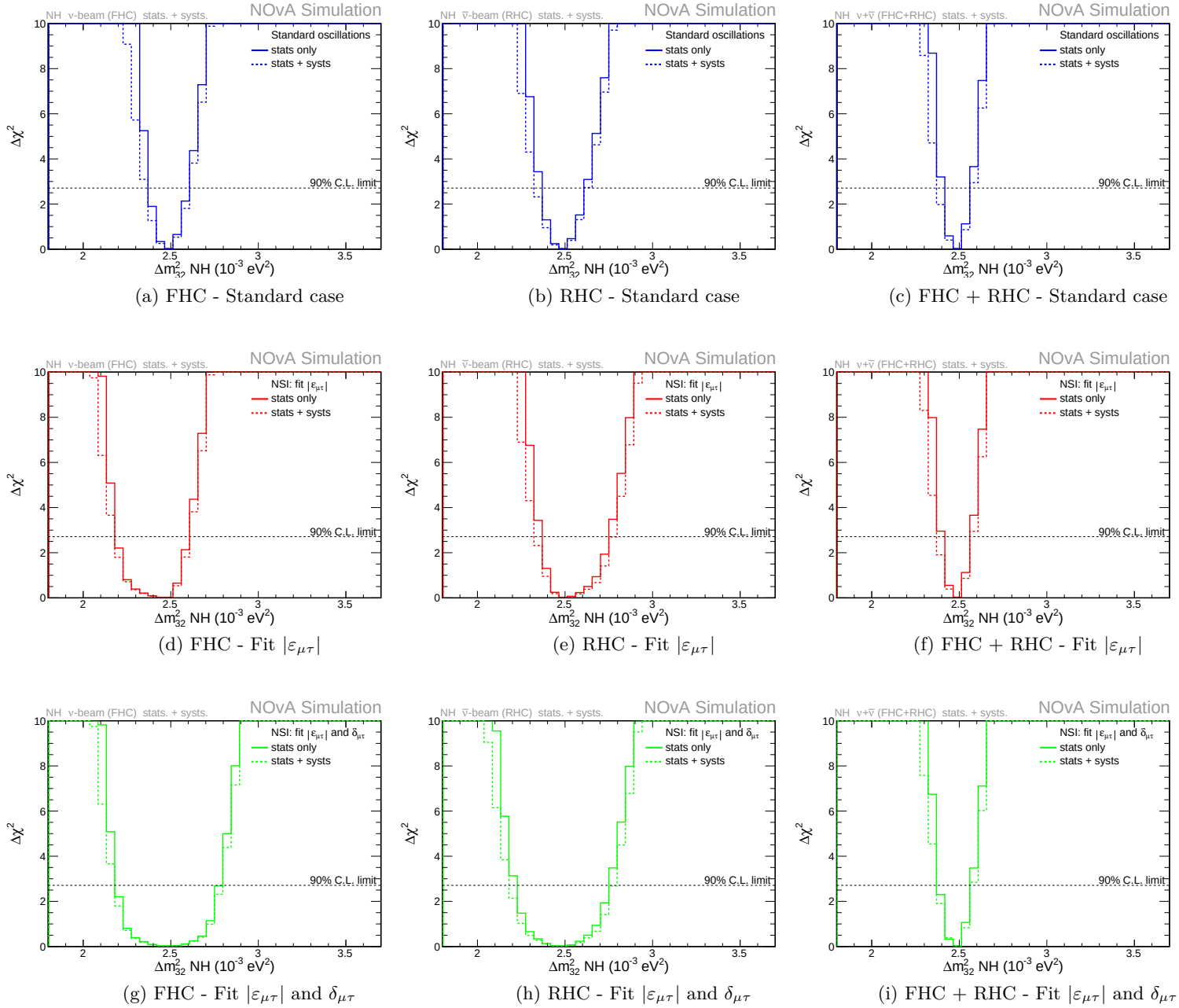

(a) FHC - Standard case (b) RHC - Standard case (c) FHC + RHC - Standard case

(d) FHC - Fit $|\varepsilon_{\mu\tau}|$ (e) RHC - Fit $|\varepsilon_{\mu\tau}|$ (f) FHC + RHC - Fit $|\varepsilon_{\mu\tau}|$

(g) FHC - Fit $|\varepsilon_{\mu\tau}|$ and $\delta_{\mu\tau}$ (h) RHC - Fit $|\varepsilon_{\mu\tau}|$ and $\delta_{\mu\tau}$ (i) FHC + RHC - Fit $|\varepsilon_{\mu\tau}|$ and $\delta_{\mu\tau}$

Figure 57 – Comparison of the impact of the inclusion of systematic uncertainties (dashed line) or not (solid line) on the measurement of the standard oscillation parameter Δm^2_{32} (Normal Hierarchy), for FHC mode, RHC mode, and the joint FHC + RHC fit. In blue is shown the standard scenario, where no NSI parameters are included in the fit, while in red we fit $|\varepsilon_{\mu\tau}|$, and in green we fit for $|\varepsilon_{\mu\tau}|$ and $\delta_{\mu\tau}$.

Δm^2_{32} - Inverted Hierarchy

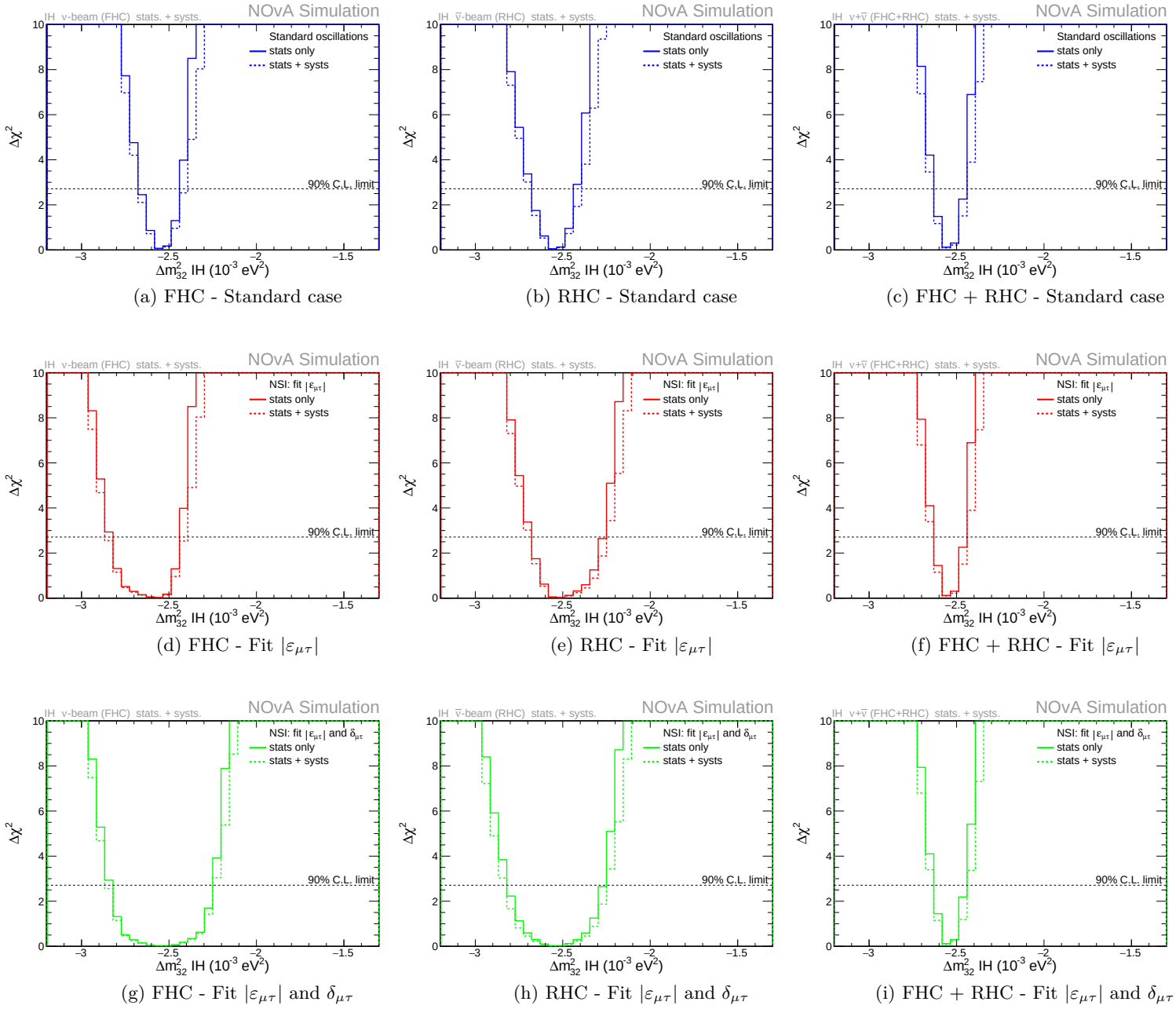

(a) FHC - Standard case (b) RHC - Standard case (c) FHC + RHC - Standard case

(d) FHC - Fit $|\varepsilon_{\mu\tau}|$ (e) RHC - Fit $|\varepsilon_{\mu\tau}|$ (f) FHC + RHC - Fit $|\varepsilon_{\mu\tau}|$

(g) FHC - Fit $|\varepsilon_{\mu\tau}|$ and $\delta_{\mu\tau}$ (h) RHC - Fit $|\varepsilon_{\mu\tau}|$ and $\delta_{\mu\tau}$ (i) FHC + RHC - Fit $|\varepsilon_{\mu\tau}|$ and $\delta_{\mu\tau}$

Figure 58 – Comparison of the impact of the inclusion of systematic uncertainties (dashed line) or not (solid line) on the measurement of the standard oscillation parameter Δm^2_{32} (Inverted Hierarchy), for FHC mode, RHC mode, and the joint FHC + RHC fit. In blue is shown the standard scenario, where no NSI parameters are included in the fit, while in red we fit $|\varepsilon_{\mu\tau}|$, and in green we fit for $|\varepsilon_{\mu\tau}|$ and $\delta_{\mu\tau}$.

$\sin^2(\theta_{23})$ - Normal Hierarchy

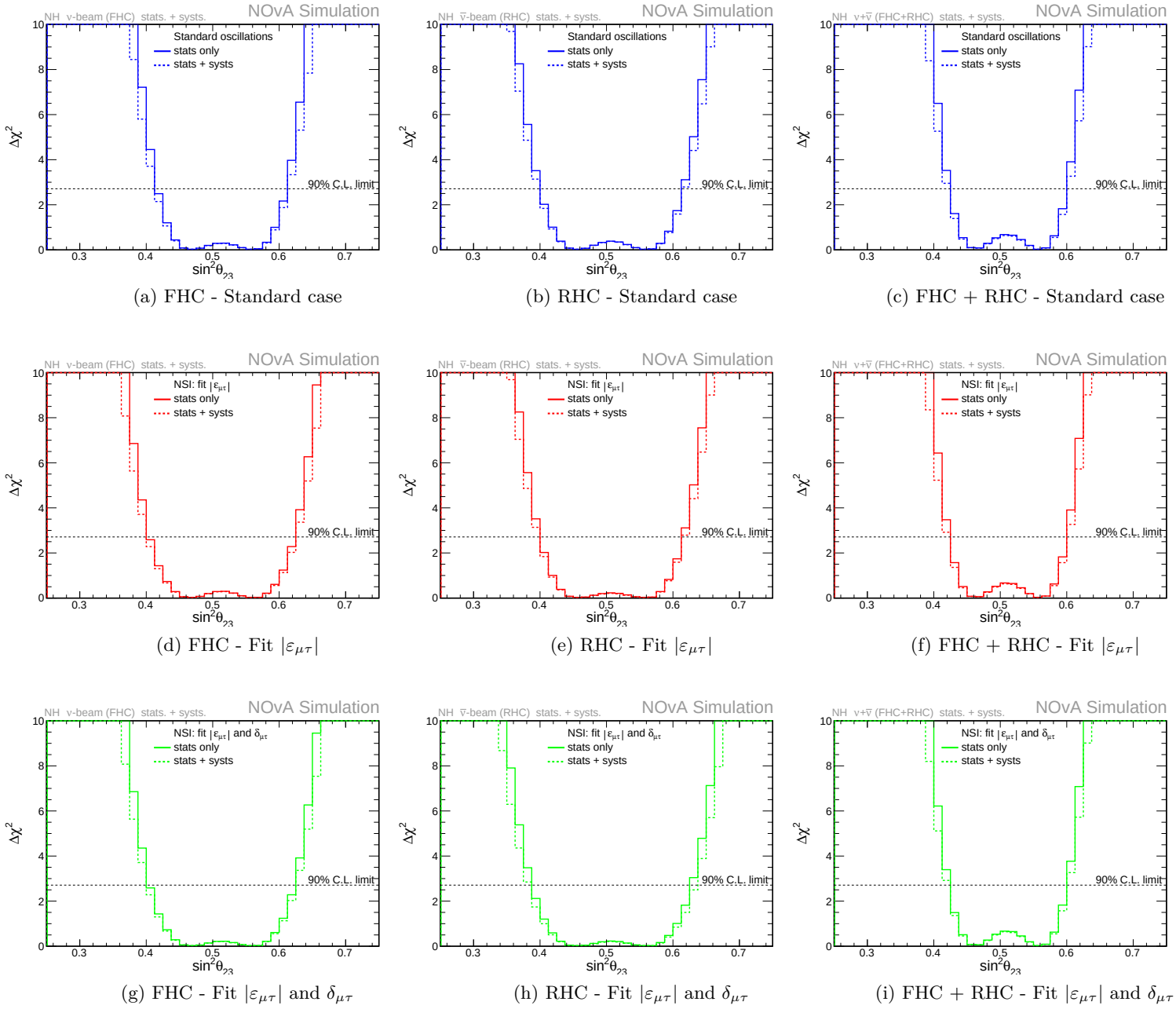

(a) FHC - Standard case (b) RHC - Standard case (c) FHC + RHC - Standard case

(d) FHC - Fit $|\varepsilon_{\mu\tau}|$ (e) RHC - Fit $|\varepsilon_{\mu\tau}|$ (f) FHC + RHC - Fit $|\varepsilon_{\mu\tau}|$

(g) FHC - Fit $|\varepsilon_{\mu\tau}|$ and $\delta_{\mu\tau}$ (h) RHC - Fit $|\varepsilon_{\mu\tau}|$ and $\delta_{\mu\tau}$ (i) FHC + RHC - Fit $|\varepsilon_{\mu\tau}|$ and $\delta_{\mu\tau}$

Figure 59 – Comparison of the impact of the inclusion of systematic uncertainties (dashed line) or not (solid line) on the measurement of the standard oscillation parameter $\sin^2(\theta_{23})$ (Normal Hierarchy), for FHC mode, RHC mode, and the joint FHC + RHC fit. In blue is shown the standard scenario, where no NSI parameters are included in the fit, while in red we fit $|\varepsilon_{\mu\tau}|$, and in green we fit for $|\varepsilon_{\mu\tau}|$ and $\delta_{\mu\tau}$.

$\sin^2(\theta_{23})$ - Inverted Hierarchy

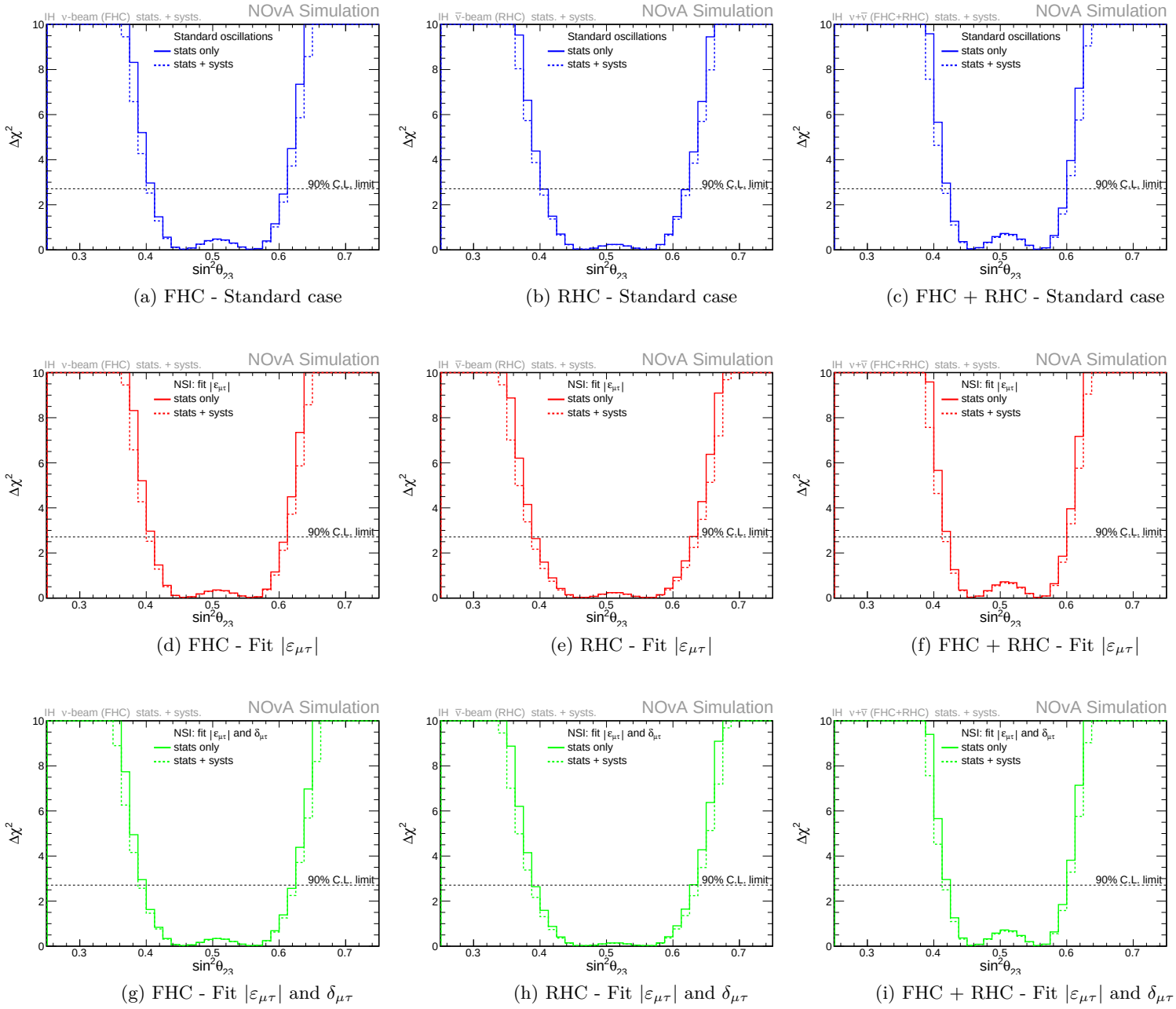

(a) FHC - Standard case (b) RHC - Standard case (c) FHC + RHC - Standard case

(d) FHC - Fit $|\varepsilon_{\mu\tau}|$ (e) RHC - Fit $|\varepsilon_{\mu\tau}|$ (f) FHC + RHC - Fit $|\varepsilon_{\mu\tau}|$

(g) FHC - Fit $|\varepsilon_{\mu\tau}|$ and $\delta_{\mu\tau}$ (h) RHC - Fit $|\varepsilon_{\mu\tau}|$ and $\delta_{\mu\tau}$ (i) FHC + RHC - Fit $|\varepsilon_{\mu\tau}|$ and $\delta_{\mu\tau}$

Figure 60 – Comparison of the impact of the inclusion of systematic uncertainties (dashed line) or not (solid line) on the measurement of the standard oscillation parameter $\sin^2(\theta_{23})$ (Inverted Hierarchy), for FHC mode, RHC mode, and the joint FHC + RHC fit. In blue is shown the standard scenario, where no NSI parameters are included in the fit, while in red we fit $|\varepsilon_{\mu\tau}|$, and in green we fit for $|\varepsilon_{\mu\tau}|$ and $\delta_{\mu\tau}$.

$|\varepsilon_{\mu\tau}|$ - Normal Hierarchy

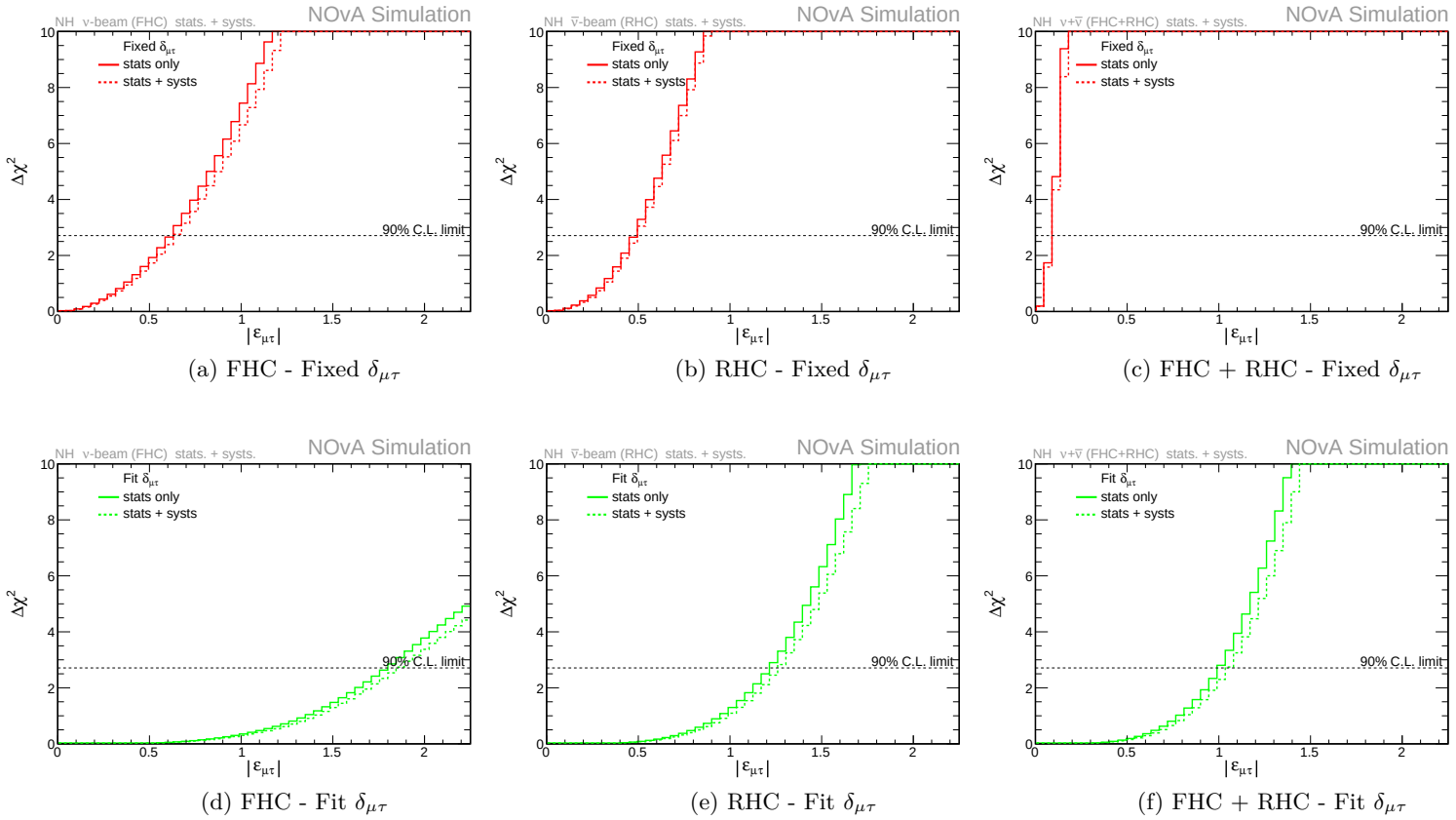

(a) FHC - Fixed $\delta_{\mu\tau}$ (b) RHC - Fixed $\delta_{\mu\tau}$ (c) FHC + RHC - Fixed $\delta_{\mu\tau}$

(d) FHC - Fit $\delta_{\mu\tau}$ (e) RHC - Fit $\delta_{\mu\tau}$ (f) FHC + RHC - Fit $\delta_{\mu\tau}$

Figure 61 – Comparison of the impact of the inclusion of systematic uncertainties (dashed line) or not (solid line) on the measurement of the NSI parameter $|\varepsilon_{\mu\tau}|$ (Normal Hierarchy), for FHC mode, RHC mode, and the joint FHC + RHC fit. In red is shown the scenario where $\delta_{\mu\tau} = 0$ is kept fixed and not fitted , while in green we fit for $\delta_{\mu\tau}$ as well.

$|\varepsilon_{\mu\tau}|$ - Inverted Hierarchy

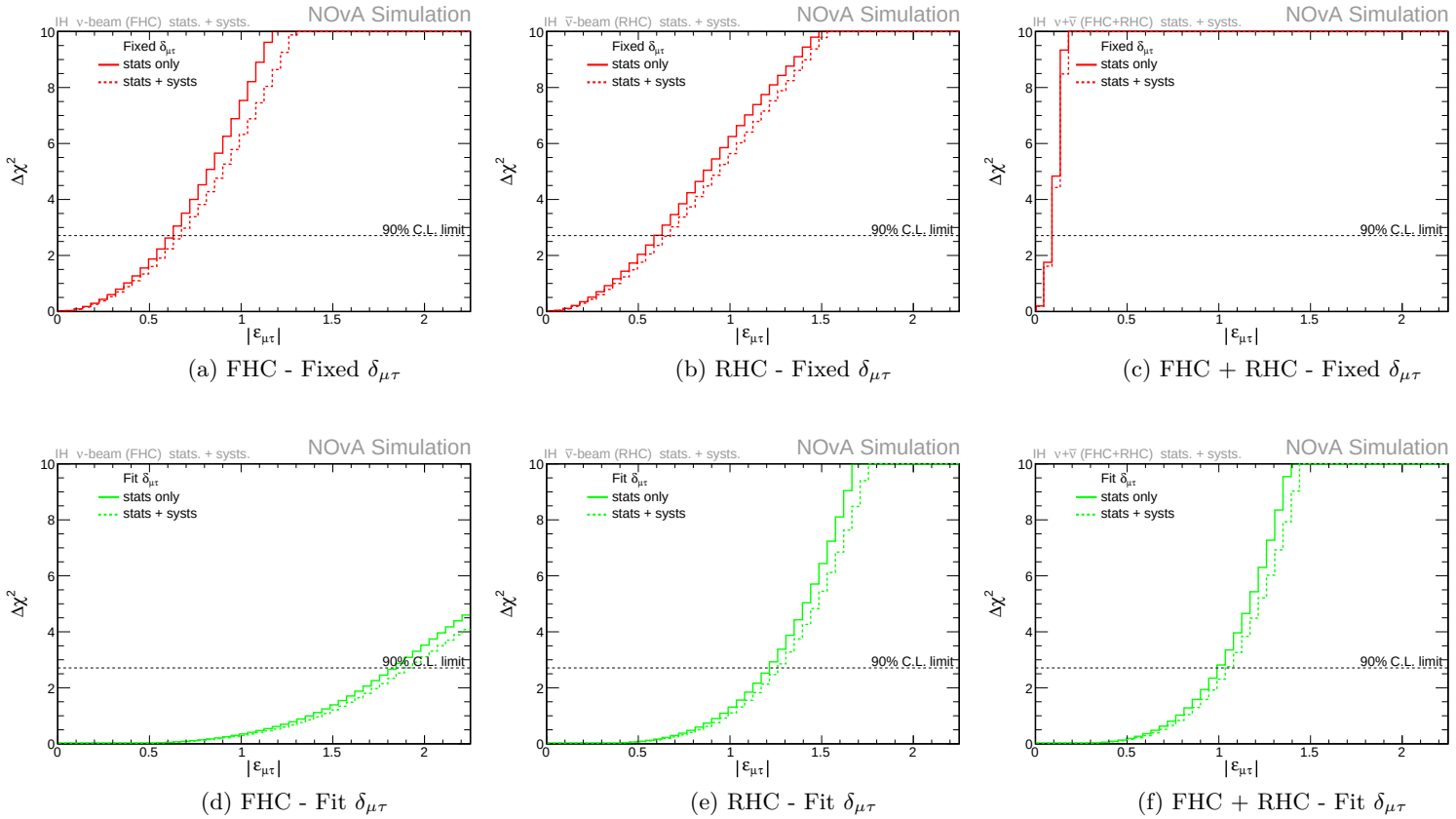

(a) FHC - Fixed $\delta_{\mu\tau}$ (b) RHC - Fixed $\delta_{\mu\tau}$ (c) FHC + RHC - Fixed $\delta_{\mu\tau}$

(d) FHC - Fit $\delta_{\mu\tau}$ (e) RHC - Fit $\delta_{\mu\tau}$ (f) FHC + RHC - Fit $\delta_{\mu\tau}$

Figure 62 – Comparison of the impact of the inclusion of systematic uncertainties (dashed line) or not (solid line) on the measurement of the NSI parameter $|\varepsilon_{\mu\tau}|$ (Inverted Hierarchy), for FHC mode, RHC mode, and the joint FHC + RHC fit. In red is shown the scenario where $\delta_{\mu\tau} = 0$ is kept fixed and not fitted , while in green we fit for $\delta_{\mu\tau}$ as well.

$\delta_{\mu\tau}$ - Normal Hierarchy

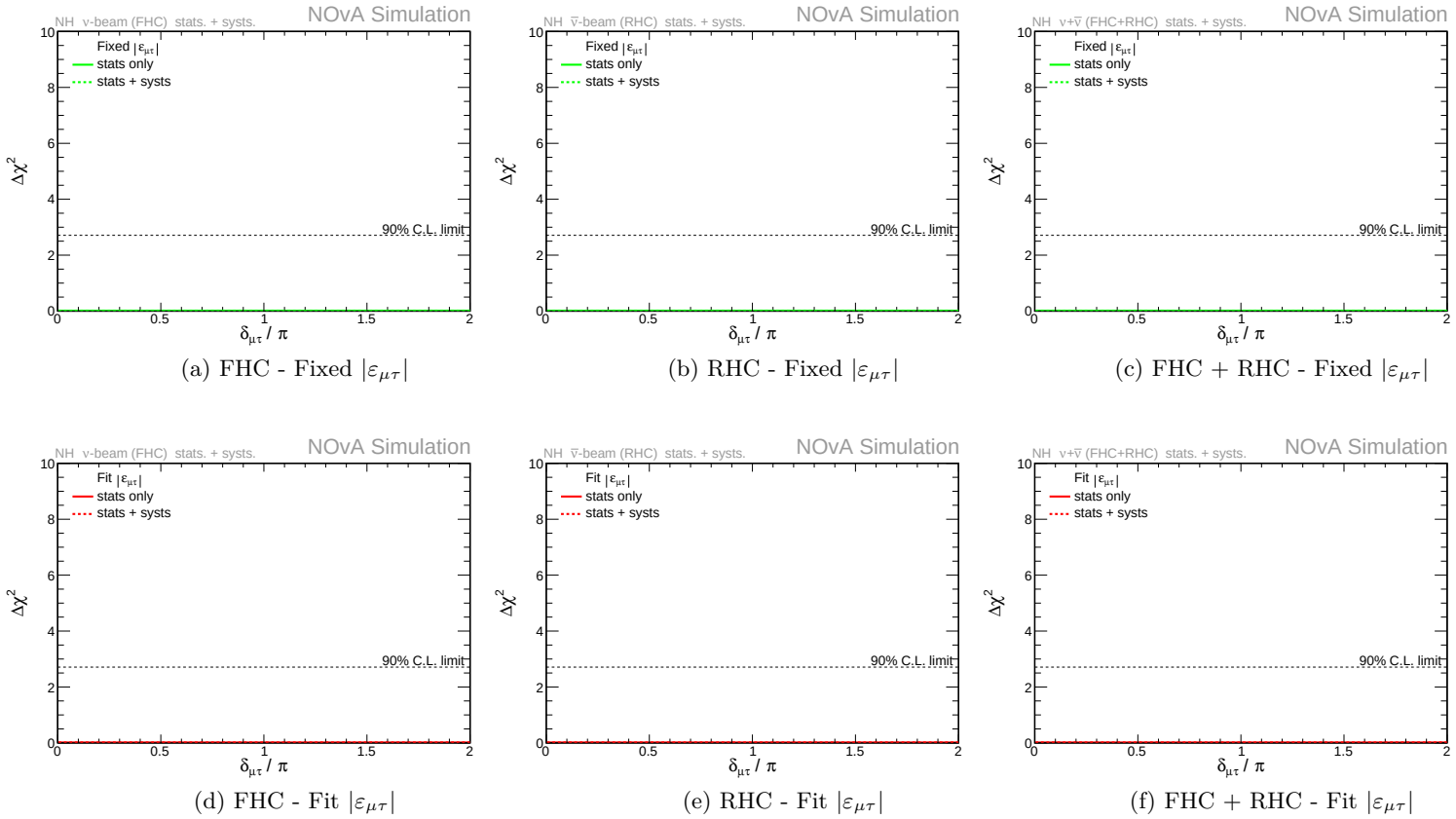

(a) FHC - Fixed $|\varepsilon_{\mu\tau}|$ (b) RHC - Fixed $|\varepsilon_{\mu\tau}|$ (c) FHC + RHC - Fixed $|\varepsilon_{\mu\tau}|$

(d) FHC - Fit $|\varepsilon_{\mu\tau}|$ (e) RHC - Fit $|\varepsilon_{\mu\tau}|$ (f) FHC + RHC - Fit $|\varepsilon_{\mu\tau}|$

Figure 63 – Comparison of the impact of the inclusion of systematic uncertainties (dashed line) or not (solid line) on the measurement of the NSI parameter $\delta_{\mu\tau}$ (Normal Hierarchy), for FHC mode, RHC mode, and the joint FHC + RHC fit. In green is shown the scenario where $|\varepsilon_{\mu\tau}| = 0$ is kept fixed and not fitted , while in red we fit for $|\varepsilon_{\mu\tau}|$ as well.

$\delta_{\mu\tau}$ - Inverted Hierarchy

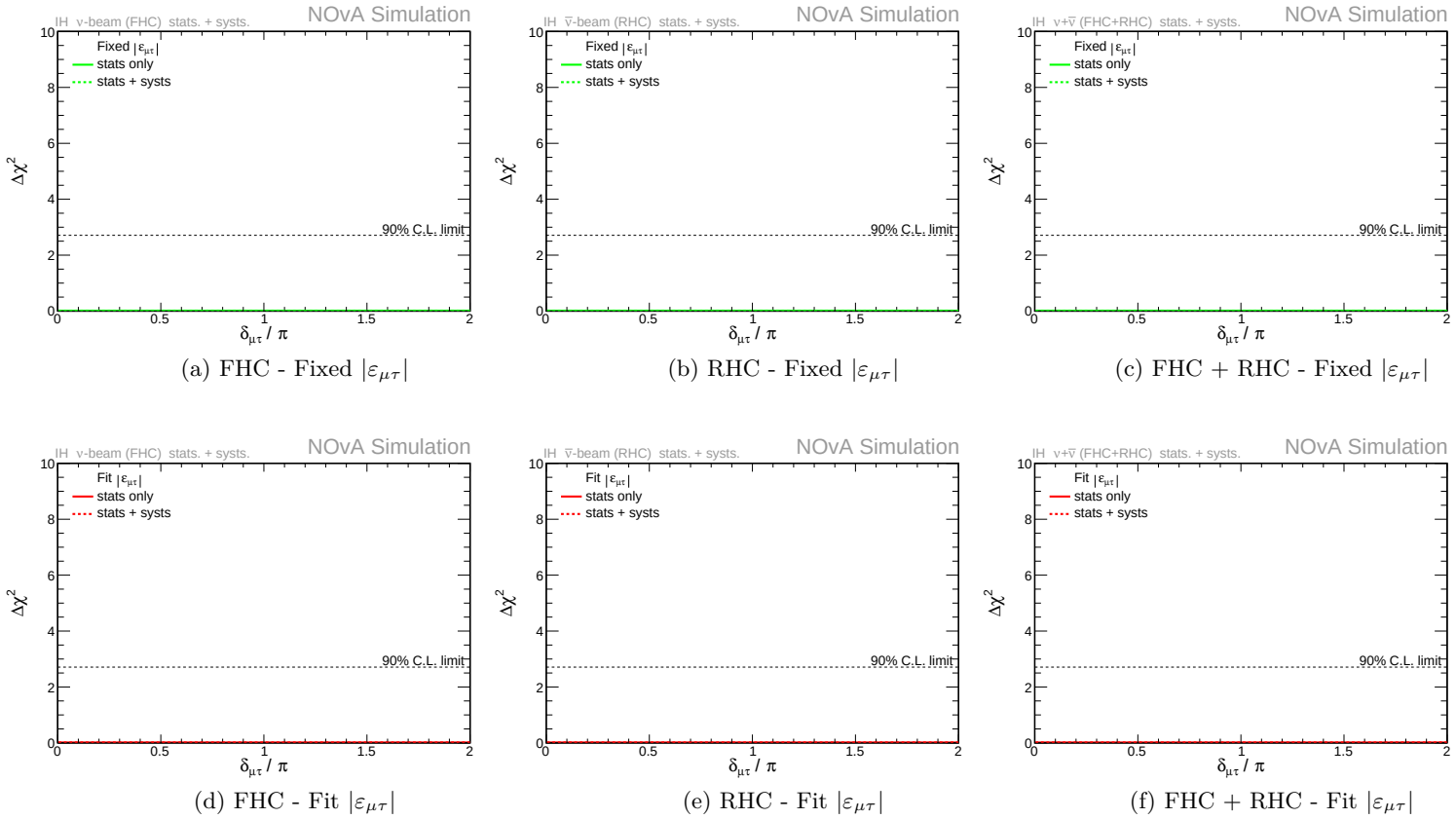

(a) FHC - Fixed $|\varepsilon_{\mu\tau}|$ (b) RHC - Fixed $|\varepsilon_{\mu\tau}|$ (c) FHC + RHC - Fixed $|\varepsilon_{\mu\tau}|$

(d) FHC - Fit $|\varepsilon_{\mu\tau}|$ (e) RHC - Fit $|\varepsilon_{\mu\tau}|$ (f) FHC + RHC - Fit $|\varepsilon_{\mu\tau}|$

Figure 64 – Comparison of the impact of the inclusion of systematic uncertainties (dashed line) or not (solid line) on the measurement of the NSI parameter $\delta_{\mu\tau}$ (Inverted Hierarchy), for FHC mode, RHC mode, and the joint FHC + RHC fit. In green is shown the scenario where $|\varepsilon_{\mu\tau}| = 0$ is kept fixed and not fitted , while in red we fit for $|\varepsilon_{\mu\tau}|$ as well.

C.1.2 2D Surfaces

$\sin^2(\theta_{23}) \times \Delta m^2_{32}$ - Normal Hierarchy

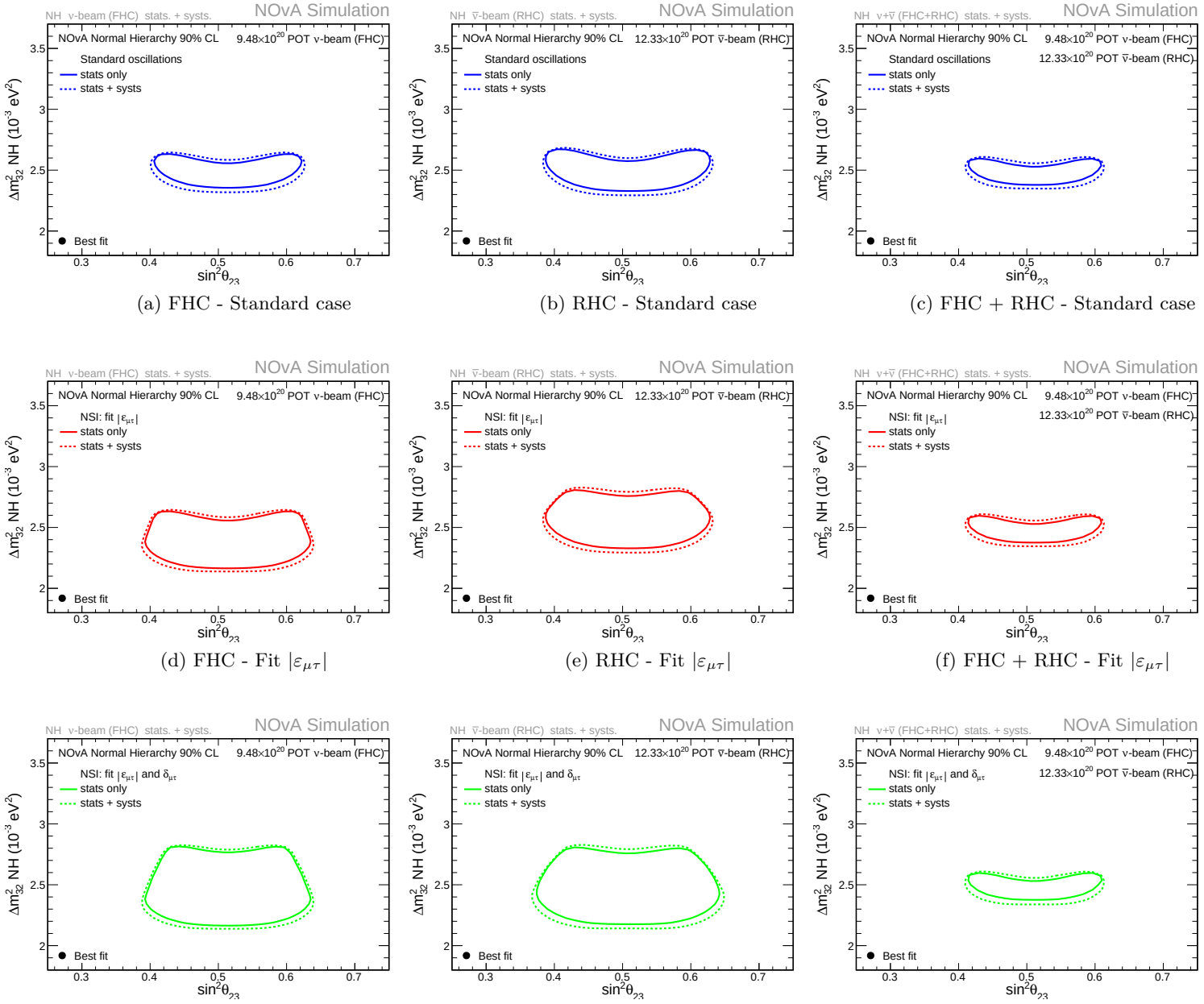

(a) FHC - Standard case (b) RHC - Standard case (c) FHC + RHC - Standard case

(d) FHC - Fit $|\varepsilon_{\mu\tau}|$ (e) RHC - Fit $|\varepsilon_{\mu\tau}|$ (f) FHC + RHC - Fit $|\varepsilon_{\mu\tau}|$

(g) FHC - Fit $|\varepsilon_{\mu\tau}|$ and $\delta_{\mu\tau}$ (h) RHC - Fit $|\varepsilon_{\mu\tau}|$ and $\delta_{\mu\tau}$ (i) FHC + RHC - Fit $|\varepsilon_{\mu\tau}|$ and $\delta_{\mu\tau}$

Figure 65 – Comparison of the impact of the inclusion of systematic uncertainties (dashed line) or not (solid line) on the $\sin^2(\theta_{23}) \times \Delta m^2_{32}$ parameter space (Normal Hierarchy), for FHC mode, RHC mode, and the joint FHC + RHC fit. In blue is shown the standard scenario, where no NSI parameters are included in the fit, while in red we fit $|\varepsilon_{\mu\tau}|$, and in green we fit for $|\varepsilon_{\mu\tau}|$ and $\delta_{\mu\tau}$.

$\sin^2(\theta_{23}) \times \Delta m^2_{32}$ - Inverted Hierarchy

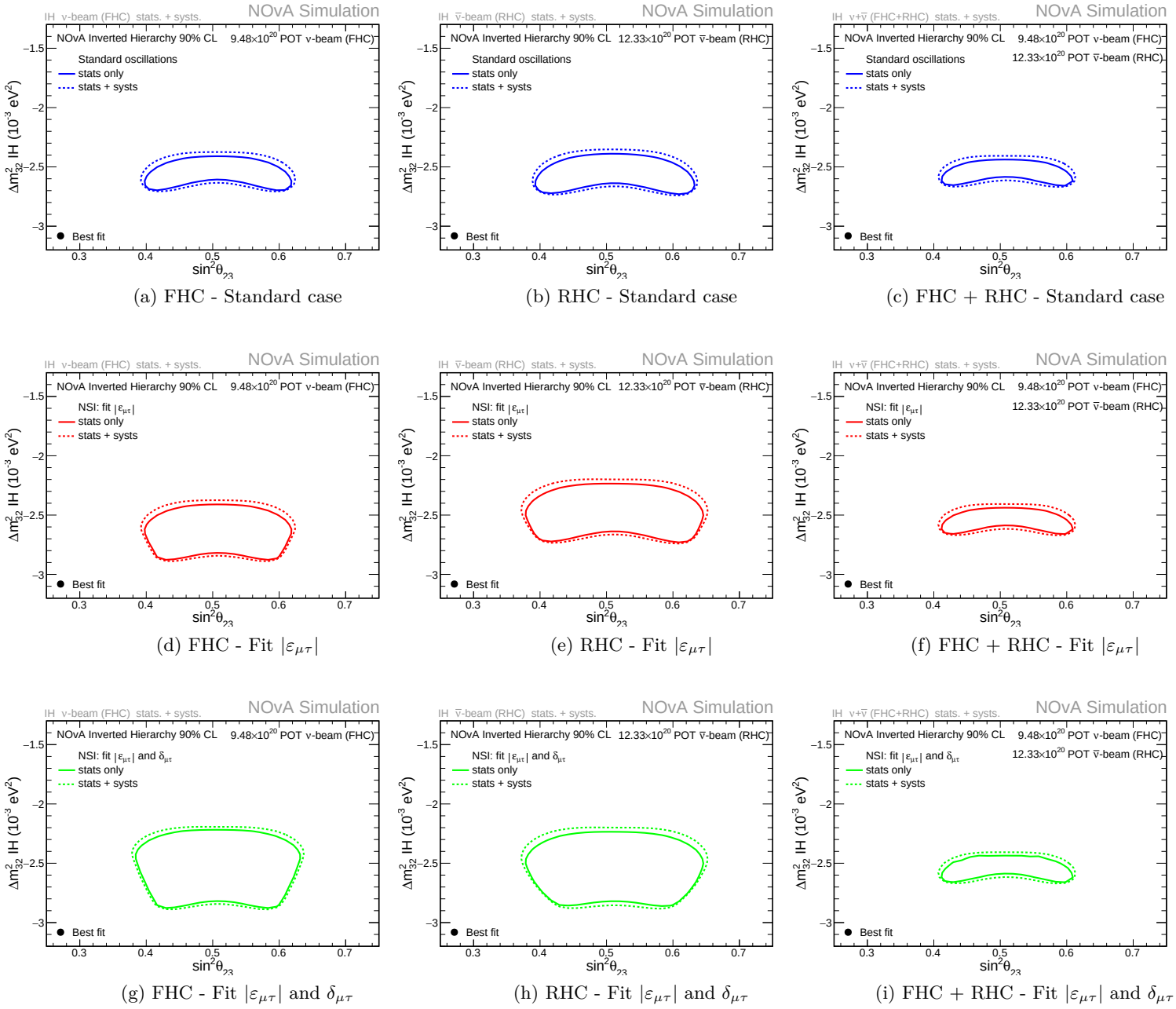

(a) FHC - Standard case (b) RHC - Standard case (c) FHC + RHC - Standard case

(d) FHC - Fit $|\varepsilon_{\mu\tau}|$ (e) RHC - Fit $|\varepsilon_{\mu\tau}|$ (f) FHC + RHC - Fit $|\varepsilon_{\mu\tau}|$

(g) FHC - Fit $|\varepsilon_{\mu\tau}|$ and $\delta_{\mu\tau}$ (h) RHC - Fit $|\varepsilon_{\mu\tau}|$ and $\delta_{\mu\tau}$ (i) FHC + RHC - Fit $|\varepsilon_{\mu\tau}|$ and $\delta_{\mu\tau}$

Figure 66 – Comparison of the impact of the inclusion of systematic uncertainties (dashed line) or not (solid line) on the $\sin^2(\theta_{23}) \times \Delta m^2_{32}$ parameter space (Inverted Hierarchy), for FHC mode, RHC mode, and the joint FHC + RHC fit. In blue is shown the standard scenario, where no NSI parameters are included in the fit, while in red we fit $|\varepsilon_{\mu\tau}|$, and in green we fit for $|\varepsilon_{\mu\tau}|$ and $\delta_{\mu\tau}$.

$|\varepsilon_{\mu\tau}| \times \Delta m^2_{32}$ - Normal Hierarchy

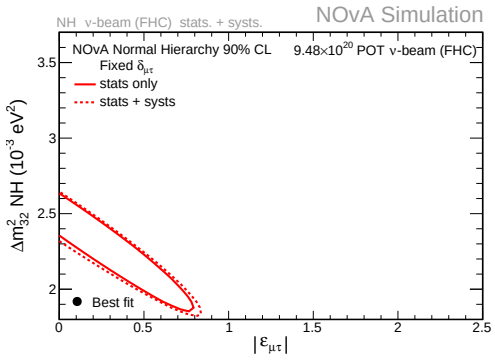

(a) FHC - Fixed $\delta_{\mu\tau}$

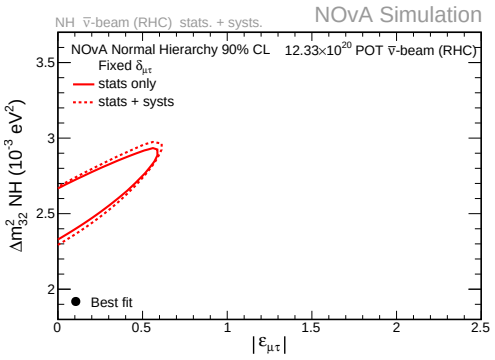

(b) RHC - Fixed $\delta_{\mu\tau}$

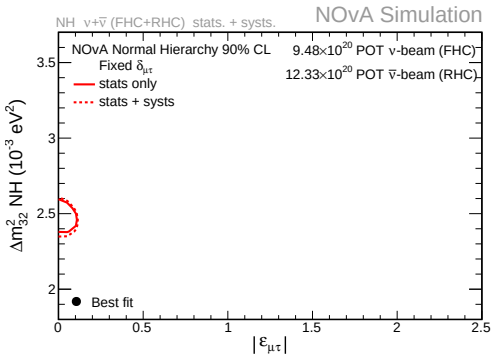

(c) FHC + RHC - Fixed $\delta_{\mu\tau}$

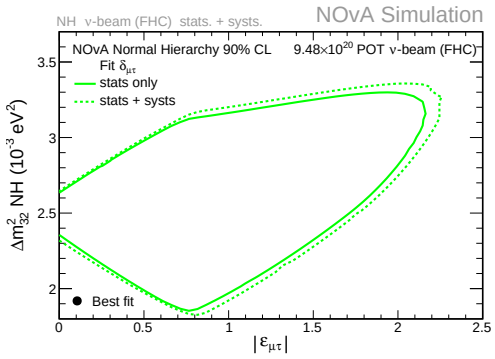

(d) FHC - Fit $\delta_{\mu\tau}$

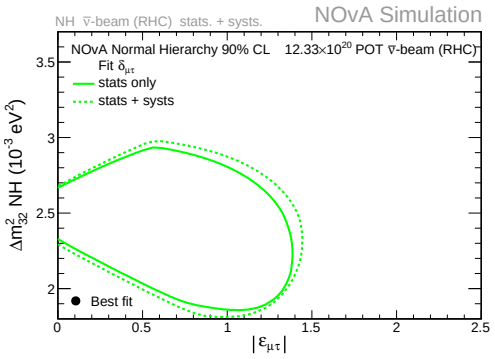

(e) RHC - Fit $\delta_{\mu\tau}$

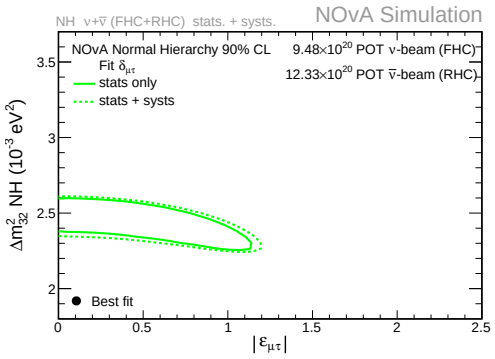

(f) FHC + RHC - Fit $\delta_{\mu\tau}$

Figure 67 – Comparison of the impact of the inclusion of systematic uncertainties (dashed line) or not (solid line) on the $|\varepsilon_{\mu\tau}| \times \Delta m^2_{32}$ parameter space (Normal Hierarchy), for FHC mode, RHC mode, and the joint FHC + RHC fit. In red is shown the scenario where $\delta_{\mu\tau} = 0$ is kept fixed and not fitted, while in green we fit for $\delta_{\mu\tau}$ as well.

$|\varepsilon_{\mu\tau}| \times \Delta m^2_{32}$ - Inverted Hierarchy

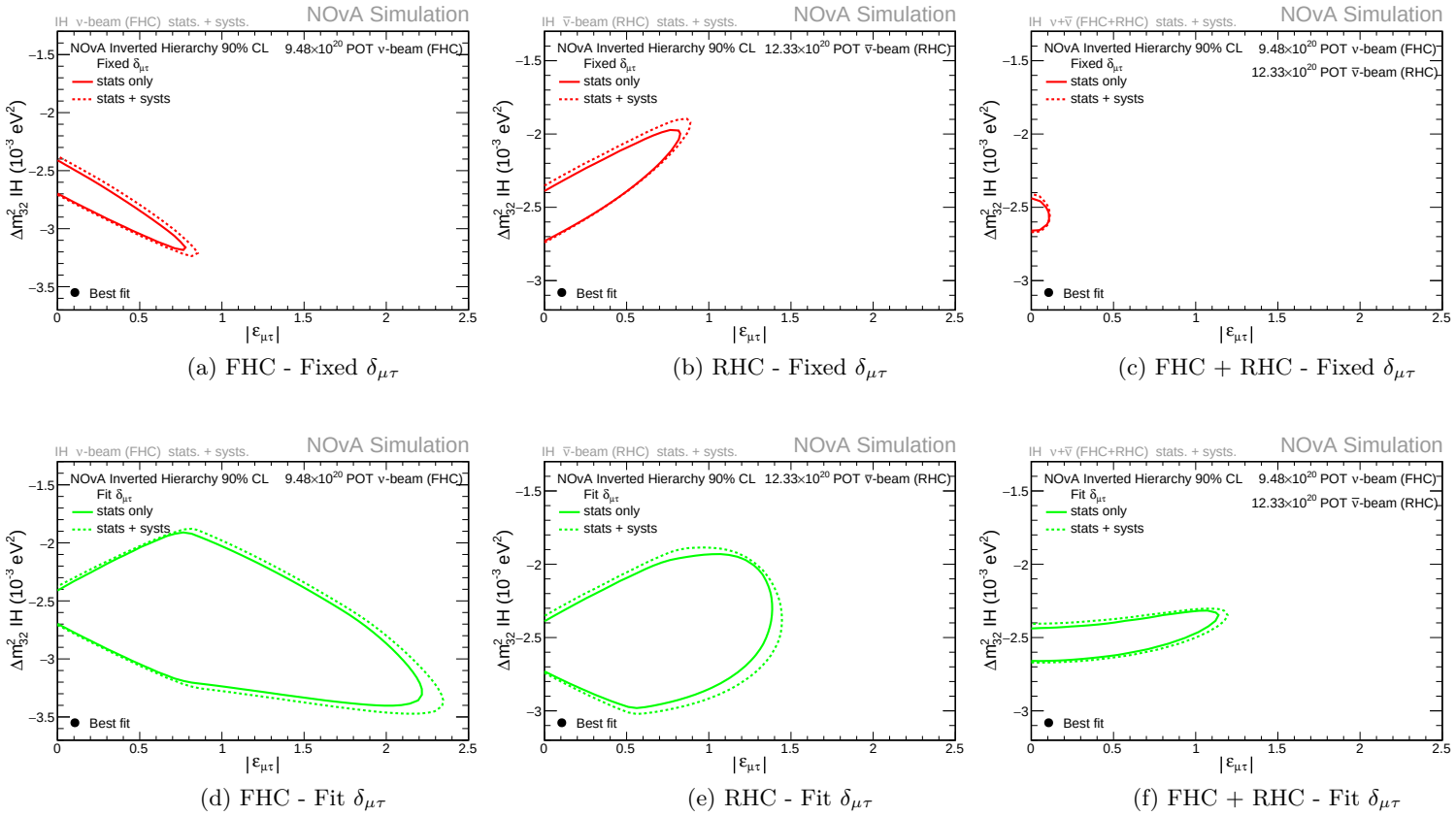

(a) FHC - Fixed $\delta_{\mu\tau}$ (b) RHC - Fixed $\delta_{\mu\tau}$ (c) FHC + RHC - Fixed $\delta_{\mu\tau}$

(d) FHC - Fit $\delta_{\mu\tau}$ (e) RHC - Fit $\delta_{\mu\tau}$ (f) FHC + RHC - Fit $\delta_{\mu\tau}$

Figure 68 – Comparison of the impact of the inclusion of systematic uncertainties (dashed line) or not (solid line) on the $|\varepsilon_{\mu\tau}| \times \Delta m^2_{32}$ parameter space (Inverted Hierarchy), for FHC mode, RHC mode, and the joint FHC + RHC fit. In red is shown the scenario where $\delta_{\mu\tau} = 0$ is kept fixed and not fitted, while in green we fit for $\delta_{\mu\tau}$ as well.

$|\varepsilon_{\mu\tau}| \times \sin^2(\theta_{23})$ - Normal Hierarchy

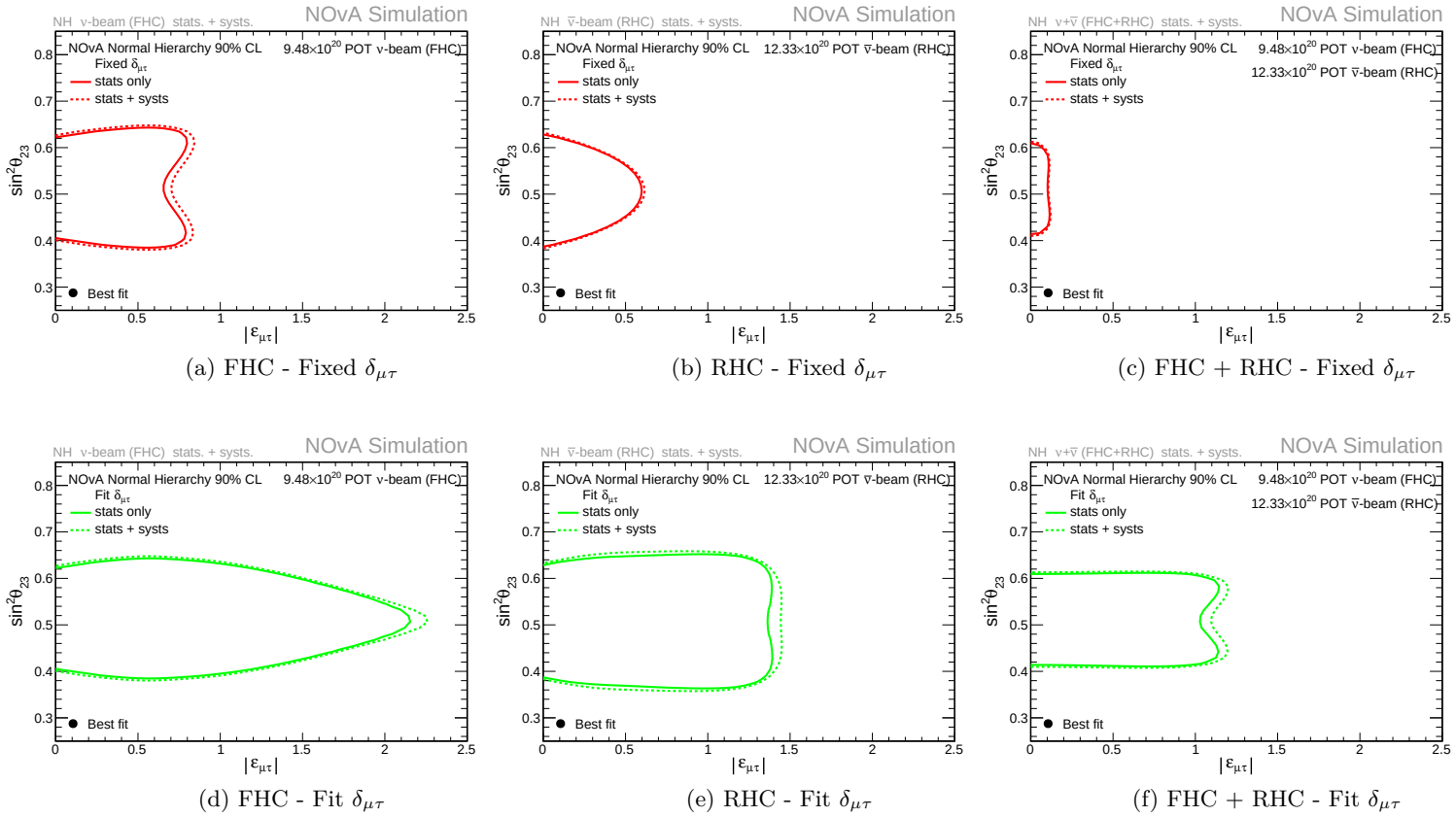

(a) FHC - Fixed $\delta_{\mu\tau}$ (b) RHC - Fixed $\delta_{\mu\tau}$ (c) FHC + RHC - Fixed $\delta_{\mu\tau}$

(d) FHC - Fit $\delta_{\mu\tau}$ (e) RHC - Fit $\delta_{\mu\tau}$ (f) FHC + RHC - Fit $\delta_{\mu\tau}$

Figure 69 – Comparison of the impact of the inclusion of systematic uncertainties (dashed line) or not (solid line) on the $|\varepsilon_{\mu\tau}| \times \sin^2(\theta_{23})$ parameter space (Normal Hierarchy), for FHC mode, RHC mode, and the joint FHC + RHC fit. In red is shown the scenario where $\delta_{\mu\tau} = 0$ is kept fixed and not fitted, while in green we fit for $\delta_{\mu\tau}$ as well.

$|\varepsilon_{\mu\tau}| \times \sin^2(\theta_{23})$ - Inverted Hierarchy

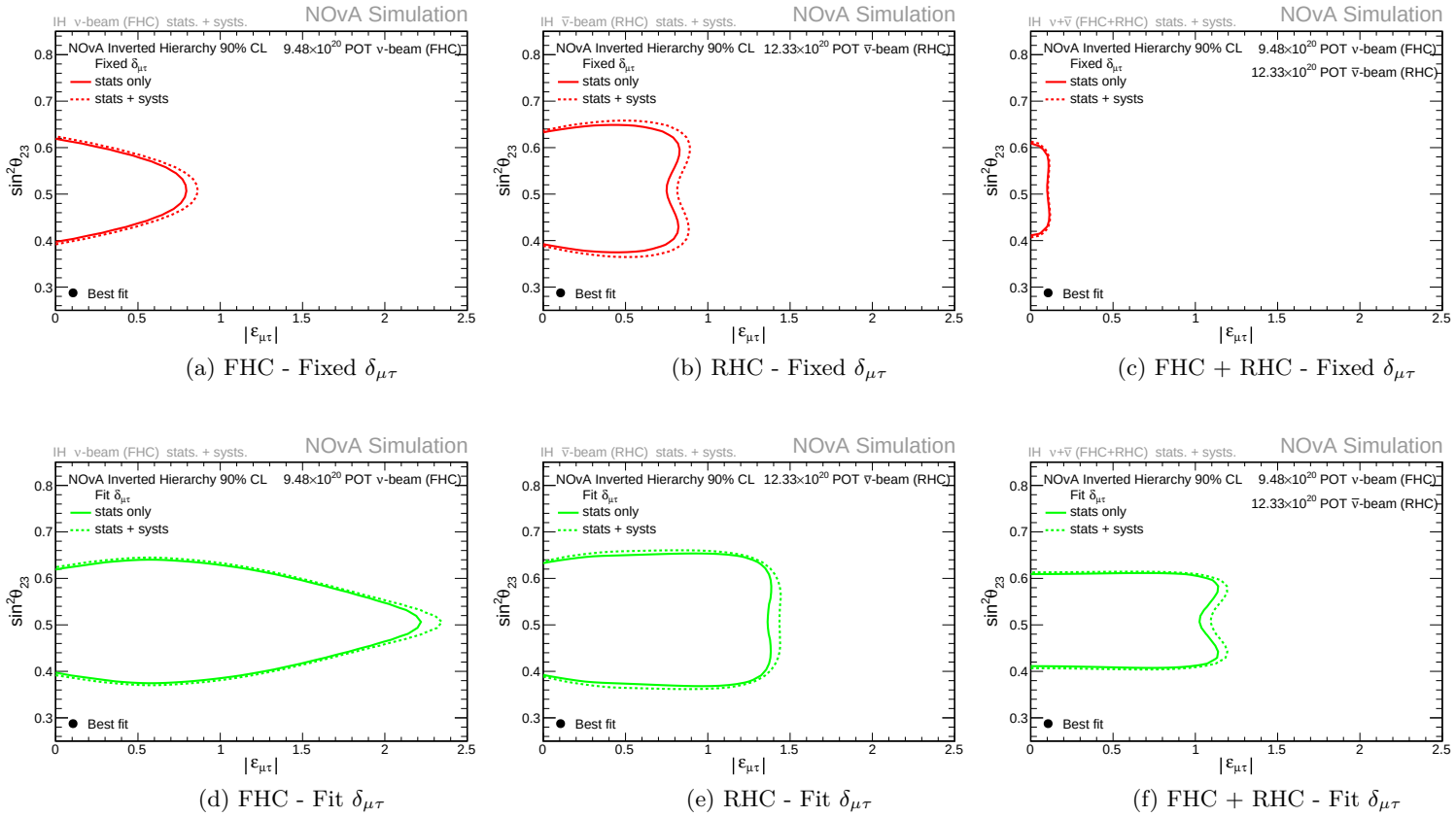

(a) FHC - Fixed $\delta_{\mu\tau}$ (b) RHC - Fixed $\delta_{\mu\tau}$ (c) FHC + RHC - Fixed $\delta_{\mu\tau}$

(d) FHC - Fit $\delta_{\mu\tau}$ (e) RHC - Fit $\delta_{\mu\tau}$ (f) FHC + RHC - Fit $\delta_{\mu\tau}$

Figure 70 – Comparison of the impact of the inclusion of systematic uncertainties (dashed line) or not (solid line) on the $|\varepsilon_{\mu\tau}| \times \sin^2(\theta_{23})$ parameter space (Inverted Hierarchy), for FHC mode, RHC mode, and the joint FHC + RHC fit. In red is shown the scenario where $\delta_{\mu\tau} = 0$ is kept fixed and not fitted, while in green we fit for $\delta_{\mu\tau}$ as well.

$\delta_{\mu\tau} \times \Delta m^2_{32}$ - Normal Hierarchy

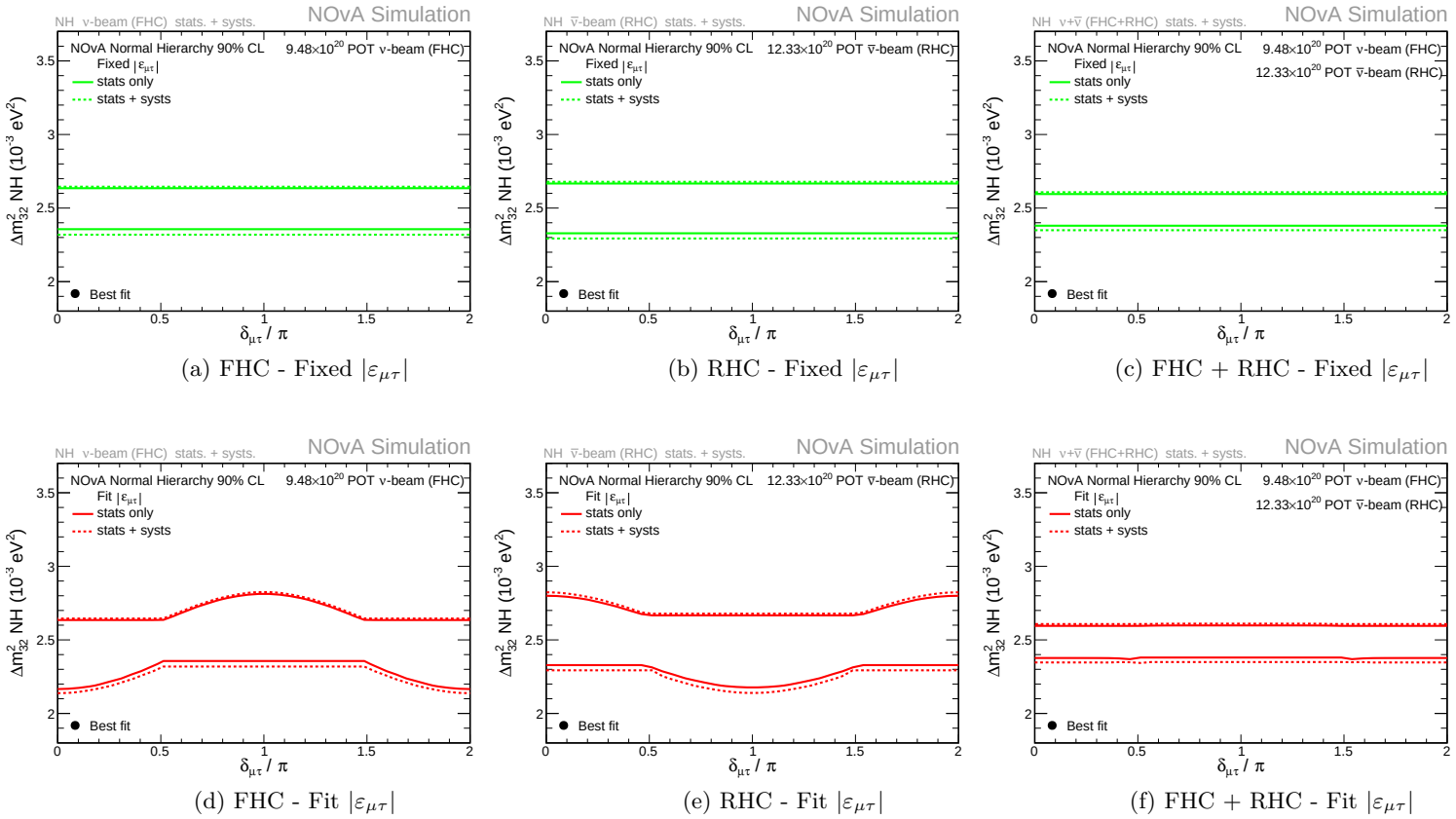

(a) FHC - Fixed $|\varepsilon_{\mu\tau}|$ (b) RHC - Fixed $|\varepsilon_{\mu\tau}|$ (c) FHC + RHC - Fixed $|\varepsilon_{\mu\tau}|$

(d) FHC - Fit $|\varepsilon_{\mu\tau}|$ (e) RHC - Fit $|\varepsilon_{\mu\tau}|$ (f) FHC + RHC - Fit $|\varepsilon_{\mu\tau}|$

Figure 71 – Comparison of the impact of the inclusion of systematic uncertainties (dashed line) or not (solid line) on the $\delta_{\mu\tau} \times \Delta m^2_{32}$ parameter space (Normal Hierarchy), for FHC mode, RHC mode, and the joint FHC + RHC fit. In green is shown the scenario where $|\varepsilon_{\mu\tau}| = 0$ is kept fixed and not fitted, while in red we fit for $|\varepsilon_{\mu\tau}|$ as well.

$\delta_{\mu\tau} \times \Delta m^2_{32}$ - Inverted Hierarchy

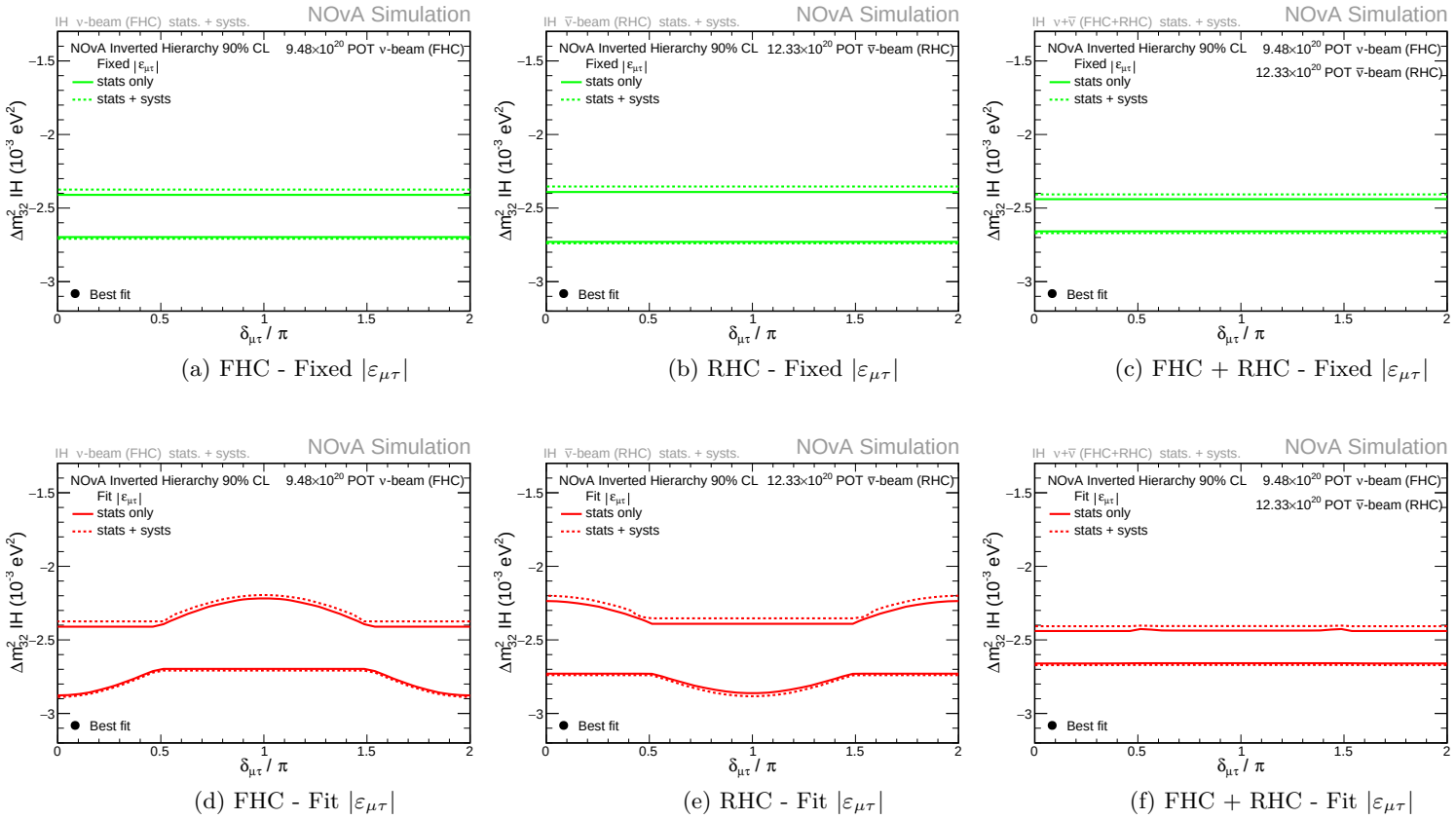

(a) FHC - Fixed $|\varepsilon_{\mu\tau}|$ (b) RHC - Fixed $|\varepsilon_{\mu\tau}|$ (c) FHC + RHC - Fixed $|\varepsilon_{\mu\tau}|$

(d) FHC - Fit $|\varepsilon_{\mu\tau}|$ (e) RHC - Fit $|\varepsilon_{\mu\tau}|$ (f) FHC + RHC - Fit $|\varepsilon_{\mu\tau}|$

Figure 72 – Comparison of the impact of the inclusion of systematic uncertainties (dashed line) or not (solid line) on the $\delta_{\mu\tau} \times \Delta m^2_{32}$ parameter space (Inverted Hierarchy), for FHC mode, RHC mode, and the joint FHC + RHC fit. In green is shown the scenario where $|\varepsilon_{\mu\tau}| = 0$ is kept fixed and not fitted, while in red we fit for $|\varepsilon_{\mu\tau}|$ as well.

$\delta_{\mu\tau} \times \sin^2(\theta_{23})$ - Normal Hierarchy

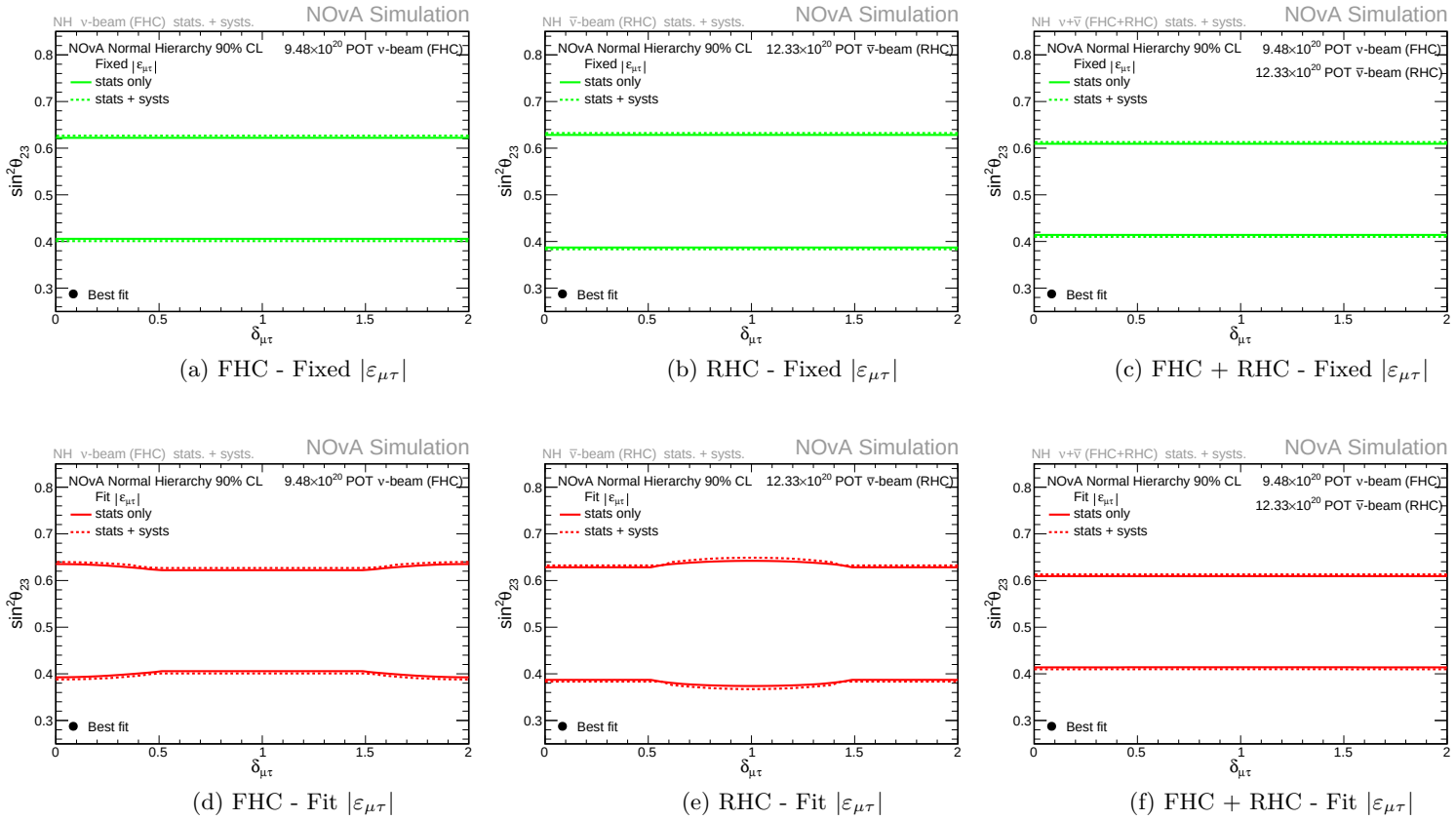

(a) FHC - Fixed $|\varepsilon_{\mu\tau}|$ (b) RHC - Fixed $|\varepsilon_{\mu\tau}|$ (c) FHC + RHC - Fixed $|\varepsilon_{\mu\tau}|$

(d) FHC - Fit $|\varepsilon_{\mu\tau}|$ (e) RHC - Fit $|\varepsilon_{\mu\tau}|$ (f) FHC + RHC - Fit $|\varepsilon_{\mu\tau}|$

Figure 73 – Comparison of the impact of the inclusion of systematic uncertainties (dashed line) or not (solid line) on the $\delta_{\mu\tau} \times \sin^2(\theta_{23})$ parameter space (Normal Hierarchy), for FHC mode, RHC mode, and the joint FHC + RHC fit. In green is shown the scenario where $|\varepsilon_{\mu\tau}| = 0$ is kept fixed and not fitted, while in red we fit for $|\varepsilon_{\mu\tau}|$ as well.

$\delta_{\mu\tau} \times \sin^2(\theta_{23})$ - Inverted Hierarchy

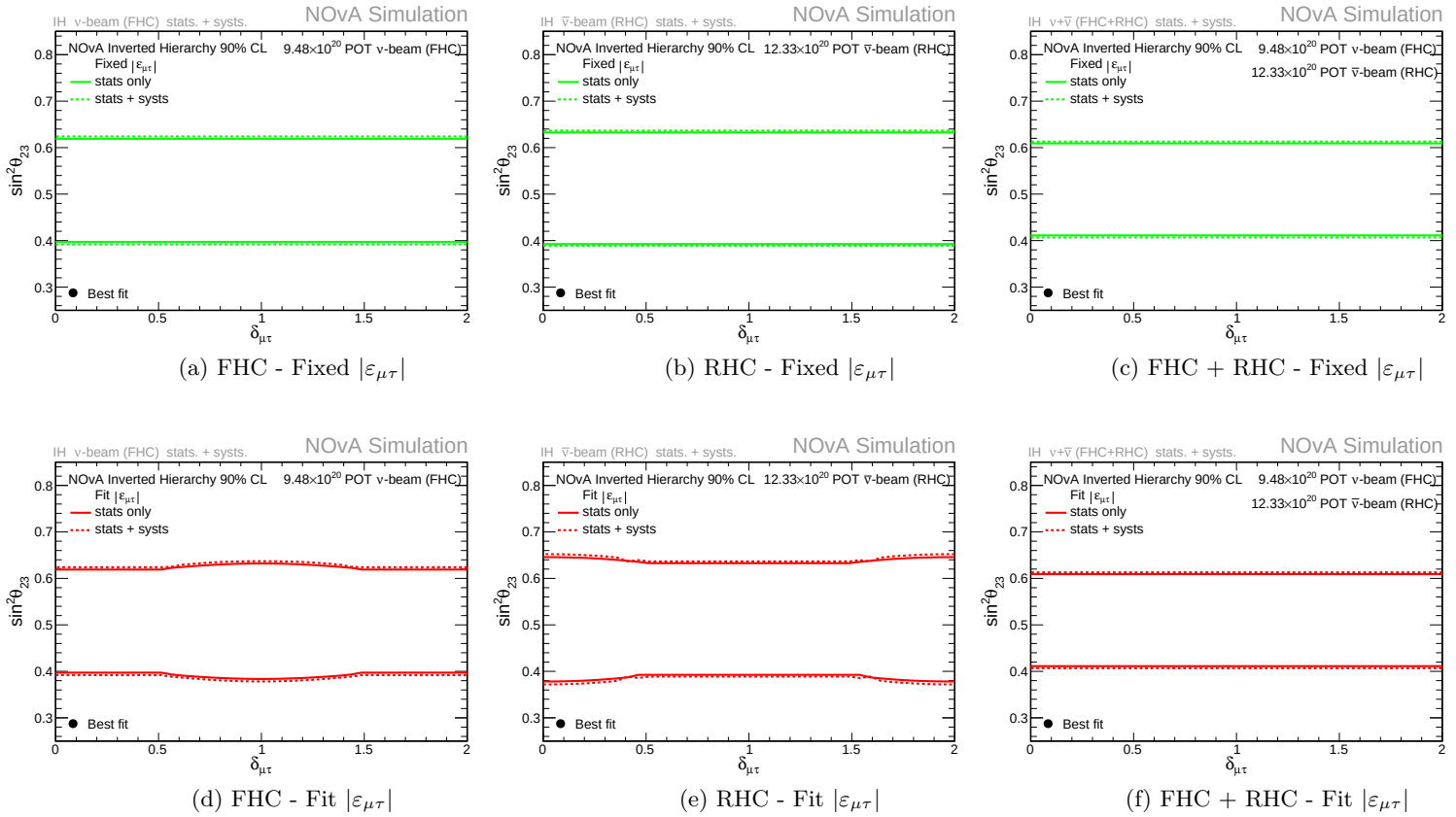

(a) FHC - Fixed $|\varepsilon_{\mu\tau}|$ (b) RHC - Fixed $|\varepsilon_{\mu\tau}|$ (c) FHC + RHC - Fixed $|\varepsilon_{\mu\tau}|$

(d) FHC - Fit $|\varepsilon_{\mu\tau}|$ (e) RHC - Fit $|\varepsilon_{\mu\tau}|$ (f) FHC + RHC - Fit $|\varepsilon_{\mu\tau}|$

Figure 74 – Comparison of the impact of the inclusion of systematic uncertainties (dashed line) or not (solid line) on the $\delta_{\mu\tau} \times \sin^2(\theta_{23})$ parameter space (Inverted Hierarchy), for FHC mode, RHC mode, and the joint FHC + RHC fit. In green is shown the scenario where $|\varepsilon_{\mu\tau}| = 0$ is kept fixed and not fitted, while in red we fit for $|\varepsilon_{\mu\tau}|$ as well.

$\delta_{\mu\tau} \times |\varepsilon_{\mu\tau}|$ - Normal Hierarchy

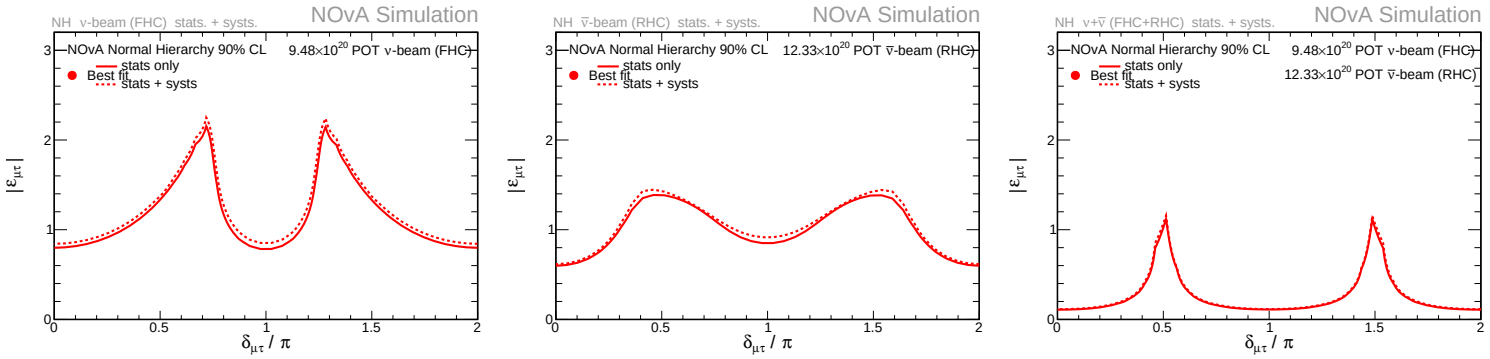

(a) FHC (b) RHC (c) FHC + RHC

Figure 75 – Comparison of the impact of the inclusion of systematic uncertainties (dashed line) or not (solid line) on the $\delta_{\mu\tau} \times |\varepsilon_{\mu\tau}|$ parameter space (Normal Hierarchy), for FHC mode, RHC mode, and the joint FHC + RHC fit.

$\delta_{\mu\tau} \times |\varepsilon_{\mu\tau}|$ - Inverted Hierarchy

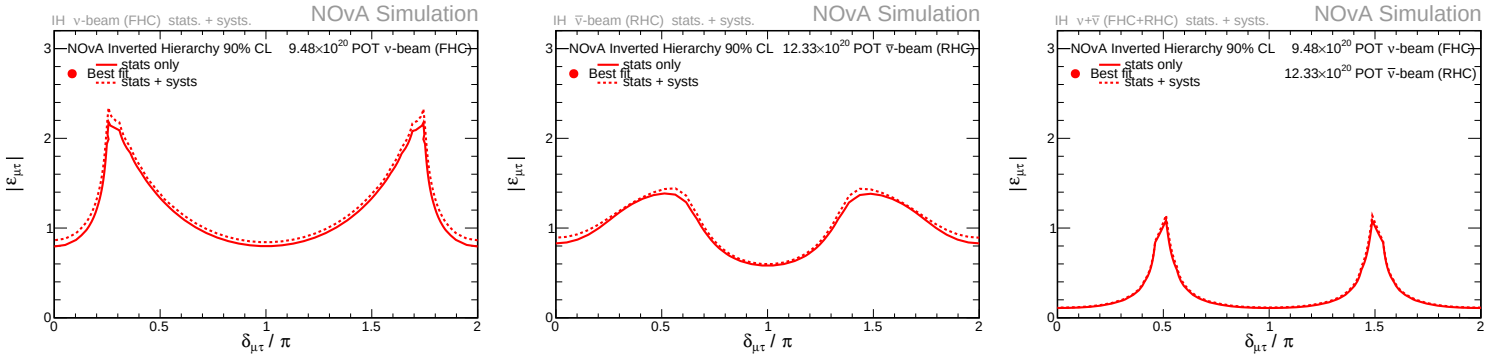

(a) FHC (b) RHC (c) FHC + RHC

Figure 76 – Comparison of the impact of the inclusion of systematic uncertainties (dashed line) or not (solid line) on the $\delta_{\mu\tau} \times |\varepsilon_{\mu\tau}|$ parameter space (Inverted Hierarchy), for FHC mode, RHC mode, and the joint FHC + RHC fit.